POWER QUALITY IMPROVEMENT IN SHUNT ACTIVE POWER FILTER-ASSISTED MICROGRID SYSTEM

BY

PRASANTA KUMAR BARIK

(Admission No. 17DP000228)

THESIS

SUBMITTED TO

INDIAN INSTITUTE OF TECHNOLOGY (INDIAN SCHOOL OF MINES), DHANBAD

For the award of the degree of

DOCTOR OF PHILOSOPHY

OCTOBER, 2024

POWER QUALITY IMPROVEMENT IN SHUNT ACTIVE POWER FILTER-ASSISTED MICROGRID SYSTEM

BY

PRASANTA KUMAR BARIK

(Admission No. 17DP000228)

THESIS

SUBMITTED TO

INDIAN INSTITUTE OF TECHNOLOGY (INDIAN SCHOOL OF MINES), DHANBAD

For the award of the degree of

DOCTOR OF PHILOSOPHY

OCTOBER, 2024

भारतीय प्रौद्योगिकी संस्थान (भारतीय खनि विद्यापीठ)
धनबाद - ८२६००४, झारखण्ड, भारत
INDIAN INSTITUTE OF TECHNOLOGY (INDIAN SCHOOL OF MINES)
DHANBAD– 826 004, JHARKHAND, INDIA

(An autonomous institute under Ministry of Education, Government of India)

17th OCTOBER, 2024

CERTIFICATE FROM THE SUPERVISOR(S)

This is to certify that the thesis entitled "**POWER QUALITY IMPROVEMENT IN SHUNT ACTIVE POWER FILTER-ASSISTED MICROGRID SYSTEM**" being submitted to the Indian Institute of Technology (Indian School of Mines), Dhanbad by **MR. PRASANTA KUMAR BARIK,** Admission No. **17DP000228**, for the award of Doctor of Philosophy (Ph.D.) Degree is a bonafide work carried out by him, in the Department of **ELECTRICAL ENGINEERING**, **IIT(ISM), Dhanbad**, under our supervision and guidance. The thesis has fulfilled all the requirements as per the regulations of this Institute and, in our opinion, has reached the standard needed for submission. The results embodied in this thesis have not been submitted to any other university or institute for the award of any degree or diploma.

Signature of Supervisor

(Dr. Gauri Shankar)
Associate Professor,
Department of Electrical Engineering,
Indian Institute of Technology (ISM), Dhanbad, Jharkhand-826004, India
Date: 17-10-2024

Signature of External Co- Supervisor

(Dr. Pradeepta Kumar Sahoo)
Associate Professor,
Department of FMPE,
College of Agricultural Engineering & Technology, Bhubaneswar, Odisha-751003, India
Date: 17-10-2024

भारतीय प्रौद्योगिकी संस्थान (भारतीय खनि विद्यापीठ)
धनबाद - ८२६००४, झारखण्ड, भारत
INDIAN INSTITUTE OF TECHNOLOGY (INDIAN SCHOOL OF MINES)
DHANBAD– 826 004, JHARKHAND, INDIA

(An autonomous institute under Ministry of Education, Government of India)

17th OCTOBER, 2024

Certificate for Classified Data

This is to certify that the thesis entitled "**POWER QUALITY IMPROVEMENT IN SHUNT ACTIVE POWER FILTER-ASSISTED MICROGRID SYSTEM"** being submitted to the Indian Institute of Technology (Indian School of Mines), Dhanbad by **Mr. Prasanta Kumar Barik** for award of Doctor of Philosophy (Ph.D.) Degree in **Electrical Engineering** does not contains any classified information. This work is original and yet not been submitted to any institution or university for the award of any degree.

Signature of Supervisor	Signature of External Co-Supervisor	Signature of Scholar
Name: Dr. Gauri Shankar Date: 17-10-2024	Name: Dr. Pradeepta Kumar Sahoo Date: 17-10-2024	Name: Prasanta Kumar Barik Date: 17-10-2024

भारतीय प्रौद्योगिकी संस्थान (भारतीय खनि विद्यापीठ)
धनबाद - ८२६००४, झारखण्ड, भारत
INDIAN INSTITUTE OF TECHNOLOGY (INDIAN SCHOOL OF MINES)
DHANBAD– 826 004, JHARKHAND, INDIA

(An autonomous institute under Ministry of Education, Government of India)

17th OCTOBER, 2024

Certificate Regarding English Checking

This is to certify that the thesis entitled "**POWER QUALITY IMPROVEMENT IN SHUNT ACTIVE POWER FILTER-ASSISTED MICROGRID SYSTEM**" being submitted to the Indian Institute of Technology (Indian School of Mines), Dhanbad by **MR. PRASANTA KUMAR BARIK,** Admission No. **17DP000228**, for the award of Doctor of Philosophy (Ph. D.) Degree has been thoroughly checked for quality of English and logical sequencing of topics.

It is hereby certified that the standard of English is good and that grammar and typos have been thoroughly checked.

It is now worthy for evaluation by the panel of examiners.

Signature of Supervisor	Signature of External Co-Supervisor	Signature of Scholar
Name: Gauri Shankar Date: 17-10-2024	Name: Pradeepta Kumar Sahoo Date: 17-10-2024	Name: Prasanta Kumar Barik Date: 17-10-2024

COPYRIGHT AND CONSENT FORM

To ensure uniformity of treatment among all contributors, other forms may not be substituted for this form, nor may any wordingof the form be changed. This form is intended for original material submitted to the IIT (ISM), Dhanbad and must accompany anysuch material in order to be published by the ISM. Please read the form carefully and keep a copy for your files.

TITLE OF THESIS: POWER QUALITY IMPROVEMENT IN SHUNT ACTIVE POWER FILTER-ASSISTED MICROGRID SYSTEM

PRASANTA KUMAR BARIK

Ph.D. Scholar, Registration No.: 17DP000228, Department of Electrical Engineering

Indian Institute of Technology (Indian School of Mines), Dhanbad-826004, Jharkhand, India

COPYRIGHT TRANSFER

1. The undersigned hereby assigns to Indian Institute of Technology (Indian School of Mines), Dhanbad all rights under copyrightthat may exist in and to: (a) the above Work, including any revised or expanded derivative works submitted to the ISM by theundersigned based on the work; and (b) any associated written or multimedia components or other enhancements accompanying the work.

CONSENT AND RELEASE

2. In the event the undersigned makes a presentation based upon the work at a conference hosted or sponsored in whole or in partby the IIT (ISM) Dhanbad, the undersigned, in consideration for his/her participation in the conference, hereby grants the ISMthe unlimited, worldwide, irrevocable permission to use, distribute, publish, license, exhibit, record, digitize, broadcast, reproduce and archive; in any format or medium, whether now known or hereafter developed: (a) his/her presentation and comments at the conference; (b) any written materials or multimedia files used in connection with his/her presentation; and (c)any recorded interviews of him/her (collectively, the "Presentation"). The permission granted includes the transcription and reproduction of the Presentation for inclusion in products sold or distributed by IIT(ISM) Dhanbad and live or recorded broadcast of the Presentation during or after the conference.
3. In connection with the permission granted in Section 2, the undersigned hereby grants IIT (ISM) Dhanbad the unlimited, worldwide, irrevocable right to use his/her name, picture, likeness, voice and biographical information as part of theadvertisement, distribution and sale of products incorporating the Work or Presentation, and releases IIT (ISM) Dhanbad fromany claim based on right of privacy or publicity.
4. The undersigned hereby warrants that the Work and Presentation (collectively, the "Materials") are original and that he/she isthe author of the Materials. To the extent the Materials incorporate text passages, figures, data or other material from the worksof others, the undersigned has obtained any necessary permissions. Where necessary, the undersigned has obtained all third-party permissions and consents to grant the license above and has provided copies of such permissions and consents to IIT (ISM) Dhanbad.

GENERAL TERMS

* The undersigned represents that he/she has the power and authority to make and execute this assignment.
* The undersigned agrees to indemnify and hold harmless the IIT (ISM) Dhanbad from any damage or expense that may arise in the event of a breach of any of the warranties set forth above.
* In the event the above work is not accepted and published by the IIT (ISM) Dhanbad or is withdrawn by the author(s) before acceptance by the IIT(ISM) Dhanbad, the foregoing copyright transfer shall become null and void and all materials embodyingthe Work submitted to the IIT(ISM) Dhanbad will be destroyed.
* For jointly authored Works, all joint authors should sign, or one of the authors should sign as authorized agent for the others.

Prasanta Kumar Barik

Prasanta Kumar Barik

(Signature of the Author)

ACKNOWLEDGEMENT

I thank the Almighty God, who gave me the opportunity and strength to carry out this work. This acknowledgement is dedicated to those people, who's beautiful, creative and unpretentious mind has made my journey worthwhile calling an experience.

Foremost, I would like to express my sincere gratitude to my advisor *Dr. Gauri Shankar,* for his exemplary academic standards, counsel, insight, support, care and encouragement. His extensive knowledge, vision and expertise, invaluable technical comments and editorial advice have played a pertinent role in the accomplishment of this work. Indeed, it was a great honor and privilege for me to pursue my doctoral research work under his guidance.

I would like to express my sincere gratitude to my external co-supervisor (Dr.) Pradeepta Kumar Sahoo for helping me throughout my research period. My heartfelt thanks go to Prof. Sukanta Das, Professor and Head of the Department of Electrical Engineering, IIT (ISM), Dhanbad for his constant support and encouragement to complete this research work.

My sincere thanks to Prof. (Dr.) Pradip Kumar Sadhu, Dr. Vivekananda Mukherjee, Department of Electrical Engineering, and Dr. Mrinal Sen, Department of Electronics and Communication Engineering, IIT (ISM), Dhanbad, for their kind guidance and supports. I do express my sincere respects to all the faculty members of Electrical Engineering Department of IIT (ISM), Dhanbad, for their kind suggestions and cooperation. My sincere thanks to the staff members of Mechanical and Electrical Engineering Department of OUAT, Bhubaneswar, for providing me all support to complete my research work

A special thanks to my family. Words cannot be expressed how grateful I am to my father, mother, brother, sisters and in-laws for their patience, understanding and encouragement during the different phases of my work. A very special thanks to my adored and supportive wife, Ruchy, who always stood nearby to me whenever I needed her, and my beloved son Pratyush, whose sacrifice has served as an inspiration to accomplish this dream.

Finally, this dissertation has become the reality with the kind support of many individuals and I would like to extend my deepest gratitude and thanks to all of them.

Prasanta Kumar Barik

Date: 17-10-2024 Prasanta Kumar Barik

Place: IIT(ISM), Dhanbad Regd. No: 17DP000228

ABSTRACT

In recent decades, a concept of modular generation systems, primarily based on renewable energy sources (RES) comprising power electronics interface, forming microgrid (MG), has emerged, where localized generation modules supplement conventional generation. Unlike fossil-fuel-based traditional generators, it is a new alternative way of producing electrical energy at the distribution level that does not pollute the environment. These can be operated either in standalone or grid-connected modes. The use of power electronics-based interfaces or nonlinear loads causes unwanted severe power quality (PQ) concerns. Any anomalous behaviour on a power system that emerges as voltage or current and issues with the regular functioning of electronics or electrical devices is referred to as a PQ issue. Voltage swell, voltage sag, voltage flicker, harmonics etc., are a few examples of PQ issues. Out of these, the presence of harmonics results in failure of highly sensitive loads, transformer overheating and drastically decreased power distribution efficacy. Hence, harmonics minimization has become essential. In the past, harmonics and reactive power have been compensated using passive filters. These filters are bulky and challenging to adjust for changes in device characteristics. Recently, harmonics mitigation in power systems has been widely carried out utilizing shunt active power filters (SAPFs) and has become a popular way to realize superior PQ levels in power systems. The SAPF injects an appropriate compensating current for the mitigation of harmonics in the source current at the point of common coupling of the power system. However, its ability to generate appropriate compensating current is dependent on the operation of three control loops utilized for reference current generation (RCG), dc-link voltage (V_{dc}) regulation, and pulse width modulation (PWM) signal for the voltage source inverter associated with the SAPF. However, its ability to generate appropriate compensatory current is dependent on the operation of three control loops utilized for RCG, V_{dc} regulation.

A literature survey reveals that the SAPF has been widely used to enhance the MG system's PQ levels in grid-connected mode. However, hardly any attention has been given to study the PQ challenges in standalone MG system. Therefore, in this dissertation work, a typical standalone MG system is adopted, which is comprised of solar photovoltaic (SPV), wind energy system (WES), and fuel cell (FC) units, to do PQ analysis using SAPF. In relation to the three control loops of SAPF, researchers around the globe have proposed numerous approaches for each. The individual proposed strategy has its own merits and limitations. However, there is still a lot of scope to either improve the existing methods or explore novel techniques related to

the mentioned control loops. Given the above, the present author has first done a detailed performance examination of the widely used conventional strategies in mitigating the PQ issues in a standalone MG system. Later, an attempt is made to propose new techniques related to the SAPF's different control loop. Finally, a comparative performance analysis is carried out between the proposed and the existing approaches to prove the superiority of one over the others.

In the first proposal, widely used synchronous reference frame (SRF) and modified SRF (MSRF) approaches for RCG (considering one at a time), proportional-integral (PI) controller or fuzzy logic controller (FLC) technique for V_{dc} control (considering one at a time), and a basic hysteresis current controller (HCC) approach for PWM signal generation have been employed to realize the SAPF model. Utilizing these, different combinations of three control loops are formed (referred to as SRF-PI-HCC, MSRF-PI-HCC, and MSRF-FLC-HCC strategies). Thereafter, the harmonics mitigation capabilities of these strategies are investigated considering the ideal source and nonlinear load-changing conditions. It is observed from the results obtained that the MSRF-FLC-HCC strategy outperforms the other. Besides, the performance of each strategy in regulating V_{dc} profile and its settling time under load-changing conditions is also examined. The best strategy found has its own limitations in regulating the V_{dc} profile. Hence, there is further scope to improve the THD and V_{dc} profiles by introducing new control schemes for the three control loops of the SAPF.

Hence, the second proposal suggests a new control technique for controlling the V_{dc} deviation during source and load-changing conditions. In this case, a novel fuzzy inverted error deviation (FIED) controller is proposed to control and diminish the ripples in the V_{dc} waveform, particularly under load-changing conditions. The benefits of FIED over FLC lie in its reduced computational load, which is achieved by employing a lesser number of membership functions and rules. Furthermore, it operates based on the principle of manipulating indirect voltage errors, thereby, minimizing voltage deviations that arise due to load-changing conditions. The main disadvantages of the HCC switching scheme (used in the first proposal) are (a) PWM frequency is not constant, (b) it is challenging to build the filter circuit and (c) it results in greater switching losses. Besides, the varying switching frequency impacts the SAPF's efficiency and reliability. Hence, in this proposal, the performance of SAPF with some advanced switching schemes is also tested under ideal and non-ideal source conditions. The adopted schemes are adaptive HCC (AHCC) and adaptive fuzzy HCC (AFHCC). Thereafter, the best combination

among strategies studied/proposed for three control loops is found based on the comparative performance analysis. Several simulation-based experiments (referred to as different scenarios) are carried out. Finally, it is concluded that the proposed MSRF-FIED-AFHCC scheme performs exceptionally well in curbing the deviation and settling time in V_{dc} waveform and improving THD profile compared to other counterparts under source and load-changing conditions. The MSRF approach fails to detect the synchronizing angle due to non-ideal source conditions, which impacts the harmonics mitigation capability of the SAPF. Hence, the performance of SAPF with an advanced synchronization technique is tested in the next proposal under both ideal and non-ideal source conditions.

In the third proposal, a novel negative feedback PLL-based MSRF (NFPLL-MSRF) method is proposed to conquer the drawbacks of the current MSRF approach. The proposed method for RCG is used in combination with the FIED for V_{dc} control, AFHCC for PWM signal generation. The effectiveness of the proposed combination (i.e., NFPLL-MSRF-FIED-AFHCC) is investigated under ideal/non-ideal source and load-changing conditions. According to simulation results, the proposed NFPLL-MSRF-FIED-AFHCC combined control technique has offered improved SAPF mitigation performance by offering the minimum THD values in source current and the best V_{dc} profile over the other combinations. The impact of asymmetrical loading and change in load parameters on the effectiveness of the proposed controller-based realized SAPF is further investigated.

It is concluded from the last three proposals that, in terms of performance, the proposed NFPLL-MSRF-FIED-AFHCC strategy is found to be the best among all. Therefore, in the fourth proposal, the performance of the proposed NFPLL-MSRF-FIED-AFHCC-based SAPF control strategy is validated using a real-time digital simulator (OPAL-RT 4510).

Table of Contents

Certificate of the Supervisor……...…… i

Certificate Regarding Classified Data ……... iii

Certificate Regarding English Check ……..... v

Copyright and Consent Form……. vii

Acknowledgement……. viii

Abstract…….. ix

Table of Contents……... xii

List of Abbreviations…….. xvii

List of Symbols …….. xix

List of Figures …… xxi

List of Tables ……. xxviiii

1 INTRODUCTION……. 1

1.1 PREAMBLE……. 2

1.2 CONCEPT OF MICROGRID ……. 3

1.2.1 Microgrid Operation…… 4

1.2.1.1 Standalone microgrid systems…… 4

1.2.1.2 Grid-connected microgrid systems……. 5

1.2.2 Solar PV System……. 10

1.2.3 Wind Energy System……... 11

1.2.4 Fuel Cell System……. 12

1.3 POWER QUALITY ISSUES……..... 13

1.3.1 Magnitude Disturbances…… 15

1.3.2 Waveform Disturbances……. 18

1.4 SOLUTION TO POWER QUALITY ISSUES……. 20

1.4.1 Power Filters…… 20

1.4.1.1 Passive power filters…… 21

1.4.1.2 Active power filters…… 22

1.4.1.3 Hybrid power filters…… 24

1.5 RESEARCH BACKGROUND……. 25

1.5.1 Shunt Active Power Filter ……... 26
1.5.1.1 Reference current generation method……. 26
1.5.1.2 Dc-link voltage regulation method……. 28
1.5.1.3 Switching pulse generation method……. 29
1.6 MOTIVATION AND CONTRIBUTION OF THE THESIS…… 32
1.7 ORGANIZATION OF THESIS……. 33

2 POWER QUALITY ANALYSIS OF MICROGRID UNDER MSRF-FLC-HCC CONTROLLER-BASED SAPF ……. 36
2.1 INTRODUCTION……. 37
2.1.1 Motivation of the Present Work……. 37
2.1.2 Contribution of the Present Chapter…… 39
2.1.3 Chapter Orientation……. 40
2.2 DESIGN OF MICROGRID……. 40
2.2.1 Modeling of Solar PV System……. 41
2.2.2 Modeling of Wind Energy System ……. 45
2.2.3 Modeling of Fuel Cell System ……. 47
2.3 DESIGN OF SAPF……... 51
2.4 CONTROL SCHEME FOR SAPF…… 53
2.4.1 Reference Current Generation Techniques …… 54
2.4.2 Dc-link Voltage Control Techniques……. 58
2.4.3 Switching Pulse Generation Techniques……. 62
2.5 RESULT AND DISCUSSION……. 63
2.5.1 Performance Analysis without SAPF and with SAPF Employing SRF-PI-HCC-based Control Scheme…… 65
2.5.2 Performance Analysis Employing MSRF-PI-HCC-based Control Scheme……... 65
2.5.3 Performance Analysis Employing MSRF-FLC-HCC-based Control Scheme…… 67
2.5.4 Comparative Performance Analysis of SAPF using Studied MSRF-FLC-HCC with those of SAPF with other Techniques for Control of Dc-link Voltage under Steady-State and Load-Changing Condition…… 69

2.6 SUMMARY …… 73

3 POWER QUALITY ENHANCEMENT USING A NOVEL FIED-BASED SAPF IN MICROGRID……. 76

3.1 INTRODUCTION……. 77

3.1.1 Motivation of the Present Work……. 79

3.1.2 Contribution of the Present Chapter…… 79

3.1.3 Chapter Orientation……. 80

3.2 DC-LINK VOLTAGE CONTROL SCHEME…… 80

3.2.1 Proposed FIED Control Technique …….……. 81

3.3 ADOPTED SWITCHING PULSE GENERATION TECHNIQUE…… 83

3.3.1 Studied AHCC Technique ……. 85

3.3.2 Studied AFHCC Technique ……. 86

3.4 RESULT AND DISCUSSION……... 88

3.4.1 SAPF employing MSRF-FLC-AHCC and MSRF-FLC-AFHCC schemes considering an ideal source …… 90

3.4.2 SAPF employing MSRF-FIED-AHCC and MSRF-FIED-AFHCC schemes considering an ideal source …… 93

3.4.3 SAPF employing MSRF-FLC-AHCC and MSRF-FLC-AFHCC schemes considering non-ideal source ……. 96

3.4.4 SAPF employing MSRF-FIED-AHCC and MSRF-FIED-AFHCC schemes considering non-ideal source …… 97

3.4.5 Comparative performance analysis of the proposed FIED control scheme with the conventional schemes (i.e., PI and FLC) for V_{dc} regulation under steady-state and load-changing conditions…… 103

3.5 SUMMARY……. 107

4 POWER QUALITY ENHANCEMENT USING A NOVEL NFPLL-MSRF-BASED TECHNIQUE FOR SAPF IN MICROGRID …… 109

4.1 INTRODUCTION……. 110

4.2.1 Motivation of the Present Work……. 113

4.2.2 Contribution of the Present Chapter…… 114

4.2.3 Chapter Orientation…… 115
4.2 DESIGN OF NFPLL-MSRF METHOD……. 115
4.2.1 Modelling of the Proposed NFPLL-MSRF Scheme……... 115
4.3 RESULT AND DISCUSSION……... 119
4.3.1 Performance analysis of the proposed NFPLL-MSRF-FLC-AFHCC method under ideal and non-ideal source conditions……. 121
4.3.2 Performance analysis of the proposed NFPLL-MSRF-FIED-AFHCC method under ideal and non-ideal source conditions……... 123
4.3.3 Performance analysis of the proposed control strategy under asymmetrical loading and change in load parameters……. 127
4.3.4 Comparative performance analysis of the proposed control scheme with that of the studied one for V_{dc} regulation under steady-state and load-changing conditions…… 131
4.4 SUMMARY……. 134

5 REAL-TIME IMPLEMENTATION OF THE NFPLL-MSRF-FIED-AFHCC-BASED SAPF USING OPAL-RT 4150 DIGITAL SIMULATOR……. 137
5.1 INTRODUCTION……. 138
5.2.1 Motivation of the Present Work……. 138
5.2.2 Contribution of the Present Chapter…… 139
5.2.3 Chapter Orientation…… 139
5.2 ARCHITECTURE OF RT-LAB SIMULATOR…… 139
5.2.1 Block Diagram and Schematic Interface ……. 140
5.2.2 Inputs and Outputs (I/O)…… 140
5.2.3 Simulator Configuration …… 141
5.2.4 Working of RT-LAB ……. 141
5.3 RESULT AND DISCUSSION……. 142
5.3.1 Performance Analysis under Ideal Source Condition with SAPF Employing NFPLL-MSRF-FIED-AFHCC Controller Approach using both MATLAB Simulation and OPAL-RT Digital 142

Simulator…….
5.3.2 Performance analysis under Non-ideal Source Condition with SAPF Employing NFPLL-MSRF-FIED-AFHCC Controller Approach using both MATLAB Simulation and OPAL-RT Digital Simulator……. 146
5.3.3 Comparative Performance Analysis of SAPF using Proposed NFPLL-MSRF-FIED-AFHCC with those of SAPF with Conventional Techniques for Control of Dc-link voltage using OPAL-RT Digital Simulator…… 149
5.4 SUMMARY……. 151

6 CONCLUSION AND FUTURE WORK……. 153
6.1 CONCLUSION……. 154
6.2 FUTURE WORK……..... 157

REFERENECES……..... 158

LIST OF PUBLICATIONS……... 174

CURRICULUM VITA…..……..…… 175

List of Abbreviations

Abbreviation	Description
AC	Alternating current
APF	Active power filter
BESS	Battery energy storage system
BW	Bandwidth
CPD	Custom power system
CFMRC	Current fed multi resonant converter
DC	Direct current
DER	Distributed energy resources
DG	Distributed generation
DFT	Discrete Fourier transform
DFIG	Doubly fed induction generator
DVR	Dynamic voltage restorer
FACTS	Flexible alternating current transmission systems
FC	Fuel cell
FD	Frequency domain
FIED	Fuzzy inverted error deviation
FFT	Fast Fourier transform
FLL	Frequency-locked loop
GI	Generalized integrator
GHG	Greenhouse gas
HPF	High pass filter
HAWT	Horizontal axis wind turbine
IEEE	Institute of electrical and electronics engineering
IGBT	Insulated gate bipolar transistor
IPT	Inverse-park transform
LPF	Low-pass filter
MSRF	Modified synchronous reference frame
MPPT	Maximum power point tracking
NFPLL	Negative feedback Phase-locked loop

Abbreviation	Description
PCC	Point of common coupling
PD	Phase detector
PE	Power electronics
PEMFC	Proton exchange membrane fuel cell
PMSG	Permanent magnet synchronous generator
P&O	Perturb and observe
PQ	Power quality
PI	Proportional-integral
PLL	Phase-locked loop
PSC	Positive sequence component
PV	Photovoltaic
PWM	Pulse width modulation
RMS	Root mean square
RCG	Reference current generation
SAPF	Shunt active power filter
STATCOM	Static compensator
SRF	Synchronous reference frame
SMPS	Switched mode power supply
SCIG	Squirrel cage induction generator
SPG	Switching pulse generation
SOFC	Solid oxide fuel cell
TSC	Thyristor switched capacitors
TSR	Thyristor switched reactors
THD	Total harmonic distortion
UPFC	Unified power flow controller
UPQC	Unified power quality conditioner
UPS	Uninterrupted power supply
VAWT	Vertical axis wind turbine
VSI	Voltage source inverter
WECS	Wind energy conversion system

List of Symbols

Symbol	Nomenclature
C	Capacitor
C_{dc}	dc-link capacitor
C_s	Source capacitance
C_l	Load capacitance
$D_{\max}$	Maximum duty ratio
$D_{\min}$	Minimum duty ratio
I_{ph}	Diode photo current
I_{pv}	Diode photo current
I_0	Diode reverse saturation current
I_{sh}	Diode leakage current
I_{sc}	Short circuit current
I_{cabc}	Compensating current
I_{sabc}	Source current
I_{labc}	Load current
K_p	Proportional gain
K_i	Integral gain
L	Inductance
mH	Milli Henry
m	Modulation index
N_p	Cells connected in parallel
N_s	Cells connected in series
P_m	Mechanical power
q	Electron charge
R_{se}	Series resistance

R_{sh}	Shunt resistance
R_s	Source resistance
T	Number of turns.
V_{oc}	Open circuit voltage
V_{mp}	Voltage at maximum power
V_{dc}	dc-link voltage
V_s	Input voltage
ϕ_m	Maximum flux
η	Efficiency
ρ	Air density
λ	Tip-speed ratio

List of Figures

Figure No.		Page No.
Figure 1.1	Block diagram of standalone MG system	05
Figure 1.2	Block diagram of grid-connected MG system	06
Figure 1.3	Voltage sag waveform	16
Figure 1.4	Voltage swell waveform	17
Figure 1.5	Harmonics distortion	18
Figure 1.6	Classification of power filters	20
Figure 1.7	Passive filter configuration	21
Figure 1.8	SAPF model	22
Figure 1.9	Series APF model	23
Figure 1.10	UPQC model	24
Figure 2.1	Block diagram of studied MG structure	41
Figure 2.2	SPV unit equivalent circuit	42
Figure 2.3	Flow chart of P&O algorithm	43
Figure 2.4	Block diagram of SPV with MPPT and boost converter	44
Figure 2.5	Output voltage waveform (V_{spv}) of SPV system	44
Figure 2.6	Block diagram of WES	45
Figure 2.7	Power output vs. rotor speed curve	45
Figure 2.8	Overall model of WES	46
Figure 2.9	Output voltage waveform (V_{wes}) of WES	46
Figure 2.10	Basic PEMFC model	48
Figure 2.11	A generalized model of FC	49
Figure 2.12	Output voltage waveform (V_{FC}) of FC	50
Figure 2.13	Studied SAPF model	51
Figure 2.14	SRF technique	55
Figure 2.15	MSRF technique	57
Figure 2.16	PI controller-based V_{dc} control scheme	58
Figure 2.17	Block diagram of FLC scheme	59

Figure No.		Page No.
Figure 2.18	MFs for FLC scheme	60
Figure 2.19	HCC-based switching pulses generation scheme	62
Figure 2.20	SAPF with MSRF-FLC-HCC-based control scheme control scheme	63
Figure 2.21	Profiles obtained under nonlinear RL- and RC-loads (a) i_{sabc} before compensation, (b) THD of i_{sabc} before compensation, (c) i_{cabc} generated using SRF-PI-HCC approach, (d) i_{sabc} after compensation and (e) THD of i_{sabc} after compensation	66
Figure 2.22	Profiles obtained under nonlinear RL-and RC-loads (a) i_{cabc} generated using MSRF-PI-HCC approach, (b) i_{sabc} after compensation and (c) THD of i_{sabc} after compensation	67
Figure 2.23	Profiles obtained under nonlinear RL-and RC-loads of (a) i_{cabc} generated using MSRF-FLC-HCC approach, (b) i_{sabc} after compensation	68
Figure 2.24	V_{dc} profiles obtained considering RL-Load and RC-Load using (a) SRF-PI (b) MSRF-PI and (c) MSRF-FLC scheme	70
Figure 2.25	Comparative profiles of V_{dc} obtained using SRF-PI-HCC, MSRF-PI-HCC and MSRF-FLC-HCC methods under load-changing conditions (RC-to RL-type).	71
Figure 2.26	Comparative profiles of V_{dc} obtained using SRF-PI-HCC, MSRF-PI-HCC and MSRF-FLC-HCC methods under load-changing conditions (RL-to RC- type).	72
Figure 3.1	Block diagram of the proposed FIED scheme	82
Figure 3.2	Relevant waveforms of the proposed FIED scheme	82
Figure 3.3	MFs for input variables	83

Figure No.		Page No.
Figure 3.4	MFs for output variables	84
Figure 3.5	AHCC-based switching pulses generation scheme	85
Figure 3.6	HB calculation block of AHCC	85
Figure 3.7	HB calculation block of AFHCC	87
Figure 3.8	MFs used for input variables $(e(HB), ce(HB))$ and output variable (HB^*)	87
Figure 3.9	SAPF with MSRF-FLC/FIED-AHCC/AFHCC -based control scheme	88
Figure 3.10	Profiles obtained under RL- and RC-type nonlinear loads (a) i_{cabc} generated using MSRF-FLC-AHCC approach, (b) i_{sabc} after compensation and (c) THD of i_{sabc} after compensation	91
Figure 3.11	Profiles obtained under RL- and RC-type nonlinear loads (a) i_{cabc} generated using MSRF-FLC-AFHCC approach, (b) i_{sabc} after compensation and (c) THD of i_{sabc} after compensation	92
Figure 3.12	Profiles obtained under RL- and RC-type nonlinear loads (a) i_{cabc} generated using MSRF-FIED-AHCC approach, (b) i_{sabc} after compensation and (c) THD of i_{sabc} after compensation	93
Figure 3.13	Profiles obtained under RL- and RC-type nonlinear loads (a) i_{cabc} generated using MSRF-FIED-AFHCC approach, (b) i_{sabc} after compensation and (c) THD of i_{sabc} after compensation	94
Figure 3.14	Profiles obtained under RL- and RC-type nonlinear loads (a) V_{sabc} under non-ideal source, (b) i_{sabc} before compensation (c) THD of i_{sabc} before compensation	97
Figure 3.15	Profiles obtained under RL- and RC-type nonlinear loads	98

Figure No.		Page No.
	(a) i_{cabc} generated using MSRF-FLC-AHCC approach, (b) i_{sabc} after compensation and (c) THD of i_{sabc} after compensation	
Figure 3.16	Profiles obtained under RL- and RC-type nonlinear loads (a) i_{cabc} generated using MSRF-FLC-AFHCC approach, (b) i_{sabc} after compensation and (c) THD of i_{sabc} after compensation	98
Figure 3.17	Profiles obtained under RL- and RC-type nonlinear loads (a) i_{cabc} generated using MSRF-FIED-AHCC control scheme, (b) i_{sabc} after compensation and (c) THD of i_{sabc} after compensation	100
Figure 3.18	Profiles obtained under RL- and RC-type nonlinear loads (a) i_{cabc} generated using MSRF-FIED controller with AFHCC switching scheme, (b) i_{sabc} after compensation and (c) THD of i_{sabc} after compensation	101
Figure 3.19	V_{dc} profiles obtained considering RL- and RC-type nonlinear loads under different controller-based SAPF (a) MSRF-PI-AFHCC scheme, (b) MSRF-FLC-AFHCC scheme, and (c) MSRF-FIED-AFHCC	104
Figure 3.20	Comparative profiles of V_{dc} obtained using MSRF-PI-AFHCC, MSRF-FLC-AFHCC and MSRF-FIED-AFHCC methods under load-changing conditions (RC- to RL-type)	105
Figure 3.21	Comparative profiles of V_{dc} obtained using MSRF-PI-AFHCC, MSRF-FLC-AFHCC and MSRF-FIED-AFHCC methods under load-changing conditions (RL- to RC- type)	106
Figure 4.1	Proposed NFPLL-MSRF-based RCG method	116
Figure 4.2	SAPF with NFPLL-MSRF-FIED-AFHCC-based control	118

Figure No.		Page No.
	scheme	
Figure 4.3	Profiles obtained for ideal source condition under RL- and RC-type nonlinear loads (a) i_{cabc} generated using NFPLL-MSRF-FLC-AFHCC approach, (b) i_{sabc} after compensation, and (c) THD of i_{sabc} after compensation	120
Figure 4.4	Profiles obtained for non-ideal source condition under RL- and RC-type nonlinear loads of (a) i_{cabc} generated by SAPF using NFPLL-MSRF-FLC-AFHCC approach, (b) i_{sabc} after compensation, and (c) THD of i_{sabc} after compensation	121
Figure 4.5	Profiles obtained under ideal source condition under RL- and RC-type nonlinear loads of (a) i_{cabc} generated by SAPF using NFPLL-MSRF-FIED-AFHCC approach, (b) i_{sabc} after compensation, and (c) THD of i_{sabc} after compensation	122
Figure 4.6	Profiles obtained under non-ideal condition under RL- and RC-type nonlinear loads of (a) i_{cabc} generated by SAPF using NFPLL-MSRF-FIED-AFHCC approach, (b) i_{sabc} after compensation, and (c) THD of i_{sabc} after compensation	123
Figure 4.7	SAPF with asymmetrical loading arrangement	127
Figure 4.8	Profiles obtained under asymmetrical loading conditions (a) i_{labc} considering RL- and RC-load, (b) i_{sabc} before compensation (c) i_{cabc} considering with and without SAPF, and (d) i_{sabc} considering with and without SAPF	128
Figure 4.9	Profiles obtained under different loading conditions (considering R_1 =45 Ω , L_1 = 5 mH , R_2=18 Ω , and C=1μF) (a) i_{labc} under RL- and RC-load, (b) i_{sabc} before	129

Figure No.		Page No.
	compensation (c) i_{cabc} considering with and without SAPF, and (d) i_{sabc} considering with and without SAPF	
Figure 4.10	Profiles obtained under different loading conditions (considering R_1=90 Ω, L_1=5 mH , R_2= 36 Ω, and C=1μF) (a) i_{labc} considering RL and RC load, (b) i_{sabc} before compensation (c) i_{cabc} considering with and without SAPF, and (d) i_{sabc} considering with and without SAPF	130
Figure 4.11	V_{dc} profiles obtained considering RL-and RC-type nonlinear loads under different controller-based SAPF (a) NFPLL-MSRF-PI-AFHCC scheme, (b) NFPLL-MSRF-FLC-AFHCC scheme, and (c) NFPLL-MSRF-FIED-AFHCC	131
Figure 4.12	Comparative profiles of V_{dc} obtained using NFPLL-MSRF-PI-AHCC, NFPLL-MSRF-FLC-AHCC, NFPLL-MSRF-FLC-AFHCC and NFPLL-MSRF-FIED-AFHCC methods under load-changing conditions (a) from RC-to RL-type and (b) from RL- to RC-type	133
Figure 5.1	RT-LAB Simulator models	141
Figure 5.2	Profiles obtained under load-changing (i.e., RL- to RC-type) and ideal source conditions (a) V_{sabc} before compensation, (b) i_{sabc} before compensation, (c) i_{cabc} generated using the proposed NFPLL-MSRF-FIED-AFHCC-based SAPF, and (d) i_{sabc} after compensation	143
Figure 5.3	Various profiles obtained using OPAL-RT 4510 under load-changing (i.e., RL- to RC-type) and ideal source conditions (a) V_{sabc} before compensation, (b) i_{sabc} before compensation, (c) i_{cabc} using the proposed NFPLL-	144

Figure No.		Page No.
	MSRF-FIED-AFHCC-based SAPF, and (d) i_{sabc} after compensation	
Figure 5.4	Various profiles obtained under load-changing (i.e., RL to RC) and non-ideal source conditions (a) V_{sabc} before compensation, (b) i_{sabc} before compensation, (c) i_{cabc} generated using the proposed NFPLL-MSRF-FIED-AFHCC-based SAPF, and (d) i_{sabc} after compensation	145
Figure 5.5	Profiles obtained using OPAL-RT 4510 under load-changing (i.e., RL to RC) and non-ideal source conditions (a) V_{sabc} before compensation, (b) i_{sabc} before compensation, (c) i_{cabc} generated using proposed NFPLL-MSRF-FIED-AFHCC-based SAPF, and (d) i_{sabc} after compensation	146
Figure 5.6	MATLAB simulation-based V_{dc} profiles obtained under ideal source condition employing proposed controller-based SAPF for (a) RL-load (b) RC-load	147
Figure 5.7	OPAL-RT simulator-based V_{dc} profiles obtained under ideal source condition employing the proposed NFPLL-MSRF-FIED-AFHCC-based SAPF for (a) RL-load (b) RC-load	148
Figure 5.8	MATLAB simulation-based V_{dc} profiles obtained under non-ideal source condition employing the proposed NFPLL-MSRF-FIED-AFHCC-based SAPF for (a) RL-load (b) RC-load	149
Figure 5.9	OPAL-RT simulator-based V_{dc} profiles obtained under non-ideal source condition employing the proposed NFPLL-MSRF-FIED-AFHCC-based SAPF for (a) RL-load (b) RC-load	150

List of Tables

Table No.		Page No.
Table 1.1	Comparison between operation of standalone MGs and grid-connected MGs	8
Table 1.2	Advantages of standalone MGs over grid-connected MGs	9
Table 1.3	Summary of relevant research on different control strategies of SAPF	31
Table 2.1	Parameters of PV system	42
Table 2.2	Boost converter parameters	44
Table 2.3	Symbols used in WES design	47
Table 2.4	FC parameters	50
Table 2.5	Rule base table for FLC method	61
Table 2.6	Parameters of the studied system	64
Table 2.7	THD comparison of i_{sabc} under various conditions	69
Table 2.8	Detail THD information of i_{sabc} under various control topology	69
Table 2.9	Comparison of V_{dc} deviation under steady-state condition	71
Table 2.10	V_{dc} deviation and t_s comparison under load-changing conditions	73
Table 3.1	Rule base table for the proposed FIED scheme	84
Table 3.2	AFHCC rule matrix	87
Table 3.3	THD comparison of i_{sabc} under ideal source condition	92
Table 3.4	Comparative THD information of i_{sabc} under ideal source condition	95
Table 3.5	THD comparison of i_{sabc} under non-ideal source condition	101
Table 3.6	Comparative THD information of i_{sabc} under non-ideal source condition	102

Table 3.7	Comparison of V_{dc} deviation under steady-state condition	103
Table 3.8	V_{dc} deviation and t_s comparison under load-changing conditions	106
Table 4.1	Comparative THD information of i_{sabc}	123
Table 4.2	Comparative THD information of i_{sabc} under ideal source condition	125
Table 4.3	Comparative THD information of i_{sabc} under non-ideal source condition	126
Table 4.4	Comparison of V_{dc} deviation under steady-state condition	132
Table 4.5	V_{dc} deviation and t_s comparison under load-changing conditions	134
Table 4.6	Comparative illustration of the proposed control topology-based SAPF with that of other reported works	135

Chapter 1

INTRODUCTION

1.1 PREAMBLE

In the twenty-first century, global energy scarcity has emerged as one of the most significant problems confronting human civilization. Today, most of the world's electricity comes from power plants that run on fossil fuels. Unfortunately, these plants are a major cause of climate change. Due to geographical diversity and the requirement to handle growing load and bidirectional power flow, transmission and distribution systems primarily need to be updated. But for the availability of power delivery, reliability and protection and significant infrastructure are required to monitor and manage asset, especially in power generation and distribution systems. To meet the world's fast growing energy needs while protecting the environment, it is now vital to prioritise power production systems that use renewable energy sources (RESs) over those that use fossil fuels [1, 2]. This entire progressive action can be fulfilled by the concept of microgrid (MG) system, which comprises of modular distributed generation (DG) systems based on RESs. Power generation and distribution policies have been conditionally depended on number of factors which differs from nation to nation. The concept of MG technology is to meet future electricity demand while mitigating the environmental effect associated with current power generation based on sources such as oil, coal and so on [3, 4].

The MG may appear as a combination of RESs (such as bio-energy, wind, solar photo voltaic (SPV), mini-hydro, fuel cell (FC), and so on)-based generating units and storage devices (such as batteries, flywheel, super capacitor, etc.) along with controllable critical loads [5, 6]. It can be operated either in standalone mode or grid connected mode. When any region is demographically inaccessible by the utility grid, in that case, standalone operation of MG is the only viable option. While, in grid connected mode, the exchange of power takes place between MG and the utility grid based on the energy requirement, quantum of power disturbance/severe fault within the system [7].

The solar and wind energies are intermittent/complementary in nature (as both depend upon climatic conditions). Hence, in the present dissertation work, to ensure an uninterrupted power supply and to maintain the continuity of load current, the proposed MG also have a FC together with solar and wind-based DGs. In MG configuration, the use of power electronics-based interfaces or nonlinear loads causes unwanted severe power quality (PQ) concerns. Any anomalous behavior on a power system that manifests

in terms of voltage or current and interferes with the normal operation of electrical or electronic equipment is referred to as PQ issues [8]. Voltage sag, voltage swell, voltage flicker, harmonics, etc. are a few examples of PQ issues.

Among the PQ issues, harmonics cause power loss in circuits, lower the power factor, distort source current and voltage waveforms, communication device interference, and equipment failure [9]. A poor power supply reduces equipment efficiency, while good PQ ensures proper operation without reducing equipment life span. As a result, harmonic minimization is a major concern in MG. As a solution to the above problems, nowadays, shunt active power filters (SAPFs) are widely used for achieving superior PQ levels. These are employed to inject compensating currents for generation/absorption of reactive power and harmonics suppression at the point of common coupling (PCC) [10].

1.2 CONCEPT OF MICROGRID

Environmental change and population expansion are increasing exponentially and have become major global concerns. The grid must produce more energy to fulfill the demands of an expanding population and industry. On the other side, traditional energy sources might not be adequate to supply the growing demand, which would then cause environmental pollution. Therefore, in recent decades, a new concept termed MG has emerged out, where conventional generation is supplemented by localized generation modules. It is a new alternative way of producing electrical energy at the distribution level that does not pollute the environment [11, 12]. However, their penetration has caused the power system operators to re-orient the operation and control aspects of power system to keep it in stable condition. Various aspects of MG modeling using DGs, like a wind energy system (WES), SPV generator, FC, and diesel engine generator have been explained in [13]. MG is nothing but the integration of the number of DGs and different power electronics converters to manage the power distribution between the grid and load. The MG system can operate either in a standalone or grid-connected mode [14].

1.2.1 Microgrid Operation

The current civilization has recently expressed apprehension regarding the escalation of its population and the alterations in its surroundings. The grid must be enhanced to

accommodate the increasing power requirements resulting from population growth and industrial development. Conventional energy sources, however, may be inadequate to satisfy increasing demand, thus, leading to environmental pollution. The notion of a MG has emerged in response to increasing electricity usage and growing environmental concerns. The design, operation, and regulation of the current power system are significantly influenced by MG. A MG is essentially a hybrid electric network that utilizes DGs, local loads, and electrical energy storage devices to supply electricity to isolated or restricted areas [15, 16]. The foremost objective of MG is to confirm the stability of the system in the event of different network disturbances. The MG offers benefits like less carbon emissions, an effective and environmentally friendly energy supply, postponing the expansion of power distribution infrastructure, and so on. MG systems have garnered significant attention in recent years due to their potential to enhance energy resilience, integrate RESs, and improve energy access in remote or underserved areas [17, 18].

1.2.1.1 Standalone microgrid systems

Standalone MG systems operate independently of the main grid and are typically deployed in remote areas or islands where grid connectivity is limited or unreliable [19, 20]. This section reviews recent literature focusing on the design, optimization, and control of standalone MG systems. Key topics include renewable energy integration, load management strategies, and reliability analysis. Figure 1.1 displays the block diagram for a generalized standalone MG system. The key benefits, developments and challenges associated with the standalone MG system are briefly highlighted below.

(a) Renewable energy integration

RESs, which provide clean and sustainable power, are crucial for autonomous MG systems. These include wind and solar energy as examples. Various factors concerning the incorporation of RESs in autonomous MGs include advancements in efficiency and design technology [21, 22], integration difficulties arising due to their intermittent nature [23] and optimization strategies for their maximum utilization have been examined in the recent literature [24].

(b) Load management strategies

Load management strategies (LMSs) such as demand-side management (DMS) [25], MG scheduling [26], and use of smart-grid technologies [27], (like advanced metering, real-time monitoring, communication and control systems etc.) are essential to optimize the operation of standalone MG systems by matching electricity supply with demand and ensure efficient utilization of RESs.

(c) Reliability analysis

Reliability analysis is essential for assessing the performance of standalone MG systems under various operating conditions and external disturbances. This includes fault detection and diagnosis system [28], resilience assessment [29], reliability modeling considering different operating scenarios [30].

1.2.1.2 Grid-connected microgrid systems

This section briefly examines the recent research on grid-connected MG systems, emphasizing their role in enhancing grid stability, supporting renewable energy integration, and enabling DMS [31, 32]. Figure1.2 shows the block diagram for a grid-connected MG system. The key benefits, developments and challenges associated with the grid-connected MG system is highlighted below.

(a) Enhancing grid stability

Grid-connected MG systems play a vital role in enhancing the stability and reliability of the main power grid by providing ancillary services, mitigating voltage fluctuations, and

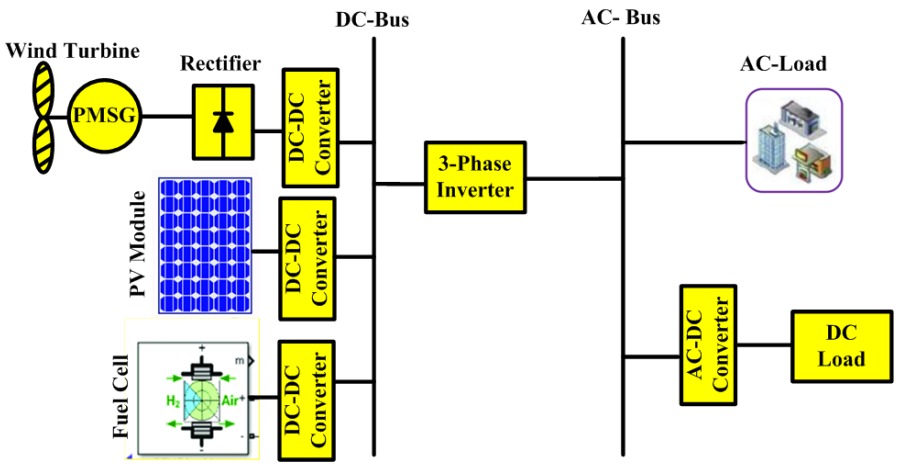

Figure 1.1 Block diagram of standalone MG system

supporting grid synchronization [33]. Recent literature on grid-connected MG systems has mainly focused on the frequency regulation [34], voltage support [35], and islanded operation aspects in relation to the grid stability [36].

(b) Supporting integration of RESs

Grid-connected MG systems play a crucial part in assisting friendly integration of RESs into the main power grid by facilitating active power control, reactive power support, voltage regulation, facilitating RESs dispatch, forecasting of RESs and enabling grid flexibility [37-39].

(c) Enabling demand-side management

DMS plays a critical role in grid-connected MG systems by improving energy consumption, enhancing grid reliability and, reducing peak demand. The DMS includes demand response program catering energy usage habit of customers [40], load-shifting strategy [41], and grid-services aspects like frequency regulation, voltage support and the congestion management [42].

A comparative study between grid-connected and standalone MG systems are presented in Table 1.1. Again, Table 1.2 revealed the advantages of standalone MG systems over grid-connected system. As compared to grid-connected MG systems, standalone MG systems provide a number of benefits. These benefits include continuous

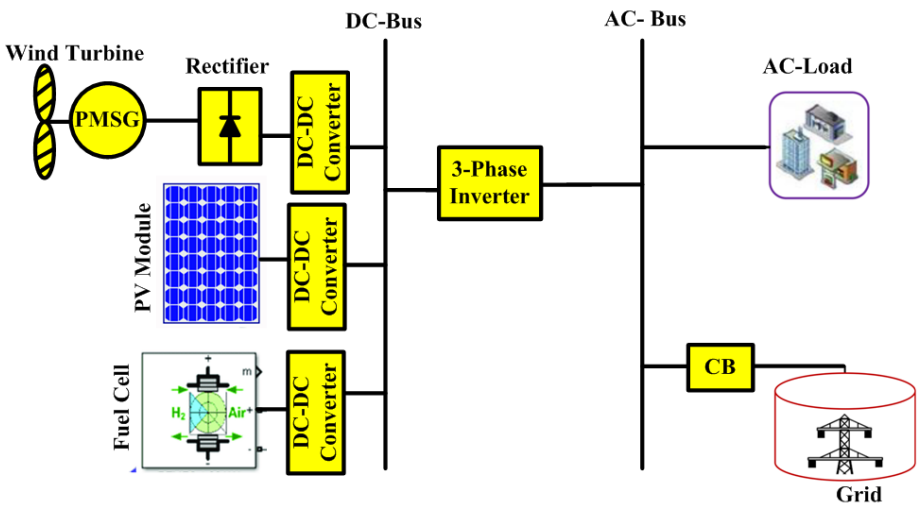

Figure 1.2 Block diagram of grid-connected MG system

electricity supply even in the event of grid failures or disruptions and enhancing energy resilience [7, 21].

- Standalone MGs operate independently of the main power grid, providing energy independence to remote or isolated communities.
- Standalone MGs are well-suited for electrifying remote or off-grid areas where grid extension is economically unfeasible or technically challenging. They enable access to electricity in underserved regions, supporting economic development, education, healthcare, and social well-being [19, 26].
- Since standalone MGs generate and consume electricity locally, they eliminate the need for long-distance transmission lines, reducing transmission losses and improving overall energy efficiency. This localized energy generation and distribution contribute to energy conservation and cost savings [21, 26].
- Standalone MGs enhance energy security by diversifying energy sources and reducing dependency on centralized power generation infrastructure. They are less vulnerable to grid disruptions, natural disasters, cyber-attacks, and geopolitical risks that may affect grid-connected systems [11, 21, 27].

Past researches reveal that many works have been carried out to study the PQ issues and their mitigation in MG under grid-mode of operation [19-21]. However, very few attempts have been made to analyze the PQ issues in MG operating in standalone mode, which has its own advantages as discussed in Table 1.2. Hence, this dissertation deal with the PQ issues and their mitigation in a MG (comprising of DGs like SPV, WES and FC) operating under standalone mode.

Table 1.1 Comparison between operation of standalone MGs and grid-connected MGs

Grid-connected mode	**Standalone mode**	**References**
a. To perform system inspections, information is obtained from the low voltage AC network, DG units, and loads (both AC and DC).	a. The main function of the MG central control is to automatically adjust the load-end voltage profile and power flow of the DG units in response to load changes and disturbances.	[3],[4],[7] [21],[26], [19]
b. Provide synchronized operations with the main grid, ensuring the power transfer at previous committed points.	b. In stand-alone mode, each DG unit must promptly resume production in order to supply its share of the load.	[3],[7], [21], [14], [16]
c. Necessary to regulate the flows of both active and reactive power between the MG and the grid	c. Not necessary to regulate the flows of active and reactive power between the MG and the load.	[5],[9],[26] [14], [18]
d. Maintaining constant voltage and frequency at the load ends by controlling the DGs' active and reactive power.	d. In response to disturbances or variation in load, the DG units' power flow and load-end voltage profile are individually regulated.	[30],[19], [11],[15], [17]
e. To regulate power balance and voltage, DMS is used to control load interruption/shedding tactics with the help of energy storage systems.	e. While operating in standalone mode, the DG units quickly resume their generation to meet their local load or any load variation.	[6],[3],[4], [11],[18], [19]

Table 1.2 Advantages of standalone MGs over grid-connected MGs

Standalone mode	**Grid-connected mode**	**References**
Less dependence on central grid infrastructure	Reliance on central grid infrastructure	[3], [4], [11]
More resilient to grid failures and outages	Vulnerable to grid failures and outages	[5],[7],[12]
Greater flexibility in system design and operation	Limited flexibility due to grid interconnection	[6],[15], 17]
Suitable for remote or off-grid locations	More suitable for urban or densely populated areas	[6],[30],[11]
Higher energy security due to localized generation	Dependent on centralized generation and transmission	[1],[2],[15]
Potential for cost savings in certain scenarios	May require higher initial investment and ongoing maintenance	[9],[14],[16]
Can facilitate integration of renewable energy sources	Integration of renewables may be constrained by grid issues	[7],[18], 19]
Operates autonomously, not reliant on external grid	Connected to the main grid, relies on grid for backup power	[3],[4],[11]
Reduced reliance on fossil fuels, potentially lower carbon footprint	Relies partially on grid power, may still contribute to carbon emissions	[6],[7], [13]
Less affected by grid failures, can continue to operate autonomously	Vulnerable to grid failures, requires backup systems for continued operation	[19],[21] [30]

Numerous academicians/researchers have focused their attention on RES due to their significant economic, environmental, and technical benefits. Owing to these benefits, DGs integration into the current conventional grid is expanding quickly. DGs are often linked to the distribution grid as opposed to the transmission network. DGs such as FC, WES, SPV, micro turbines, and others are accessible in different sizes [22-24]. The use of SPV, WES, and FCs in the standalone MG design is necessary for several reasons, each contributing to the overall effectiveness, reliability, and sustainability of the system:

- Incorporating multiple RESs such as SPV, WES, and FC diversifies the energy mix of the MG. This diminishes dependency on a single energy source and enhances energy security and resilience, as on account of variations in weather conditions the resource availability for one source can be compensated by others.
- SPV and WES are inherently intermittent energy sources with generation varying depending on factors such as sunlight availability and wind speed. FCs, on the other hand, provide continuous power generation through electrochemical reactions. By integrating FCs alongside SPV and WES, the MG can mitigate the impact of intermittent RESs, thus, ensure a more reliable and consistent power supply.
- SPV, WES, and FC are all clean and renewable energy technologies that produce electricity without emitting greenhouse gases or pollutants. By utilizing these technologies in MG design, the reliance on fossil fuels is reduced, leading to lower carbon emissions, improved air quality, and mitigated environmental impact compared to the conventional power generation methods.

In summary, the incorporation of SPV, WES, and FC in the standalone MG design is necessary to achieve a sustainable, reliable, and resilient energy supply. These technologies provide diversification, intermittency mitigation, complementary energy profiles, environmental benefits, energy independence, and long-term cost savings, making them essential components of modern standalone MG systems.

1.2.2 Solar PV System

Among the various RESs, the solar energy functions as the primary energy source for the earth. Virtually all other sources of energy are drawn either directly or indirectly from the sun. The SPV is one of the straightforward technique for capturing the plentiful energy emitted by the sun. SPV cells transform incoming solar radiation into electrical energy

[43, 44]. The SPV inverter transforms the electrical power generated by PV cells into AC power, which can be directly used or fed into the main utility grid for consumption. A detail on PV system modeling can be found in [45, 46]. Because of its time-varying properties (I-V and P-V characteristics) and nonlinear nature with regard to temperature and irradiance, SPV systems have low energy conversion efficiency. To enhance its efficiency in producing electrical energy, the maximum power point tracking (MPPT) controller is used [47, 48]. Hence, MPPT controller is regarded as a crucial part of a SPV system.

Research is continuously going on in either exploring new MPPT techniques or for enhancing the performance of the existing MPPT techniques viz. perturb and observe (P&O) [49, 50], incremental conductance [51, 52], voltage/current feedback [53, 54], fuzzy logic or adaptive neuro-fuzzy inference system-based MPPT techniques [55-57] and so on. However, the P&O technique due to its simplicity and easy implementation is mostly used by the researchers [58]. An essential part of an SPV system, a dc-dc converter serves as an interface between the load and the SPV module. The converter working in coordination with MPPT algorithm helps SPV system to deliver the maximum power to the load [59-61]. Therefore, in the adopted MG model of the present work, SPV modules, a dc-dc converter and a P&O MPPT controller are all coupled together to produce an appropriate output voltage that matches the required dc-bus voltage.

1.2.3 Wind Energy System

India is presently experiencing a surge in renewable energy with wind power technology becoming an appealing alternative. The WES produces no carbon emissions during power generation [62]. Major components of a wind plant are a wind turbine, a generator, a three-phase power electronic converter and a transformer that connects inverter to the grid [63]. Various turbine design structures have been proposed, tested and implemented in [64, 65]. The wind turbines are basically classified as horizontal axis wind turbine (HAWT) [66-68] and the vertical axis wind turbine (VAWT) [69-71] based on shaft position with respect to the earth. VAWTs are more efficient, cheaper, simpler and easier to maintain as compared to HAWTs [72, 73]. Other benefits of VAWTs include less noise and having greater surface area for energy capture. HAWTs, on the other hand, are designed with blades that rotate perpendicular to the wind. These turbines require heavy

and expensive gear box, generator and blades [74]. Taking all these factors into consideration, VAWTS are preferred over HAWTs to produce electricity. However, HAWTs are more practical and still remain the most focused research area [75]. The wind turbine coupled with the generator (like squirrel-cage induction generator (SCIG) and doubly-fed induction generator (DFIG)) produces electricity. In the past, the performance of WES model comprising of a SCIG, a constant speed wind turbine having a multi-gear box have been extensively studied [76-78]. Later, DFIG-based WES comprising a variable speed wind turbine with gearbox having merits over SCIG-based WES is proposed in [79]. Further, a gearless wind turbine system coupled with a low-speed high-torque synchronous generator having power electronic interface is proposed [80]. Permanent magnet synchronous generators (PMSG) coupled with VAWTs are favored by the researchers due to their high efficiency, light weight and high-power density. The PMSG-based WES eliminates the requirement of gearbox, thus, decreasing the burden of related cost and maintenance, which ultimately results in improved system reliability [81, 82]. In this configuration as well, a MPPT algorithm needs to be employed in order to extract the maximum power out of the system. Several MPPT methods have been presented in [83-89]. Indirect power control (IPC), direct power control (DPC), smart MPPT algorithms, and hybrid approaches are the categories under which they fall. Tip speed ratio (TSR), power signal feedback (PSF), and optimum torque (OT) are examples of conventional MPPT approaches that are included in the IPC methodology [83, 84], the optimal-relation-based (ORB) [85], P&O [86], and incremental conductance (INC) [87] are some of the techniques included in the DPC scheme. The majority of conventional algorithms are based on DPC and IPC systems. The studied literature makes evident the widespread usage as well as popularity of the traditional P&O approach, which has benefits including simplicity, no need for a sensor, ease of application, and compatibility with PMSG [88, 89]. Hence, in this work, PMSG-based WES is used. The PMSG output is fed to an unregulated rectifier which is finally coupled with a dc-dc converter. The adopted WES output is regulated using P&O MPPT approach.

1.2.4 Fuel Cell System

Without using traditional combustion, the FC is an electrochemical device that directly transforms the potential chemical energy of fuel into electrical energy. The merits of FC

are (a) clean electricity generation, (b) high efficiency and reliability, (c) modularity, (d) high current generation capability, and (e) has no geographical limitation. It can be used in uninterrupted power supply backup system design for critical facilities like hospitals, data centers, telecommunication system etc., and electric vehicle application [90, 91].

As surveyed in literature, a variety of FCs have been developed, each having unique features and applications. There exists FC technologies like proton exchange membrane fuel cells (PEMFC) [92, 93], solid oxide FC [94, 95], direct methanol FC [96, 97], alkaline FC [98], molten carbonate FC [99], and phosphoric acid FC [100]. Even if other FC technologies have unique advantages of their own, the literature reveals that the PEMFC is the most flexible and promising FC technology. PEMFCs' high-power density, short start-up times, and low operating temperatures make them suitable for both stationary and mobile applications. Furthermore, PEMFCs may run on a range of fuels, including hydrogen, methanol, and ethanol, and they have very low emissions and high efficiency. Therefore, it is believed that the PEMFC represents a significant technological breakthrough in the direction of a sustainable energy future.

The major problems faced by FC applications are less output dc voltage and associated ripple content in it. This issue can be overcome by using a dc-dc boost converter of proper rating [101, 102]. In this dissertation work, the adopted MG design also comprises of a PEMFC, which can quickly adapt to load changes. The PEMFC is coupled with a dc-dc converter to generate an output voltage that aligns with the desired dc-bus voltage of the MG system.

1.3 POWER QUALITY ISSUES

Electricity is the most reliable and widely used form of energy. The availability of electricity is essential for the development and sustainability of modern civilization. It has become an essential requirement of life on which the working of various machineries and equipment depend. However, the quality and consistency of the electric power supplied has a significant impact on how well they function. Most commercial and industrial loads require consistent, high-quality power. Thus, maintaining the qualitative power is essential [103]. The quality of the electricity is affected by variations in the voltage and frequency levels at which it is supplied. This affects the longevity and effectiveness of the equipment used by the end user. A lot of power

electronics devices are being used to make the power system more flexible and efficient, but this has raised the levels of harmonic distortion in end-use facilities and on the power system as a whole [104]. The use of modern electronic gadgets in factories, offices, and homes (such as electronic fluorescent light ballasts, arc furnaces, switch-mode power supply, adjustable-speed drives., etc.) results in excess harmonics, reactive power demand, and negative sequence currents injection into the power grid, posing a serious threat to the safe operation of power networks and other electrical equipment [105]. Thus, ensuring quality power to all consumers has become a major challenge for the power utilities. Among the various PQ issues, the presence of harmonics in the grid causes reduced power factor, and distortion in source current and voltage waveforms. This may also result in power losses, communication device interference, and equipment failure. As a result, harmonic mitigation is a major concern in the power distribution system (PDS) [106, 107]. Besides, the quality of electricity supplied is also impacted by interruptions caused by fault clearance and utility switching equipment. Thus, the description, identification, and prevention of PQ issues have been major areas of study for the many researchers round the globe. To understand the PQ problem and to analyze the performance of power system under various loads, a common point is defined which is referred as a PCC [108, 109]. The PCC is a point in the power system where multiple loads or multiple customers may be connected. According to international standards, PQ refers to the physical attributes of the electrical supply that are supplied in typical operating conditions and do not interfere with or disturb the operations of the customers. On the other hand, there is a PQ problem if there is any variation in voltage, current, or frequency that results in a customer's equipment malfunctioning or operating very poorly. PQ is an idea of powering and grounding sensitive equipment in a way that is appropriate for that equipment's. PQ problems can be broadly classified into the following categories, namely [110, 111],

a) Magnitude Disturbances

i) Periodic disturbances

-under voltage disturbances

-over voltage disturbances

ii) Transient disturbances

-voltage sag

-voltage swell

-voltage flicker

b) Waveform Disturbances-Harmonics

- voltage harmonics

- current harmonics

1.3.1 Magnitude Disturbances

PQ disturbances that are associated with the variations in magnitude of system variables are sometimes referred to as magnitude disturbances. There are two further categories of magnitude disturbances (i) periodic and (ii) transient.

i) Periodic disturbances

A magnitude disturbance is considered periodic if it persists for a duration over 60 seconds. Periodic disturbances occur as a result of excessive load on power system components and prolonged malfunctions [112]. It is further sub-classified as:

(a) Under voltage disturbances

It can be mentioned as long-duration voltage variation phenomena. It can be described as the reduction of RMS AC voltage, typically 80% to 90% of rated voltage at power frequency for a time period of more than 60 seconds [113]. Distribution transformers and transmission lines under over loading conditions and high reactive loads cause under voltage problem. Every load will be affected in different way due to under voltage issue. Under voltages can create overheating in motors. Constant power loads like voltage stabilizers, switched mode power supply (SMPS) and steel mills draw high current during under voltage situation. Induction motors draw increased magnetizing current which deteriorates their performance and life time.

(b) Over voltage disturbances

It can be defined as a condition when the utility voltage increases to 110% of rated voltage or more, for at least one minute. Over voltages are common in areas where distribution transformer tap settings are set imperfectly and loads are reduced. When electrical or electronic equipment is exposed to excessive voltage, it can cause malfunctions, overheating, early failure, shutdown, and shortened working life. Over voltage in supply

causes insulators failure, increase in the magnetic current induction machines and transformers, thereby, saturating the core of the equipment, and so on [114, 1115].

ii) Transient disturbances

Transient disturbances are a short duration faults last for less than 60 seconds. Transient disturbances are due to bulk load startup/shut down [116]. This is classified as:

(a) Voltage sag

It is defined as decrease in root mean square (RMS) voltage at the utility frequency for duration from half cycle to 60 seconds as shown in Figure 1.3. Sags are usually caused by temporary faults, switching on heavy loads with heavy startup currents and sudden load changes. Modern industrial equipment such as process controllers, variable speed drives, programming logic controller are more sensitive to voltage sags [117, 118].

Causes:

- Sudden increase in the load
- Starting of motor
- Faults in the power system

Consequences:

- Malfunction of adjustable speed drives (ASD's)
- Breakdown of switchgear and contactors
- Damage or shut down of the equipment

(b) Voltage swell

It is defined as an increase in RMS voltage at the power frequency for durations of 0.5 to 60 seconds as depicted in Figure 1.4. High impedance neutral connections, lighting, shut-down of bulk loads, sudden disconnection of neighboring lines or feeders are common

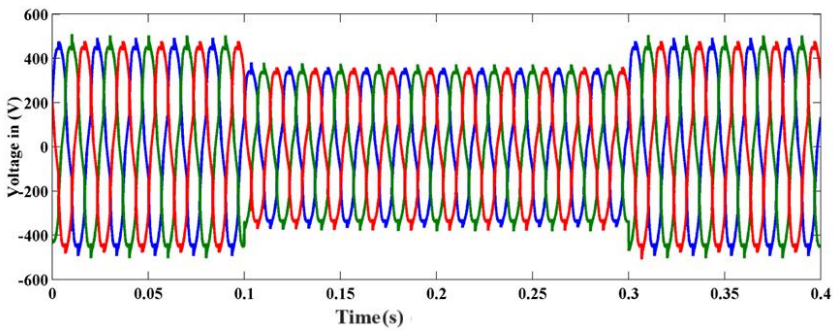

Figure 1.3 Voltage sag waveform

causes for voltage swell problem [119, 120]. If the duration of voltage swell is more than three cycles, illumination of the incandescent lamp increases but reduces its life time [121]. The momentary increase in voltage might break down semiconductor devices in SMPS and uninterruptable power supply (UPS) units.

Causes:

- Capacitor bank charging
- Abrupt interruption of current
- De-energization of huge load

Consequences:

- Over voltage
- Overheating
- Insulation breakdown

(c) Voltage flicker

It is described as systematic deviation of the voltage waveform envelope modulated with sub harmonics (<25Hz). Normally, the deviation ranges from 0.1% to 7% of rated voltage. Loads that exhibit continuous, fast change in current variations like electric arc furnaces, rolling mill drives and static frequency converters cause voltage fluctuations and light flickering. The filament lamp fed from a flickering source could affect working environment by causing irritation. It might lead to unwanted tripping of UPS units to change over to backup mode [122, 123].

1.3.2 Waveform Disturbances: Harmonics

Deviation of shape of voltage/current waveforms can be considered as waveform disturbances. Power systems are specifically engineered to function at the fundamental

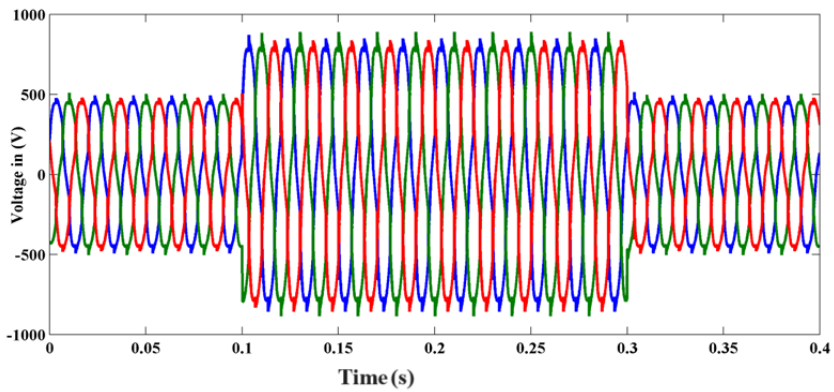

Figure 1.4 Voltage swell waveform

frequency of either 50 or 60 Hz. There are several loads that generate voltages and currents in integral multiples of the fundamental frequency. These frequency components constitute harmonic distortion, a type of electrical pollution. The term "harmonics" refers to "a sinusoidal element of a periodic wave or quantity containing a frequency which is an integral multiple of the fundamental supply frequency"[124, 125]. Harmonics when combined with the fundamental frequency produces a distorted waveform. In this regard, Figure 1.5 indicates that adding the signal's 3rd, 5th, and 7th order harmonics to its fundamental component results in a distorted waveform [126, 127]. Harmonic content present in a distorted waveform can be expressed in terms of total harmonic distortion (THD). It is defined as the RMS value of harmonic content divided by the RMS value of the fundamental quantity. The following formula may be applied to determine THD in a current signal (1.1)

$$THD_i = \frac{\sqrt{\sum_{n=2}^{\infty} I_n^2}}{I_1} \tag{1.1}$$

where, I_1 is the fundamental component and I_n is the *n*th order harmonic component of the current waveform. Likewise, THD of voltage signal may be found using (1.2)

$$THD_v = \frac{\sqrt{\sum_{n=2}^{\infty} V_n^2}}{V_1} \tag{1.2}$$

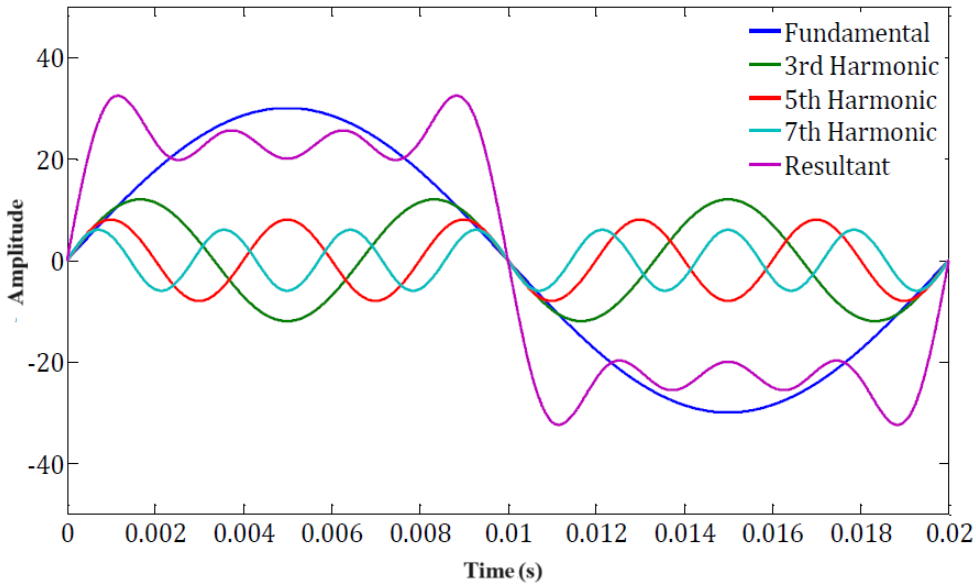

Figure 1.5 Harmonic distortion

where, V_1 is the fundamental component and V_n is the *n*th order harmonic component of the voltage waveform. Waveform disturbances are further classified as current and voltage disturbances.

(a) Voltage harmonics

It is the deviation of voltage waveform from sinusoidal wave shape. Power electronic converters in renewable generation and nonlinear loads at utility side can cause voltage harmonics. Application of these harmonic voltages to induction motors results in circulating harmonic currents in winding, thereby, increases the losses and temperature of motor. The existence of harmonics in the power system can lead to various issues practically at every level of the system which includes electric utility, the power distribution system, and equipment connected to it [128, 129]. Since distorted harmonic numbers have an impact on power sources and loads, their sensitivity determines the impact of harmonic distortion. Reactive power disruptions and power factor reduction are caused by harmonics, which can also lead to overvoltage due to resonance, increased heating in the conductors, and malfunctioning of sensitive equipment [130].

(b) Current harmonics

It is the deviation of current waveform from sinusoidal shape. The major source for current harmonic distortion in the power distribution system is power electronic devices and nonlinear loads and equipment. The loads that are most accountable for producing harmonic currents are household loads (like computer systems and other electronic loads), commercial load (like fluorescent lighting, adjustable speed drives for HVAC etc.), and industrial load (like three-phase power converters, arcing devices, etc.). High harmonic distortions cause malfunction and failure of the system besides creating additional power losses, overheating in neutral wire, additional acoustic noise in the motor and electronic apparatus, interference in telephone line and reduction of overall system efficiency [131-132].

1.4 SOLUTION TO POWER QUALITY ISSUES

From the above discussion, it is evident that the compensation of harmonics is essential for improving PQ and for satisfactory operation of power system. There are two techniques of mitigating PQ issues. The first method is known as load compensation. In

this, the apparatus is less susceptible to power disturbances and enables it to operate even when there is severe voltage distortion. The alternative option is to build line conditioning systems that reduce or mitigate power system problems, which includes the use of power filters (PFs).

1.4.1 Power Filters

Day by day, the PQ issues have become increasingly serious. As a result, PFs have received a lot of attention because of their superior harmonic reduction capabilities. PFs can be used in many applications or to tackle specific electrical problems [133,134]. The harmonic PFs are classified into three basic types (passive power filter (PPF), active power filter (APF) and hybrid power filter (HPF)) for mitigation of harmonics as shown in Figure 1.6.

1.4.1.1 Passive power filters

A PPF consists of resistors, inductors and capacitors as shown in Figure 1.7. Due to its simple construction and design, they are very economical. They are frequently employed to minimize the impact of harmonics caused by nonlinear loads by preventing harmonic currents from entering the power system. However, their effectiveness is restricted to particular harmonics and it may result in resonance in the power system. PPFs are always

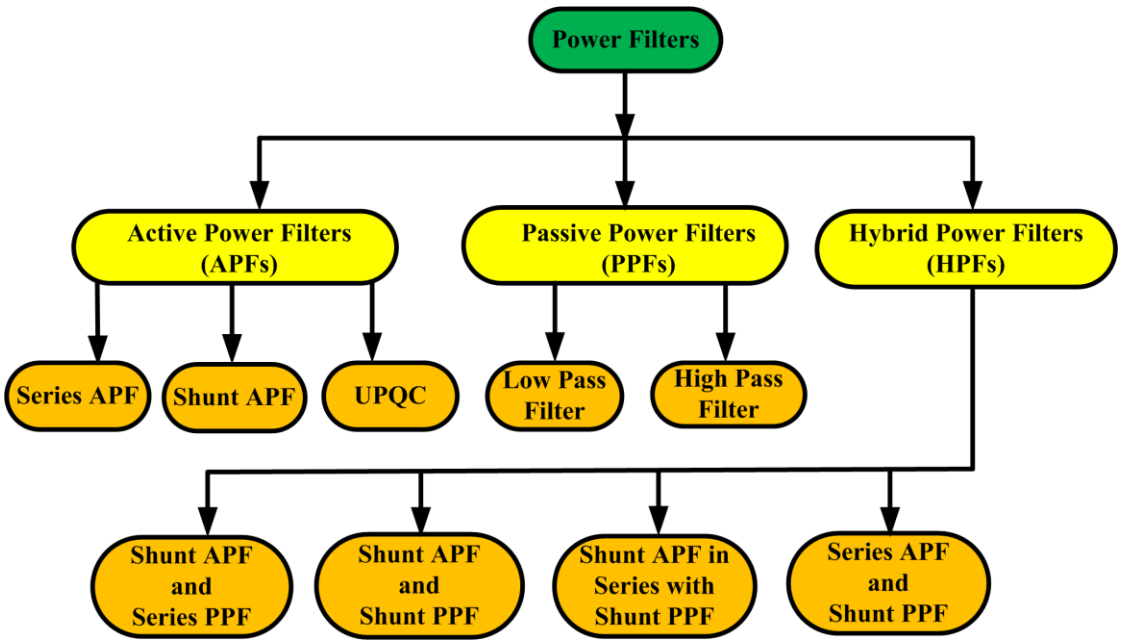

Figure 1.6 Classification of power filters

maintained in close proximity to the harmonic source [135, 136]. By doing this, the PPFs reduce the harmonic impact more effectively. In the past, passive filtering has been the most practical and least complicated way to improve the system's reactive power demand and compensate for current harmonics. PPFs are tuned to offer very low impedance path for a particular frequency. PPFs are further classified into two types based on its connection as (i) series PPFs and (ii) shunt PPFs. It is observed that PPFs have several drawbacks, which are listed below.

Disadvantages of PPFs

- Higher number of PPFs are required to attenuate multiple dominant harmonics.
- Connection of PPFs necessities a specific analysis of each installation.
- Non-adaptability to system variations.
- Tendency to resonate with the other load.
- Bulky in size.
- Cannot function under saturated condition.

1.4.1.2 Active power filters

The complex design process, limited capability to reduce harmonics, and significant losses incurred by passive filters lead to the utilisation of power electronic devices/converters-based designed filters (referred as APFs) to enhance harmonic compensation. APFs operate by introducing current/voltage harmonics of equivalent magnitude but opposite polarity into the power supply. An APF must possess the

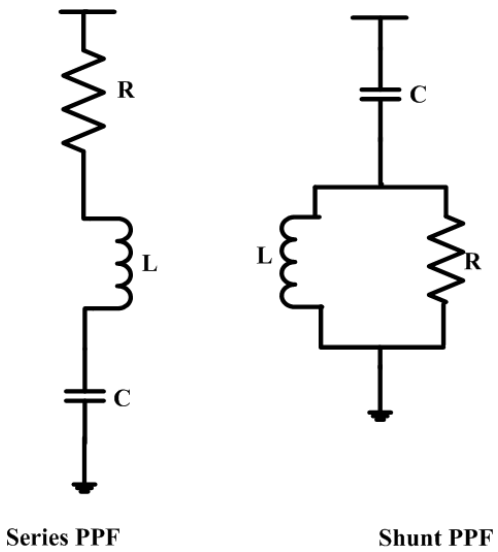

Figure 1.7 Passive power filter configuration

capability to alter the impedance it offers to the power supply in a dynamic manner [137, 138]. This allows the filter to react to unwanted currents/voltages. APFs can be divided into three types based on the circuit configuration and function, and these are described in the following subsections.

(a) Shunt active power filter

The advantage of SAPF over PPF is that, with the proper control mechanism, it can inject equal but opposite harmonic compensating currents that are needed by the power system to mitigate harmonics. As shown in Figure 1.8, a shunt active power filter (SAPF) is connected in parallel to the harmonic producing source. Here, the SAPF serves as a controlled current source, injecting a 180° phase-shifted harmonic compensating current. The system comprises a power converter, an inductor, and a capacitor [139, 140]. The power converter can function as either a current source or a voltage source. The SAPF based on a voltage sourced inverter (VSI) is the most prominent structure commonly used in active filtering applications. SAPF functions as a source of electrical current introducing additional frequencies, and is compatible with any kind of load that produces harmonics. Furthermore, it assists in increasing the load power factor [141].

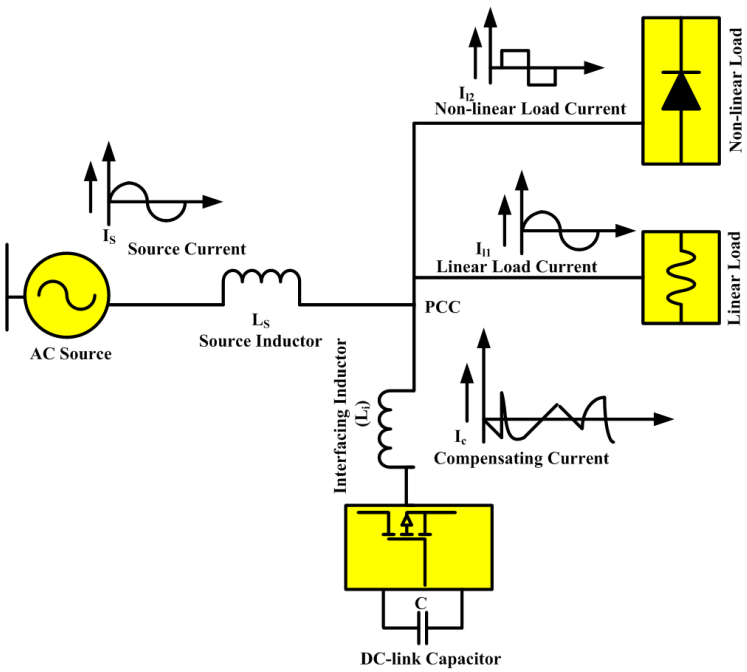

Figure 1.8 SAPF model

(b) Series active power filter

As seen from Figure 1.9, series active filters can be linked in series with electricity lines.

The SAPF and series active power filter are identical in terms of operation. Unlike SAPF, it uses a transformer to inject voltage corrections into the power lines. This filter injects compensatory voltage in series with the supply to mitigate voltage sag or swell. These filters are impractical because they must handle high current ratings, which increases their size and losses [142, 143].

(c) Unified power quality conditioner

The combination of series APF and SAPF leads to the creation of the unified power quality conditioner (UPQC). It combines together the advantages of both series APF and SAPF and, thus, capable of effectively mitigating both voltage and the current harmonics. This filter can therefore handle almost any PQ problem that a power system network might run into. The circuit diagram for a power system using UPQC is shown in Figure 1.10. Here, two VSIs use the dc-link capacitor, enabling it to serve as both a shunt and a series filter. Its primary disadvantages are the control circuit's intricacy and the high cost involved [144, 145].

1.4.1.3 Hybrid power filters

Hybrid power filters (HPFs) address the limitations of both active and passive filters. Multiple APFs or PPFs are amalgamated to form HPFs. HPFs are regarded as one of the

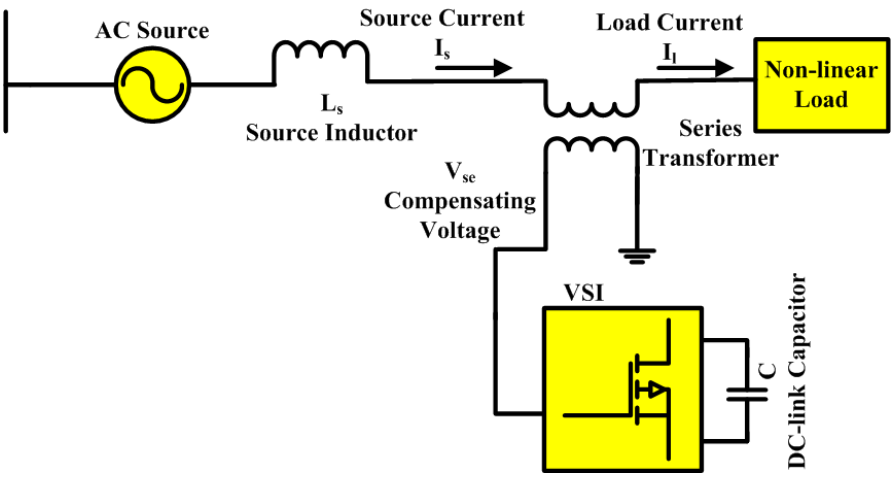

Figure 1.9 Series APF model

optimal methods for improving power quality for several reasons. Numerous hybrid filters have been documented in the literature, contingent upon the circuit arrangement, as outlined below [146, 147].

i) Series APF and SAPF
ii) SAPF and shunt PF
iii) Shunt APF and shunt PF
iv) Series APF in series with shunt PF

This dissertation work primarily focus on mitigation of harmonics in a standalone MG system generated by the nonlinear load using SAPF. The working of SAPF primarily depends upon the three control loops associated with it and are used for (i) reference current generation (RCG), (ii) dc-link voltage control, and (iii) switching pulse generation. Thus, the primary goal of this dissertation work is to identify the best combination of control strategies for these three control loops in order to maximize the performance of the SAPF. For RCG, the performance of studied synchronous reference frame (SRF), modified SRF, and the proposed negative feedback PLL-based MSRF (NFPLL-MSRF), are meticulously investigated and compared. Similarly, to address the dc-link voltage regulation, three distinct controllers like PI, fuzzy logic controller (FLC), and the proposed fuzzy inverted error deviation (FIED) have been implemented. Further, three distinct switching schemes like hysteresis current controller (HCC), adaptive HCC (AHCC), and adaptive fuzzy HCC (AFHCC) have been employed to find the one that would work best to lower the switching losses in the VSI of SAPF. All of the

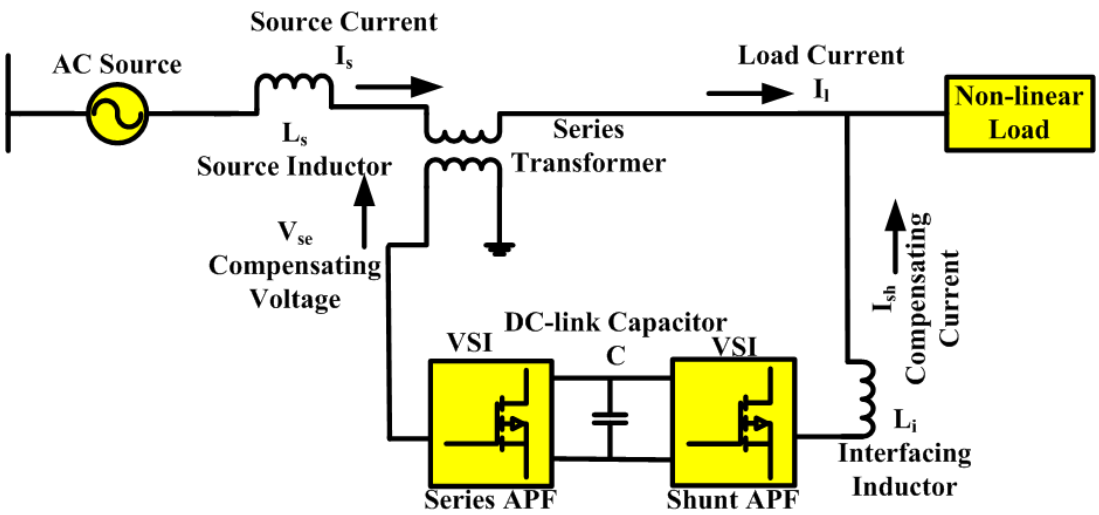

Figure 1.10 UPQC model

aforementioned SAPF control techniques are assessed based on their ability to compensate for source current harmonics while taking various source and load scenarios into account. To achieve this, a series of simulation-based experiments have been carried out under MATLAB environment presented as difference scenarios. Later, the results obtained is validated using OPAL-RT, a real-time digital simulator.

1.5 RESEARCH BACKGROUND

Every year, severe harmonics produced by electronic devices such as electronic ballasts, variable frequency motors, computers, battery chargers, and switch mode power supply result in substantial economic losses. As a result, issues with PQ and compensation strategies worry both power providers and customers. The 1980s saw the emergence of the buzzword "harmonics," which has always posed a danger to the regular operation of power systems and user devices [141-144]. Engineers and building designers are particularly concerned about harmonic issues because, in addition to distorted voltage waveforms, harmonics can cause random end-user device failures, nuisance tripping and overheating of transformer units and building wiring. Hence, the mitigation of harmonics has become more significant at present. As a solution to the above, the use of SAPFs have gained popularity due to their effective harmonic and reactive power reimbursement capabilities in both single- and three-phase alternating current power networks having nonlinear loads [139-141]. Despite using different designs, control schemes, and solid-state devices, SAPFs have been found effective for industrial applications over more than thirty years of study and development. In spite of significant development in SAPF's operation and control, yet researchers round the globe are tirelessly putting their effort in furthering either its design or associated control topologies. This thesis aims to provide a comprehensive investigation on the performance of SAPF in mitigating PQ issues in the studied standalone MG system under the action of proposed control strategies.

1.5.1 Shunt Active Power Filter

The power electronic devices behave like nonlinear loads and create unwanted PQ distortion, but interestingly, they themselves provide solution for PQ distortions. Traditionally, harmonics and reactive power are compensated using passive filters. These

filters are large in size and difficult to tune against changes in device parameters [148-150]. On the other hand, SAPFs are a popular way to realize superior PQ levels in power distribution system. It is usually employed in parallel to the load and injects a compensating current to cancel out the harmonics. As reported above, the working of SAPFs is mainly dominated by three control techniques predominantly used for RCG, switching pulses generation for VSI, and regulation of dc-link voltage (V_{dc}). In the past, numerous works have been documented in the literature highlighting different approaches to realize the above three functionalities [151- 153].

1.5.1.1 Reference current generation method

The RCG control loop plays a crucial role in generating desired compensating current to nullify the harmonics present in the system. Hence, its proper design is crucial from SAPF point of view. As reported in literature, there exist many control approaches for RCG each of them having their own unique merit, and all of these are basically improved version of two basic control techniques [154-172]. The basic control techniques are based on instantaneous active and reactive power theory (termed as p-q theory) [153-156] and SRF theory or d-q theory [157, 158]. Among the two, SRF technique is widely accepted due to its simple design and ease in implementation. However, the above approach suffers from a major drawback because of the requirement of reference phase angle generated using a phase-locked loop (PLL) for synchronization. When the source voltages are imbalanced and/or distorted, the designing of PLL block must be carefully executed [159, 160]. The authors in [161] have presented a modified PLL approach for RCG. The addressed technique helps to adjust the small power losses occurring due to the additional harmonic current. The authors in [162] have designed the SRF-based multi-loop control method, especially, for the SAPF-assisted DG system. Authors in [163] have presented a *d-q* based SRF technique for RCG along with a basic pulse width modulation (PWM) scheme for generating switching pulses for the VSI used in SAPF. The authors conclude that the control scheme works satisfactorily for fixed load conditions. The authors in [164] have adopted a PLL-based SRF (SRF-PLL) approach for the extraction of reference current from load currents. The above approach suffers from a major drawback because of the requirement of reference phase angle generated using a PLL for synchronization, thus, results in late response. Particularly, when the source voltages are imbalanced and/or

distorted, the PLL design must be carefully implemented. A PLL design is similar to a nonlinear closed loop feedback control system that uses measured frequency and phase angle to synchronize its output with input signal. A simple PLL is comprised of three parts i.e., a phase detector (PD), a loop filter (LF), and a voltage-controlled oscillator (VCO). There exist different PLL architectures, which are differentiated based on the design of the PD block. The SRF-PLL-based SAPF produces a reasonable performance in terms of the phase/frequency tracking capabilities and the dynamic response under optimum grid circumstances. However, in the event of grid voltage imbalance, the performance of the system is diminished, resulting in high magnitude steady-state oscillations in the estimated phase/frequency.

In recent years, numerous improved PLLs have been presented as replacements to the typical SRF-PLL for reliable phase/frequency prediction. The main principle behind these improved PLLs is to retrieve the fundamental frequency positive-sequence element using a particular filtering approach, and then to feed the output of this process into a standard SRF-PLL [165]. An improved PLL (IPLL)-based RCG technique is proposed in [166]. A new deadbeat-based PLL is proposed in [167] for dynamic response, however, it suffers from time-delay in control action. A decoupled double synchronous reference frame PLL (DDSRF-PLL) has been proposed by authors in [168] to eliminate double-frequency recognition issues brought on by the fundamental frequency negative-sequence component. A multiple reference frame-based PLL (MRF-PLL) is presented in [169]. Similar to the DDSRF-PLL, the MRF-PLL operates on the same principle but is easier to implement. The authors in [170] have presented a modified synchronous reference frame (MSRF)-based PLL approach for RCG. The addressed technique helps to adjust the small power losses occurring due to the additional harmonic current. The MSRF strategy, on the other hand, employs comparable approaches to the regular SRF system. However, the most significant distinction is in the estimation of the theta angle needed for synchronization [171]. The main advantage of this strategy is that the theta angle can be directly retrieved from the supply, rendering it frequency-independent and unaffected by the load changes. Hence, owing to the inherent benefits of the well-reported MSRF strategy, the authors of the present work have also adopted it for RCG in the studied SAPF model. Further, a MSRF-PLL approach as proposed in [172] have exhibited desired performance under low distortion and unbalanced system voltage conditions. However,

under highly distorted source conditions, the performance of its PD and filtering blocks degrade. Thus, the MSRF-PLL is unable to adequately extract the positive sequence signal required for the calculation of the synchronization angle. It has been noted that a lot of emphasis is given to the proper design of filter and PD blocks (which helps to extract the fundamental positive sequence component) while tuning these advanced PLLs (i.e., SRF, MRF-PLL, DDSRF-PLL, and MSRF-PLL). However, under non-ideal source and load-changing conditions, proper phase sequence signal extraction is not feasible due to non-linearity that is discovered during signal alterations [173]. In light of the foregoing, this work proposes a reconfiguration of the MSRF structure to extract positive sequence signals from the source by employing a negative feedback loop in the low pass filter (LPF) and a nonlinear adaptive-filter in the PD unit. The combination of a negative feedback loop and nonlinear adaptive-filter PD unit is able to track changes in amplitude, phase angle, and frequency of the input signal. Further, it can accurately estimate the fundamental component of an extremely distorted signal by eradicating harmonics. Therefore, in contrast to the traditional PLLs, the proposed negative feedback PLL (NFPLL)-based MSRF controller increases system bandwidth while offering a greater level of immunity against noise and other signal-related disruptions during extreme grid perturbations. The performance of the proposed method is compared with that of existing methods.

1.5.1.2 DC-link voltage regulation method

Another critical issue in the design of SAPF is V_{dc} regulation. The SAPF's dc-link capacitor is utilized to keep the system's power balanced. When the load is substantially increased, the capacitor discharges and supplies power, enabling the source and load power balance to be achieved. Similarly, the capacitor overcharges and maintains power balance when the load is suddenly removed. To carry out this process, a well-designed control strategy must be used to modulate the V_{dc} [174]. The works carried out in [175, 176] conclude that if the SAPF's V_{dc} remains stable, it will operate effectively and deliver precisely the required compensating current. Therefore, the design of V_{dc} controllers is also an important assignment in realizing SAPF. Usually, V_{dc} of SAPF is regulated either

by a PI controller or FLC, where the control approach is based on the direct voltage error management concept [177]. In [178], the authors present a technique for detecting harmonics under changing load conditions that combine the PI controller with the sliding mode controller. The authors in [179] describe the demerits of using a conventional PI controller in comparison to FLC for V_{dc} control. The performance characteristic of the PI controller under load-changing circumstances exhibits severe overshoot and a protracted settling time. It also has a number of flaws, such as ineptitude when it comes to parametric variation and load-changing conditions. FLC, on the other side, is known for its speed, reliability, and effectiveness in harmonic monitoring, V_{dc} control, and reactive power compensation. However, the main drawback of FLC is that its computational burden is increased due to the use of a greater number of membership functions and rules [180]. Moreover, it also works on the principle of direct voltage error manipulation technique, which may not entirely reduce the V_{dc} deviation that occurs during load-changing conditions [181, 182]. In view of the above demerits associated with reported PI and FLC approaches, in the present study, the dynamic performance of SAPF is improved by employing a proposed novel FIED controller to control and diminish the ripples in the V_{dc} waveform, particularly under load-changing conditions. Its offers superior performance as compared to that of existing approaches based on PI and FLC.

1.5.1.3 Switching pulse generation method

The choice of the PWM generator for the VSI of SAPF also plays a crucial role in mitigating harmonics. Various PWM generation techniques are reported in the literature like the hysteresis current controller (HCC) [183,184], adaptive hysteresis current controller (AHCC) [185], and adaptive fuzzy HCC (AFHCC) approach [186, 187] and so on. Researchers in [188] suggested a feedback control technique for PWM pulse production that eliminates harmonics of higher orders and requires less time to stabilize voltage during load-change. HCC-based approaches are easier to implement than other ones, although they exhibit uneven switching frequency, according to the authors of [189]. As reported in [190], the HCC technique involves variable switching frequency leading to higher switching losses and causing injection of high-frequency harmonics/noise to the system current. To overcome the disadvantages of HCC, the

AHCC technique is proposed, which uses a variable hysteresis band (HB) for tracking system current. The authors in [191] suggested an AHCC technique for SAPF to reduce the THD of the source current where, AHCC modifies the bandwidth (BW) as per the V_{dc} profile, frequency of modulation, reference current, and input voltage. However, during high frequency operation, AHCC causes more switching losses. The problem associated with AHCC is resolved by AFHCC as presented in [192]. The AFHCC technique calculates the BW of the HB using the FLC approach, where exact information of the SAPF parameters like interface inductor and V_{dc} of the capacitor are not required. The authors in [193, 194] have also used the AFHCC technique for better harmonics compensation and parametric optimization of a SAPF. Further, their study reveals that the AFHCC is not only used to obtain the switching signals but also to find the best value of the interfacing inductance, which is not possible in the case of HCC and AHCC techniques. Above review confirms the superior performance of AFHCC technique, hence, in the present work, less explored AFHCC technique is applied for the switching scheme for the projected SAPF. As surfaced above, a large number of control approaches for SAPF have been developed, but they mostly concentrate on grid-connected systems; in contrast, standalone mode of operation frequently overlooks controller design. Consequently, in the current study, in order to guarantee consistent operation and enhance the performance of the implemented MG system in standalone mode, a comparative study of different control techniques used for synchronization (i.e., SRF, MSRF and NFPLL-MSRF) employing PI, FLC and FIED) are proposed in this dissertation work through series of simulation-based investigations under MATLAB/Simulink environment. The experiments are carried out considering different operating conditions such as in the presence of ideal and non-ideal sources and steady-state and dynamic nonlinear load-changing conditions. Thereafter, the results obtained are validated using OPAL-RT 4510 real-time digital simulator platform. Also, the regulation of dc-link capacitor voltage and reduction of its settling time are verified using the proposed controller under load-changing conditions. A summary of the most relevant literatures on different control techniques of SAPF with research gaps are manifested in Table 1.3.

Table 1.3 Summary of relevant researches on different control strategies of SAPF

SAPF control methods	References	Control strategy	Degree of complexity	Transient response time	Settling time under load-changing conditions	Performance under unbalanced load conditions	Performance under non-ideal source conditions	**Research gaps**
RCG methods	[154],[156],[160]	P-Q theory	High	Not good	High	Not good	Not good	It is revealed from the RCG methods that the MSRF-PLL works best among all, however, still some improvements are needed like (i) the performance is not better under unbalanced load condition, (ii) the V_{dc} deviation is still more and its settling time is not up to the desired value and (iii) under non-ideal or distorted source condition, the THD mitigation is not better.
	[161],[162],[163]	SRF-PLL theory	High	Good	Medium	Good	Not good	
	[168]	DDSRF-PLL	Low	Good	Medium	Good	Good	
	[169],[170], [172],	MSRF-PLL	Low	Good	Medium	Better	Good	
DC-link voltage regulation methods	[177],[178],[180]	PI controller	High	Not good	High	Not good	Not good	The FLC technique is best for V_{dc} control but the limitations are (i) the V_{dc} deviation and settling time are not reduced to desired level during load-changing conditions and (ii) under non-ideal or distorted source conditions, the THD mitigation is not better.
	[181],[182],[178]	FLC technique	Low	Good	Medium	Better	Good	
Switching pulse generation methods	[183],[184]	HCC	High	Not good	High	Not good	Not good	The HCC method is used by many researchers due to its simple structure but the switching loss is more at higher frequency. The AFHCC method is the best among all as it performs better in all conditions.
	[185], [190]	AHCC	High	Good	Medium	Good	Not good	
	[192],[193],[194]	AFHCC	Low	Better	Low	Better	Better	

1.6 MOTIVATION AND CONTRIBUTION OF THE THESIS

As surfaced in the literature above, the PQ improvement in a standalone MG system connected with nonlinear load is a challenging issue now days. Among the many PQ issues, the harmonics compensation is the foremost objective of this thesis work. In the recent development, most of the researchers concentrated on PQ improvement of a grid connected system. The main challenge of the proposed research work is to develop SAPF with an optimum compensation capability to protect both MG and sensitive loads simultaneously from the wide range of PQ distortions. The optimum compensation capability of SAPF is achieved by suitable control strategies. In traditional control technique, fixed gain PI controller is designed to control the dc-link voltage at constant reference value. Under distorted environment, fixed gain PI controller exhibits poor control of dc-link voltage. Moreover, the performance characteristic of the PI controller under load-changing circumstances exhibits severe overshoot and a protracted settling time. Similarly, in the case FLC, the computational burden is increased due to the use of a greater number of membership functions and rules. Again, it also works on the principle of direct voltage error manipulation technique, which may not entirely reduce the V_{dc} deviation that occurs during load-changing conditions. Hence, a novel FIED controller is implemented to control and diminish the ripples in the V_{dc} waveform, particularly under load-changing conditions and improve the THD mitigation capability of the SAPF.

This work also proposes a reconfiguration of the MSRF structure to extract positive sequence signals from the source by employing a negative feedback loop in the LPF and a nonlinear adaptive-filter in the PD unit. The combination of a negative feedback loop and nonlinear adaptive-filter PD unit is able to track changes in amplitude, phase angle, and frequency of the input signal. Further, it can accurately estimate the fundamental component of an extremely distorted signal by eradicating harmonics. Therefore, in contrast to the traditional PLLs, the proposed novel negative feedback PLL (NFPLL)-based MSRF controller increases system bandwidth while offering a greater level of immunity against noise and other signal-related disruptions during extreme grid perturbations.

In order to address the switching technique required in the operation of SAPF, this work advocates the application of a less explored AFHCC technique used for reducing

the switching loss, monitoring the frequency of modulation and adapting proper hysteresis band.

The main contributions of the thesis are enumerated below.

(a) To examine the comparative performance analysis of MSRF-based RCG in combination with FLC and HCC for dc-link voltage control and switching pulse generation approaches, respectively, of SAPF in improving the PQ of an adopted standalone MG system under different source and nonlinear load conditions.

(b) To develop a novel FIED based dc-link voltage control approach for maintaining dc-link voltage constant. Its performance is evaluated in combination with MSRF and HCC/AHCC approaches in extracting the three-phase reference currents for harmonics mitigation under various source and load conditions.

(c) To develop a novel NFPLL-MSRF-based RCG technique and test its performance under different sources and load conditions in the presence of FLC and AFHCC-based methods employed for dc-link voltage regulation and PWM signal generation, respectively.

(d) To verify the performance of the SAPF under the proposed best combination of strategy i.e., NFPLL-MSRF-FIED-AFHCC-based approach over others in improving the PQ issues of the studied standalone MG system under different source and load conditions. The results are also compared with that of other reported work.

(e) To validate the performance of the proposed NFPLL-MSRF-FIED-AFHCC-based SAPF in improving the PQ of the adopted MG system under different source and load conditions using OPAL-RT 4510 real-time digital simulator platform.

1.7 ORGANIZATION OF THE THESIS

This dissertation comprised of six different chapters and the summaries of each chapter are given below.

Chapter 1 elaborates on the introduction to the work carried out in the thesis. This provides a comprehensive literature on standalone MG system, PQ issues and its mitigation techniques. Reviews on SAPF and its control techniques are also elaborately focused in this chapter.

Chapter 2 presents the modelling of adopted MG and SAPF employing different control techniques. The performances of the different control strategies of SAPF have been evaluated and compared in terms of harmonic mitigation and V_{dc} regulation using MATLAB/SIMULINK environment. In this chapter, superiority of the combined control strategy comprised of MSRF, FLC and HCC (used for RCG, V_{dc} control and PWM signal generation, respectively) is compared over SRF, PI and HCC- based combination in the presence of considered source and load-changing conditions.

In *Chapter 3*, the PQ issues of a standalone MG system are studied under the action of a proposed novel V_{dc} control approach referred as FIED technique-based realized SAPF. Apart from this, in terms of achieving the minimum THD level, the best combination among the methods used for the RCG, regulation of V_{dc}, and generation of switching pulse for the VSI is found by doing a comparative analysis of results obtained through a series of simulation-based experiments. It is observed that the MSRF-FIED-AFHCC combination has offered the best results over others in terms of THD and V_{dc} regulation.

In *Chapter 4*, a novel negative feedback phase-locked loop-based modified synchronous reference frame (NFPLL-MSRF) technique is proposed to overcome the drawback of the existing approaches used for RCG. In order to improve the performance of SAPF, a comparative study of different control techniques i.e., NFPLL-MSRF for synchronization, FLC and FIED for V_{dc} control, and AFHCC for switching pulse generation are proposed. Further, the compensation of PQ issue mainly THD in source current waveform is analyzed under both ideal and non-ideal source conditions in the presence of different nonlinear loads. In this, in terms of ability to mitigate harmonics, the best combination of control strategy is found as NFPLL-MSRF-FIED-AFHCC.

In *Chapter 5*, the performance of the proposed NFPLL-MSRF-FIED-AFHCC control strategy-based SAPF is further examined through a series of simulation-based experiments under load-changing conditions in the presence of both ideal and non-ideal source conditions. Thereafter, the obtained results are validated using the OPAL-RT 4510 real-time digital simulator.

Chapter 6 summarizes the essential findings of this dissertation and highlights the scope of future work.

Chapter 2

POWER QUALITY ANALYSIS OF MICROGRID UNDER MSRF-FLC-HCC-BASED SAPF

2.1 INTRODUCTION

In the 21st century, the availability of sustainable energy has become a major and complicated issue with sociological, political, and economic facets. Globally speaking, the transportation and electrical industries have already caused serious environmental issues by either directly or indirectly releasing greenhouse gases (GHGs) into the atmosphere. GHG emissions are a contributing factor to the phenomena of global warming, which in turn causes pollution in the atmosphere and limitations on the preservation of natural resources [3, 5]. The effects of global warming and climate change are evident since previous centuries. Extreme weather (hurricanes, tsunamis, catastrophic flooding etc.), variations in seasonal patterns and precipitation patterns, sea level rise, and an increase in the global average temperature across all regions of the planet are some of the main pieces of evidence. In addition, distant villages are typically characterized by low population density per unit area, underdeveloped infrastructure, low levels of economic activity, communication barriers brought on by natural constraints, and a host of additional issues related to a lack of conventional electrical sources [12, 13]. Microgrids (MGs) seem to be the only technological solutions that can both alleviate the aforementioned global concerns and facilitate the growth of rural areas with limited grid power availability. MGs are proving to be a more efficient solution for delivering sustainable energy services because they are economical and environmentally favourable methods for generating electricity [14, 15]. It advocates the widespread use of renewable energy sources (RESs) and the efficient use of smart power and energy management skills. As the most environmentally friendly way to reduce energy-related emissions, RESs-based MGs are nevertheless subject to a number of restrictions in the production of electricity. The most difficult problem with RESs is that they behave intermittently, depending on the seasons and weather, unlike traditional energy sources.

Some parts of this chapter have been published in the following paper of international journal.

1. **Barik, P.K.,** Shankar, G. and Sahoo, P.K., (2020). Power quality assessment of microgrid using fuzzy controller aided modified SRF based designed SAPF. *International Transactions on Electrical Energy Systems*, *30*(4), pp.12289.

It is well known that the present power supply infrastructure is predominantly influenced by power electronics-based nonlinear loads, such as switch-mode power supplies, arc furnaces, converters, industrial/house hold electronic devices, and so on, fixed at the distribution side [10]. Thus, ensuring quality power to all consumers becomes a foremost task for the power utilities. Moreover, the power quality (PQ) problems associated with currents are mostly due to unbalanced loads, harmonics, and insufficient reactive power. Additionally, these factors also impact the operation of other equipment connected at the point of common coupling (PCC) as well [9,10]. The MG system makes use of power electronics converters for the efficient energy utilization while operating either in standalone or grid connected mode. Operation in either mode is easy when the load in the system is of linear type. However, the presence of power electronics-based equipment or nonlinear loads generate unwanted serious PQ issues in the MG structure. In such instance, to mitigate the PQ issues, the use of custom power devices such as active power filters become inevitable. Literature survey reveals that PQ issues in grid connected MG system have been widely addressed in the past by the researchers worldwide. On the other hand, very few works have been reported regarding PQ mitigation of MG operating in islanding mode. Therefore, in this chapter, the PQ issues are investigated in a typical standalone MG comprising of solar photovoltaic (SPV), wind energy systems (WES) and fuel cell (FC)-based distributed generations (DGs) developed under MATLAB/SIMULINK^{R} platform.

2.1.1 Motivation of the Present Chapter

Recently, several studies have concentrated on improving the PQ of a grid-connected system, whereas, there has not been much research done on the PQ mitigation of standalone MG systems. Therefore, exhaustive study on how to improve the PQ level in the adopted standalone MG system has been carried out in this dissertation work. As reviewed in Chapter 1, SAPFs are widely used in distribution systems to attain high-quality power levels. Particularly, SAPF is an effective approach for improving PQ by lowering current harmonics. The working of SAPF depends on coordinated action of three different control loops used for reference current generation (RCG), dc-link voltage

(V_{dc}) control and switching pulse generation. An exhaustive review on different concept pertaining to each of the control loops have been presented in the previous chapter highlighting their individual merits and demerits. However, there is continuous effort being invested by the researchers round the globe to further improve the performance of SAPF by adopting the different designs of these control loops. This acts an inspiration to the present author to explore the novel and the best combination of control topologies to enhance the SAPF performance further and, thus, accordingly the work is carried out and presented in this dissertation. Hence, in this chapter, to get an idea of working of SAPF, firstly, less explored control approaches are simulated and their impact on the performance of SAPF in the adopted standalone MG system is deeply investigated considering the practical operation conditions. In later chapters, the performance of the proposed new control topologies will be analyzed and compared.

2.1.2 Contribution of the Present Chapter

As surface in the literature, the SAPF finds applications mostly in mitigating PQ issues in grid-connected MG systems, whereas, its performance, testing and application are often ignored for standalone mode of operation of MG. Therefore, in the present chapter, to ensure higher PQ levels of the studied standalone MG system in the presence of nonlinear loads, a detailed analysis on the performance of SAPF is carried out. A comparative performance study among the different combinations of control techniques used of RCG, dc-link voltage control and pulse-width modulated (PWM) signal generations is investigated. Synchronous reference frame (SRF) and modified-SRF (MSRF) for RCG, PI and FLC technique for V_{dc} control and hysteresis current control (HCC) for switching pulse generation are studied for the modeling of SAPF under MATLAB/SIMULINK^{R} environment. Among the various PQ issues as discussed elaborately in the previous chapter, mainly, the THD in source current waveform is analyzed in the presence of different nonlinear load conditions. Besides this, the regulation of V_{dc} and reduction of its settling time are also studied under load changing conditions.

The following are the main findings of the current work.

a) A MG system comprising of SPV, wind and FC-based DGs is modeled for standalone mode of operation.
b) Modeling of SAPF based on conventional SRF and MSRF approaches (considering one at a time) for RCG, PI and FLC methods for V_{dc} control (considering one at a time) and HCC method for PWM signal generation to mitigate harmonics in the proposed standalone MG system is carried out.
c) To find the best combinations of control strategies for SAPF among the studied SRF-PI-HCC, MSRF-PI-HCC and MSRF-FLC-HCC approaches, a simulation-based comparative performance analysis between them in mitigating harmonics and curbing deviation in V_{dc} profile and its settling time is carried out under load-changing conditions.

2.1.3 Chapter Orientation

The remainder of this chapter is structured as follows. Modeling of studied MG system is presented in Section 2.2. In Section 2.3, the basic structure of SAPF is explained. Section 2.4 presents the concept of different control schemes associated with SAPF. In Section 2.5, the simulation results from the different studied scenarios are presented and discussed. Finally, the research findings of the present chapter are summarized in Section 2.6.

2.2 DESIGN OF MG

RESs are widely acknowledged as the most promising technologies for the successful implementation of modern sustainable energy policies, despite the periodic fluctuations in their availability. Enormous technical potential of RES is already identified in the global energy sectors. It is estimated that by the year 2020 the global total power consumption is expected to grow to 20TW. On the other hand, the irradiation falling on the earth surface is about 173,000TW. This shows that the power from solar energy alone when harnessed can supply the total global electricity demand [16].

As mentioned, because RESs are dependent on atmospheric conditions, their intermittency presents the greatest challenge. The efficiency of a single RES in giving continuous energy to customers is still being investigated by researchers. In order to improve their integration into the mix of energy sources, more research is therefore required. This problem can be solved by MGs employing a combination of RESs to provide more reliable and constant energy than a single RES [17]. A detailed description on MG system has been presented in Section 1.2 of Chapter 1.

Hence, this chapter presents the preliminary work on modeling of a typical isolated MG system (comprising of SPV, WECS, and FC-based DG units) based on MATLAB/SIMULINK platform. Thereafter, the role of SAPF is investigated in curbing the harmonics arisen due to nonlinear loads present in the adopted MG system. The basic structure of studied MG system interfacing different DGs is shown in Figure 2.1. The modeling detail of each of the DG is explained in the subsequent subsections.

2.2.1 Modeling of SPV

In this work, a single diode-based SPV model is used as depicted in Figure 2.2. The model is easy to implement in contrast to other existing models [45, 46]. The SPV voltage and current equations are described by (2.1)-(2.3)

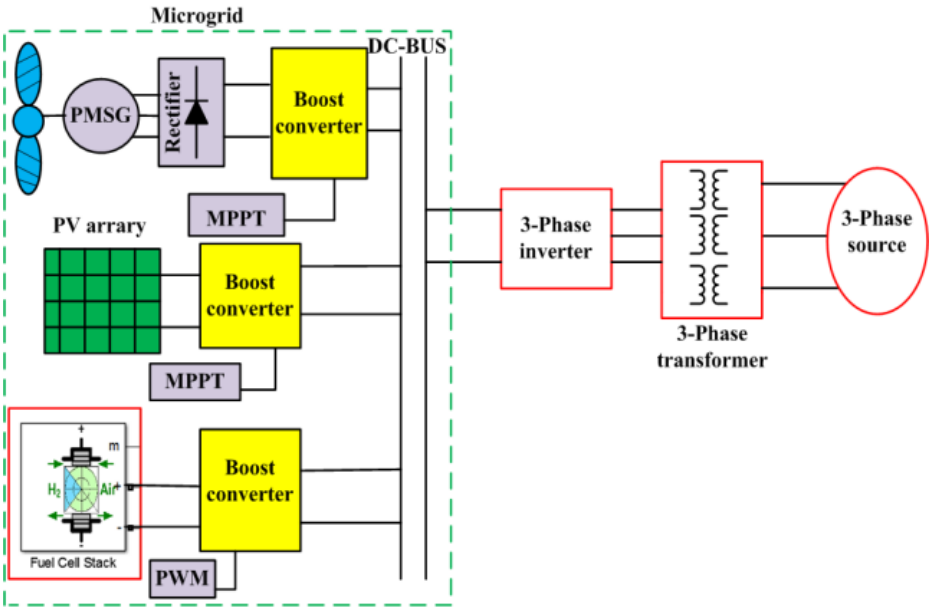

Figure 2.1 Block diagram of studied MG structure

$$I_{ph} = \left[I_{sc} + K_i \left(T_r - T \right) \right] \times \frac{G}{1000} \tag{2.1}$$

$$I_d = I_{rs} \left[\frac{T}{T_r} \right]^3 \exp\left[\frac{q \times E_{go}}{Ak} \left\{ \frac{1}{T_r} - \frac{1}{T} \right\} \right] \tag{2.2}$$

$$I_{pv} = N_p \times I_{ph} - N_p \times I_d \left[\exp\left\{ \frac{q \times V_{pv} + I_{pv} \times R_{se}}{N_s \times AkT} \right\} - 1 \right] \tag{2.3}$$

where, I_{ph}, I_d and I_{sh} are the photocurrent, the diode current, and the current due to parallel resistance, respectively. I_{sc} is the short circuit current, I_{pv} is the diode photo current, V_{pv} is the diode voltage , N_P indicates number of cells connected in parallel and N_s represents number of cells connected in series, R_{se} is the series resistance, V_{oc} refers to open circuit voltage, G is the solar irradiation, R_{sh} is the shunt resistance, q is the electron charge, k is the Boltzmann constant, T is the operating temperature, T_r is the

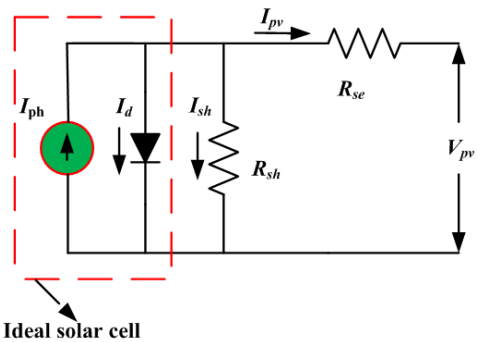

Figure 2.2 SPV unit equivalent circuit

Table 2.1: Parameters of PV system

Different Parameters	Values
Cell terminal voltage (V_{pv})	80 V
Current at maximum power (I_{mp})	8.6A
Open circuit voltage (V_{oc})	90.5V
Short circuit current (I_{sc})	10.2A
Voltage at maximum power (V_{mp})	81.5V

reference temperature taken as 25 ^{o}C, and A is the diode ideality factor. In Table 2.1, the values of various parameters used in the modelling of SPV array are presented. The fact that the quantity of power produced by the SPV depends on the weather is its main drawback. The maximum power point tracking (MPPT) method with a quick response function helps the SPV system to generate the maximum amount of power in any weather condition [47,48]. Various MPPT technique have been studied in the literatures [47-57], with Perturb and Observe (P&O) algorithm being one of the most commonly employed approach. Figure 2.3 illustrate the flow chart of the P&O algorithm-based MPPT controller. The P&O method guarantees a quick and easy response to the solar irradiance, which is always fluctuating. Because of this, in the present work, P&O method is used as an effective MPPT strategy to extract the highest power possible out of the SPV system irrespective of the intensity of irradiation. To match the voltage level of the MG, each DG should contribute equal amount of voltage. So, a boost converter is used to increase the SPV voltage to a level that matches the level of other DGs output [58, 60].

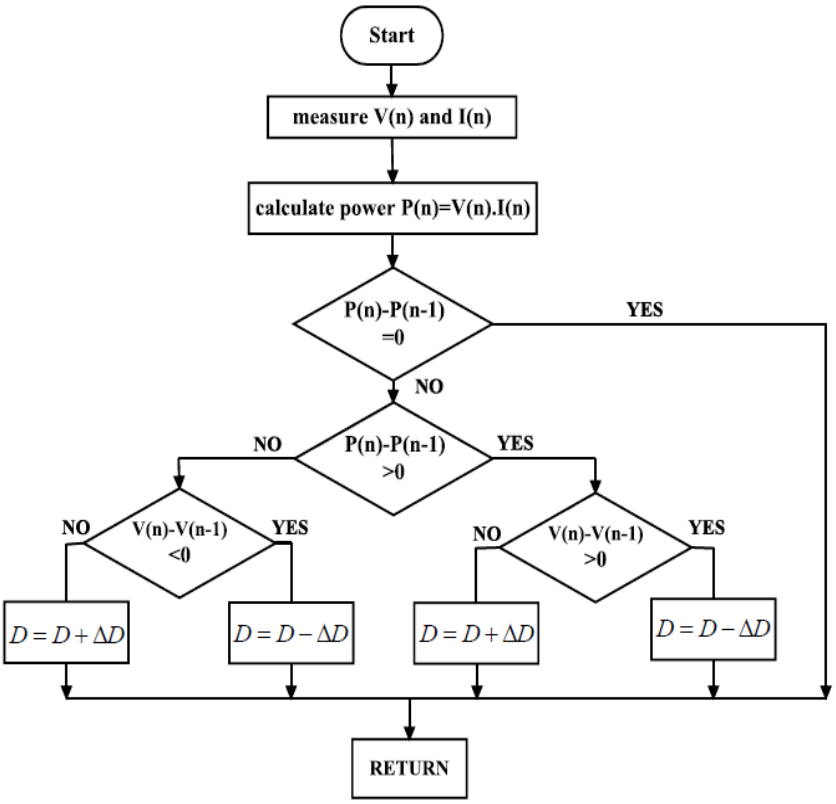

Figure 2.3 Flow chart of P&O MPPT algorithm

The simulation model of SPV system involving MPPT and boost converter is presented in Figure 2.4 and its corresponding output voltage (V_{spv}) is shown in Figure 2.5, where the required voltage of 230 V is achieved. The parameters of boost converter are presented in Table 2.2 [60, 61].

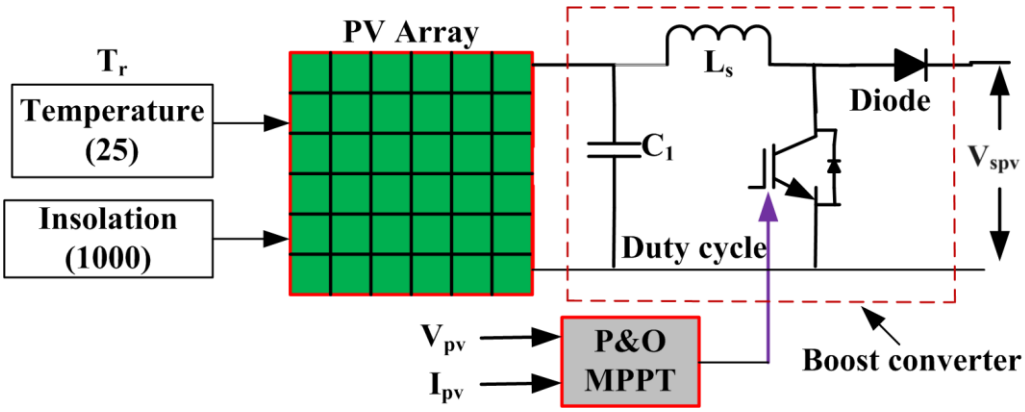

Figure 2.4 Block diagram of SPV with MPPT and boost converter

Table 2.2: Boost converter parameters

Different Parameters	Values
Load capacitance (C_l)	0.002 F
Source inductance (L_s)	0.01 H
Supply voltage (V_{pv})	80 V
Output voltage (V_{spv})	230 V

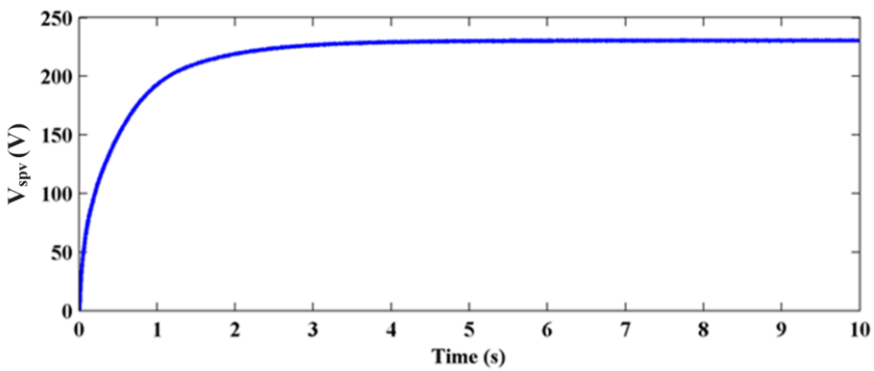

Figure 2.5 Output voltage (V_{spv}) waveform of SPV system

2.2.2 Modeling of WES

The wind generator considered for the studied MG system is realized based on permanent magnet synchronous generator (PMSG). The wind turbine transforms wind kinetic energy into mechanical energy, which is then supplied into the shaft of a PMSG to produce electricity as presented in Figure 2.6. The PMSG is connected to an unregulated rectifier, which converts AC to DC power [62-66]. A boost converter is coupled to the rectifier to get an adequate output voltage. The power produced by the wind is expressed as

$$P_m = \frac{1}{2} A V_\omega^{\,3} \rho C_P(\lambda, \beta) \tag{2.4}$$

where, ρ is the density of air, A is the rotor swept area, C_P is the coefficient of performance, λ and β represent the tip-speed ratio and pitch angle, respectively. The rotor speed (ω_m) is expressed in terms of wind velocity (V_ω) as per the equation (2.5).

$$\lambda = \frac{\omega_m R_r}{V_w} \tag{2.5}$$

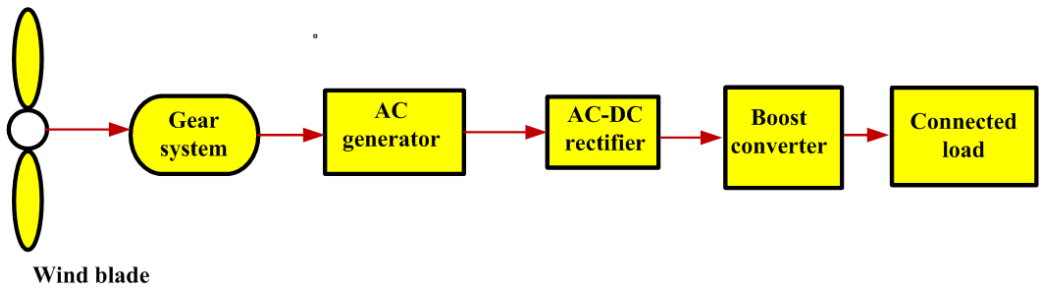

Figure 2.6 Block diagram of WES

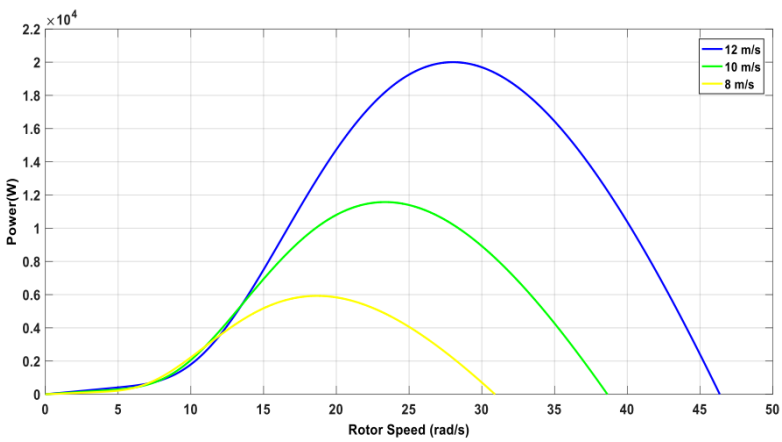

Figure 2.7 Power output vs. rotor speed curve

The torque of the turbine on the shaft (T_m) is given by the equations (2.6)-(2.8)

$$T_m = \frac{P_m}{\omega_m} = \frac{1}{2}\rho\pi R_r^{\,5}\frac{\omega_m^3}{\lambda^3}C_P(\lambda,\beta) \tag{2.6}$$

$$C_P(\lambda,\beta) = 0.5176\left(\frac{116}{\lambda_i} - 0.4\beta - 5\right)e^{\frac{-21}{\lambda_i}} \tag{2.7}$$

$$\lambda_i = \left[\frac{1}{\lambda + 0.08\beta} - \frac{0.035}{\beta^3 + 1}\right]^{-1} \tag{2.8}$$

where, P_m represents the mechanical power and R_r is the rotor radius. The MPPT algorithm is used to keep C_P at its maximum ($C_P = C_{p\max}$ and $\lambda_i = \lambda_{opt}$) (optimal tip-speed ratio) [81, 82].

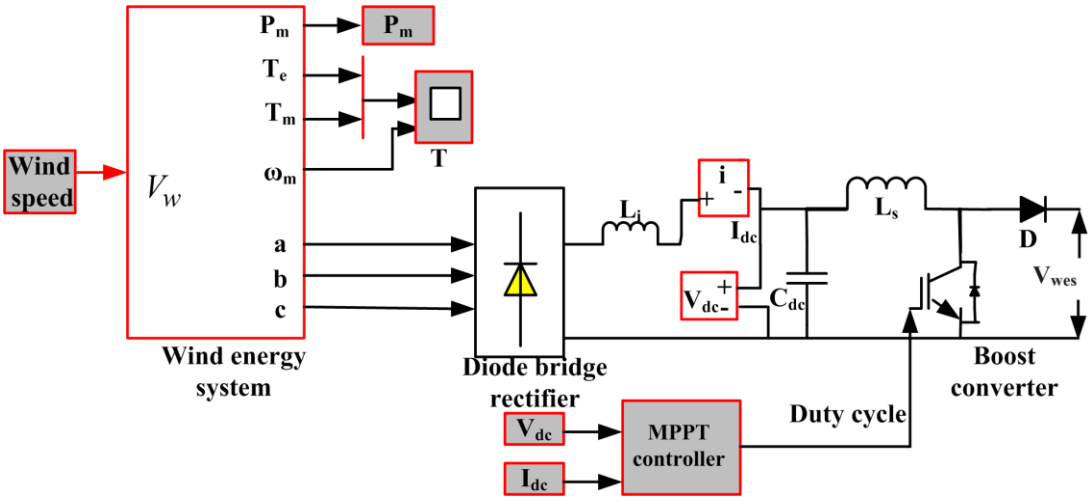

Figure 2.8 Overall model of WES

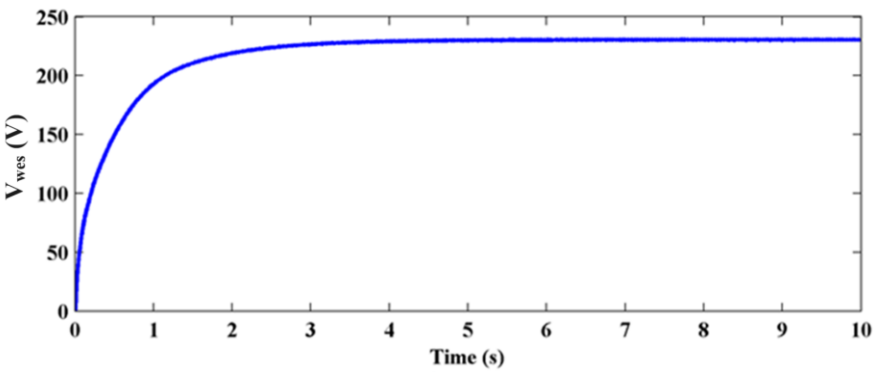

Figure 2.9 Output voltage (V_{wes}) waveform of WES

$$\omega_{ref} = \frac{V_w \lambda_{opt}}{R_r} \tag{2.9}$$

The power from a wind turbine in terms of rotor speed is given by (2.10).

$$P_m = \frac{1}{2} \rho A C_{P\max} \left(\frac{R_r \omega_{ref}}{\lambda_{opt}} \right) \tag{2.10}$$

The variations in the power output vs. rotor speed curve of the turbine with changing wind speed is depicted in Figure 2.7 [83, 84]. In Table 2.3, various symbols used in WES are tabulated. As per the proposed MG design, to obtain a dc voltage of 230 V, the dc output obtained from the rectifier is connected to a boost converter whose duty cycle is controlled by P&O-based MPPT technique [88, 89]. The simulation of PMSG-based wind generator system together with rectifier and boost converter is shown in Figure 2.8 and its corresponding output voltage is presented in Figure 2.9.

2.2.3 Modeling of Fuel Cell System

FCs technology converts the hydrogen energy to electrical energy through chemical reactions. There are several types of FC available that are classified as per their electrolytes. Proton exchange membrane (PEM)-based FC is one of them and it is adopted

Table 2.3: Symbols used in WES design

Symbol	Description
P_m	turbine output power in (w)
ω_s	wind speed in (r.p.s)
T_m	mechanical torque in ($N-m$)
ρ	density of air in (kg/m^2)
r	radius of the blade in (m)
T_e	electromagnetic torque in ($N-m$)
V_0	Output voltage in (v)
β	pitch angle in (rad/s)
W_p	wind power in (w)
ω_m	shaft power in (w)
λ	tip-speed ratio
V_ω	velocity of wind in (m/s)

as another DG in the development of the adopted MG system. FC has several benefits, including high efficiency, low working temperature, and a compact structure. It consists of a positive electrode (known as the cathode), a negative electrode (known as the anode), and an electrolyte. The pressurized hydrogen gas is introduced into the FC from the anode side, while oxygen is supplied to the cathode [90, 91]. Figure 2.10 displays a diagram of a typical PEMFC model depicting the movement of reactants/product gases and the flow of ion conduction within the cell. Expressions pertaining chemical reactions are shown in (2.11)-(2.13) [92, 93].

$$2H^{+} + 2e^{-} = H_2 \tag{2.11}$$

$$2H^{+} + 2e^{-} + \frac{1}{2}O_2 = H_2\mathrm{O} \tag{2.12}$$

$$H_2 + \frac{1}{2}O_2 = H_2\mathrm{O} \tag{2.13}$$

The reactions at anode, cathode and the overall reaction are expressed by (2.11)-(2.13), respectively. The modeling of the FC is carried out using the electro-chemical equations given by (2.14)-(2.19) [94-97].

$$E_{thermo} = 1.229 - 0.00085 \times (T - 298.15) + 4.31 \times 10^{5} \times T \times \ln(P_{H_2}) + \frac{1}{2}\ln(P_{O_2}) \tag{2.14}$$

$$V_{act} = -\left[\xi 1 + \xi 2 \times T + \xi 3 \times T \times \ln\left(CO_2\right)\right] \tag{2.15}$$

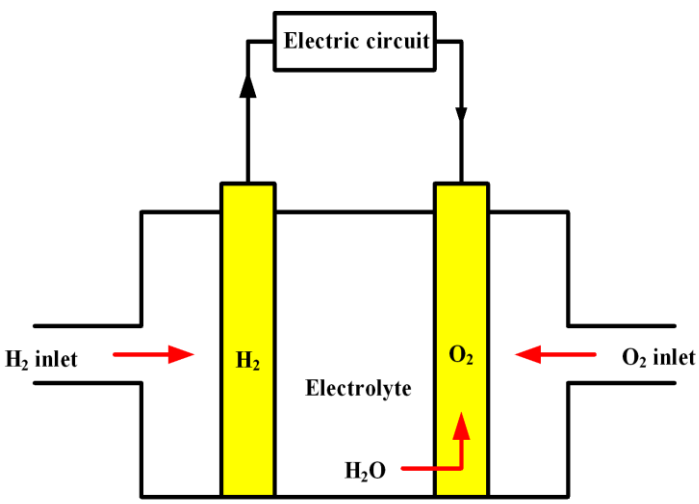

Figure 2.10 Basic PEMFC model

$$V_{ohmic} = i_{fc}\left(R_m + R_c\right) \tag{2.16}$$

$$V_{fc} = E_{thermo} - V_{act} - V_{ohmic} - V_{con} \tag{2.17}$$

$$V_s = k \times V_{fc} \tag{2.18}$$

$$V_{con} = \ln(1 - \frac{J}{J_{\max}}) \times (-B) \tag{2.19}$$

The thermodynamically predicted voltage (E_{thermo}) of FC is the potential obtained in an open circuit thermodynamic balance [100, 101]. The voltage of the FC (V_{fc}) is given by (2.17) and the stack voltage (V_{stac}) is simply the product of the voltage of the cell and the number of cells (k). V_{ohmic}, V_{act} and V_{con} are the ohmic loss, activation loss and concentration loss, respectively. R_c and R_m are the equivalent membrane resistances due to proton and electron conductions (in Ω), respectively, ξ is the model coefficient and for each cell it is represented by ξ_1, ξ_2 ξ_3, ξ_4 and so on. P_{H_2} and P_{O_2} are the pressures of hydrogen and oxygen (in atm), respectively. $T_{\max}$ is the temperature (in ^oK), J is the current density (in A/cm^2) and $J_{\max}$ is its maximum value.

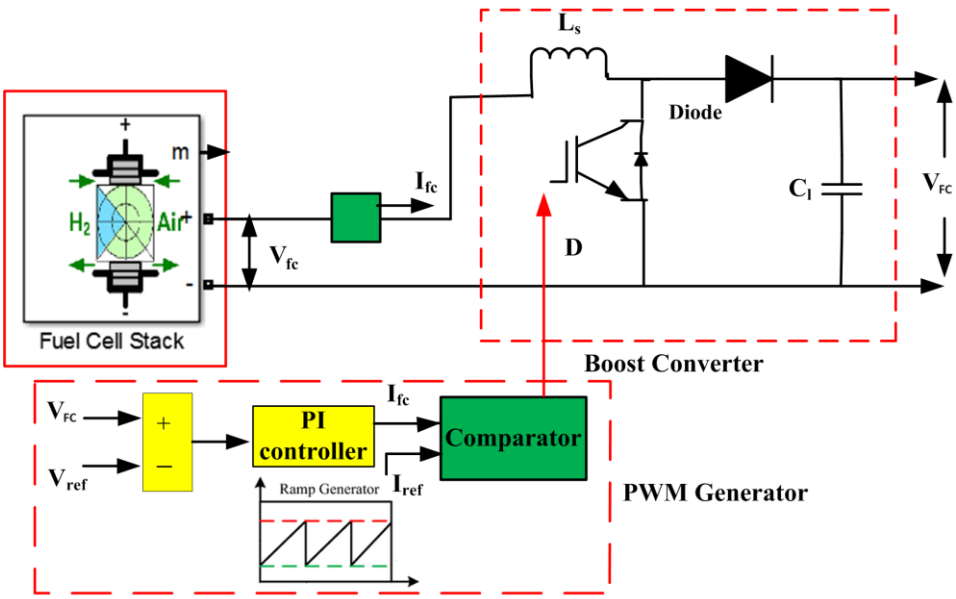

Figure 2.11 A generalized model of FC

In this study, the FC is capable of withstanding a maximum voltage of 80 V. To increase the voltage to a level of 230 V, a boost converter is used. The duty cycle (*D*) in the case of a boost converter is produced using a traditional PWM approach considering switching frequency of 20 kHz. The carrier wave and a constant signal are compared in order to produce the PWM signal, which controls the boost converter's switch. When the switch is closed, the diode becomes reverse-biased and the inductor stores energy within it. The diode gets forward-biased when the switch is opened, providing a path for the current. As a result, the output voltage exceeds the input voltage. A single FC generates a small amount of DC voltage. In practice, many FCs are usually assembled into a stack. In the present work, the FC produces an output voltage (V_{FC}) of 230 V. The FC is used in conjunction with boost converter as shown in Figure 2.11. The profile of output voltage of the adopted FC is portrayed in Figure 2.12. The parameters required for design of FC is illustrated in Table 2.4 [102].

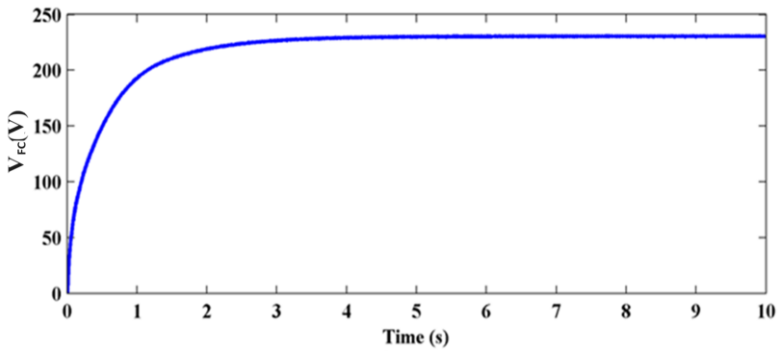

Figure 2.12 Output voltage **(**V_{FC}) waveform of FC

Table 2.4: FC parameters

Different Parameters	Values
Percentage of Hydrogen (H_2)	99.56%
Percentage Oxygen (O_2)	59.13%
Cell voltage (v_s)	1.128V
Resistance of cell (R_t)	0.7083 Ω
Total number of cell (k)	65
Load resistance (R_l)	6 Ω
FC output voltage (V_{FC})	230 V

2.3 DESIGN OF SAPF

The schematic diagram of the SAPF with all its control blocks is shown in Figure 2.13. The SAPF works as a controlled current source and generates compensating currents having equal magnitude but opposite in phase to the actual harmonic currents produced by the connected loads. The present study uses a VSI having a series inductance (L_f) and a dc-link capacitor (C_{dc}) connected in shunt at the point of common coupling (PCC).

a) *Voltage Source Inverter*: The VSI is composed of six bidirectional switches. Depending on the power levels, the switches can be IGBTs, MOSFETs, or GTOs. The controlled behavior of SAPF is implemented by controlling the switching time of the inverter switches. To achieve the desired pole voltages, the inverter's switches operate at a high frequency. Practically, the pole voltage variation is limited by the V_{dc}, switching frequency and modulation strategy.

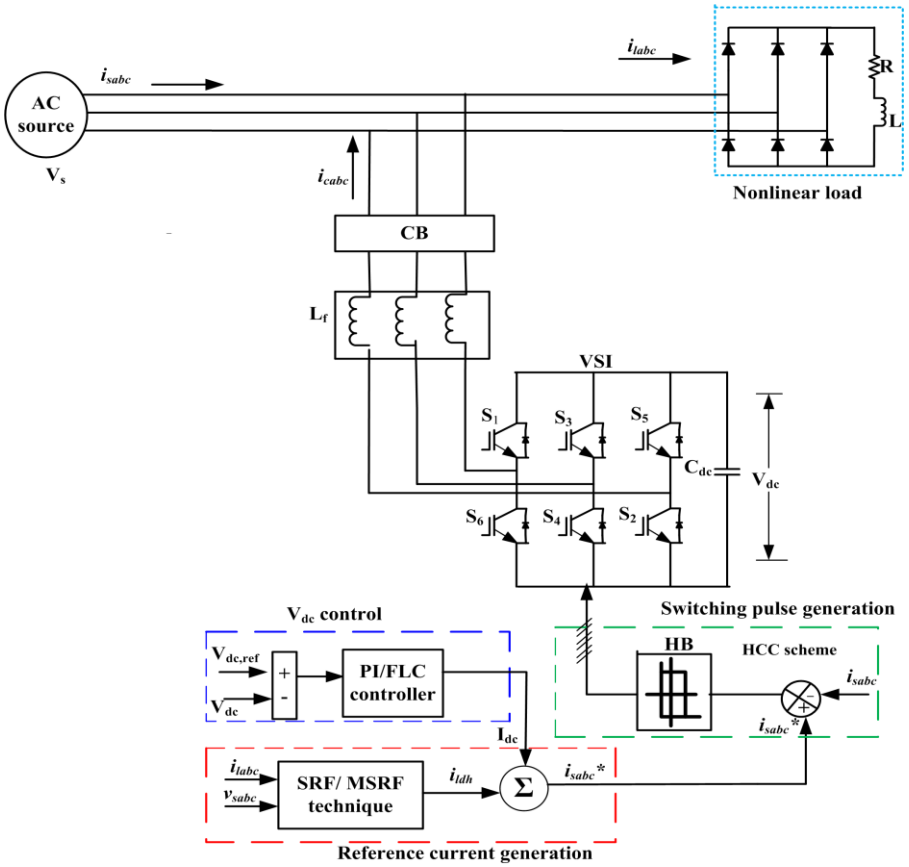

Figure 2.13 Studied SAPF model

b) *DC-link Capacitor*: Large size capacitors are typically chosen to maintain a constant V_{dc} profile, however, their value should be between the defined minimum and the maximum limits. The main functions of C_{dc} are: (i) to maintain the constant V_{dc} profile with low ripple content, (ii) to act as an energy storage element to provide support in mitigating active power imbalance during transient conditions and other system disturbances, (iii) to provide reactive power support for the system under steady-state and transient conditions. The selection of C_{dc} is made using (2.20)

$$C_{dc} = \frac{i_c}{\sqrt{3} \times \omega t \times V_{dc,\max}} \tag{2.20}$$

$$V_{dc} = \left(2\sqrt{\frac{2}{3}} \times V_{LL} \right) m \tag{2.21}$$

where, $V_{dc,\max}$ is the maximum value of the V_{dc} (considered as 700 V in the present work), i_c is the compensating current, ω is the angular frequency (*i.e.* 314 rad/s) and *t* is the recovery time of V_{dc}. The choice of V_{dc} depends on the line voltage at PCC and the modulation index (m) of the VSI. The expression for V_{dc} is given in (2.21).

c) *Series Inductor*: A major function of the L_f is to attenuate the switching frequency components in the AC side line current. The L_f is connected between VSI and AC mains to achieve controlled current source behavior of input circuit and to provide boost feature. By controlling the voltage across the inductors, filter current can be controlled. The L_f is calculated as per (2.22)

$$L_f = \frac{V_{dc}}{2 \times (\Delta I_{r,\max}) \times f_{s,\max}} \tag{2.22}$$

where, $\Delta I_{r,\max}$ is the change in the maximum ripple current and $f_{s,\max}$ is the maximum switching frequency.

2.4 CONTROL SCHEME FOR SAPF

The control circuits involved with the SAPF are designed in such way that their coordinated actions inject a current to compensate for the harmonics present, and thereby, enhancing performance of the system. As mentioned earlier, the present work focuses on performance of SAPF under the various combinations of control methods used for RCG, dc-link voltage control and switching pulse generation. Hence, firstly, the traditional control approaches for RCG is detailed in this section. Thereafter, a fuzzy and PI controller-based strategy for V_{dc} regulation is described followed by HCC technique for switching pulse generation. The SAPF is normally connected at the PCC for the mitigation of harmonics of the source current (i_{sabc}). To eradicate the harmonics from i_{sabc}, an equal amount of compensating current (i_{cabc}) is injected by SAPF in opposite phase to that of harmonics current. The instantaneous source current ($i_s(t)$) and the source voltage $(v_s(t))$ of the SAPF are expressed by (2.23) and (2.24), respectively.

$$i_s(t) = i_l(t) - i_c(t) \tag{2.23}$$

$$v_s(t) = V_s \sin \omega t \tag{2.24}$$

The load current $i_l(t)$ containing harmonics is expressed by (2.25)

$$i_l(t) = i_1(\sin \omega t + \varphi_1) + \sum_{n=2}^{\infty} i_n(\sin n\omega t + \varphi_1) \tag{2.25}$$

where, $\boldsymbol{i_1}$ is the fundamental current and φ_1 is the angle between current and voltage phasors. The power components are presented in (2.26)

$$p_l(t) = p_f(t) + p_r(t) + p_h(t) \tag{2.26}$$

where, $p_f(t)$, $p_r(t)$ and $p_h(t)$ are the active power, reactive power and harmonic power, respectively. The real power is given by (2.27).

$$p_f(t) = v_s(t) \times i_s(t) \tag{2.27}$$

After compensation, the $\boldsymbol{i_s}$ is presented by (2.28)

$$i_s(t) = \frac{p_f(t)}{v_s(t)} = i_l \cos\varphi_1 * \sin\omega t = I_{sm} \sin\omega t \tag{2.28}$$

where, $I_{sm} = i_l \cos\varphi_1$. The source should offer some extra current to sustain the active power demand in order to minimize the inverter's conduction losses. So, the total source current (I_{sp}) is now represented as per (2.29)

$$I_{sp} = I_{sm} + I_{dc} \tag{2.29}$$

where, I_{dc} is the maximum current achieved from the V_{dc} controller. The compensating current (i_c) of the SAPF can be extracted from (2.23). The generation of i_c depends upon (i) generation of RCG, (ii) V_{dc} and (iii) pulses given to VSI. All these factors depend on the performance of the three control loops of the SAPF. The various topologies related to these control loops, employed in this chapter, are briefly discussed below.

2.4.1 Reference Current Generation Technique

The control approaches for generating compensation currents can be achieved using either frequency domain or time domain strategies. Under frequency domain approach, the control method for extracting compensation current involves conducting Fourier analysis on the current signals. Nevertheless, this method involves complicated mathematical calculations that may take more time to give output. On the other hand, the time domain method is mathematically simpler and very easy to implement. In addition, the numerical filter plays a crucial role in separating the fundamental components from the harmonics to extract the necessary information on the compensation current that needs to be injected. In the present work, realization of control strategy is carried out based on the two widely used basic techniques (which are easy to implement) such as (a) SRF method and (b) MSRF method. Each of these is briefly discussed in the subsequent subsections.

(a) SRF technique

The working of conventional SRF method is revealed in Figure 2.14. The control mechanism contains the conversion of i_{sabc} from abc to d - q reference frame [154]. The Park-transformation technique is used to transform the 3-phase instantaneous load

currents (i_{la}, i_{lb} and i_{lc}) to d-q frame ($i_{ld} - i_{lq}$) as shown in (2.30). These currents are synchronized at the PCC by means of a phase-locked loop (PLL). The information of theta angle is highly necessary for the transformation of current waveforms from abc to d-q or d-q to abc reference frame, which is obtained from SRF-based PLL.

$$\begin{pmatrix} i_{l0} \\ i_{ld} \\ i_{lq} \end{pmatrix} = \sqrt{2/3} \begin{pmatrix} \sqrt{1/2} & \sqrt{1/2} & \sqrt{1/2} \\ \sin\omega t & \sin(\omega t - \frac{2\pi}{3}) & \sin(\omega t + \frac{2\pi}{3}) \\ \cos\omega t & \cos(\omega t - \frac{2\pi}{3}) & \cos(\omega t + \frac{2\pi}{3}) \end{pmatrix} \begin{pmatrix} i_{la} \\ i_{lb} \\ i_{lc} \end{pmatrix} \tag{2.30}$$

The d-axis component of the current is used for the mitigation of harmonic components. It is viewed from Figure 2.14 that the d-axis current is passed through a low pass filter (LPF) to remove the DC part of it, and finally, results in harmonics component of d-axis current (*i.e.*, i_{ldh}). The output signals generated by the SAPF, after d-q transformation, is dependent upon the unit vector angle (θ), which is obtained from the PLL circuit. The θ will help to continue the synchronization with supply voltage and current. The error between V_{dc} and the reference dc-link capacitor voltage ($V_{dc,ref}$) is passed through the voltage controller block to obtain the output current (I_{dc}), which will

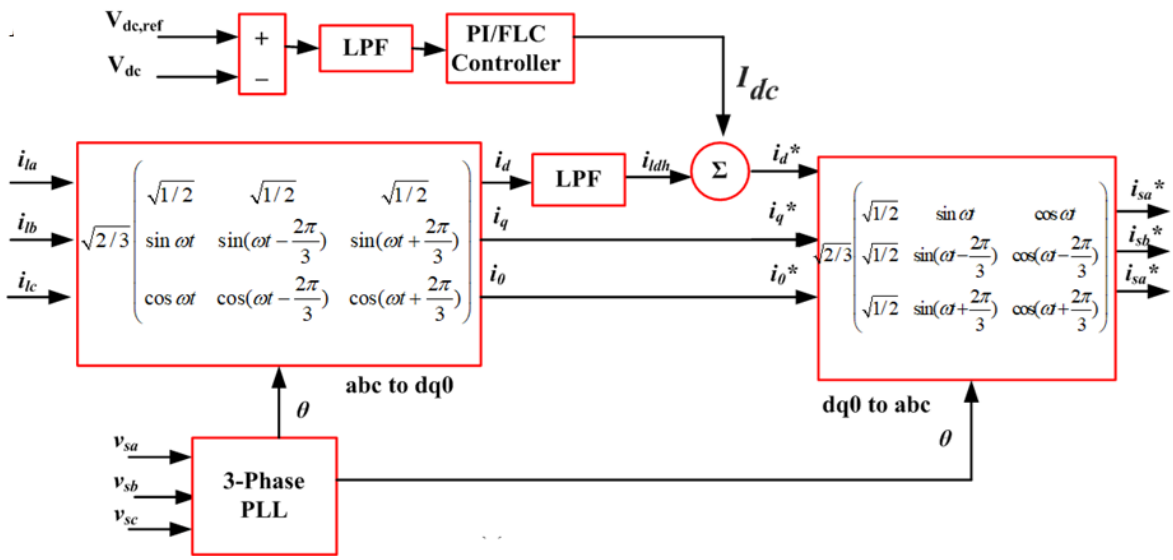

Figure 2.14 SRF technique

diminish the switching losses occurring in VSI. This I_{dc} is then added with i_{ldh} to get the reference d-axis current (i_d^*). The reference *q*-axis current (i_q^*) and zero-axis current (i_0^*) are set to zero. These i_d^*, i_q^*, and i_0^* currents are transformed to 3-phase reference source currents $(i_{sa}^*$, i_{sb}^* and $i_{sc}^*)$ using inverse Park-transformation technique as mentioned in (2.31) and, thereafter, compared with the corresponding actual source currents $(i_{sa}$, i_{sb} and $i_{sc})$ to produce switching pulses for the VSI.

$$\begin{pmatrix} i_{sa}^* \\ i_{sb}^* \\ i_{sc}^* \end{pmatrix} = \sqrt{2/3} \begin{pmatrix} \sqrt{1/2} & \sin\omega t & \cos\omega t \\ \sqrt{1/2} & \sin(\omega t - \frac{2\pi}{3}) & \cos(\omega t - \frac{2\pi}{3}) \\ \sqrt{1/2} & \sin(\omega t + \frac{2\pi}{3}) & \cos(\omega t + \frac{2\pi}{3}) \end{pmatrix} \begin{pmatrix} 0 \\ i_{ld} \\ 0 \end{pmatrix} \qquad 2.31$$

On the other hand, a PLL-circuit dependent on the supply voltage is needed for vector orientation in the conventional-SRF control method. Nonetheless, when repeated zero crossings occur in the supply voltage and other non-idealities arise, designing a high performance PLL circuit becomes a challenge. The challenges faced by the SRF method in the unit vector generation is alleviated by a straightforward and an effective MSRF technique.

(b) MSRF technique

Unlike the PLL circuit utilized in the SRF method, the MSRF scheme uses a basic unit vector generation strategy to realize synchronization [162, 163]. The block diagram representation of the MSRF scheme is shown in Figure 2.15. Here, v_{sabc} is first converted to $V_{s\alpha}$ and $V_{s\beta}$ in the $\alpha-\beta$ reference frame according to (2.32) and (2.33). Thereafter, the unit vectors ($\sin\theta$ and $\cos\theta$) are generated using equations (2.34) and (2.35). These unit vectors are required for obtaining *d*-*q* axis currents ($i_d - i_q$) from the load current i_{labc} as per (2.32) and (2.33). For regulating V_{dc}, some active power is extracted from the source through the SAPF. Hence, the V_{dc} is evaluated in comparison to its reference

value ($V_{dc,ref}$) and the error between them is fed to PI/ fuzzy controller for generation of the peak value of source current I_{dc}. This I_{dc} is added with *d*-axis harmonics component of load current i_{ldh} and the *q*-axis component of current i_{lqh} is directly used to generate reference *d*-*q* currents i.e., i_d^* and i_q^*, respectively. The desired i_{sa}^*, i_{sb}^* and i_{sc}^* are deduced employing reference i_α^* and i_β^* components according to (2.38)-(2.39).

$$V_{s\alpha} = \frac{\sqrt{3}}{2} V_{sm} \sin \omega t \tag{2.32}$$

$$V_{s\beta} = \frac{\sqrt{3}}{2} V_{sm} \cos \omega t \tag{2.33}$$

$$\sin \theta = \frac{V_{s\alpha}}{\sqrt{\left(V_{s\alpha}^2 + V_{s\beta}^2\right)}} \tag{2.34}$$

$$\cos \theta = \frac{V_{s\beta}}{\sqrt{\left(V_{s\alpha}^2 + V_{s\beta}^2\right)}} \tag{2.35}$$

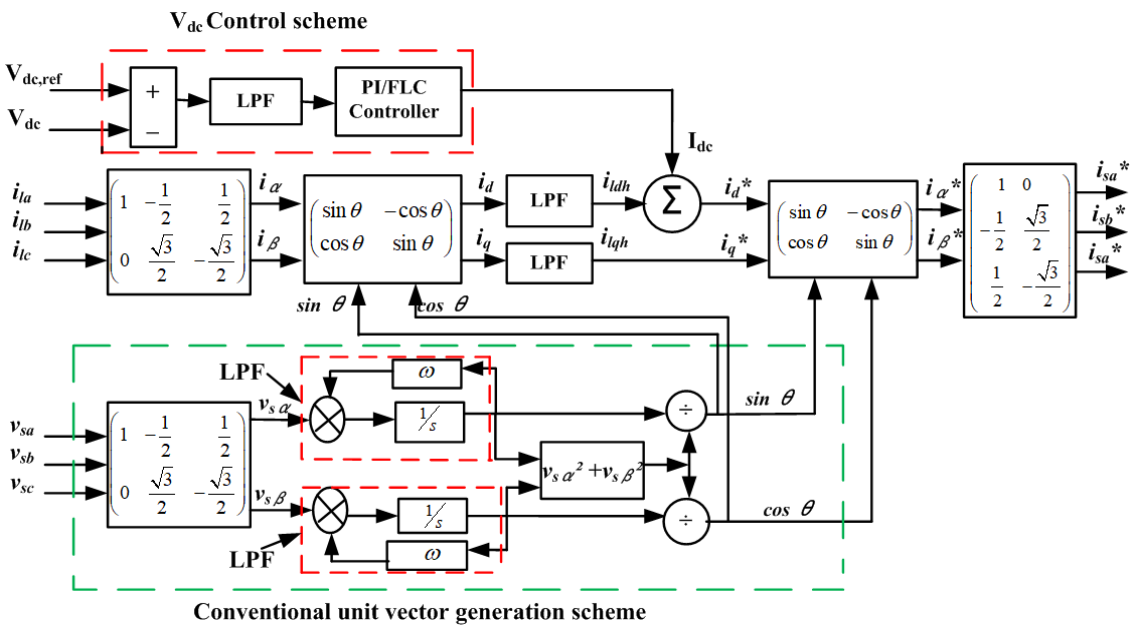

Figure 2.15 MSRF technique

$$\begin{pmatrix} i_\alpha \\ i_\beta \end{pmatrix} = \begin{pmatrix} 1 & -\frac{1}{2} & \frac{1}{2} \\ 0 & \frac{\sqrt{3}}{2} & -\frac{\sqrt{3}}{2} \end{pmatrix} \begin{pmatrix} i_{la} \\ i_{la} \\ i_{lc} \end{pmatrix} \tag{2.36}$$

$$\begin{pmatrix} i_d \\ i_q \end{pmatrix} = \begin{pmatrix} \sin\theta & -\cos\theta \\ \cos\theta & \sin\theta \end{pmatrix} \begin{pmatrix} i_\alpha \\ i_\beta \end{pmatrix} \tag{2.37}$$

$$\begin{pmatrix} i_\alpha^* \\ i_\beta^* \end{pmatrix} = \begin{pmatrix} \sin\theta & -\cos\theta \\ \cos\theta & \sin\theta \end{pmatrix} \begin{pmatrix} i_d^* \\ i_q^* \end{pmatrix} \tag{2.38}$$

$$\begin{pmatrix} i_{sa}^* \\ i_{sb}^* \\ i_{sc}^* \end{pmatrix} = \begin{pmatrix} 1 & 0 \\ -\frac{1}{2} & \frac{\sqrt{3}}{2} \\ \frac{1}{2} & -\frac{\sqrt{3}}{2} \end{pmatrix} \begin{pmatrix} i_\alpha^* \\ i_\beta^* \end{pmatrix} \tag{2.39}$$

The i_{sa}, i_{sb} and i_{sc} are compared with the i_{sa}^*, i_{sb}^* and i_{sc}^*, respectively, to generate the switching signals for the VSI using HCC-based switching technique. Subsequently, the VSI outputs the desired compensating current and is fed at PCC to mitigate the harmonics.

2.4.2 Dc-link voltage control technique

The performance of SAPF depends on the V_{dc} control because it looks after the power balance in the system and generates desired current for compensating the switching losses arising in the VSI. Therefore, V_{dc} regulation is a crucial issue for SAPF performance improvement. In the present chapter, two well studied techniques i.e., PI controller and FLC are used for controlling dc-side voltage of the SAPF.

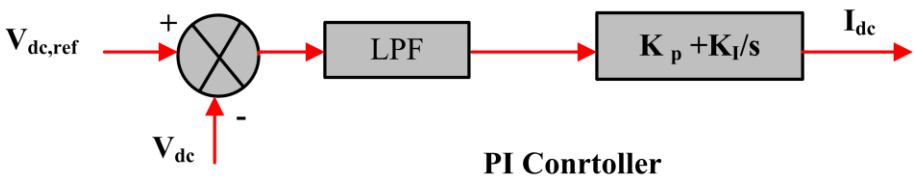

Figure 2.16 PI controller-based V_{dc} control scheme

(a) *PI controller*

The PI controller's mechanism is described in Figure 2.16. Firstly, the error $(e(n))$ between actual V_{dc} and the reference $V_{dc,ref}$ is passed through an LPF for eliminating the harmonics and to keep only the basic element. Firstly, the $e(n)$ is passed through a LPF to eliminate the harmonics from the fundamental component. Thereafter, the fundamental component is fed to the PI controller to obtain I_{dc}, which is added to the pre-load disturbance maximum value of the source current (I_{sm}) as per equation (2.29). This is done to compensate for any deviation in the V_{dc} profile following any load change by modifying the current drawn by the dc-link capacitor. The necessary gating pulse to the switches for injecting the compensating current at the PCC is then produced by multiplying I_{dc} by the calculated reference currents. In this work, the value of K_p and K_i are evaluated using (2.40) and (2.41), respectively, where ζ = 0.707 is the damping ratio and ω_n is the undamped frequency [177, 178].

$$K_p = 2 \times \zeta \times \omega_n \times C_{dc} \tag{2.40}$$

$$K_i = \omega_n^2 \times C_{dc} \tag{2.41}$$

(b) *FLC technique*

FLC is realized from fuzzy set theory propounded in 1965. FLCs are excellent choice where accurate mathematical formula-based calculations are impossible. The FLC technique (in discrete mode) is depicted in Figure 2.17. It comprises of fuzzy controller with LPF [179, 180], $V_{dc,ref}$ signal and the feedback V_{dc} signal. In this method also, the

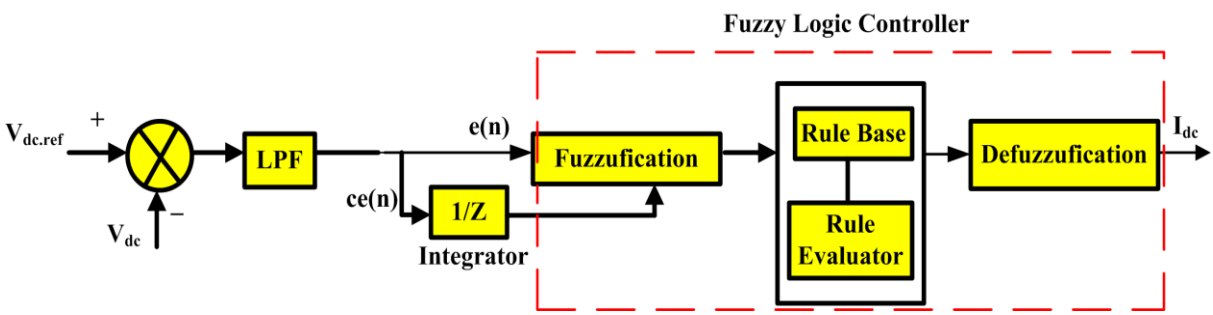

Figure 2.17 Block diagram of FLC scheme

error $(e(n))$ between V_{dc} and $V_{dc,ref}$ is passed through LPF with a cut-off frequency of 50 Hz to allow only the fundamental component to pass. A FLC translates a linguistic control approach into an automatic control approach, and for this, fuzzy rules are constructed based on the expert experience or knowledge database [181]. The $e(n)$ and its integral $(ce(n))$ are the two input variables considered for the FLC design. The maximum value of the reference current I_{dc} is considered as the output of FLC. This I_{dc} is multiplied with the MSRF output for generating the desired reference current (i^*_{sabc}). The different membership functions (MFs) for the two inputs ($e(n)$ and $ce(n)$) and one output (I_{dc}) are shown in Figure 2.18 [182]. Basically, FLC consist of four key processes such as fuzzification, rule evaluator, defuzzification and data/rule base.

(a) Fuzzification: It is the process of converting numerical variable to a linguistic variable. In the proposed system, triangular MFs are used for fuzzification of the concerned variables ($e(n)$, $ce(n)$ and I_{dc}). These are assigned using seven MFs such as: negative big (NB), negative medium (NM), negative small (NS), zero (Z), positive small (PS), positive medium (PM), and positive big (PB).

(b) Rule evaluator: In case of conventional PI controller, the control variables are the combination of numerical values, but FLC uses linguistic variables instead of numerical variables. In this process, the basic operations of FLC requires AND (∩), NOT (−) and OR (U) logical operations for intersection, complement and union functions, respectively, for the evaluation of fuzzy set rules.

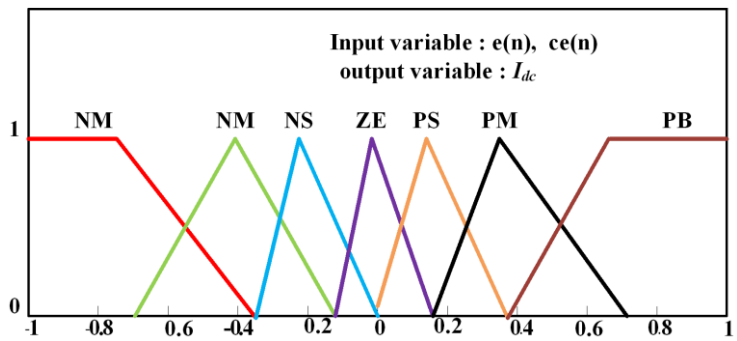

Figure 2.18 MFs for FLC scheme

(c) Defuzzification*:* The process of converting linguistic variable to numerical values is known as defuzzification. Among the various available method, "centroid method" of defuzzification is used in this work as it is easy to execute.

(d) Data/rule base: The data base stores the triangular membership function which is required by rule evaluator. The 49 rules used in this proposed controller are presented in Table 2.5.

The four concepts in FLC are fuzzification, rule base, inference mechanism, and defuzzification. In fuzzification, the real-world inputs are fuzzified to produce fuzzy sets. These input fuzzy sets interact with the fuzzy rule base, producing fuzzy set outputs through the inference process [178-180]. The defuzzification block then converts these fuzzy set outputs back to the crisp and real-world outputs. In designing a fuzzy logic-based V_{dc} controller, two crisp inputs (i.e., (i) the $e(n)$ between V_{dc} and $V_{dc,ref}$ and (ii) the integration of $e(n)$ expressed as $ce(n)$) and one crisp output (i.e. I_{dc}, the maximum output current from the V_{dc} controller) are considered. Both input and output variables are fuzzified using seven membership functions defined as *NB*, *NM*, *NS*, *ZE*, *PS*, *PM*, and *PB*, which are represented in Figure 2.18 [182]. The rule base contains 49 control rules (refer Table 2.5), which interact with the input variables to fire a specific set of rules to offer fuzzy output as I_{dc}. Finally, using the centroid method of defuzzification, the fuzzy I_{dc} is converted into crisp I_{dc}. Further, like PI controller, in

Table 2.5: Rule base table for FLC method

$ce(n)$ \ $e(n)$	I_{dc}						
	NB	*NM*	*NS*	*ZE*	*PS*	*PM*	*PB*
NB	*NB*	*NB*	*NB*	*NB*	*NM*	*NS*	*ZE*
NM	*NB*	*NB*	*NB*	*NM*	*NS*	*ZE*	*PS*
NS	*NB*	*NB*	*NM*	*NS*	*ZE*	*PS*	*PM*
ZE	*NB*	*NM*	*NS*	*ZE*	*PS*	*PM*	*PB*
PS	*NM*	*NS*	*ZE*	*PS*	*PM*	*PB*	*PB*
PM	*NS*	*ZE*	*PS*	*PM*	*PB*	*PB*	*PB*
PB	*ZE*	*PS*	*PM*	*PB*	*PB*	*PB*	*PB*

this approach as well, the crisp I_{dc} adds up to the maximum value of the source current (I_{sm}) to compensate for any deviation occurring in the V_{dc} profile.

2.4.3 Switching Pulse Generation Technique

There are several types of pulse generation techniques available in the literature such as sinusoidal PWM, space vector PWM, sinusoidal PWM with instantaneous current control, HCC-based PWM, selected harmonic elimination-based PWM and so on [183]. As reported in the literature, HCC approach is widely used in SAPF due to its inherent advantages such as rapid current controllability, absolute consistency, quick response, and easy implementation [184], hence, this technique is implemented in present chapter. The configuration of hysteresis band current regulator which generates the required switching pulse for the inverter is shown in Figure 2.19. The current regulator generates the error signal by comparing the reference source current (i^*_{sabc}) and the actual source current (i_{sabc}). The PWM pulses needed for the inverter are carefully designed to ensure that when the error signal exceeds the upper limit of the hysteresis loop, the lower switches of the inverter are turned ON while the upper switches are turned OFF. In a similar fashion, the upper switches are turned ON and the lower switches are turned OFF when the error signal surpasses the lower band. By tracking the actual current in relation to the reference current within the hysteresis band, a precise measurement is maintained.

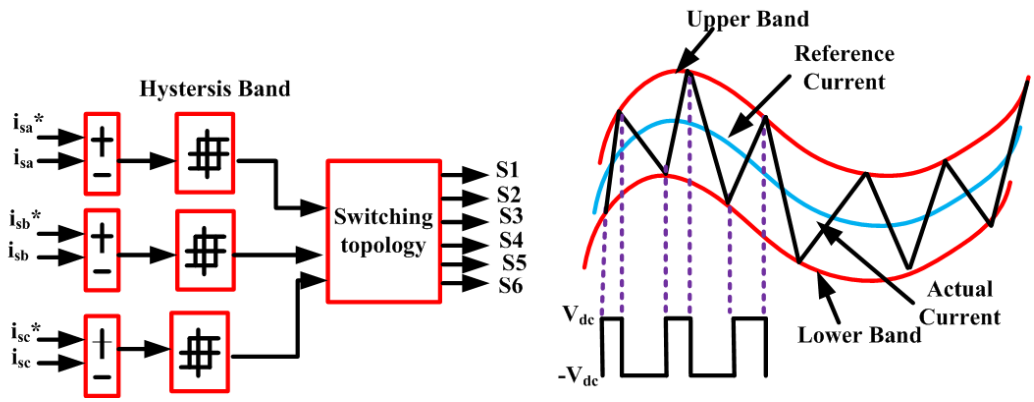

Figure 2.19 HCC-based switching pulses generation scheme

2.5 RESULTS AND DISCUSSIONS

This section investigates the performance of SAPF under different load-changing conditions. For better harmonic filtering, a SAPF is appended with the studied control algorithms (i.e., SRF and MSRF techniques) for RCG. Apart from the above, the V_{dc} regulation and PWM pulse generation are realized using the existing PI/FLC techniques and HCC scheme, respectively. In the present study, the combinations of scheme employing the conventional SRF method (for RCG), either PI or FLC controller (for V_{dc} control), and HCC (for PWM signal generation) used for producing compensating current i_{cabc} are referred as SRF-PI-HCC and SRF-FLC-HCC techniques. On the other hand, the combination of MSRF approach with either PI or FLC and HCC are referred to as MSRF-PI-HCC and MSRF-FLC-HCC techniques.

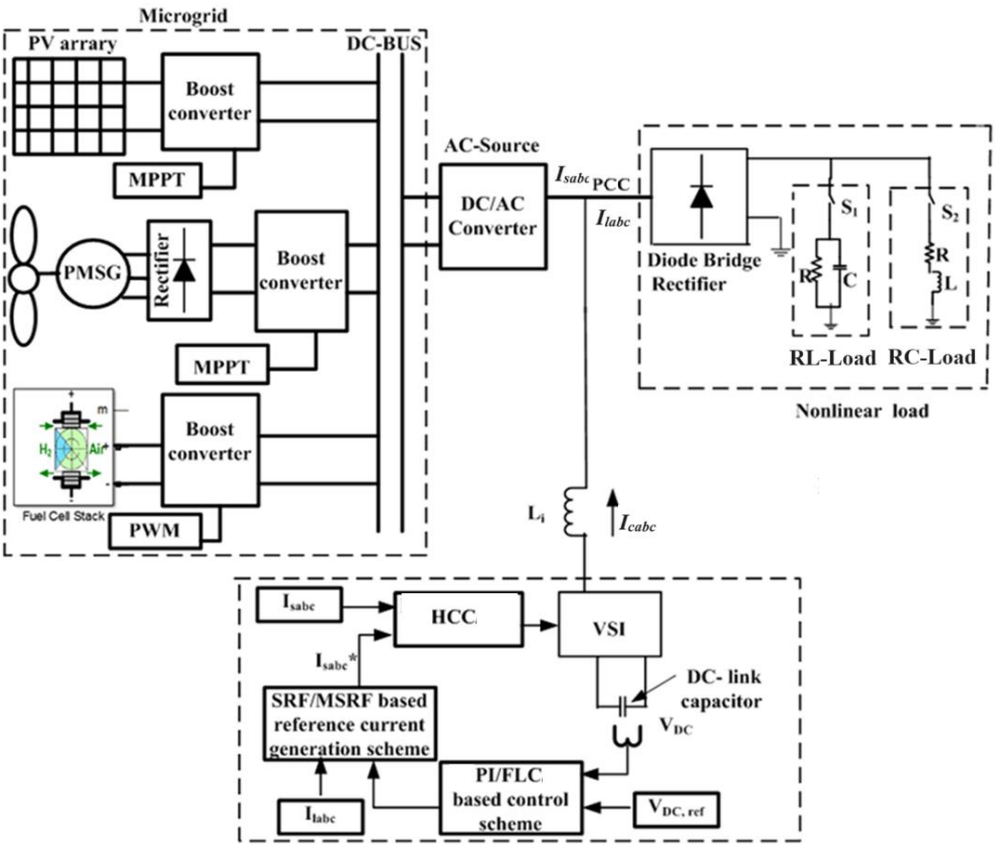

Figure 2.20 SAPF with MSRF-FLC-HCC-based control scheme

The studied SAPF model employing the above-mentioned combination of control methods is simulated in MATLAB/Simulink[R] platform. The results obtained from each method are examined to establish the superiority of one over the other. In this study, the nonlinear load consisting of a 3-phase bridge rectifier with resistance and inductance in series on its dc side is considered as the inductive type nonlinear load (i.e., nonlinear RL-load), and a rectifier with resistance and capacitance in parallel is referred to as the capacitive type nonlinear load (i.e., nonlinear RC-load). The model of SAPF with different control loops is illustrated in Figure 2.20, and its various parameters are tabulated in Table 2.6. Firstly, the model is simulated with the nonlinear RL- and RC-loads without connecting the SAPF. The performance analyses of the studied MG system is investigated without SAPF as well as with SAPF under the action of different controllers at different loading conditions and are denoted as different scenarios. The results of interest under each scenario are highlighted in bold in the respective table.

a) Scenario 1: Performance analysis without SAPF and with SAPF employing SRF-PI-HCC scheme.
b) Scenario 2: Performance analysis of SAPF with employing MSRF-PI-HCC scheme.

Table 2.6: Parameters of the studied system

Parameters	Values
Source voltage (V_{srms})	230 V
Frequency (f)	50 Hz
Source resistance (R_s)	1 Ω
Source inductance (L_s)	0.1mH
Load resistor (R_L)	20 Ω
Load inductor (L_L)	50 mH
Resistor (R_C)	50 Ω
Load capacitor (C_C)	2200 µF
Power converter	6-IGBTs/6-diodes
Interfacing inductor (L_f)	1.35 mH
Dc-link capacitor (C_{dc})	3000 µF
Dc-link reference voltage ($V_{dc,ref}$)	700 V

c) Scenario 3: Performance analysis of SAPF employing MSRF-FLC-HCC scheme.
d) Scenario 4: Comparative performance analysis of SAPF using studied MSRF-FLC-HCC approach with that of SAPF with SRF-PI-HCC and MSRF-PI-HCC techniques.

2.5.1 Performance Analysis Pertaining to Scenario 1

In this scenario, firstly, the performance of adopted MG system is analyzed without SAPF in the presence of the nonlinear load (inductive (or RL) and capacitive (or RC) types) taken into consideration, The profile of i_{sabc} is shown in Figure 2.21(a) and its harmonics Figure 2.21(b). It may be observed from Figures 2.21(a) and (b) that the source current waveform is non-sinusoidal in nature having very high total harmonic distortion (THD) content of 26.74% and 20.25% of RL- and RC-type nonlinear loads, respectively. In order to make i_{sabc} to be sinusoidal, SAPF (employing SRF-PI-HCC controller) is turned on, which injects compensating current (i_{cabc}) at the PCC as displayed in Figure 2.21(c). As a result, THD level comes down to 3.52% and 3.40% for RL- and RC-type nonlinear loads, respectively. The i_{sabc} after compensation and its corresponding FFT analysis are portrayed in Figures 2.21(d) and (e), respectively.

2.5.2 Performance Analysis Pertaining to Scenario 2

Performance of the SAPF employing MSRF-PI-HCC controller is investigated in this scenario. The profile of i_{cabc} generated by MSRF-based SAPF in the presence of RL- and RC-type nonlinear loads are shown in Figure 2.22(a). Figure 2.22(b) illustrates that the profile of i_{sabc} is nearly sinusoidal in nature due to the injection of i_{cabc} by the SAPF. In comparison to Scenario 1, the FFT analysis of i_{sabc} (after compensation) presented in Figure 2.22(c) shows further reduction of THD content to 3.42% and 3.31% for RL-and RC-type loads, i_{sabc} waveform obtained after compensation**.** It may be viewed from the output waveform respectively.

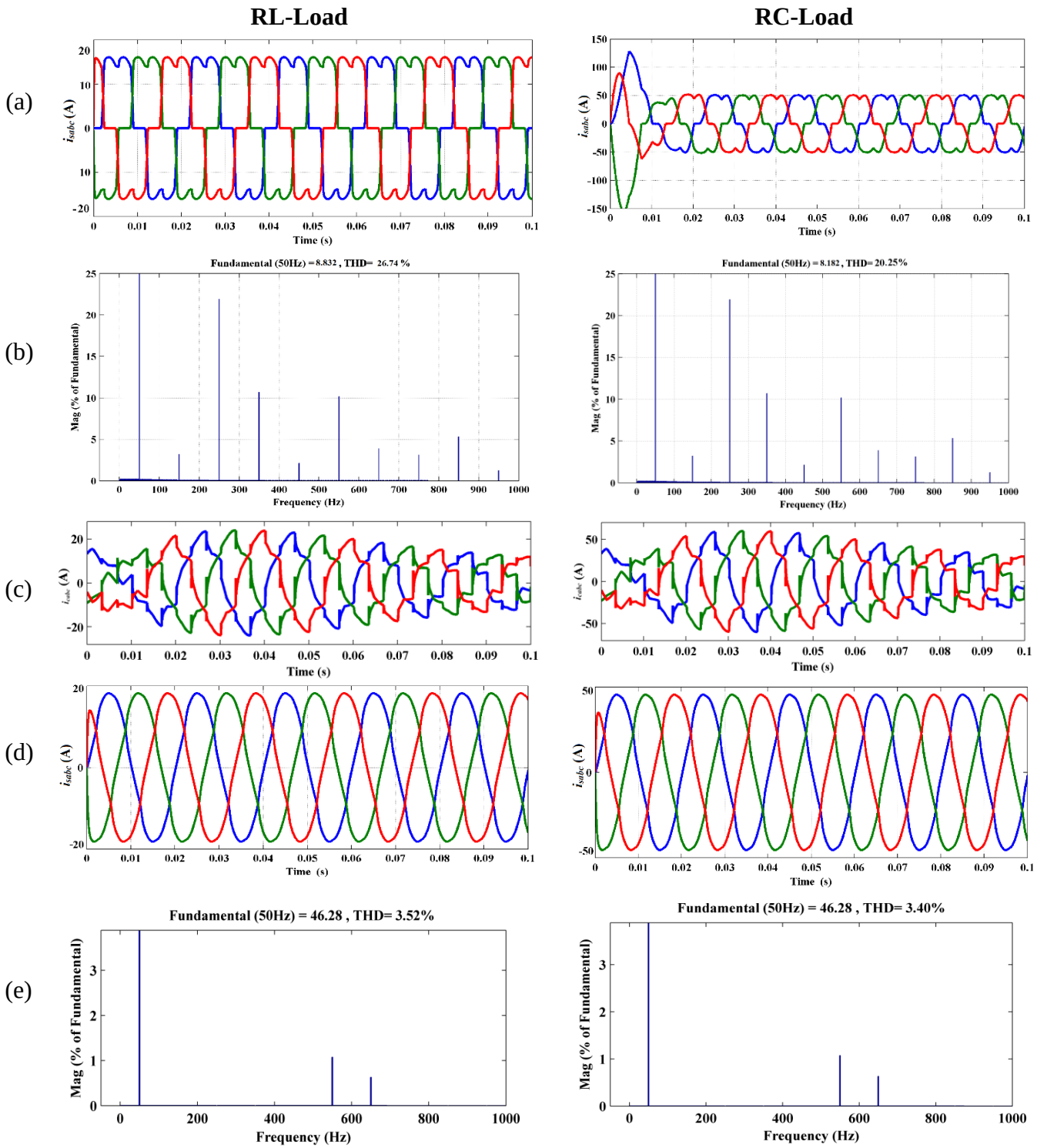

Figure 2.21 Profiles obtained under nonlinear RL- and RC-loads (a) i_{sabc} before compensation, (b) THD of i_{sabc} before compensation, (c) i_{cabc} generated using SRF-PI-HCC approach, (d) i_{sabc} after compensation and (e) THD of i_{sabc} after compensation (**Scenario 1**)

2.5.3 Performance Analysis Pertaining to Scenario 3

This scenario considers the performance analysis of the studied SAPF under the action of MSRF-FLC-HCC-based combined control strategy. The i_{cabc} generated under this scheme is portrayed in Figure 2.23(a). The profile of i_{sabc} (after compensation) is shown in Figure 2.23(b) and its harmonics content (after compensation) as a result of FFT analysis is presented in Figure 2.23(c). The result demonstrates that the i_{sabc} is almost sinusoidal with very less THD content of 2.63% and 2.54% % for RL- and RC-type loads, respectively. A comparative result of THD content under various conditions is presented in Table 2.7. In comparison to the topologies of Scenario 1 (i.e., SRF-PI-HCC) and Scenario 2 (i.e., MSRF-PI-HCC), the Scenario 3 topology (i.e., MSRF-FLC-HCC) has

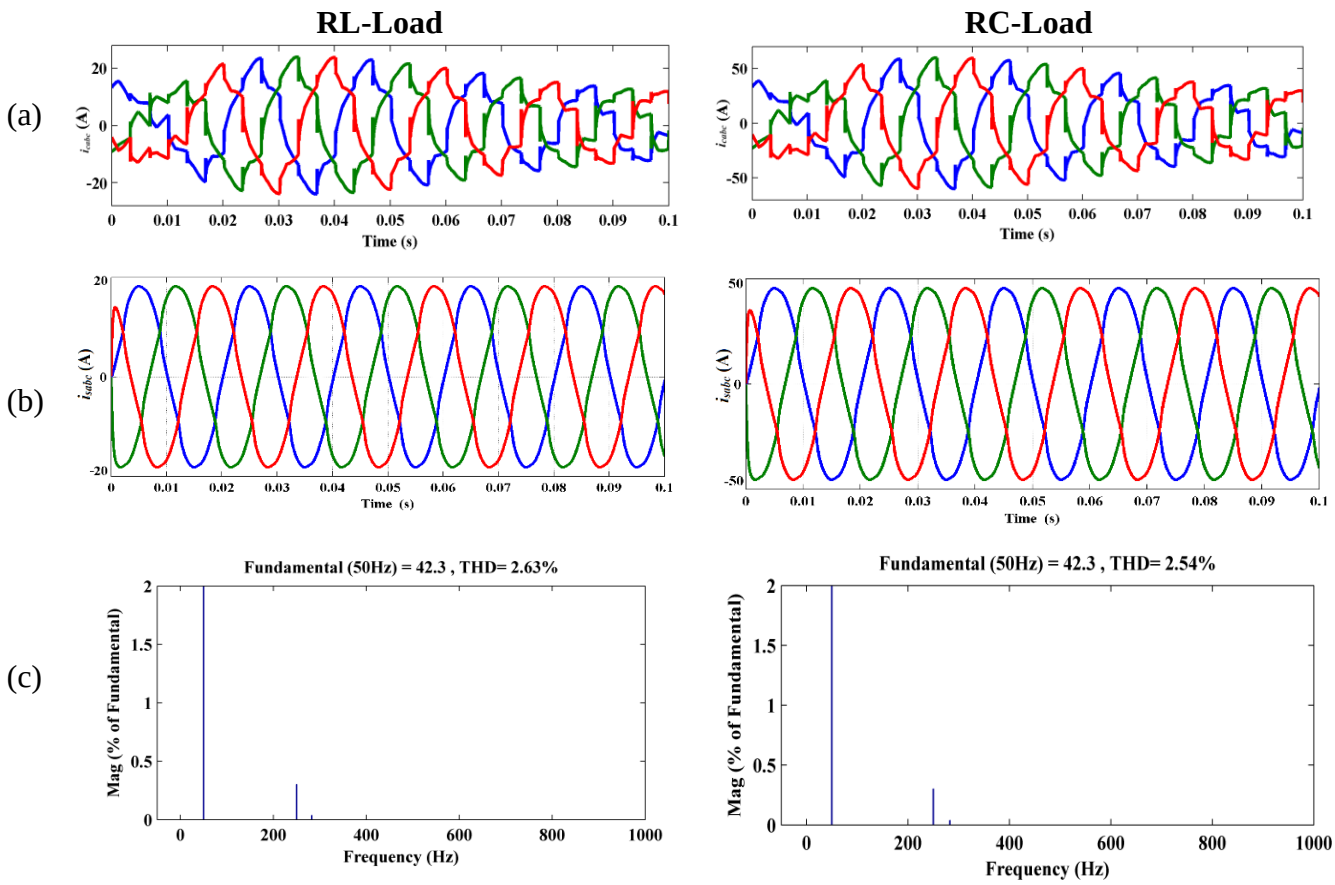

Figure 2.22 Profiles obtained under nonlinear RL-and RC-loads (a) i_{cabc} generated using MSRF-PI-HCC approach, (b) i_{sabc} after compensation and (c) THD of i_{sabc} after compensation (**Scenario 2**)

offered a further reduction in the THD level by (i) 65.90% and 54.37%, respectively, in case of RL-type nonlinear load; and (ii) 66.17% and 54.72%, respectively, for RC-type nonlinear load. A detail on THD information, including individual harmonics order of i_{sabc} (in %) resulted after using different control schemes are presented in Table 2.8. From Table 2.8, it is seen that out of the various harmonic components, the 5th harmonic is the predominant one contributing 20.76% and 21.21% to the harmonic distortion of i_{sabc} for RL- and RC-loads, respectively. Apart from the above, 7th, 11th, 13th and 17th harmonics also appeared in the source current with magnitudes of 12.66%, 6.86%, 4.09%, and 1.97%, respectively, in case of RL-load; and 17.23%, 8.64%, 5.11%, and 2.91% for RC-load, respectively. It is also observed from Tables 2.8 that the minimum THD of

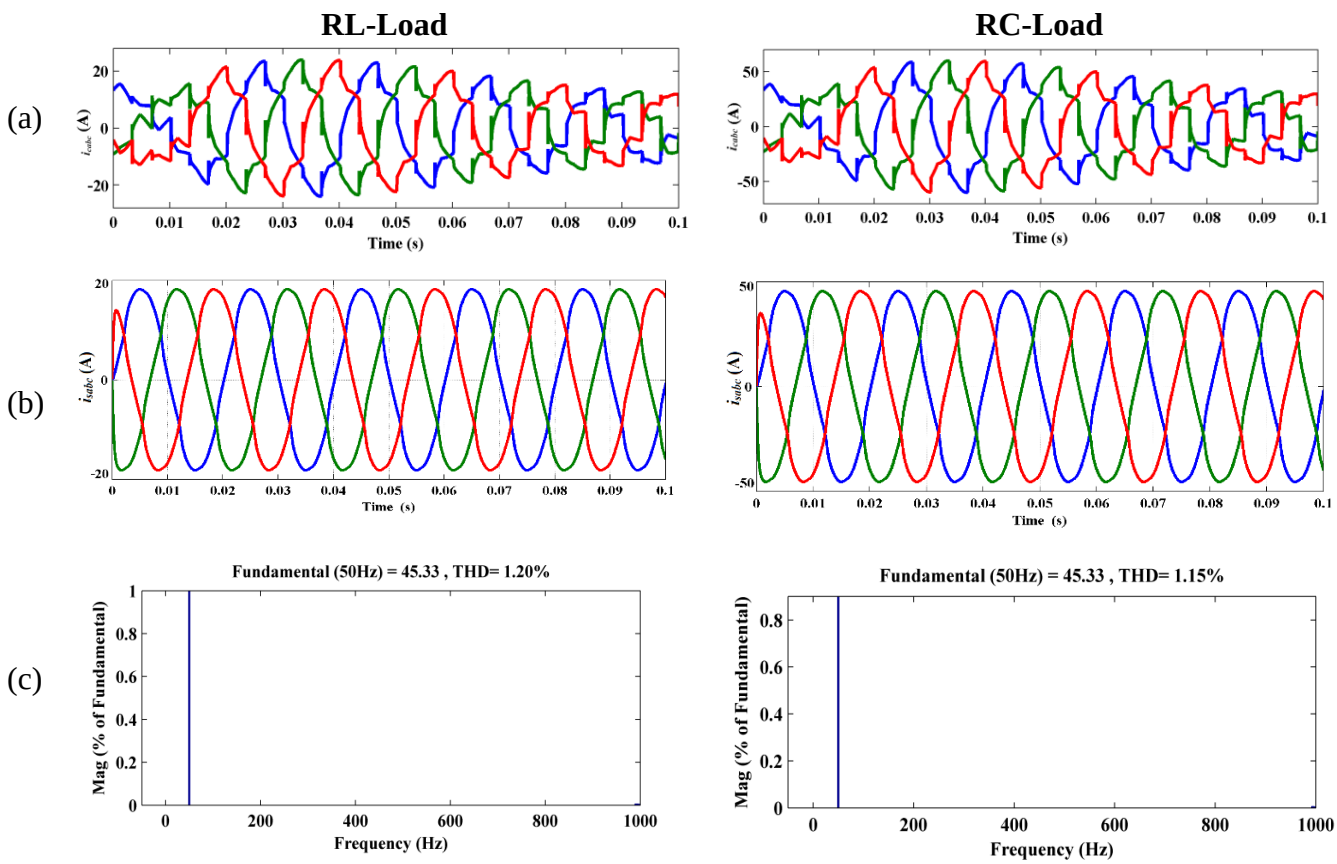

Figure 2.23 Profiles obtained under nonlinear RL-and RC-loads of (a) i_{cabc} generated using MSRF-FLC-HCC approach, (b) i_{sabc} after compensation and (c) THD of i_{sabc} after compensation (**Scenario 3**)

1.20% (for RL-load) and 1.15% (for RC-load), are obtained employing the proposed MSRF-FLC-HCC-based designed SAPF. Again, referring to the presence of an individual THD component, the contribution of 5th, 7th, 11th, 13th and 17th harmonics is almost reduced to zero.

As we know that i_{cabc} and V_{dc} are interrelated, if V_{dc} is not regulated properly then more harmonics will be present in the source current. The FLC is used to estimate the magnitude of I_{dc} by controlling the V_{dc} effortlessly in comparison to conventional PI controller. Moreover, the FLC approach also reduces the switching power loss and improves the performance of the SAPF in comparison to the conventional PI controller.

Table 2.7: THD comparison of i_{sabc} under various conditions

Nonlinear load type	THD without SAPF	THD with different controller-based SAPF		
		SRF-PI-HCC	MSRF-PI-HCC	**MSRF-FLC-HCC**
RL-load	26.74%	3.52%	2.63%	**1.20%**
RC-load	20.25%	3.40%	2.54%	**1.15%**

Table 2.8: Detail THD information of i_s under various control topology

Studied Control Scheme	Nonlinear Load Type	THD of the i_{sabc} (%)	Individual harmonics order of i_{sabc} (in %)				
			5th	7th	11th	13th	17th
Without SAPF	RL-Load	26.74	20.76	12.66	6.86	4.09	1.97
	RC-Load	28.25	21.21	17.23	8.64	5.11	2.91
SRF-PI-HCC	RL-Load	3.52	1.52	0.65	0.86	0.54	0.31
	RC-Load	3.40	1.45	0.56	0.67	0.45	0.24
MSRF-PI-HCC	RL-Load	2.63	1.05	0.84	0.65	0.48	0.37
	RC-Load	2.54	1.22	1.34	0.83	0.64	0.41
MSRF-FLC-HCC	**RL-Load**	**1.20**	**0.62**	**0.54**	**0.23**	**0.16**	**0.42**
	RC-Load	**1.15**	**0.53**	**0.48**	**0.22**	**0.14**	**0.33**

2.5.4 Performance Analysis Pertaining to Scenario 4

In this scenario, the performance of the proposed MSRF-FLC-HCC-based combined strategy is compared with that of studied traditional methods like SRF-PI-HCC and MSRF-PI-HCC in regulating V_{dc} profile and reducing its settling time (t_s) during

steady-state and load-changing conditions and presented in the following subsections of this scenario.

(a) V_{dc} *profile under steady-state conditions*

The V_{dc} regulation method is tested for its accuracy under steady-state conditions. To analyse the accuracy, a performance indicator called as percentage of accuracy (% ACC) is used. It is defined in (2.42).

$$\%ACC = (1 - \frac{V_{dc,ref} - V_{dc}}{V_{dc,ref}}) \times 100 \tag{2.42}$$

The deviations in V_{dc} profiles obtained under the action of various adopted controller-based SAPF considering steady-state conditions are shown in Figures 2.24(a)-(c). It is

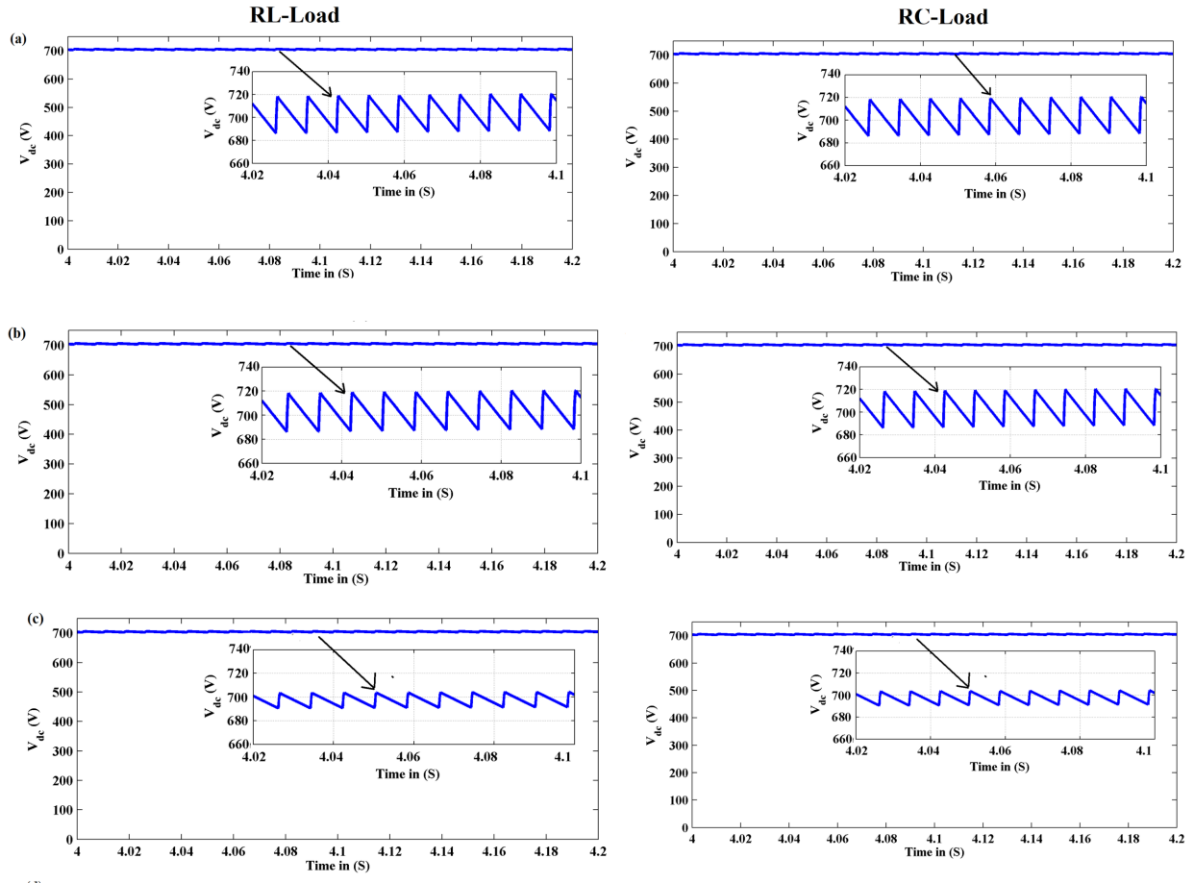

Figure 2.24 V_{dc} profiles obtained considering RL-and RC-type nonlinear loads under different controller-based SAPF (a) SRF-PI-HCC (b) MSRF-PI-HCC, and (c) MSRF-FLC-HCC schemes **(Scenario 4)**

evident from the figures and from Table 2.9 that the maximum deviation of 24V and 28V in V_{dc} waveform is observed under SRF-PI-HCC approach for RL- and RC-load types, respectively. Also, the %ACC of 96.54% and 96.00% are found for RL- and RC-load types, respectively. While the same is further reduced to 22V and 24V for RL- and RC-load type, respectively, employing the MSRF-PI-HCC topology (Scenario 2) and the %ACC improved to 96.90% and 96.58 % for RL- and RC-load types, respectively. However, the MSRF-FLC-HCC (Scenario 3) control topology offers the least deviation of 18V and 20V with further improvement in %ACC to 97.50% and 97.20% for RL- and RC-type nonlinear loads, respectively.

Table 2.9: Comparison of V_{dc} deviation under steady-state condition

Control approach	Voltage deviation (in V)		(% ACC)	
	RL-load	RC-load	RL-load	RC-load
SRF-PI-HCC	24	28	96.54%	96.00%
MSRF-PI-HCC	22	24	96.90%	96.58%
MSRF-FLC-HCC	**18**	**20**	**97.50%**	**97.20%**

(b) V_{dc} *profile under load-changing conditions*

Under load-changing conditions, the performance of the studied controllers are evaluated in terms of the overshoot (O_s), undershoot (U_s), and settling time (t_s). Two dynamic load situations are considered in this study (i) switching the nonlinear load from RC- to RL-type and (ii) from RL- type to RC-type. Figure 2.25 and Figure 2.26 show the effect

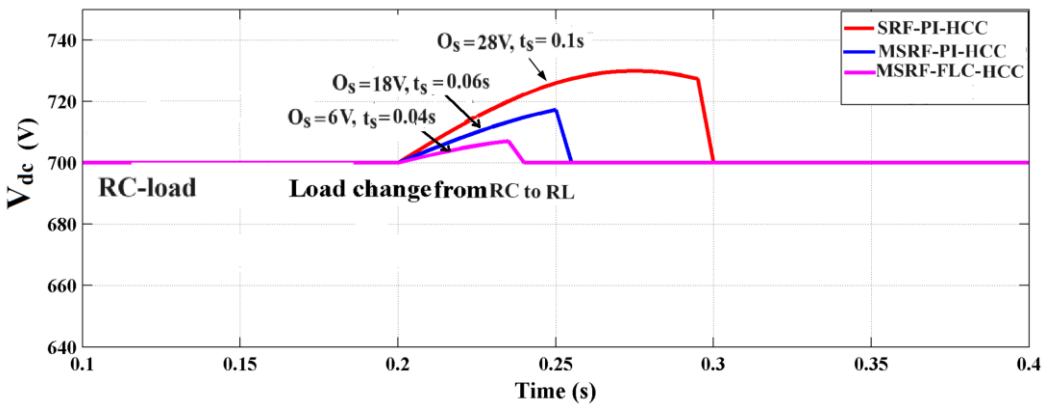

Figure 2.25 Comparative profiles of V_{dc} obtained using SRF-PI-HCC, MSRF-PI-HCC and MSRF-FLC-HCC methods under load-changing conditions (RC-to RL-type).

of each of the studied technique in regulating V_{dc} profile under load-changing conditions i.e., switching of RC-type to RL-type nonlinear load and vice-versa, respectively. Firstly, the model is simulated with RC-type nonlinear load and steady-state position is achieved. The findings from Figure 2.25 show that the V_{dc} profile is in steady-state condition till $t = 0.2$ s with RC-type nonlinear load. When the nonlinear load is altered from RC- to RL-types at $t = 0.2$ s, V_{dc} is deviated from its reference value of 700 V. The responses in terms of deviation in V_{dc} with respect to $V_{dc.ref}$ together with the settling time are summarized in Table 2.10. It is revealed from the Table 2.10 that the conventional SRF-PI-HCC controller performs poorly offering O_S of 28V (i.e. 4 % of the reference value) and high t_S of 0.1 s. In case of MSRF-PI-HCC controller, the O_S reduces to 18V (i.e. 2.57% of the reference value) and t_S reduces to 0.06 s. However, the MSRF-FLC-HCC technique performs outstandingly offering the least O_S of 6V (i.e., 0.85% of the reference value) and the fastest t_S of 0.04 s, thus, establishing itself as the best one among the three. Similarly, in case of change of nonlinear load from RL- to RC-type, as revealed in Figure 2.26, the projected MSRF-FLC-HCC technique again offers the best outcome with the minimum U_S of 8V (i.e., observed to be 1.14% of the reference value) and the fastest t_S of 0.03 s. Whereas, the same MSRF-PI-HCC controller offers an U_S of 21V (i.e. a

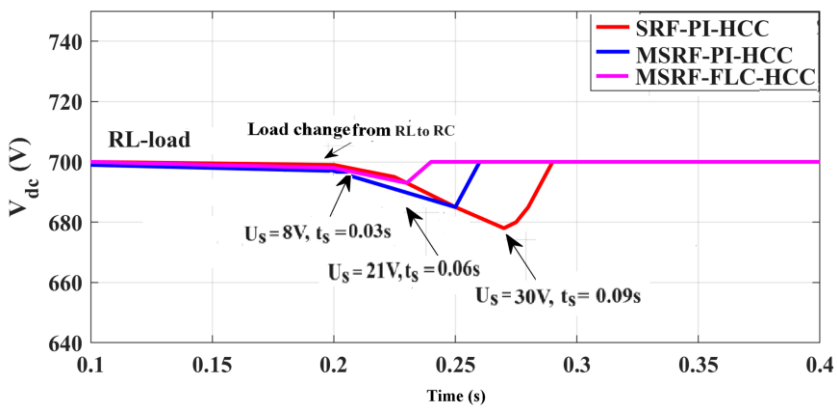

Figure 2.26 Comparative profiles of V_{dc} obtained using SRF-PI-HCC, MSRF-PI-HCC and MSRF-FLC-HCC methods under load-changing conditions (RL-to RC- type).

deviation of 3 %) and t_s of 0.06 s. The SRF-PI-HCC controller still has an U_s of 30V (i.e., a deviation of 4.28%) and t_s of 0.09 s. Based on all the results obtained from simulation works, it is shown that the studied controller confirms that the source current is almost sinusoidal after compensation and the settling time, overshoot and undershoot of V_{dc} is very less.

Table 2.10: V_{dc} deviation and t_s comparison under load-changing conditions

Studied control approach	Change of load from RC- to RL-type		Change of load from RL- to RC-type	
	O_s (V)	t_s (s)	U_s (V)	t_s (s)
SRF-PI-HCC	28 (4.0%)	0.1	30(4.28%)	0.09
MSRF-PI-HCC	18 (2.57%)	0.06	21 (3.0%)	0.06
MSRF-FLC-HCC	**6 (0.85%)**	**0.04**	**8 (1.14%)**	**0.03**

2.6 SUMMARY

In this chapter, SRF and MSRF techniques (considering one at a time) for RCG, PI controller and FLC techniques (considering one at a time) for V_{dc} regulation and HCC-based switching scheme in SAPF are used for improving the PQ problem in the adopted standalone MG system. The performance of the different combined control strategies have been evaluated in terms of harmonics mitigation and V_{dc} regulation under different load conditions. The simulation results illustrate the effectiveness of the MSRF-FLC-HCC control algorithm in mitigating the harmonics present in the source current and regulation of V_{dc} waveform in comparison to the other counterparts i.e., SRF-PI-HCC and MSRF-PI-HCC. The results obtained confirms that the MSRF-FLC-HCC method has offered the lowest THD value of 1.20% and 1.15% in the presence of RL and RC- type nonlinear loads, respectively. It is also observed that the MSRF-FLC-HCC technique has offered the best results in terms reduction of THD with respect to SRF-PI-HCC, and MSRF-PI-HCC, which is better by (i) 65.90%, and 54.37%, respectively, in case of RL-type nonlinear load; and (ii) 66.17%, and 54.72%, respectively, for RC-type nonlinear load. Thus, in terms of harmonics mitigation, the MSRF-FLC-HCC control topology has

offered the best results. Apart from this, the performance of the MSRF-FLC-HCC controller is also investigated in comparison to other counterparts in curbing the deviation and settling time in V_{dc} profile under steady-state and load-changing conditions. It is observed from the results obtained that the MSRF-FLC-HCC scheme has offered the minimum V_{dc} deviation of 6 V and the quickest response time of 0.04 s, when switching the load from RC- to RL-type. Likewise, the minimum deviation of 8 V and the fastest response time of 0.03 s is obtained during switching of the load from RL- to RC-type.

There is a still scope for either the novel development or improvement in the existing design of the control strategies used for RCG, V_{dc} control and PWM signal generation in realizing the SAPF model. This is required for further improving the harmonics mitigation capabilities of SAPF. Hence, in the next chapter of this dissertation work, a novel control technique for dc-link voltage control is proposed, whose performance with the best combination of strategies used for RCG and PWM signal generation is evaluated by conducting a series of simulation-based experiments. Apart from the load-changing conditions, the effect of ideal and non-ideal source conditions are also considered to test the efficacy of the proposed control approach.

Chapter 3

POWER QUALITY ENHANCEMENT USING A NOVEL FIED CONTROLLER-BASED SAPF IN MICROGRID

3.1 INTRODUCTION

As discussed in Chapter 2, the working of shunt active power filters (SAPFs) is mainly dominated by three control techniques predominantly used for reference current generation (RCG), switching pulses generation for voltage source inverter (VSI), and the regulation of dc-link voltage (V_{dc}). In the past, numerous works have been documented in the literature on different approaches to realize the above three functionalities. In the previous chapter, the realization of control strategy for RCG is carried out based on two widely used basic techniques (which are easy to implement) such as (a) synchronous reference frame (SRF) method and (b) modified synchronous reference frame (MSRF) method. The simulation results shown in the previous chapter illustrate the effectiveness of the MSRF technique in mitigating the harmonics present in the source current and achieving the desired regulation of V_{dc} profile. Hence, the studied MSRF scheme is used for RCG in this chapter as well.

Another critical issue in the design of SAPF is V_{dc} regulation. Research carried out in [174-176] reveals that if the V_{dc} profile remains stable, then it will operate effectively and precisely deliver the required compensating current. Therefore, the design of V_{dc} controller is also an important assignment. Usually, V_{dc} of SAPF is regulated either by a proportional-integral (PI) controller or fuzzy logic controller (FLC), where the control approach is based on the direct voltage error management concept [177-180]. The authors in [181, 182] describe the demerits of using a conventional PI controller in comparison to FLC for V_{dc} control. The performance characteristic of the PI controller under load-changing circumstances exhibits severe overshoot and a protracted settling time. It also has a number of flaws, such as ineptitude when it comes to parametric variations and load-shifting conditions. FLC, on the other side, is known for its speed, reliability, and effectiveness in harmonic monitoring, V_{dc} control, and reactive power compensation. However, the main drawback of FLC is that its computational burden is increased due to the use of a greater number of membership functions and rules [178]. Moreover, it also

works on the principle of direct voltage error manipulation technique, which may not entirely reduce the V_{dc} deviation that occurs during load-changing conditions. In view of the above, in this chapter, the dynamic performance of SAPF is improved by employing a proposed novel fuzzy inverted error deviation (FIED)-based controller to control and diminish the ripples in the V_{dc} waveform, particularly under load-changing conditions.

As pointed out earlier, the topology for generating pulse-width modulation (PWM) signals for the VSI of SAPF plays a pertinent function in reducing harmonics. So, this needs to be given due attention as well. In the previous chapter, a hysteresis current control (HCC)-based switching scheme was used for the generation of switching pulses for the VSI. The HCC approach is easier to implement than the other counterparts, although they exhibit uneven switching frequency. To overcome the shortcomings of HCC, authors in [185] suggested an adaptive HCC (AHCC) technique for SAPF to reduce the THD of the source current. The AHCC modifies the bandwidth (BW) as per the V_{dc} profile, modulation frequency, reference current, and input voltage. However, during high-frequency operations, AHCC causes more switching losses. The problem associated with AHCC is resolved by adaptive fuzzy HCC (AFHCC) as presented in [186-192]. The AFHCC technique calculates the BW of the hysteresis band (HB) using the FLC approach, where exact information of the SAPF parameters like interface inductor and V_{dc} of the capacitor is not required. The authors in [194] have also used the AFHCC technique for better harmonics compensation and parametric optimization of a SAPF. Hence, this chapter tests the efficacy of both AHCC and AFHCC techniques in generating switching pulses for the VSI of the SAPF. The mitigation of harmonics is not up to the mark when the THD of the source current is more due to the presence of a non-ideal source. Besides, the deviation in V_{dc} profile needs to be checked during load-changing conditions of nonlinear type (i.e., from RL-load to RC-load and RC-load to RL-load). Therefore, in this chapter, the harmonic issues are investigated in a typical standalone MG (comprising of solar photovoltaic (SPV), wind energy system (WES) and fuel cell (FC)-based distributed generators (DGs)) under different source and load-changing conditions in the presence of control strategies like MSRF technique-based RCG, the

proposed FIED controller-based V_{dc} regulation and the AHCC/AFHCC-based switching method for pulse generation.

3.1.1 Motivation of the Present Chapter

In recent years, most studies have concentrated on improving the PQ under balanced source conditions, but there has been little exploration of PQ mitigation under distorted source conditions. Accordingly, in the current work, balanced and unbalanced source conditions are considered while examining the performance of SAPF. Among the control algorithm used for RCG, V_{dc} control, and switching pulse generation, the V_{dc} control plays a crucial role in mitigating harmonics. Despite various existing controllers used for V_{dc} control, most of them produce unsatisfactory outcomes when applied to non-ideal source conditions. The performance of SAPF with standard PI and FLC techniques-based V_{dc} control is reported to be unsatisfactory when dealing with non-ideal source situations. It is also observed that most previous works have ignored the V_{dc} regulation of SAPF in their methodology during source and load-changing conditions. Therefore, based on the preceding chapter's explanation, it is clear that the SAPF is a viable approach for enhancing PQ by reducing current harmonics. Nevertheless, there is always a possibility of enhancing the efficiency of SAPF by employing appropriate techniques to provide a constant dc-link voltage. The dc-link voltage profile can serves as a measure of the SAPF's performance during source and load-changing conditions. There is still scope either to develop new V_{dc} control techniques or to improve the existing one. Hence, this serve as the main source of motivation for the present chapter.

3.1.2 Contribution of the Present Chapter

In the present chapter, to improve the performance SAPF, a comparative study of different control techniques i.e., (MSRF for RCG), (FLC and FIED for V_{dc} control), and (AHCC and AFHCC for switching pulse generation) are proposed. Further, the PQ issue, mainly THD in the source current waveform is analyzed under both ideal and non-ideal source

conditions and different nonlinear loads. Moreover, the regulation of V_{dc} and reduction of its settling time are also verified using the proposed FIED controller under load-changing conditions.

The main contributions of this chapter are as follows.

a) A novel FIED controller is proposed for THD mitigation through V_{dc} regulation under both ideal and non-ideal source conditions.
b) Under different nonlinear load conditions, the SAPF performance is compared among the PI, FLC, and the proposed FIED controllers in terms of THD reduction.
c) Furthermore, a performance comparison of the proposed FIED controller with that of other studied controllers in terms of V_{dc} regulation and settling time reduction is addressed under load-changing conditions.

3.1.3 Chapter Orientation

The remaining portion of the present chapter is organized as follows. Modeling of the proposed novel FIED control technique is presented in Section 3.2. In Section 3.3, different studied switching schemes are presented. In Section 3.4, the simulation results obtained under the different studied operating scenarios are presented and discussed. Finally, the research findings of the present chapter are summarized in Section 3.5.

3.2 DESIGN OF DC-LINK VOLTAGE REGULATOR

The dynamic performance of SAPF depends on the V_{dc} control because it looks after the power balance in the system and generates the desired current to compensate for the switching losses arising in the VSI. Therefore, V_{dc} regulation is a crucial issue for the performance improvement of SAPF. The SAPF's capacity to compensate for harmonics is vital to the successful generation of i_c, which is dependent on V_{dc} control. V_{dc} is regulated properly when the switching losses arising in the VSI is compensated by the source. This chapter suggests a new control technique for V_{dc} regulation known as the

FIED control approach. To prove its effectiveness, its performance is compared to that of conventional control schemes employing PI controller and FLC techniques, whose details are presented in Section 2.4.2 of Chapter 2.

3.2.1 Modeling of the Proposed FIED Controller

As described in Section 2.4.2 of Chapter 2, the V_{dc} regulation algorithm using PI and FLC techniques has a few advantages. However, both these techniques work on the direct voltage error cancellation method and may not entirely eradicate the severe V_{dc} variation (i.e., both undershoot and overshoot) that arises during load-changing conditions. Conventionally, V_{dc} signal is obtained through a direct voltage error cancellation technique, where the difference between the reference and the actual values of dc-link voltages (i.e., $e(n) = V_{dc} - V_{dc,ref}$) is directly fed to either PI controller or FLC technique (discussed in detail in Chapter 2) to produce an estimated output (I_{dc}) (refer Figures. 2.13 and 2.14 of Chapter 2). To further address the smooth dynamic operation of V_{dc} control, an improvement to the existing conventional algorithms with the introduction of the FIED control technique has been proposed.

The concept of the FIED technique is implemented in this work to tackle the V_{dc} deviation that occurs during load-changing conditions. In general, V_{dc} is successfully regulated at its desired value if the magnitude of I_{dc} (indicated in Fig. 3.1) is maintained at zero. However, during load-changing conditions, $e(n)$ occurs, thereby, resulting in the overshoots and undershoots in the V_{dc} waveform. The FIED technique is implemented in such a way that controlling action is initiated whenever any overshoot or undershoot is observed in the V_{dc} profile. The FIED control scheme diagram is shown in Figure 3.1, which generates a FIED voltage signal to cancel out the variations that take place in the form of $e(n)$ and a new voltage error signal (E_n). The generation of E_n is presented by (3.1) and (3.2).

$$E_n = e(n) + FIED \tag{3.1}$$

$$E_n = (V_{dc} - V_{dc,ref}) + FIED \tag{3.2}$$

The I_{dc} signal is generated using the equation (3.3).

$$I_{dc} = \frac{2C_{dc}}{3V_m T} E_n{}^2 \tag{3.3}$$

The above technique is implemented using an indirect voltage error approach, where a path is created to indirectly control the $e(n)$ by reducing the effects of undershoot and overshoot that take place in the V_{dc} profile during load-changing conditions as depicted in Figure 3.2. This scheme diminishes the computational efforts and concurrently improves the V_{dc} performance in load-changing conditions. The FIED signal is generated depending on the magnitude of $e(n)$. If $e(n) = 0$, no FIED signal is

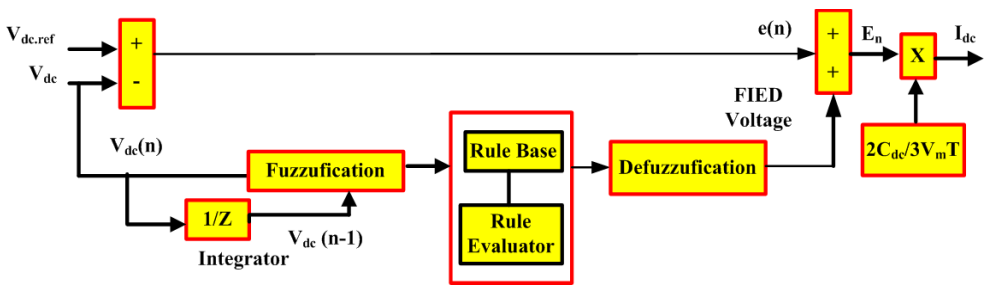

Figure 3.1 Block diagram of the proposed FIED scheme

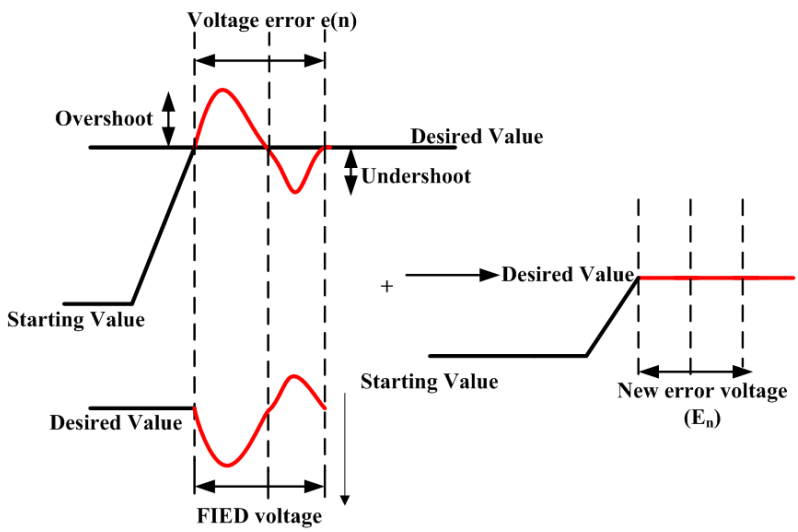

Figure 3.2 Relevant waveforms of the proposed FIED scheme

generated. For $e(n) > 0$ (representing overshoot), a negative FIED signal is produced by the controller to neutralize the sudden increase of $e(n)$. Similarly, for $e(n) < 0$, the FIED signal is increased to a level that is most suitable to cancel out the undershoot in $e(n)$. The use of a fuzzy approach to control the FIED signal will result further in accurate and precise cancellation of overshoot and undershoot in the V_{dc} profile occurring out of load-changing conditions. The proposed FIED scheme uses two input variables i.e., current dc-link voltage $(V_{dc}(n))$ and previous dc-link voltage $(V_{dc}(n-1))$, in place of $e(n)$ and $ce(n)$ as used in typical FLC technique, and one output variable as FIED signal. Both the input and output variables are fuzzified using five membership functions (MFs) defined as negative big (*NB*), negative small (*NS*), zero (*ZE*), positive small (*PS*), and positive big (*PB*). The MFs for the input variables $V_{dc}(n)$ and $V_{dc}(n-1)$ are presented in Figure 3.3, and the output FIED signal is shown in Figure 3.4. The rule

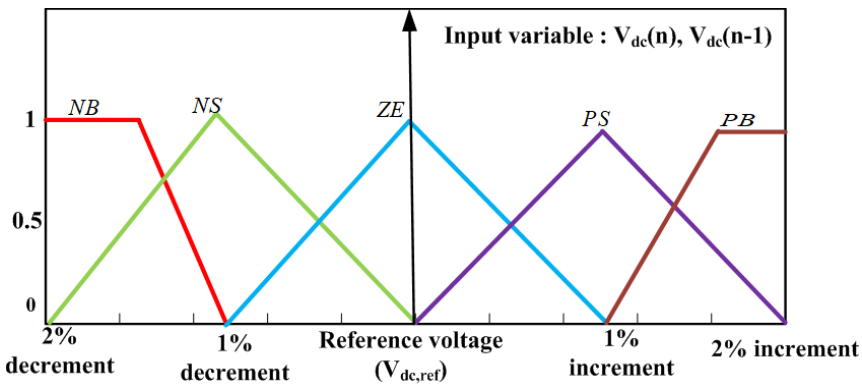

Figure 3.3 MFs for input variables

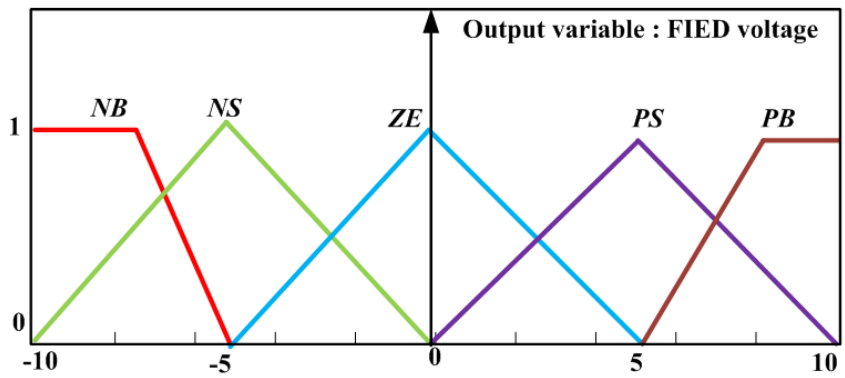

Figure 3.4 MFs for output signal

base for the FIED technique is presented in Table 3.1. It is viewed from Table 3.1 that only five MFs with 25 control rules are considered to design the projected technique. Hence, the computation load to the controller reduces, which makes it effortless for practical implementation. Therefore, the proposed FIED-based control technique may regulate the V_{dc} accurately.

Table 3.1: Rule base table for the proposed FIED scheme

$V_{dc}(n)$ / $V_{dc}(n\text{-}1)$	FIED				
	NB	*NS*	*ZE*	*PS*	*PB*
NB	*PB*	*PB*	*PB*	*PS*	*ZE*
NS	*PB*	*PB*	*PS*	*ZE*	*NS*
ZE	*PB*	*PS*	*ZE*	*NS*	*NB*
PS	*PS*	*ZE*	*NS*	*NB*	*NB*
PB	*ZE*	*NS*	*NB*	*NB*	*NB*

3.3 STUDIED SWITCHING PULSE GENERATION SCHEMES

The SAPF's performance is also dependent on the switching pulse generation technique. As discussed in the previous chapter that the sensed actual source current (i_{sabc}) is compared with the reference source current (i^*_{sabc}) and the error between them is fed to the hysteresis band (HB) for initiating suitable switching action. Employing the concept of HB, a range of schemes, such as hysteresis current control (HCC), adaptive hysteresis current control (AHCC) and adaptive fuzzy hysteresis current control (AFHCC) techniques are reported in the literature. The HCC approach, explained in Section 2.4.3 of the Chapter 2, is widely used in SAPF due to its inherent advantages such as rapid current controllability, absolute consistency, quick response, and easy implementation [183,184]. However, the main disadvantages of this technology are that the PWM frequency is not constant, it is challenging to build the filter circuit, and it results in greater switching losses. The varying switching frequency impacts the SAPF's efficiency and

reliability. However, the AHCC technique overcomes the drawbacks of HCC by changing the bandwidth (BW) in response to the variations in the compensating current (i_{cabc}) produced by the SAPF. Thus, as a solution to the aforementioned issue, the AHCC technique has been widely recommended by several researchers.

3.3.1 Studied AHCC Scheme

In AHCC, bandwidth of hysteresis band (HB) is adjusted in conjunction with the system components to maintain a nearly constant PWM frequency. In this scheme, the switching pattern is derived from the falling and rising currents inside the HB. Figure 3.5 displays the single-line switching illustration of the AHCC-based switching scheme [185,186]. The block diagram of HB calculation is presented in Figure 3.6. In this scheme, the bottom switch turns ON when the source current error is greater than the upper limit of

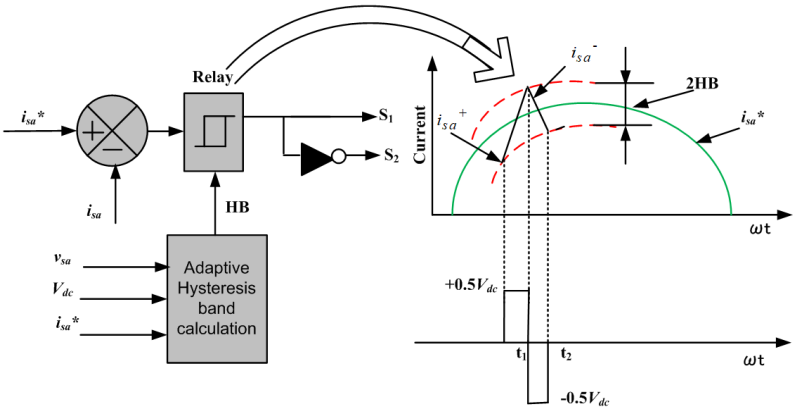

Figure 3.5 AHCC-based switching pulses generation scheme

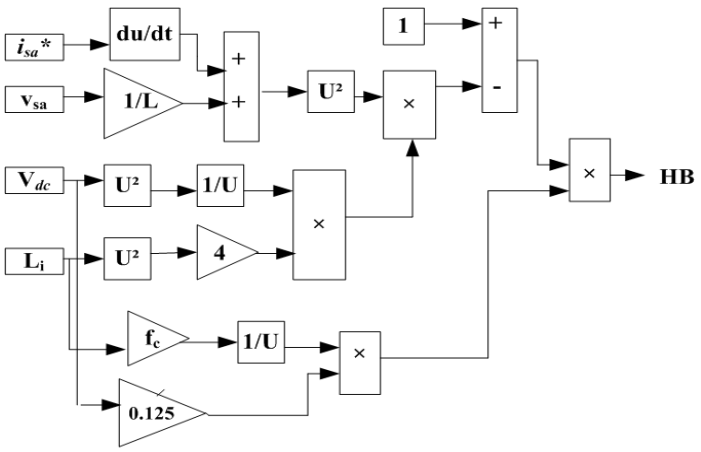

Figure 3.6 HB calculation block of AHCC

HB. The upper switch is turned ON when the erroneous current exceeds the lower limit of HB. As a result, within the HB, the actual source current is constrained to follow the reference source current. The calculation of HB is expressed by (3.4)-(3.9). Equations (3.4) and (3.5) are used to express the rising current (i_{sa}^{+}) and the falling current (i_{sa}^{-}). These currents are further modified to equations (3.6) and (3.7), respectively. The total turn-on period $(t_1 + t_2)$ and switching frequency (f_c) are defined in (3.8).

$$\frac{d(i_{sa}^{+})}{dt} = \frac{1}{L_f}\left(0.5V_{dc} - V_s\right) \tag{3.4}$$

$$\frac{d(i_{sa}^{-})}{dt} = -\frac{1}{L_f}\left(0.5V_{dc} + V_s\right) \tag{3.5}$$

These may be further represented by (3.6)-(3.8).

$$\frac{d(i_{sa}^{+})}{dt}t_1 - \frac{d(i_{sa}^{*})}{dt}t_2 = 2HB \tag{3.6}$$

$$\frac{d(i_{sa}^{-})}{dt}t_1 - \frac{d(i_{sa}^{*})}{dt}t_2 = -2HB \tag{3.7}$$

$$t_1 + t_2 = \frac{1}{f_c} \tag{3.8}$$

Simplifying (3.5)-(3.7), the HB may be represented as (3.9).

$$HB = \frac{0.125V_{dc}}{f_c L_i}[1 - \frac{4L_i^2}{V_{dc}^2}(\frac{V_s}{L_i} + \frac{di_{sa}^{*}}{dt})] \tag{3.9}$$

The major issue with the AHCC scheme is that the f_c is quite high, resulting in considerable switching losses in the VSI. Owing to the disadvantages of AHCC approach, in this work, an AFHCC technique is implemented for PWM signal generation.

3.3.2 Studied AFHCC Scheme

To enhance the SAPF performance further without exact information of its parameters, the HB value may be implemented using fuzzy logic represented by a set of defined MFs. Figure 3.7 displays the single-line diagram of the studied fuzzy logic-based calculation

of HB for PWM signal generation [186]. It is observed from the Figure 3.7 that the FLC technique is used to calculate the hysteresis band (HB^*) efficiently. The difference between the working of AFHCC and AHCC approaches is that, in AHCC, the HB is calculated based on (3.9), while in AFHCC, instead of direct use of HB, its error signal $(e(HB))$ and change of error signal $(ce(HB))$ are used as inputs for fuzzy logic processing, which produces HB* as an output. The five MFs are assigned for each of the inputs (i.e., for $e(HB)$ and $ce(HB))$ and the output (HB^*).

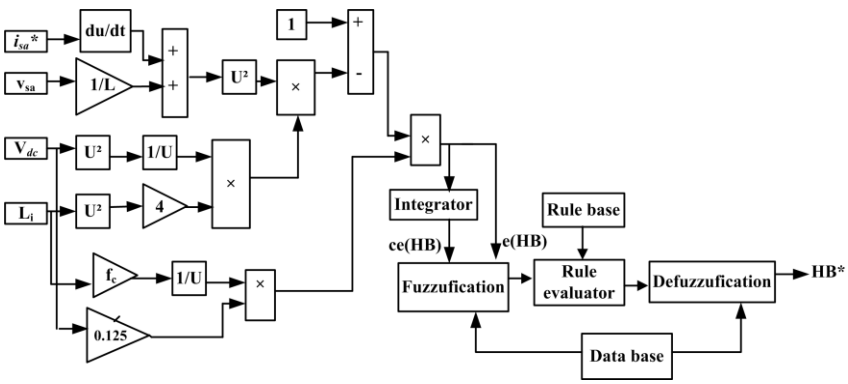

Figure 3.7 HB calculation block of AFHCC

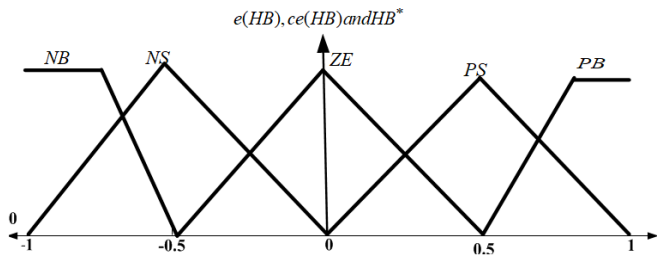

Figure 3.8 MFs used for input variables $(e(HB)$, $ce(HB))$ and output variable (HB^*)

Table 3.2: AFHCC rule matrix

$ce(HB)$ / $e(HB)$	HB^*				
	NB	*NS*	*ZE*	*PS*	*PB*
NB	*PS*	*ZE*	*ZE*	*ZE*	*PB*
NS	*PS*	*ZE*	*NS*	*ZE*	*PB*
ZE	*PB*	*ZE*	*NB*	*ZE*	*NB*
PS	*PS*	*ZE*	*NS*	*ZE*	*PS*
PB	*PS*	*ZE*	*ZE*	*ZE*	*PS*

These are named as NB, NS, ZE, PS, and PB. Figure 3.8 displays the different MFs, while the fuzzy rule matrix is presented in Table 3.2. The suggested AFHCC is designed to calculate the HB^* by keeping the modulation frequency f_c constant. The results obtained show that the adopted AFHCC method significantly enhances the SAPF's performance by drastically reducing inverter switching losses.

3.4 RESULTS AND DISCUSSIONS

This section investigates the performance of SAPF under different load conditions. For better harmonic filtering, a SAPF is appended with the studied and the proposed control algorithms i.e., MSRF technique for RCG, a novel FIED technique for V_{dc} regulation and AHCC/AFHCC scheme (considering one at a time) for PWM pulse generation.

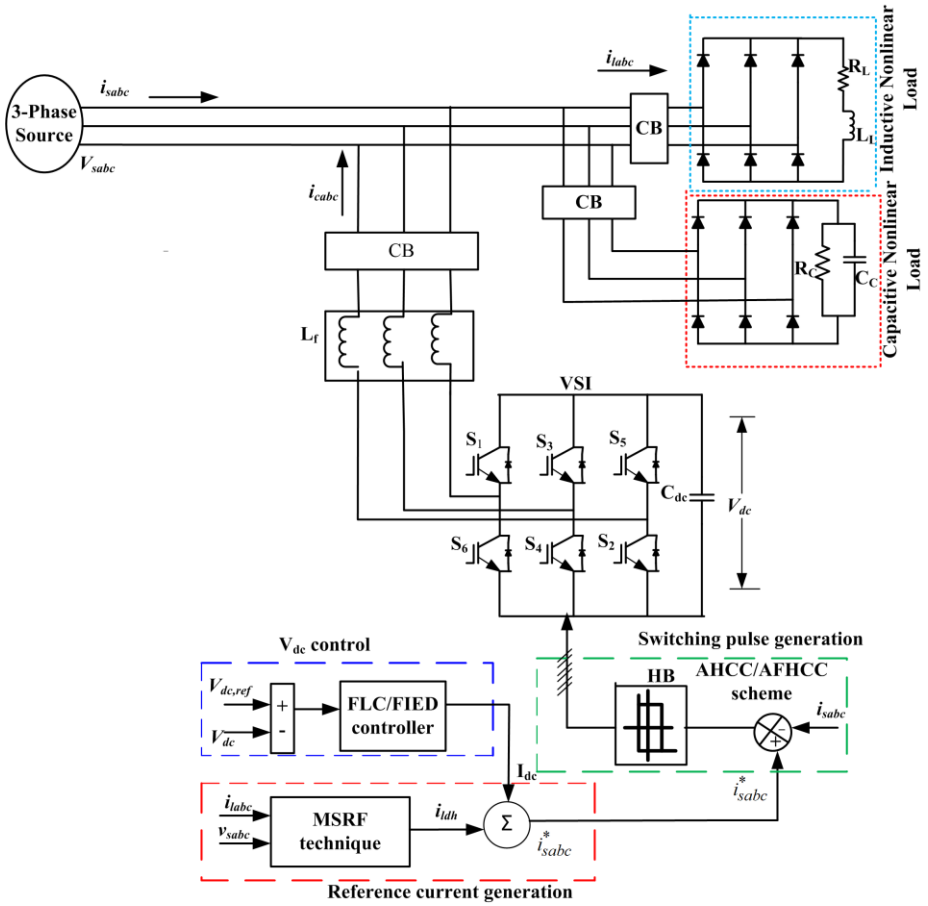

Figure 3.9 SAPF with MSRF-FLC/FIED-AHCC/AFHCC-based control scheme

In the present study, the schemes employing the different combinations of MSRF method (for RCG), either of FLC or the proposed FIED controller (for V_{dc} control), and either of AHCC or AFHCC (for PWM pulses) for producing an appropriate three-phase compensation current (i_{cabc}) are named differently as MSRF-FLC-AHCC, MSRF-FLC-AFHCC, MSRF-FIED-AHCC, and MSRF-FIED-AFHCC control techniques. The SAPF model employing the above-mentioned combination of control schemes (considering one combination at a time) is simulated in MATLAB/Simulink platform. The results obtained under the action of each approach are compared and discussed to establish the superiority of one over the other. The model is illustrated in Figure 3.9. The associated various parameters along with its values may be referred from Table 2.6 of Chapter 2. The studied MG model with the nonlinear RL- and RC-loads is already simulated without connecting the SAPF. Figures 2.31(a) and (b) of Chapter 2 conclude that in the absence of SAPF the source current (i_{sabc}) waveform is non-sinusoidal in nature, having very high total harmonic distortion (THD) content of 26.74% and 20.25% for RL and RC-type nonlinear loads, respectively. In order to make i_{sabc} to be sinusoidal, SAPF (employing MSRF scheme with either of FLC or the proposed FIED controller) is turned on, which produces reference source current i^*_{sabc}. The sensed actual source current i_{sabc} is compared with the reference i^*_{sabc} and the error between them is fed to the HB for initiating suitable switching action. The switching schemes used in this work are AHCC and AFHCC (considering one at a time). The resulting compensating current (i_{cabc}) from the inverter is injected at the PCC to mitigate the harmonics. The performance analyses of the studied MG system are investigated with SAPF under the action of different controllers at different loading conditions and are denoted as different scenarios. The results of interest under each scenario are highlighted in bold in the respective table.

a) Scenario 1: SAPF employing MSRF-FLC-AHCC and MSRF-FLC-AFHCC schemes considering an ideal source.
b) Scenario 2: SAPF employing MSRF-FIED-AHCC and MSRF-FIED-AFHCC schemes considering an ideal source.

c) Scenario 3: SAPF employing MSRF-FLC-AHCC and MSRF-FLC-AFHCC schemes considering a non-ideal source.
d) Scenario 4: SAPF employing MSRF-FIED-AHCC and MSRF-FIED-AFHCC schemes considering a non-ideal source.
e) Scenario 5: Comparative performance analysis of the proposed FIED control scheme with the conventional schemes (i.e., PI and FLC) for V_{dc} regulation under steady-state and load-changing conditions.

3.4.1 Performance Analysis Pertaining to Scenario 1

The performance of SAPF based on the studied MSRF-FLC-AHCC and MSRF-FLC-AFHCC schemes (considering one at a time) is analyzed in this scenario. The profile of i_{cabc} generated under the MSRF-FLC-AHCC-based scheme is revealed in Figure 3.10(a) for both RL- and RC-type nonlinear loads. The profiles of i_{cabc} generated by MSRF-FLC-AHCC-based scheme are revealed in Figure 3.10(a) for both RL-and RC-type nonlinear loads. Figure 3.10(b) illustrates the i_{sabc} waveform obtained after compensation for each type of load**.** The THD investigation reports (with SAPF) for both types of loads are presented in Figure 3.10(c). Similarly, related to the MSRF-FLC-AFHCC-based scheme, the profiles of i_{cabc}, i_{sabc} after compensation and THD of i_{sabc} are presented in Figure 3.11(a), Figure 3.11(b) and Figure 3.11(c), respectively. The THD comparison of i_{sabc} under ideal source condition has been presented Table 3.3. The results demonstrate that the i_{sabc} is nearly sinusoidal exhibiting very low THD values of 2.22% and 2.15% obtained for RL- and RC-type nonlinear loads, respectively, in the presence of MSRF-FLC-AHCC-based technique. However, in the MSRF-FLC-AFHCC-based control technique, the THD is further reduced to 1.25% and 1.15% for RL-and RC-type nonlinear loads, respectively. In Chapter 2, it was concluded that the MSRF-FLC-HCC strategy has outperform the other studied strategies (SRF-PI-HCC and MSRF-PI-HCC) and has offered the lowest THD value of 1.20% and 1.15% in the presence of RL-and RC-type nonlinear loads, respectively. However, in this scenario,

combination of MSRF-FLC-AFHCC-based approach has performed the best and offered THD improvement of (i) 61.18% in comparison to MSRF-FLC-HCC (of Chapter 2) under RL-type nonlinear load, and (ii) 63.14% under RC-type nonlinear load, respectively. Similarly, in comparison to MSRF-FLC-AHCC approach, the THD level is found to be improved by (i) 43.69% under RL-type nonlinear load, and (ii) 46.51% under RC-type nonlinear load, respectively, under ideal source condition (refer Table 3.4).

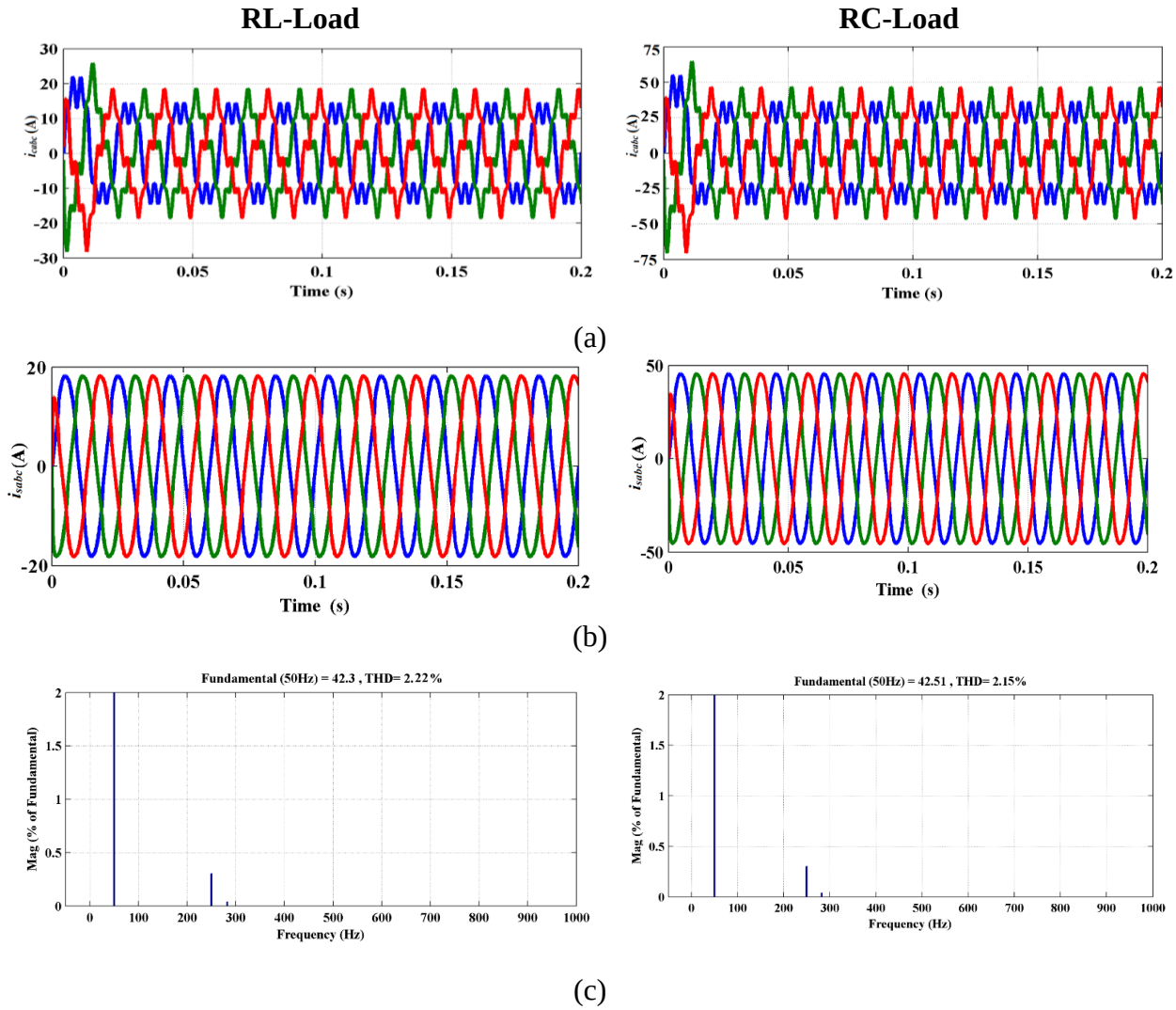

Figure 3.10 Profiles obtained under RL- and RC-type nonlinear loads (a) i_{cabc} generated using MSRF-FLC-AHCC approach, (b) i_{sabc} after compensation and (c) THD of i_{sabc} after compensation (**Scenario 1**)

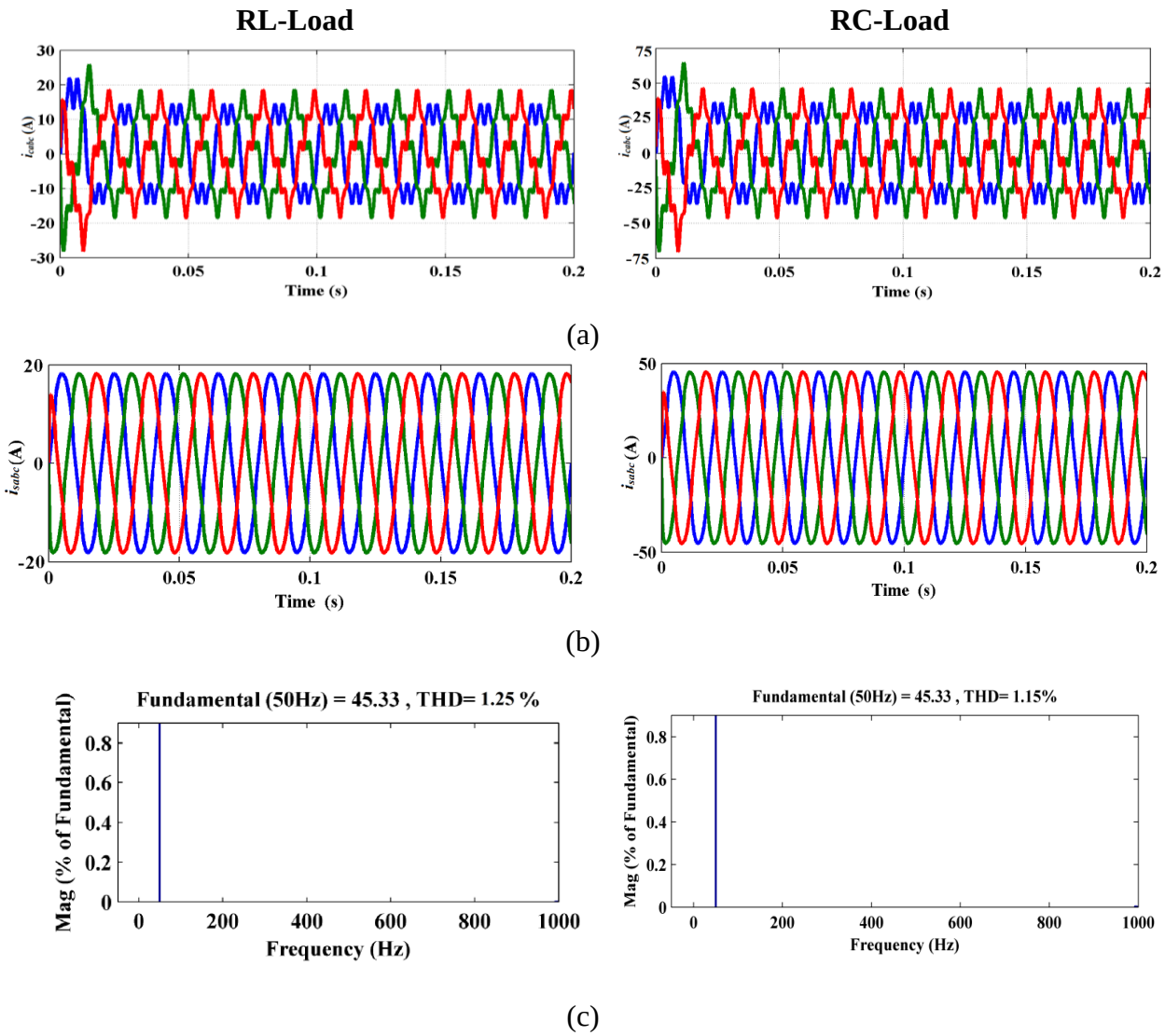

Figure 3.11 Profiles obtained under RL- and RC-type nonlinear loads (a) i_{cabc} generated using MSRF-FLC-AFHCC approach, (b) i_{sabc} after compensation and (c) THD of i_{sabc} after compensation (**Scenario 1**)

Table 3.3 THD comparison of i_{sabc} under ideal source condition

Nonlinear load type	THD without SAPF	THD with SAPF		
		Studied control approach	PWM switching scheme AHCC	AFHCC
RL-Load	26.74%	MSRF-FLC	2.22%	1.25%
		MSRF-FIED	**2.05%**	**1.05%**
RC-Load	20.25%	MSRF-FLC	2.15%	1.15%
		MSRF-FIED	**2.03%**	**1.00%**

3.4.2 Performance Analysis Pertaining to Scenario 2

The performance of SAPF based on the proposed FIED-based combination i.e., MSRF-FIED-AHCC control approach, is analyzed in this scenario. The i_{cabc} generated using MSRF-FIED-AHCC-based combined control strategy are portrayed in Figure 3.12(a) for RL- and RC-type nonlinear loads. The profiles of i_{sabc} and THD contents (after compensation) are presented in Figure 3.12(b) and Figure 3.12(c) for RL- and RC- type nonlinear loads, respectively.

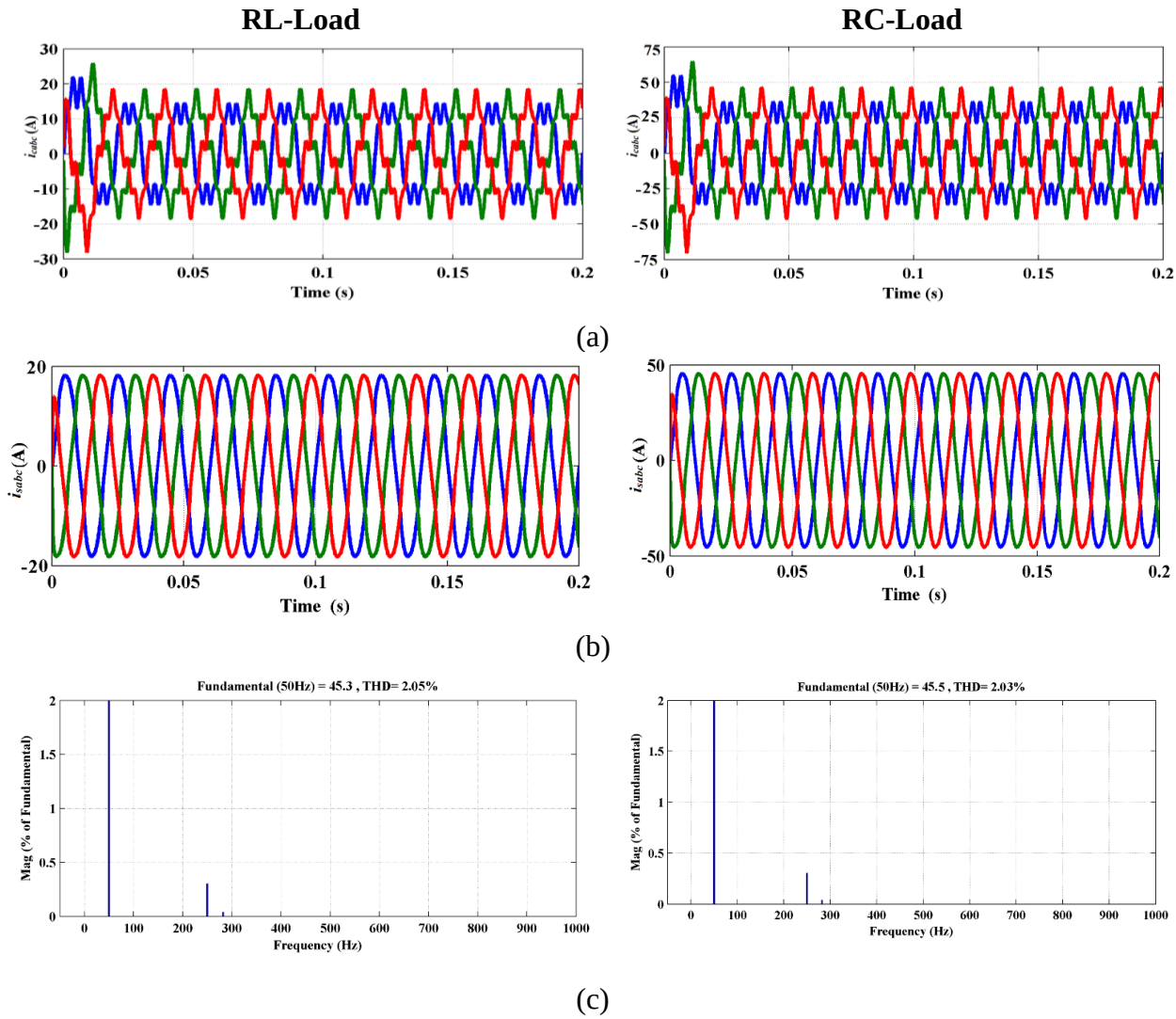

Figure 3.12 Profiles obtained under RL- and RC-type nonlinear loads (a) i_{cabc} generated using MSRF-FIED-AHCC approach, (b) i_{sabc} after compensation and (c) THD of i_{sabc} after compensation (**Scenario 2**)

The results demonstrate that the i_{sabc} profile after compensation is nearly sinusoidal having very low THD values of 2.05% for RL-load and 2.03% for RC- load (refer Table 3.3). Similarly, for the proposed MSRF-FIED-AFHCC-based scheme, the profiles of i_{cabc} generated are portrayed in Figure 3.13(a) for both RL and RC-type nonlinear loads. The profiles of i_{sabc} and its THD contents (after compensation) are presented in Figures 3.13(b)-(c) for RL- and RC- type nonlinear loads, respectively. It is viewed from the profile of i_{sabc} that the waveform is nearly sinusoidal with very less THD values of

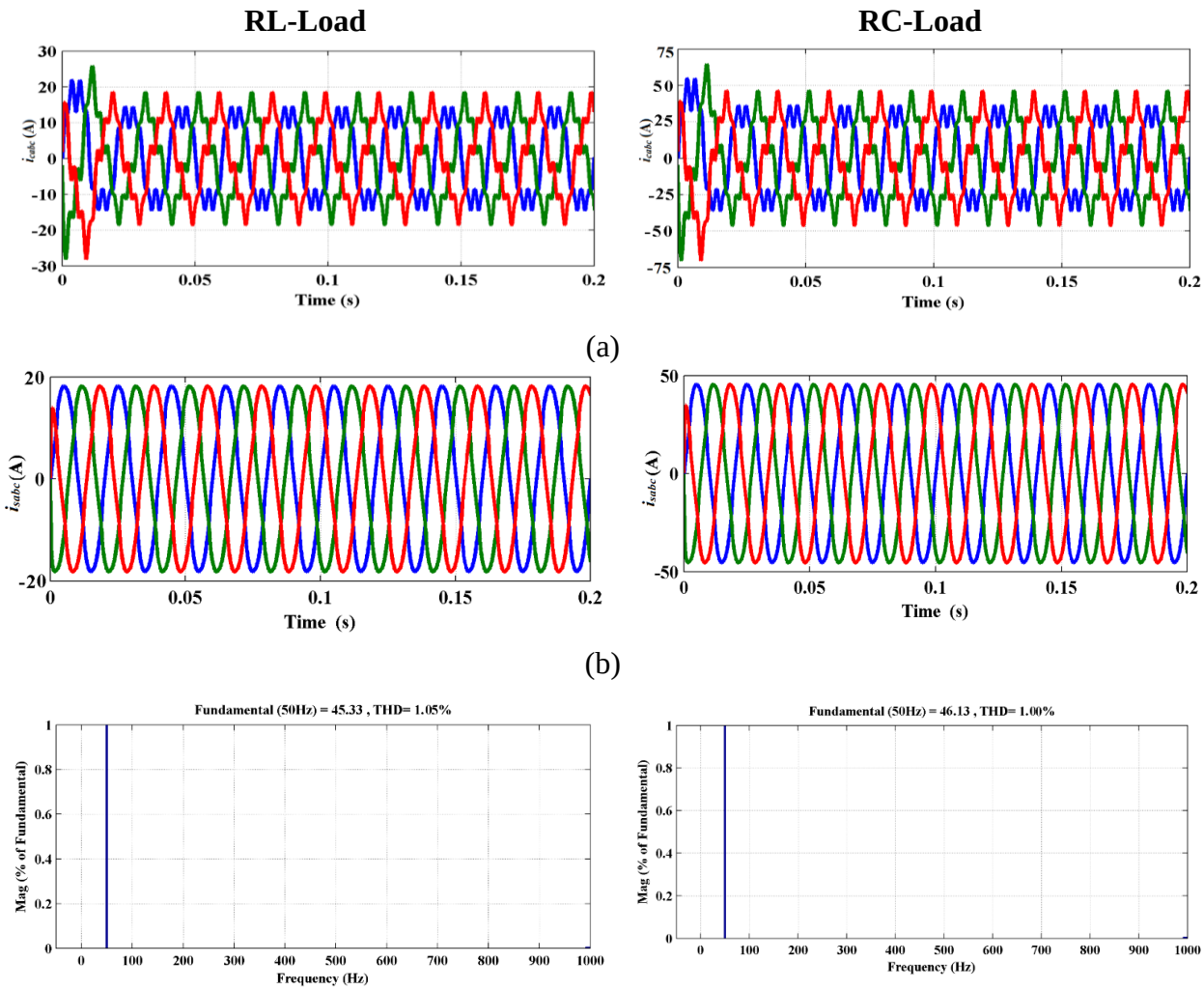

Figure 3.13 Profiles obtained under RL- and RC-type nonlinear loads (a) i_{cabc} generated using MSRF-FIED-AFHCC approach, (b) i_{sabc} after compensation and (c) THD of i_{sabc} after compensation (**Scenario 2**)

1.05% (for RL- load) and 1% (for RC-load) under the action of the proposed MSRF-FIED-AFHCC-based approach (refer Table 3.3). Further, the MSRF-FIED-AFHCC approach has presented THD level improvement of (i) 67.39% in comparison to MSRF-FLC-HCC (the best approach of Chapter 2) under RL-type nonlinear load, and 70.51% under RC-type nonlinear loads, respectively, and (ii) 48.78% and 50.73% in comparison to MSRF-FIED-AHCC under RL-type and RC-type nonlinear loads, respectively. It is observed from the results obtained that the combination of MSRF-FIED-AFHCC topology has offered the best result under ideal source condition in comparison to other studied control approaches.

A detail on THD information, including individual harmonics order of i_{sabc} (in percentage) resulted after using different control topologies is presented in Table 3.4. From Table 3.4, it is seen that out of the various harmonic components, the 5th harmonic is the predominant one contributing 20.76% and 15.85% to the harmonic distortion of i_s for RL-and RC-type loads, respectively. Besides, 7th, 11th, 13th and 17th harmonics also appeared in the source current with magnitudes of 12.66%, 6.86%, 4.09% and 1.97%, respectively, in the case of RL-load; and 10.56%, 4.08%, 2.15%, and 1.36% for RC-load,

Table 3.4: Comparative THD information of i_{sabc} under ideal source condition

Studies control schemes	Nonlinear load type	THD of i_{sabc} (in %)	Individual harmonics order of i_{sabc} (in %)				
			5th	7th	11th	13th	17th
Without SAPF	RL-Load	26.74	20.76	12.66	6.86	4.09	1.97
	RC-Load	20.25	15.85	10.56	4.08	2.15	1.36
MSRF-FLC-HCC	RL-Load	3.22	1.36	0.85	0.67	0.56	0.44
	RC-Load	3.12	1.06	0.89	0.67	0.45	0.31
MSRF-FLC-AHCC	RL-Load	2.22	1.28	1.34	0.87	0.68	0.47
	RC-Load	2.15	0.50	1.23	0.22	0.32	0.67
MSRF-FLC-AFHCC	RL-Load	1.25	0.62	0.54	0.23	0.16	0.42
	RC-Load	1.15	0.53	0.48	0.22	0.14	0.33
MSRF-FIED-HCC	RL-Load	3.05	1.32	0.87	0.56	0.63	0.47
	RC-Load	3.03	1.22	0.81	0.52	0.61	0.43
MSRF-FIED-AHCC	RL-Load	2.05	0.50	0.71	0.22	0.32	0.33
	RC-Load	2.03	0.48	0.67	0.26	0.34	0.32
MSRF-FIED-AFHCC	**RL-Load**	**1.05**	**0.42**	**0.32**	**0.29**	**0.19**	**0.35**
	RC-Load	**1.00**	**0.40**	**0.29**	**0.18**	**0.17**	**0.29**

respectively. It is observed from Table 3.4 that the minimum THD of 1.05% (for RL-load) and 1.00% (for RC-load) are obtained under the proposed MSRF-FIED-AFHCC-based designed SAPF. Further, referring to the presence of individual THD components, the contribution of 5th, 7th, 11th, $13^{th,}$ and 17th harmonics is almost zero under the proposed topology.

3.4.3 Performance Analysis Pertaining to Scenario 3

This scenario investigates the performance of the SAPF under non-ideal source condition. In order to realize the non-ideal source condition, a 3-phase programmable voltage source block from Simulink library is added along with the existing model and harmonics is introduced in phase 'a' of the source voltage. Initially, the system performance is evaluated without SAPF considering different nonlinear loads (RL- and RC- types). The profiles of source voltage V_{sabc} under both loads are presented in Figure 3.14(a). Similarly, the profiles of i_{sabc} without SAPF are shown in Figure 3.14(b), and its THD contents are revealed in Figure 3.14(c). It is viewed from Figure 3.14(c) that the THD profiles of i_{sabc} are highly distorted and found to be 35.51% for RL-load and THD of 74.29% for RC-load. In order to reduce the harmonics from i_{sabc}, SAPF with MSRF-FLC-AHCC and MSRF-FLC-AFHCC control scheme (considered one at a time) are used to generate the required compensating current i_{cabc} (refer Figure 3.15(a)) to be injected at the PCC. Under the MSRF-FLC-AHCC technique, the THD level decreases to 2.35% for RL-type nonlinear load and 2.18% for RC-type nonlinear load, respectively. The profiles of i_{sabc} and its THD content (after reimbursement) are portrayed in Figure 3.15(b) and Figure 3.15(c), respectively, for RL- and RC- type nonlinear loads. Similarly, employing the MSRF-FLC-AFHCC approach, the profiles of i_{cabc} generated in the presence of RL- and RC- type nonlinear loads are portrayed in Figure 3.16(a). While the respective profiles of i_{sabc} and its THD contents (after compensation) are presented in Figures 3.16(b)-(c), respectively. It is viewed from the profiles of i_{sabc} that the waveform

is nearly sinusoidal, having low THD values of 1.65% (for RL- load) and 1.45% (for RC-load) obtained under the action of the studied MSRF-FLC-AFHCC-based controller (refer Table 3.5). The THD comparison of i_{sabc} under non-ideal source condition has been presented in Table 3.5. Further, the MSRF-FLC-AFHCC approach has offered (i) 29.78% and 33.48% improvement in THD level in comparison to MSRF-FLC-AHCC in the presence of RL-type and RC-type nonlinear loads, respectively.

3.4.4 Performance Analysis Pertaining to Scenario 4

The performance of SAPF based on the proposed FIED-based control strategies i.e., MSRF-FIED-AHCC and MSRF-FIED-AFHCC control approaches, are analyzed in this

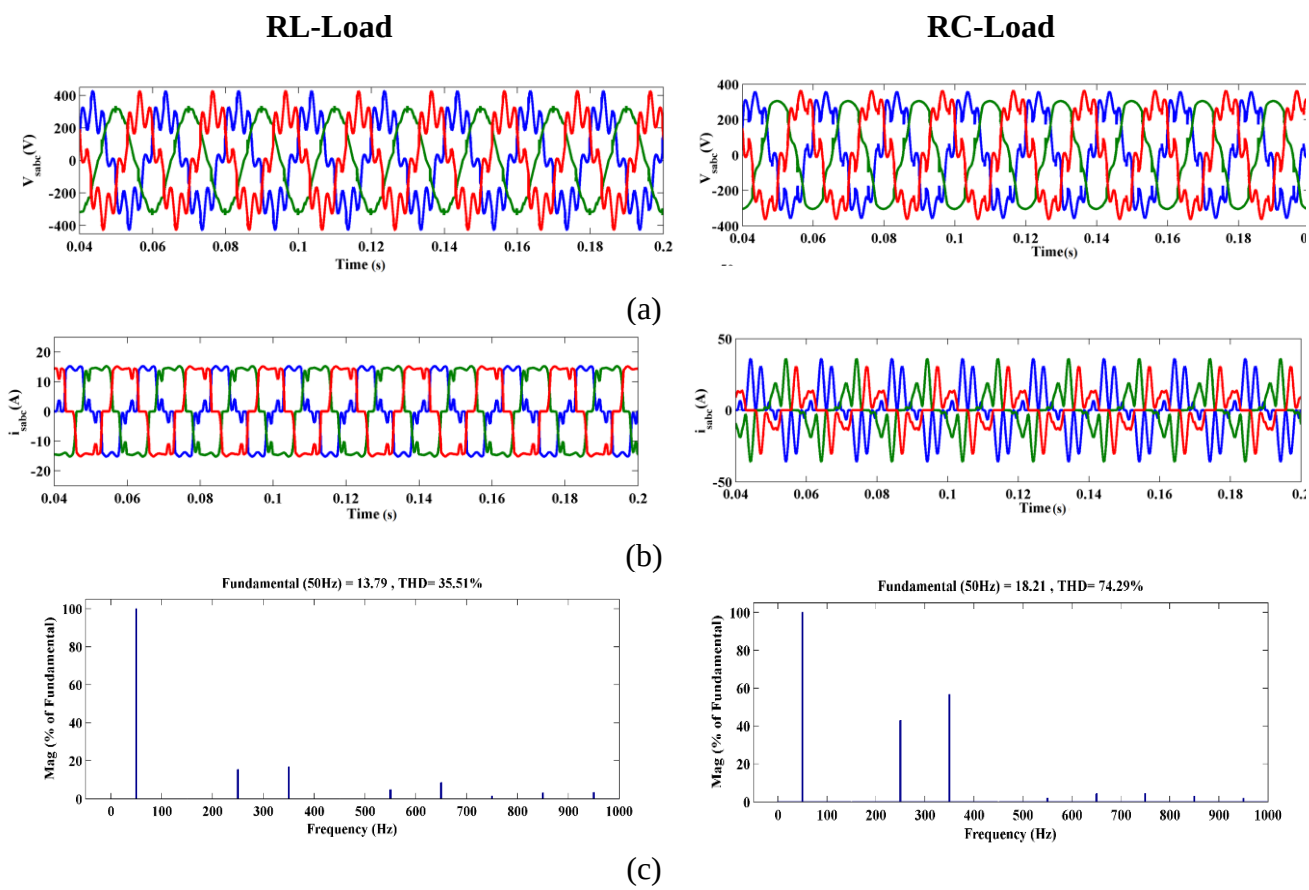

Figure 3.14 Profiles obtained under RL- and RC-type nonlinear loads (a) V_{sabc} under non-ideal source, (b) i_{sabc} before compensation (c) THD of i_{sabc} before compensation (**Scenario 3**)

scenario. The compensating signals i_{cabc} generated for RL- and RC- type nonlinear loads using MSRF-FIED-AHCC scheme are portrayed in Figure 3.17(a).

The associated profiles of i_{sabc} and its THD contents (after compensation) for RL- and RC-type nonlinear loads are presented in Figures 3.17(b)-(c), respectively. The results demonstrate that the i_{sabc} after compensation are nearly sinusoidal having very low THD values of 1.43% for RL-load and 1.32% for RC-load (refer Table 3.5).

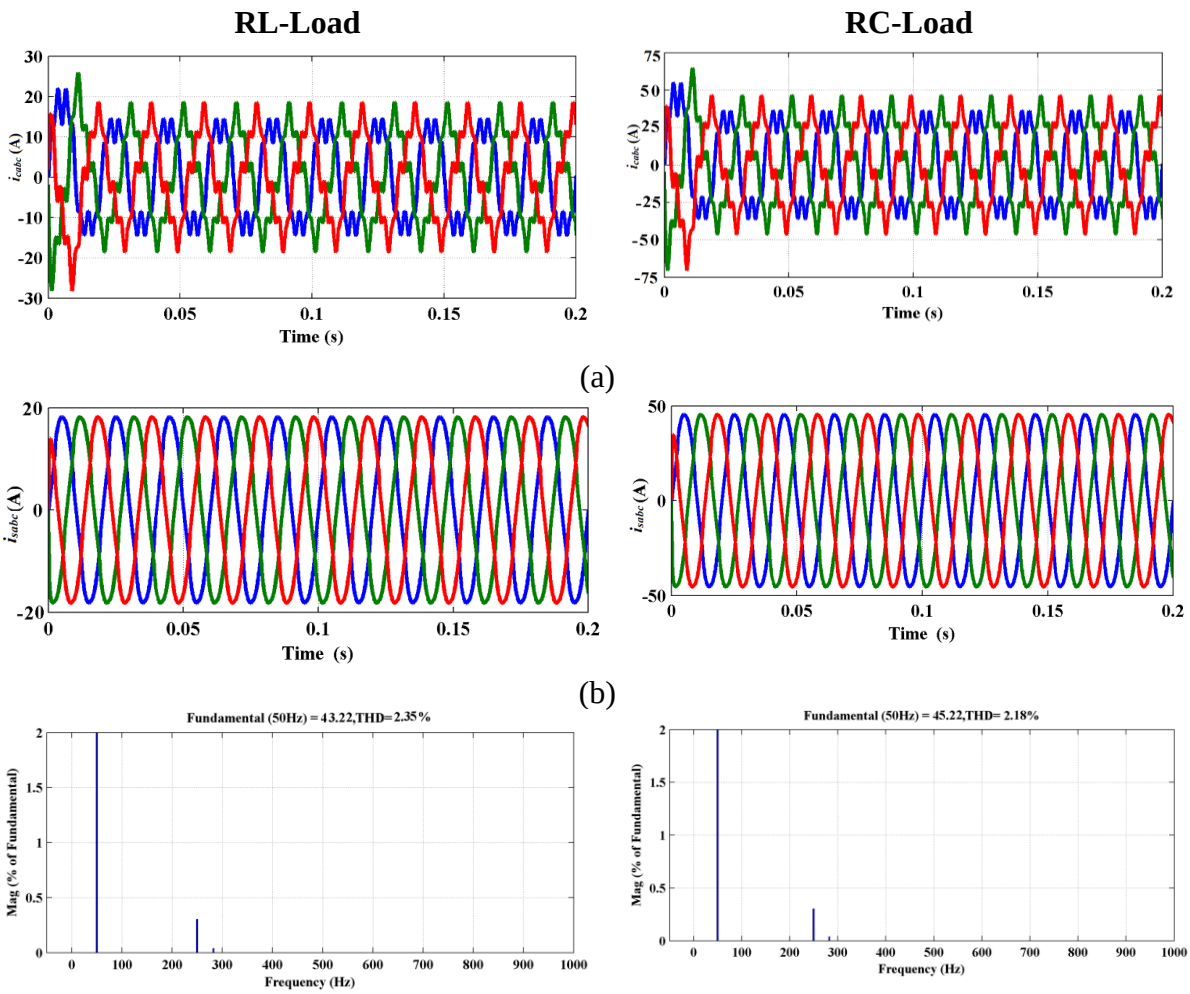

(c)

Figure 3.15 Profiles obtained under RL- and RC-type nonlinear loads (a) i_{cabc} generated using MSRF-FLC-AHCC approach, (b) i_{sabc} after compensation and (c) THD of i_{sabc} after compensation (**Scenario 3**)

Similarly, in the case of the proposed MSRF-FIED-AFHCC technique, the profiles of i_{cabc} generated are portrayed in Figure 3.18(a).

On the other hand, the profiles of i_{sabc} and its THD contents (after compensation) are presented in Figures 3.18(b)-(c) for RL- and RC-type nonlinear loads, respectively. It is viewed from the profiles of i_{sabc} that the waveform is nearly sinusoidal displaying a very low THD values of 1.08% (for RL- load) and 1.05% (for RC-load) under the action of the proposed MSRF-FIED-AFHCC technique (refer Table 3.5). It is observed from the

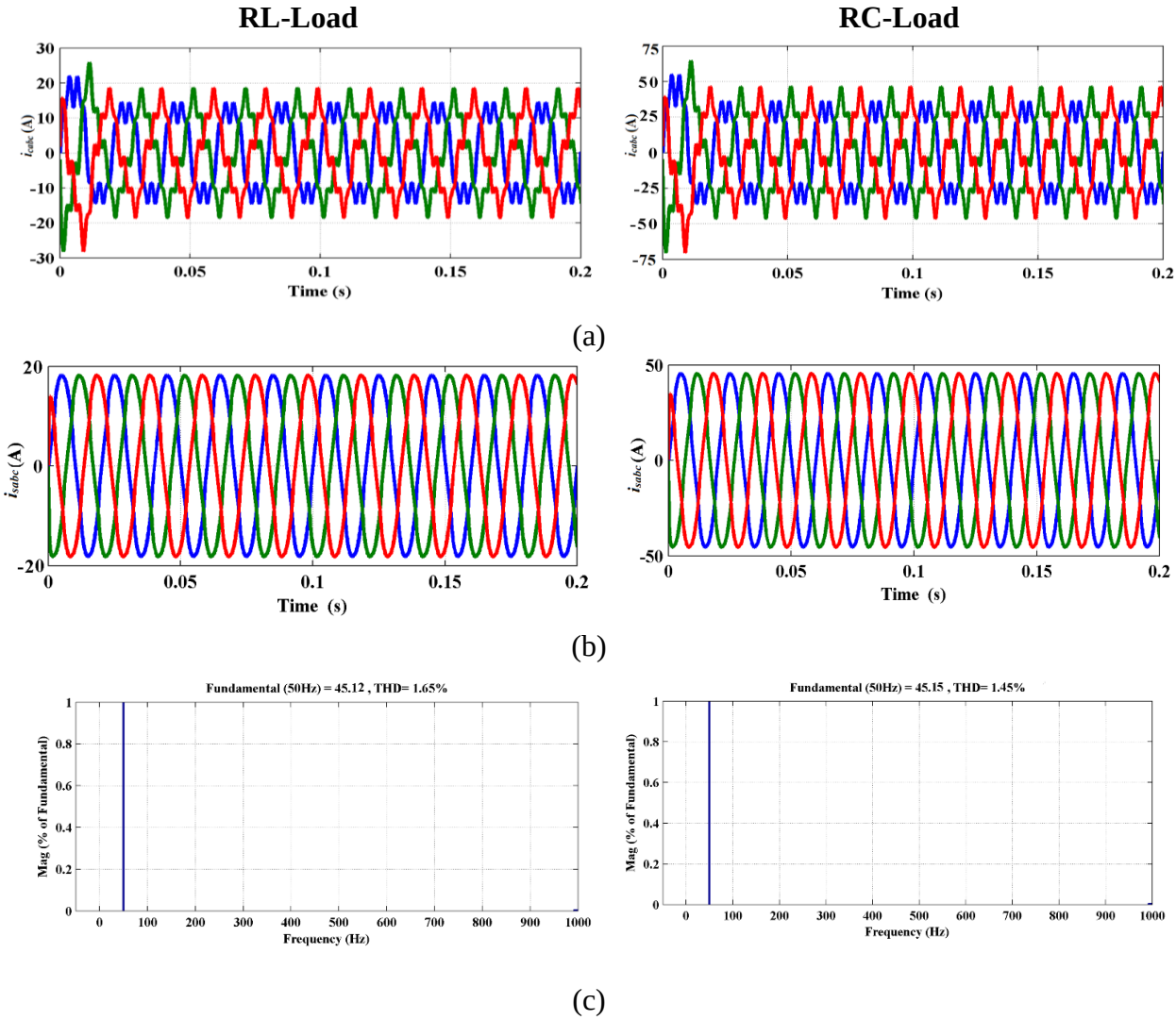

Figure 3.16 Profiles obtained under RL- and RC-type nonlinear loads (a) i_{cabc} generated using MSRF-FLC-AFHCC approach, (b) i_{sabc} after compensation and (c) THD of i_{sabc} after compensation (**Scenario 3**)

results obtained that the proposed MSRF-FIED-AFHCC technique gives the best result under non-ideal source condition in comparison to other studied control approaches.

A detail on THD information, including individual harmonics order of i_{sabc} (in percentage) resulting after using different control topologies under non-ideal source condition are presented in Table 3.6. It is observed from Table 3.6 that the proposed MSRF-FIED-AFHCC-based combined approach offers the best result in comparison to all other studied control approaches presented in this scenario. Further, the MSRF-FIED-AFHCC approach has offered (i) 71.2% improvement in THD level in contrast to MSRF-

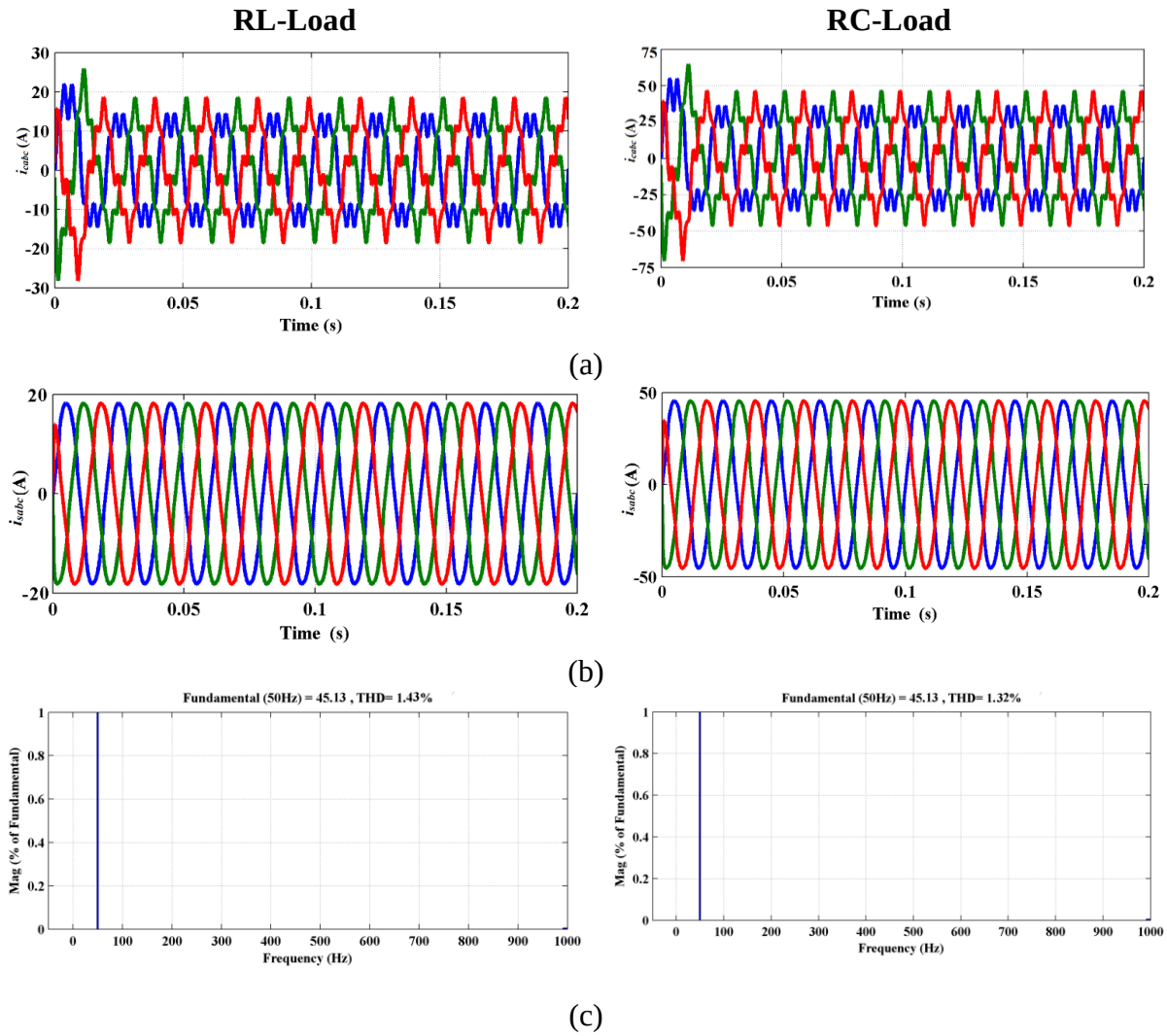

Figure 3.17 Profiles obtained under RL- and RC-type nonlinear loads (a) i_{cabc} generated using MSRF-FIED-AHCC control scheme, (b) i_{sabc} after compensation and (c) THD of i_{sabc} after compensation (**Scenario 4**)

FLC-HCC (best combination of Scenario 2) under RL-type nonlinear load, and 66.34% improvement in THD level under RC-type nonlinear loads, respectively.

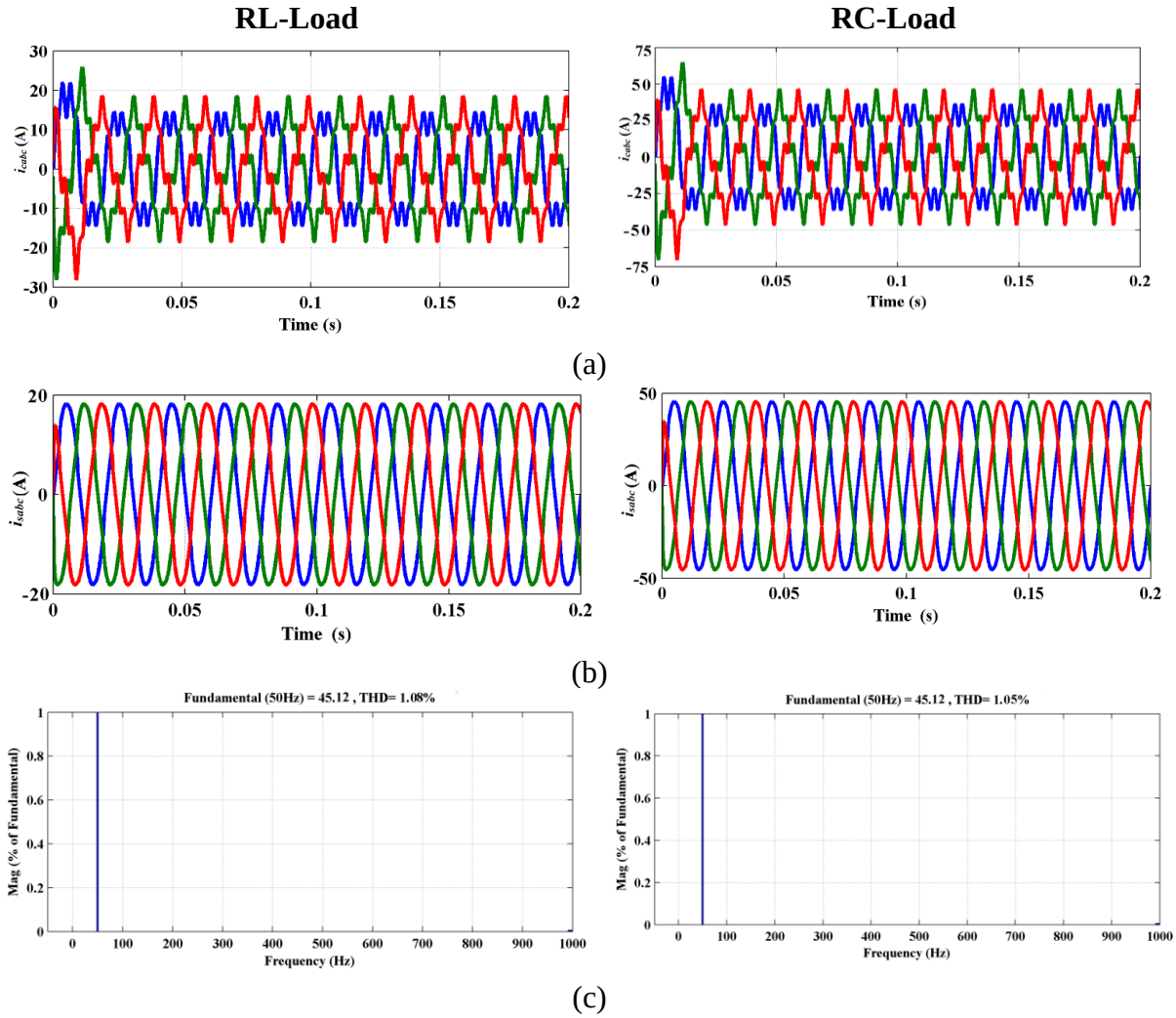

Figure 3.18 Profiles obtained under RL- and RC-type nonlinear loads (a) i_{cabc} generated using MSRF-FIED-AFHCC control scheme, (b) i_{sabc} after compensation and (c) THD of i_{sabc} after compensation (**Scenario 4**)

Table 3.5 THD comparison of i_{sabc} under non-ideal source condition

Nonlinear load type	THD without SAPF	THD with SAPF		
		Studied control approach	PWM switching scheme AHCC	AFHCC
RL-Load	35.51%	MSRF-FLC	2.35%	1.65%
		MSRF-FIED	**1.43%**	**1.08%**
RC-Load	74.29%	MSRF-FLC	2.18%	1.45%
		MSRF-FIED	**1.32%**	**1.05%**

Besides the approach offers improved THD level of (ii) 24.47% and 20.45% compared to MSRF-FIED-AHCC under RL-type and RC-type nonlinear loads, respectively. From Table 3.6, it is seen that out of the various harmonic components, the 5th harmonic is the predominant one, contributing 32.57% and 56.69% to the overall harmonic distortion of i_{sabc} for RL-and RC-type nonlinear loads, respectively. Apart from the above, 7th, 11th, 13th and 17th harmonics also appeared in the source current with magnitudes of 16.41%, 11.92%, 8.83% and 3.05%, respectively, in case of RL-load; and 28.54%, 12.89%, 4.20%, and 2.93% , respectively , for RC-load. It is observed from Table 3.6 that the minimum THD of 1.08% (for RL-load) and 1.05% (for RC-load) are obtained employing the proposed MSRF-FIED-AFHCC-based designed SAPF. Again, referring to the presence of individual THD components, the contribution of 5th, 7th, 11th, 13^{th,} and 17th harmonics is almost reduced to zero. Hence, it is concluded from the above study that the proposed MSRF-FIED-AFHCC-based designed SAPF works effectively under both ideal and non-ideal source conditions in mitigating harmonics from the source current. However, in order to test the V_{dc} regulation performance, further study has been conducted in Scenario 5.

Table 3.6: Comparative THD information of i_{sabc} under non-ideal source condition

Studies control schemes		Nonlinear load type	THD of i_{sabc} (in %)	Individual harmonics order of i_{sabc} (in %)				
				5th	7th	11th	13th	17th
Without SAPF		RL-Load	35.51	32.57	16.41	11.92	8.83	3.05
		RC-Load	74.29	56.69	28.54	12.89	4.20	2.93
SAPF with control scheme	MSRF-FLC-HCC	RL-Load	3.75	1.35	1.24	0.78	0.45	0.13
		RC-Load	3.12	1.37	0.85	0.64	0.52	0.24
	MSRF-FLC-AHCC	RL-Load	2.35	0.61	0.54	0.32	0.21	0.54
		RC-Load	2.18	0.50	0.71	0.22	0.32	0.33
	MSRF-FLC-AFHCC	RL-Load	1.65	0.35	0.46	0.15	0.12	0.17
		RC-Load	1.45	0.46	0.15	0.12	0.21	0.23
	MSRF-FIED-HCC	RL-Load	2.82	1.32	0.87	0.56	0.63	0.47
		RC-Load	2.45	1.25	0.54	0.32	0.45	0.53
	MSRF-FIED-AHCC	RL-Load	1.43	0.43	0.32	0.27	0.19	0.35
		RC-Load	1.32	0.52	0.46	0.28	0.18	0.32
	MSRF-FEID-AFHCC	**RL-Load**	**1.08**	**0.54**	**0.83**	**0.31**	**0.21**	**0.54**
		RC-Load	**1.05**	**0.64**	**0.52**	**0.25**	**0.18**	**0.43**

As reviewed from the literature, the V_{dc} regulation is very significant during load-changing conditions, as it causes overshoots and undershoots in the V_{dc} waveform, which would produce more harmonics in i_{sabc} profile. The proposed FIED control technique regulates the I_{dc} in such a way that V_{dc} deviation is less than the conventional controllers. Moreover, it diminishes the ripple in the V_{dc} profile to an acceptable level which causes reduction in the harmonics present in the i_{sabc}. The uniqueness of this work is that it mitigates the i_{sabc} harmonic components while keeping the deviation of V_{dc} waveform low under both ideal and non-ideal source conditions subject to different loads. However, to verify the superiority of the projected approach under steady-state and load-changing conditions, a comparative performance analysis with that of other studied controllers is presented in Scenario 5.

3.4.5 Performance analysis pertaining to Scenario 5

In this scenario, maintaining the approaches used for RCG (i.e., MSRF) and PWM signal generation (i.e., AFHCC method) same, the performance of the proposed FIED-based V_{dc} control strategy is compared with that of studied traditional methods (i.e., PI and FLC) in regulating V_{dc} profile and reducing its settling time (t_s) during steady-state and load-changing conditions and are presented in the following subsections of this scenario.

(a) V_{dc} *profile under steady-state conditions*

In this scenario, the V_{dc} regulation method is tested for its accuracy under steady-state conditions. To analyse the accuracy of the studied methods, a performance indicator called as percentage of accuracy (% ACC) is used as presented in equation (2.42) of

Table 3.7: Comparison of V_{dc} deviation under steady-state condition

Control approach	Voltage deviation (in V)		(% ACC)	
	RL-Load	RC-Load	RL-Load	RC-Load
MSRF-PI-AFHCC	20	22	97.15%	96.86%
MSRF-FLC-AFHCC	16	18	97.72%	97.43%
MSRF-FIED-AFHCC	**6**	**7**	**99.15%**	**99.00%**

Section 2.54 of Chapter 2. Figures 3.19(a)-(c) show the ripple present in the V_{dc} waveforms obtained under the impact of different studied controller-based designed SAPFs. It is evident from Figures 3.19(a)-(c) and from Table 3.7 that the maximum deviation of 20V and 22V in V_{dc} waveform is observed under MSRF-PI-AFHCC technique for RL- and RC- type nonlinear loads, respectively. Also, the %ACC of 97.15% and 96.86% are found for RL- and RC-load types, respectively. While the same is further reduced to 16V and 18V for R- and RC- load types, respectively, employing the MSRF-FLC-AFHCC approach and the %ACC improved to 97.72% and 97.43% for RL- and RC-load types, respectively. However, the proposed MSRF-FIED-AFHCC control topology offers the least deviation of 6V and 7V with further improvement in %ACC to 99.15% and 99 % for RL- and RC-type nonlinear loads, respectively.

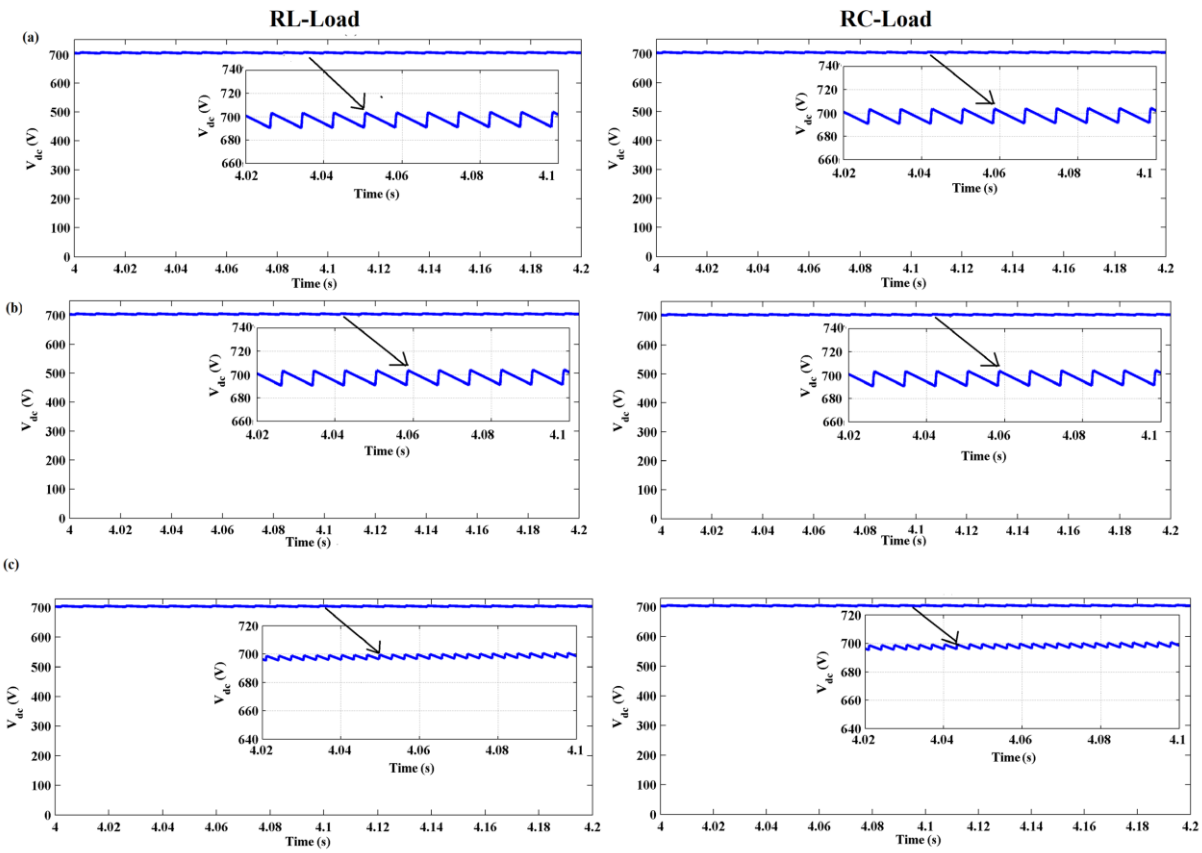

Figure 3.19 V_{dc} profiles obtained considering RL- and RC-type nonlinear loads under different controller-based SAPF (a) MSRF-PI-AFHCC scheme, (b) MSRF-FLC-AFHCC scheme, and (c) MSRF-FIED-AFHCC

(b) *V_{dc} profile under load-changing conditions*

Under load-changing conditions, the performance of the studied controllers are evaluated in terms of the overshoot (O_s), undershoot (U_s), and settling time (t_s). Two dynamic load situations are considered in this study (i) switching the nonlinear load from RC- to RL-type and (ii) from RL- type to RC-type. Figures 3.20 and 3.21 show the effect of each of the studied techniques in regulating V_{dc} profile under load-changing conditions like switching from RC- to RL-type and vice-versa, respectively. Firstly, the simulation model is run with a RC-type load and a steady-state condition is obtained. It is revealed from Figure 3.20 that the V_{dc} waveform remains steady up to $t = 0.2$ s. At $t = 0.2$ s, when the load is switched from RC- to RL-type, V_{dc} deviates from its reference value (i.e., 700 V). It is also observed from Figure 3.20 that the MSRF-PI-AFHCC control technique does not offer better performance and results in O_s of 19V (i.e., 2.71 % deviation from the reference value) with t_s of 0.1s (see Table 3.8).

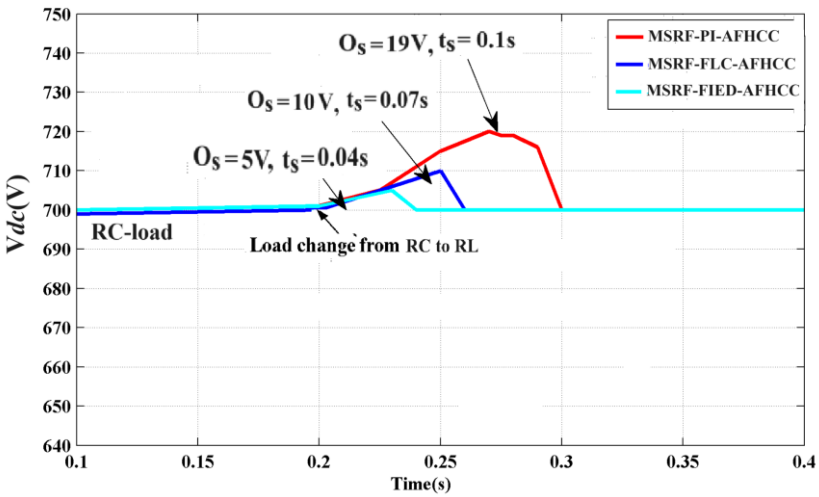

Figure 3.20 Comparative profiles of V_{dc} obtained using MSRF-PI-AFHCC, MSRF-FLC-AFHCC and MSRF-FIED-AFHCC methods under load-changing conditions (RC- to RL-type) (**Scenario 5**)

In the case of the MSRF-FLC-AFHCC technique, the deviation in V_{dc} profile still exists, but the O_s decreases further to 10V (i.e., 1.42% deviation from the reference value) with t_s reduce to 0.07 s. Whereas, the proposed MSRF-FIED-AFHCC topology performs exceptionally well offering the minimum O_s of 5V (i.e., a deviation of 0.71 %) and the quickest t_s of 0.04 s. In the case the load type changes from RL- to RC-type, as revealed in Figure 3.21, the projected MSRF-FIED-AFHCC technique again offers the best outcome with the minimum U_s of 6V (i.e., a deviation of 0.85% from the reference value) and the fastest t_s of 0.03 s. Whereas, the MSRF-PI-AFHCC controller results in the maximum U_s of 22V (i.e., 3.14% deviation from the reference value) and t_s of 0.09 s. The

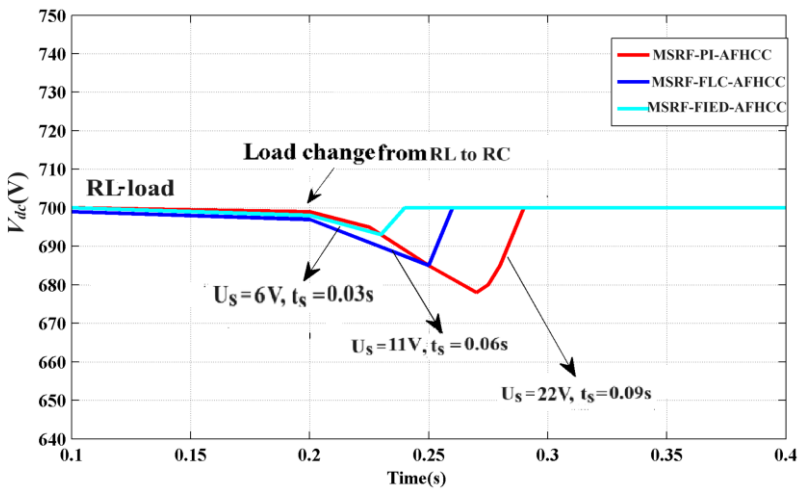

Figure 3.21 Comparative profiles of V_{dc} obtained using MSRF-PI-AFHCC, MSRF-FLC-AFHCC and MSRF-FIED-AFHCC methods under load-changing conditions (RL- to RC- type) (**Scenario 5**)

Table 3.8: V_{dc} deviation and t_s comparison under load-changing conditions

Studied control approach	Changing the load from RC- to RL-type		Changing the load from RL- to RC-type	
	O_s (V)	t_s (s)	U_s (V)	t_s (s)
MSRF-PI-AFHCC	19 (2.71%)	0.10	22 (3.14%)	0.09
MSRF-FLC-AFHCC	10 (1.42%)	0.07	11 (1.57%)	0.06
MSRF-FIED-AFHCC	**5 (0.71%)**	**0.04**	**6 (0.85%)**	**0.03**

MSRF-FLC-AFHCC approach, even if it is better than the MSRF-PI-AFHCC controller, yet it results in an U_s of 11V (i.e., 1.57% deviation from the reference value) and t_s of 0.06 s with respect to the proposed one. Based on all the results obtained from simulation works, it is observed that the proposed MSRF-FIED-AFHCC technique outperforms the other studied approaches and renders the source current almost sinusoidal after compensation. Besides, it also offers the best V_{dc} profile.

3.5 SUMMARY

In this chapter, the PQ issues of a standalone MG system are studied under the action of SAPF realized employing MSRF technique for RCG, a novel algorithm/approach referred as FIED technique implemented for V_{dc} regulation and AHCC/AFHCC-based switching scheme. Apart from this, the best combination among the methods used for the RCG, regulation of V_{dc}, and generation of switching pulse for the inverter is explored based on the comparative performance analysis. According to the findings of several simulation-based experiments, the suggested combination named MSRF-FIED-AFHCC control technique performs exceptionally well in curbing the deviation and settling time in V_{dc} profile in comparison to other counterparts under load-changing conditions. It is observed that the proposed MSRF-FIED-AFHCC technique has offered better improvement in reduction of THD with respect to MSRF-FLC-AHCC, MSRF-FIED-AHCC, and MSRF-FLC-AFHCC, which is (i) 52.78%, 48.74%, and 12.5%, respectively, in case of RL-type nonlinear load; and (ii) 53.48%, 50.73% and 13.04%, respectively, for RC- type nonlinear load. Moreover, the performance of V_{dc} profiles is also investigated under both steady-state and load-changing conditions. It is observed that the minimum deviation in V_{dc} profile is obtained, i.e., 6V for RL-load and 7V for RC-load under steady-state conditions. Again, under load-changing conditions, the MSRF-FIED-AFHCC technique resulted in the minimum V_{dc} deviation of 5V and the quickest response time of 0.04 s, when switching the load from RC- to RL-type. Likewise, the minimum deviation of 6V and the fastest response time of 0.03 s is obtained during switching of nonlinear load from RL-

to RC- type. Hence, the proposed MSRF-FIED-AFHCC technique provides improved harmonic mitigation performance by offering the lowest THD value under all operating scenarios, which is well within the limit prescribed by the IEEE-519 standard. The capability of SAPF in mitigating of harmonics may be reduced when the source is non-ideal or distorted. This is due to the fact that during distorted source conditions, the synchronization method used in RCG fails to track the exact source current. Hence, the performance of SAPF with an advanced RCG technique is explored in the next chapter under both ideal and non-ideal source conditions.

Chapter 4

POWER QUALITY ENHANCEMENT USING A NOVEL NFPLL-MSRF-BASED TECHNIQUE FOR SAPF IN MICROGRID

4.1 INTRODUCTION

As explained in the preceding chapters, the operation of three control loops, i.e., reference current generation (RCG), dc-link voltage regulation, and switching pulse generation, determines how well the shunt active power filter (SAPF) generates sufficient compensating current. The complexity of the current RCG techniques is intrinsic, and they are unable to extract the positive sequence signals needed to achieve the synchronization angle under source disturbance conditions. In order to address the shortcomings of the current methods, this chapter suggests a brand-new negative feedback phase-locked loop-based modified synchronous reference frame (NFPLL-MSRF) strategy.

In order to eliminate the harmonics that are present in the system, the RCG control loop is essential for producing the required compensatory current. Thus, from the perspective of the SAPF, its proper design is essential. According to published research works [154-175], there are numerous RCG control strategies and each has its own advantages. In general, these strategies are the better versions of the two fundamental control strategies, such as instantaneous active and reactive power theory [156] (termed as p-q theory) and synchronous reference frame (SRF) theory or d-q theory [157]. Among the two, the SRF technique is widely accepted due to its simple design and ease of implementation. However, the above approach suffers from a major drawback because of the requirement of a reference phase angle generated using a phase-locked loop (PLL) for synchronization. When the source voltages are imbalanced and/or distorted, the design of the PLL block must be carefully executed. A PLL design is similar to a nonlinear closed-loop feedback control system that uses measured frequency and phase angle to synchronize its output with the input signal [165].

Some parts of this chapter have been published in the following paper of international journal.

1. **Barik PK**, Shankar G, Sahoo PK, Elavarasan RM, Kumar S, Ibanez FM, Abou Houran M, Srivastava AK. and Terzija V. A novel negative feedback phase locked loop-based reference current generation technique for shunt active power filter. *International Journal of Electrical Power & Energy Systems, 2023, 153, p.109389.*

A simple PLL is comprised of three parts: a phase detector (PD), a loop filter (LF), and a voltage-controlled oscillator (VCO). There exist different PLL architectures, which are differentiated based on the design of the PD block. For SAPF realization, the use of SRF-based PLL (referred as SRF-PLL) has been widely reported [158]. The SRF-PLL produces a reasonable performance in terms of the phase/frequency tracking capabilities and the dynamic response under optimum grid circumstances. However, when the grid voltage is unbalanced and/or harmonically distorted, it performs worse, showing high amplitude steady-state oscillations in the anticipated phase and frequency.

In recent years, for accurate phase/frequency prediction, many enhanced PLLs have been proposed as alternatives to the conventional SRF-PLL. The essential idea behind these PLLs is to use a specific filtering technique to retrieve the fundamental frequency positive-sequence element and then to feed the output of this process into a conventional SRF-PLL [162]. An improved PLL (IPLL)-based RCG technique is proposed in [166]. A new deadbeat-based PLL is proposed in [167] for dynamic response, however, it suffers from time-delay in control action. A decoupled double synchronous reference frame-based PLL (DDSRF-PLL) has been proposed in [168] to eliminate double-frequency recognition issues caused by the fundamental frequency negative-sequence component. A multiple reference frame-based PLL (MRF-PLL) is presented in [169]. Similar to the DDSRF-PLL, the MRF-PLL operates on the same principle but is easier to implement. A modified SRF-PLL (MSRF-PLL) approach is proposed in [163] and has exhibited desired performance under low distortion and unbalanced system voltage conditions. However, under highly distorted grid conditions, the performance of its PD and filtering blocks degrade. Thus, the MSRF-PLL is unable to adequately extract the positive sequence signal required for the calculation of the synchronization angle. It has been noted that a lot of emphasis is given to the proper design of filter and PD blocks (which helps extract the fundamental positive sequence component) while tuning these advanced PLLs (i.e., MRF-PLL, DDSRF-PLL, and MSRF-PLL). However, under high grid perturbations, proper phase sequence signal extraction is not feasible due to the non-linearity that is discovered during signal alterations.

In light of the foregoing, this chapter proposes the reconfiguration of the MSRF structure to extract positive sequence signals from the source by employing a negative feedback loop in the low pass filter (LPF) and a nonlinear adaptive filter in the PD unit. The combination of a negative feedback loop and nonlinear adaptive-filter PD unit is able to track changes in amplitude, phase angle, and frequency of the input signal. Further, it can accurately estimate the fundamental component of a highly distorted signal by eradicating harmonics. Therefore, the proposed NFPLL-MSRF-based controller offers a higher level of immunity against noise and other signal-related disruptions during extreme grid perturbations than the traditional PLLs while increasing system bandwidth. The SAPF's dc-link capacitor is utilized to keep the system's power balanced. When the load is substantially increased, the capacitor discharges and supplies power, enabling the source and load power balance to be achieved. Similarly, the capacitor overcharges and maintains power balance when the load is suddenly removed. To carry out this process, a well-designed control strategy must be used to modulate the voltage across the dc-link capacitor. This helps SAPF to compensate for the reactive and harmonic currents. As explained in Chapter 2, the fuzzy logic-based nonlinear model-free controller can effectively handle the V_{dc} deviation arising under source and load side perturbations compared to the conventional controllers. Furthermore, the fuzzy logic controller (FLC) approach is known for its performance, durability, and ability to track harmonics, regulate V_{dc} , and adjust power factor. However, the main drawback of FLC is that its computational burden is increased due to the use of a greater number of membership functions and rules. Moreover, it also works on the principle of direct voltage error manipulation technique, which may not entirely reduce the V_{dc} deviation that occurs during load-changing conditions. In view of the above, in Chapter 3, the dynamic performance of SAPF is improved by employing a proposed novel fuzzy inverted error deviation (FIED) controller to control and diminish the ripples in the V_{dc} waveform, particularly under load-changing conditions. Hence, in this chapter, both FLC and FIED controllers are used individually along with the proposed NFPLL-MSRF approach to maintain stability under extreme load and source-side perturbations.

The choice of the pulse-width modulation (PWM) generator for the voltage source inverter (VSI) of SAPF also plays a crucial role in mitigating harmonics. In Chapter 3, it is confirmed that the adaptive fuzzy hysteresis current control (AFHCC) technique in SAPF achieves better harmonics compensation and parametric optimization than hysteresis current control (HCC) and adaptive hysteresis current control (AHCC) techniques. Further, the simulation results reveal that the AFHCC is not only used to obtain the switching signals but also to find the best value of the interfacing inductance, which is not possible in the case of HCC and AHCC techniques. Hence, in this chapter, AFHCC technique is further applied to the switching scheme of the studied SAPF.

In this chapter, the FLC and FIED approaches (considering one at a time) are adopted to regulate the V_{dc}, the proposed NFPLL-MSRF technique is used to provide the RCG signal, and the AFHCC technique is employed to generate a switching pulse. The different combinations of the above-mentioned methods associated with the three control loops examined in this chapter are named as NFPLL-MSRF-FLC-AFHCC and NFPLL-MSRF-FIED-AFHCC. The details on FLC and FIED approaches for the V_{dc} control and AFHCC for PWM signal generation may be referred from Chapter 2 and Chapter 3 of this dissertation, respectively. The proposed controller (i.e., NFPLL-MSRF) in association with the other control loops, effectively reduces THD in the source current to make the SAPF adaptable to all diverse conditions. Moreover, the primary goal of the NFPLL-MSRF technique is to retrieve reference current without using a LPF. Additionally, a performance comparison between the suggested NFPLL-MSRF-based SAPF and the traditional MSRF-based SAPF is conducted for better analysis. The details

4.1.1 Motivation of the Present Chapter

The effectiveness of SAPF mainly relies on the choice of the method used to derive the reference current. Out of several reported RCG control strategies, the MSRF method is the most commonly employed. However, the aforementioned method becomes overflowing by a significant limitation due to the necessity of generating a reference phase angle using a PLL to achieve synchronization. When the source voltages exhibit

imbalance and/or distortion, it is important to precisely develop the PLL block. Several advanced PLLs have been suggested as substitutes for the MSRF-PLL to improve the precision of phase and frequency prediction. The primary concept underlying these PLLs is to employ a specialized filtering approach to extract the positive-sequence component of the fundamental frequency, which is subsequently fed into a MSRF-PLL. Nevertheless, when subjected to severely distorted supply conditions, the PD and filtering blocks of the system experience a decline in performance. Therefore, the MSRF-PLL is unable to effectively extract the positive sequence signal necessary for computing the synchronization angle. Therefore, based on the above discussion, it is clear that there is potential for enhancing the performance of SAPF by incorporating an appropriate PLL to calculate the synchronization angle. This motivates the author to work further on the modification of the conventional MSRF-PLL technique.

This chapter introduces a new PLL that is used to extract positive sequence signals from the source. This is achieved by incorporating a negative feedback loop in the low-pass filter and a nonlinear adaptive filter in the PD unit. The integration of a negative feedback loop with a nonlinear adaptive-filter PD unit enables precise monitoring of variations in the amplitude, phase angle, and frequency of the input signal.

4.1.2 Contribution of the Present Chapter

In the present chapter, to improve the performance of SAPF, a comparative study of different combinations of control techniques, i.e., (NFPLL-MSRF for RCG), (FLC and FIED for V_{dc} control), and (AFHCC for switching pulse generation) is proposed. Further, using different nonlinear loads, the PQ issue (mainly THD) in the source current waveform is analyzed under ideal and non-ideal source conditions.

The main contributions of the present work are as follows.

a) A novel NFPLL-MSRF-based improved control circuit of the SAPF is proposed to reduce THD in source current.

b) The performance of the proposed NFPLL-MSRF scheme (along with FLC/FIED and AFHCC-based techniques used for V_{dc} regulation and PWM signal generation,

respectively) under different sources and load-changing conditions has been deeply analyzed through a series of simulation-based experiments.

c) To prove the effectiveness of the proposed approach, a comparative performance analysis is carried out between the proposed approach and the existing conventional methods under both steady-state and load-changing conditions for V_{dc} regulation.

4.1.3 Chapter Orientation

The remaining portion of the present chapter is organized as follows. Modeling of the proposed novel NFPLL-MSRF-based technique for synchronization is presented in Section 4.2. In Section 4.3, the simulation results obtained from the different studied scenarios are presented and discussed. Finally, the research findings of the present chapter are summarized in Section 4.4.

4.2 DESIGN OF NFPLL-MSRF METHOD

Previously, researchers have proposed various methods for producing reference current based on instantaneous active and reactive power theory, notch filter technique, SRF and MSRF methods, synchronous detection algorithm, adaptive linear neuron algorithm, etc. Among these, the MSRF method has been adopted in many reported works. There is still room for further enhancement of its performance capability. Therefore, the current work employs this MSRF technique with certain modifications for superior performance.

4.2.1 Modeling of the Proposed NFPLL-MSRF Scheme

The proposed NFPLL-MSRF scheme is shown in Figure 4.1. In this, the NFPLL-based unit vector generation scheme is suggested, which replaces the existing MSRF's unit vector generation topology as presented in Section 2.4.1 of Chapter 2. The architecture of the proposed NFPLL block consists of a negative feedback signal given to the LPF block, a nonlinear adaptive filter-based PD circuit and a VCO block, which help to extract positive sequence signals from the supply. Negative feedback improves the bandwidth of

the LPF. This, in turn, enhances the filtering capacity of LPF; as a result, impurity in the signal is suppressed. Thus, a negative feedback signal helps in mitigating the impacts of noise and disturbances on the system's performance, thereby, enhancing its stability.

Similarly, the nonlinear adaptive filter-based PD approach can track changes in the input signal's amplitude, phase angle, and frequency while effectively calculating the fundamental component. The LPF block is made up of a PI control block with a negative feedback loop. The VCO block consists of an adder, an integrator, and a sine block. The adder in the VCO block adds the fundamental angular frequency signal (ω_c) to the frequency deviation components ($\Delta\omega$). The VCO block takes input from the LPF block and produces its output (θ'). This θ' is given as an input to a sine block for the production of unit vectors ($\sin\theta$ and $\cos\theta$), as shown in Figure 4.1. The operation of the proposed controller is explained in detail below.

Initially, the source voltage ($V_{s\alpha bc}$) is applied at the input of NFPLL. Then, the in-phase ($V_{ab} = V_m \sin(\omega t + \phi)$) and in-quadrature phase ($V_{bc} = V_m \cos(\omega t + \phi)$) voltages are produced by subtracting the phase-*b* voltage (V_{sb}) from the phase-*a* (V_{sa}), and

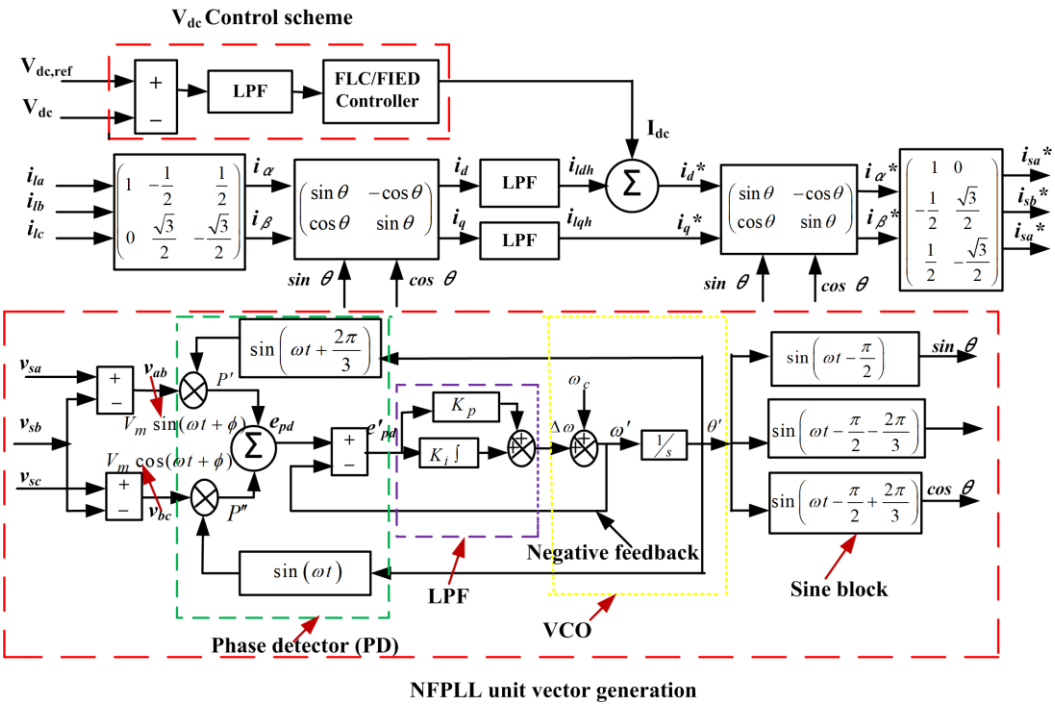

Figure 4.1 Proposed NFPLL-MSRF-based RCG method

phase-*c* voltages (V_{sc}) from phase-*b* voltage V_{sb}, respectively, as given in equation (4.1) and (4.2), respectively. The θ' is used to produce the signals P' and P'' as represented by (4.3) and (4.4), respectively. Thereafter, these P' and P'' are added to obtain the phase error signal (e_{pd}), which is further subtracted from the negative feedback signal (ω') before being given as an input to the PI controller (e'_{pd}) as mentioned in (4.5) and (4.6). The ω' signal is obtained by adding ω_c with $\Delta\omega$ as presented in (4.7). The e'_{pd} is processed in the PI controller to generate $\Delta\omega$ as per (4.8).

$$V_{ab} = V_{sa} - V_{sb} = V_m \sin(\omega t + \phi) \tag{4.1}$$

$$V_{bc} = V_{sb} - V_{sc} = V_m \cos(\omega t + \phi) \tag{4.2}$$

$$P' = V_m \sin(\omega t + \phi) \times \sin(\omega t + \frac{2\pi}{3}) \tag{4.3}$$

$$P'' = V_m \cos(\omega t + \phi) \times \sin(\omega t) \tag{4.4}$$

$$P' + P'' = e_{pd} \tag{4.5}$$

$$e'_{pd} = e_{pd} - \omega' \tag{4.6}$$

$$\omega' = \Delta\omega + \omega_c \tag{4.7}$$

$$\Delta\omega = K_p e_{pd}(t) + K_i \int e_{pd}(t) dt \tag{4.8}$$

The output (θ') of the VCO block is used to generate unit vector signals ($\sin\theta$ and $\cos\theta$), which are utilized to produce the desired 3-phase reference source currents (i^*_{sa}, i^*_{sb}, and i^*_{sc}) as per (4.9)-(4.12).

$$\begin{pmatrix} i_\alpha \\ i_\beta \end{pmatrix} = \begin{pmatrix} 1 & -\frac{1}{2} & \frac{1}{2} \\ 0 & \frac{\sqrt{3}}{2} & -\frac{\sqrt{3}}{2} \end{pmatrix} \begin{pmatrix} i_{la} \\ i_{la} \\ i_{lc} \end{pmatrix} \tag{4.9}$$

$$\begin{pmatrix} i_d \\ i_q \end{pmatrix} = \begin{pmatrix} \sin\theta & -\cos\theta \\ \cos\theta & \sin\theta \end{pmatrix} \begin{pmatrix} i_\alpha \\ i_\beta \end{pmatrix} \tag{4.10}$$

$$\begin{pmatrix} i_\alpha^* \\ i_\beta^* \end{pmatrix} = \begin{pmatrix} \sin\theta & -\cos\theta \\ \cos\theta & \sin\theta \end{pmatrix} \begin{pmatrix} i_d^* \\ i_q^* \end{pmatrix} \tag{4.11}$$

$$\begin{pmatrix} i_{sa}^* \\ i_{sb}^* \\ i_{sc}^* \end{pmatrix} = \begin{pmatrix} 1 & 0 \\ -\frac{1}{2} & \frac{\sqrt{3}}{2} \\ \frac{1}{2} & -\frac{\sqrt{3}}{2} \end{pmatrix} \begin{pmatrix} i_\alpha^* \\ i_\beta^* \end{pmatrix} \tag{4.12}$$

The maximum value of the reference current (I_{dc}) is considered as the output of FLC or FIED. This I_{dc} is multiplied with the NFPLL-MSRF output to generate the desired

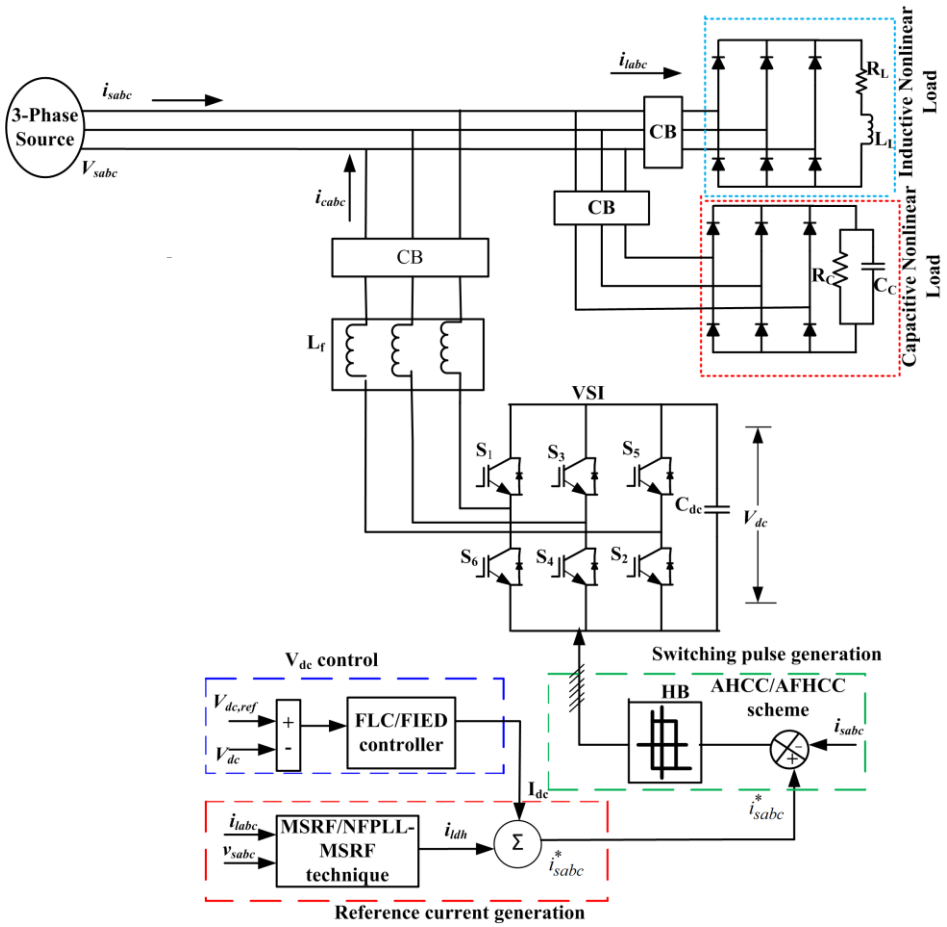

Figure 4.2 SAPF with NFPLL-MSRF-FIED-AFHCC-based control scheme

three-phase reference current (i^*_{sabc}). Then, the actual source currents (i_{sa}, i_{sb} and i_{sc}) are compared with their reference currents (i^*_{sa}, i^*_{sb} and i^*_{sc}) to generate the switching signals for the VSI using the studied AFHCC technique. Subsequently, the VSI outputs the desired compensating current and is fed at PCC to mitigate the harmonics.

4.3 RESULTS AND DISCUSSIONS

This section investigates the performance of SAPF under different source and load-changing conditions. For better harmonic filtering, a SAPF is appended with the proposed control algorithm (i.e., NFPLL-MSRF technique) for RCG. Apart from the above, the V_{dc} regulation and PWM pulse generation are realized using the studied FLC or FIED technique and AFHCC scheme, respectively. In the present chapter, the scheme employing the conventional MSRF method with either FLC or FIED controller (for V_{dc} control) and AFHCC scheme (for switching pulse generation) used for producing compensating current (i_{cabc}) is referred to as MSRF-FLC-AFHCC or MSRF-FIED-AFHCC technique, respectively. The performance of the above-mentioned controller are compared with the proposed NFPLL-MSRF-FLC-AFHCC and NFPLL-MSRF-FIED-AFHCC techniques. The studied SAPF model is simulated in the MATLAB/Simulink platform employing the above control methods, and the results obtained from each control method are discussed to establish the superiority of one over the other. In this study as well, the nonlinear load consisting of a 3-phase bridge rectifier with resistance and inductance in series on its dc-side is considered as the inductive type nonlinear load (i.e., nonlinear RL-load), and a rectifier with resistance and capacitance in parallel is referred to as the capacitive type nonlinear load (i.e., nonlinear RC-load). The model is illustrated in Figure 4.2, and its various parameters are tabulated in Table 2.6 of Chapter 2. In Chapter 2, the standalone MG model with the nonlinear RL- and RC-loads without connecting the SAPF under ideal source conditions is simulated. It was observed from the results showcased in Figures 2.31(a) and (b) of Chapter 2 that the source current

(i_{sabc}) waveform is non-sinusoidal in nature, having very high total harmonic distortion (THD) content of 26.74% and 20.25% for RL- and RC- type nonlinear loads, respectively. Similarly, the performance of the studied MG system without SAPF is examined under non-ideal source condition in Chapter 3. It may be viewed from Figure 3.14(c) of Chapter 3 that the THD of i_{sabc} are also highly distorted and found to be 35.51% and 74.29% for RL- and RC-type nonlinear loads, respectively. In order to make i_{sabc} sinusoidal, SAPF (employing the proposed approach) is turned on, which produces reference current i^*_{sabc}. The sensed i_{sabc} is compared with the reference i^*_{sabc} and the error between them is fed to the hysteresis band (HB) of the AFHCC scheme to initiate a suitable switching action. After this, the compensating current (i_{cabc}) is generated from the inverter and injected at the PCC.

In this chapter, SAPF with various control techniques is utilized to reduce THD from the source current, which is referred to as different scenarios. The results of interest under each scenario are highlighted in bold in the respective table.

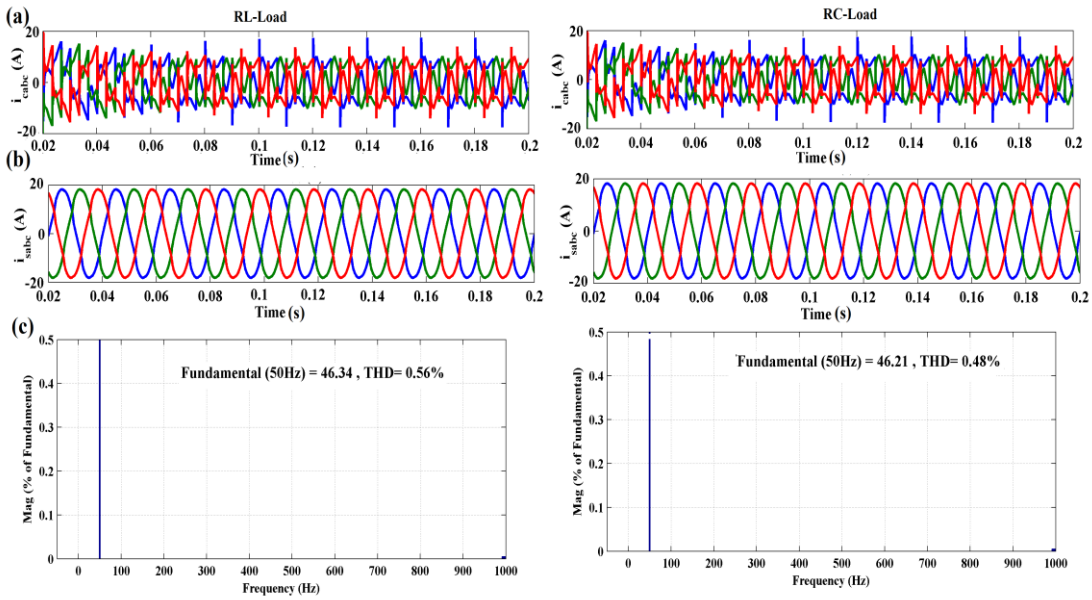

Figure 4.3 Profiles obtained for ideal source condition under RL- and RC-type nonlinear loads (a) i_{cabc} generated using NFPLL-MSRF-FLC-AFHCC approach, (b) i_{sabc} after compensation, and (c) THD of i_{sabc} after compensation (**Scenario 1**)

(a) Scenario 1: Performance analysis of the proposed NFPLL-MSRF-FLC-AFHCC method under ideal and non-ideal source conditions.

(b) Scenario 2: Performance analysis of the proposed NFPLL-MSRF-FIED-AFHCC method under ideal and non-ideal source conditions.

(c) Scenario 3: Performance analysis of the proposed control strategy under asymmetrical loading and change in load parameters.

(d) Scenario 4: Comparative performance analysis of the proposed control scheme with that of the studied one for V_{dc} regulation under steady-state and load-changing conditions.

4.3.1 Performance Analysis Pertaining to Scenario 1

The i_{cabc} generated (see Figure 4.3(a) and Figure 4.4(a) for ideal and non-ideal source conditions, respectively) using the projected NFPLL-MSRF-FLC-AFHCC-based combined control scheme is injected at the PCC, due to which the THD of i_{sabc} is

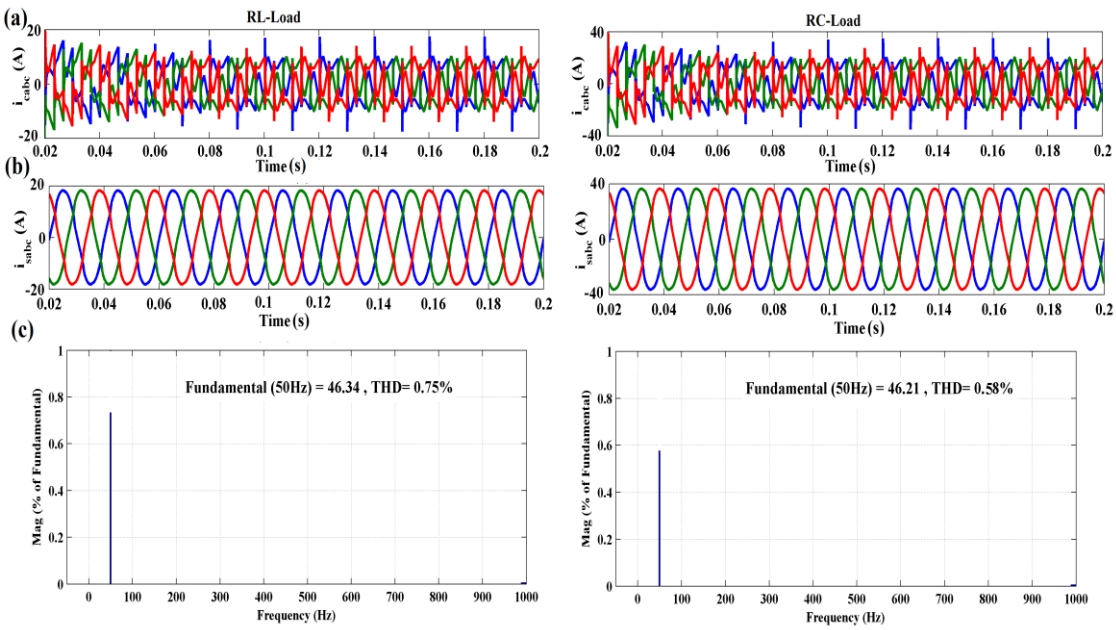

Figure 4.4 Profiles obtained for non-ideal source condition under RL- and RC-type nonlinear loads of (a) i_{cabc} generated by SAPF using NFPLL-MSRF-FLC-AFHCC approach, (b) i_{sabc} after compensation, and (c) THD of i_{sabc} after compensation (**Scenario 1**)

reduced to a lower value (refer Figure 4.3(c) and Figure 4.4(c)). The i_{sabc} waveform after reimbursement is addressed in Figure 4.3(b) and Figure 4.4(b) for both ideal and non-ideal source conditions, respectively. Table 4.1 presents comparative THD information of the source current in the absence and the presence of SAPF with the proposed schemes. It is observed from Table 4.1 that the minimum THD of 0.56% (for RL-load) and 0.48% (for RC-load), and 0.75% (for RL-load) and 0.58% (for RC-load) are obtained under ideal and non-ideal source conditions, respectively, employing NFPLL-MSRF-FLC-AFHCC controller-based designed SAPF.

4.3.2 Performance Analysis Pertaining to Scenario 2

As explained in the Chapter 3, the FIED control technique, performs exceptionally well in curbing the deviation and settling time in V_{dc} profile compared PI and FLC both under steady-state and load-changing conditions. Similarly, it is also observed from Chapter 3 that the AFHCC method significantly enhances the SAPF's performance by drastically reducing inverter switching losses. Hence, in this case, the performance of SAPF is analyzed employing the proposed NFPLL-MSRF-FIED technique incorporated with

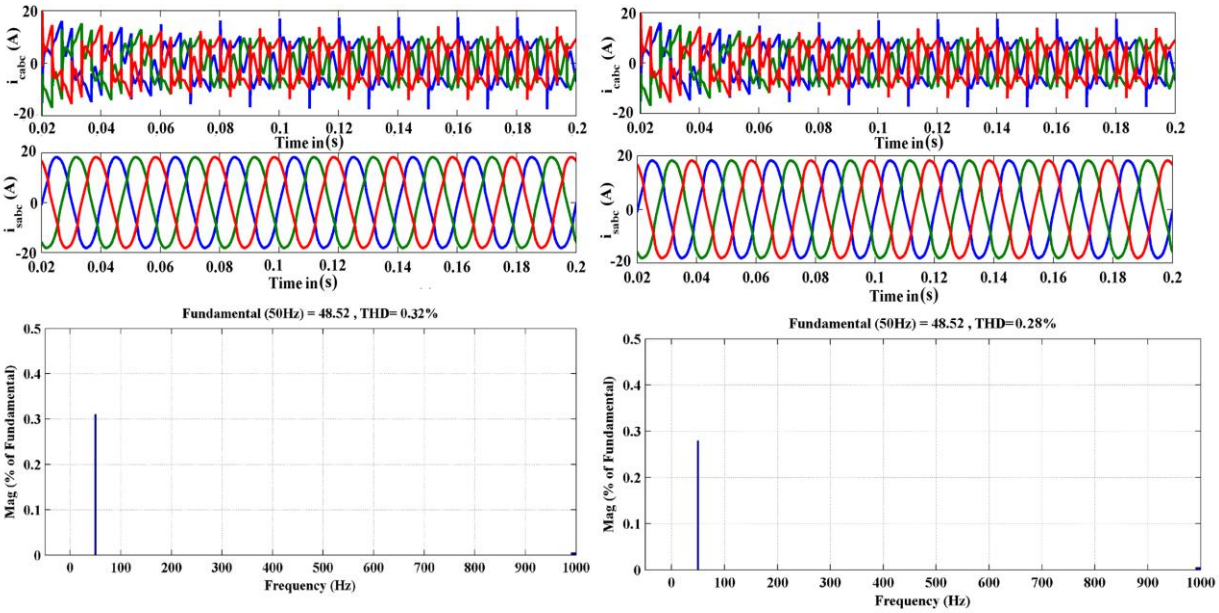

Figure 4.5 Profiles obtained under ideal source condition under RL- and RC-type nonlinear loads of (a) i_{cabc} generated by SAPF using NFPLL-MSRF-FIED-AFHCC approach, (b) i_{sabc} after compensation, and (c) THD of i_{sabc} after compensation (**Scenario 2**)

AFHCC switching approach termed earlier as NFPLL-MSRF-FIED-AFHCC. In this scenario, the performance of the SAPF is tested with the best of methods found for RCG (NFPLL-MSRF), V_{dc} control (FIED) and switching pulse generation (AFHCC). The i_{cabc} generated (see Figure 4.5(a) and Figure 4.6(a) for ideal and non-ideal source

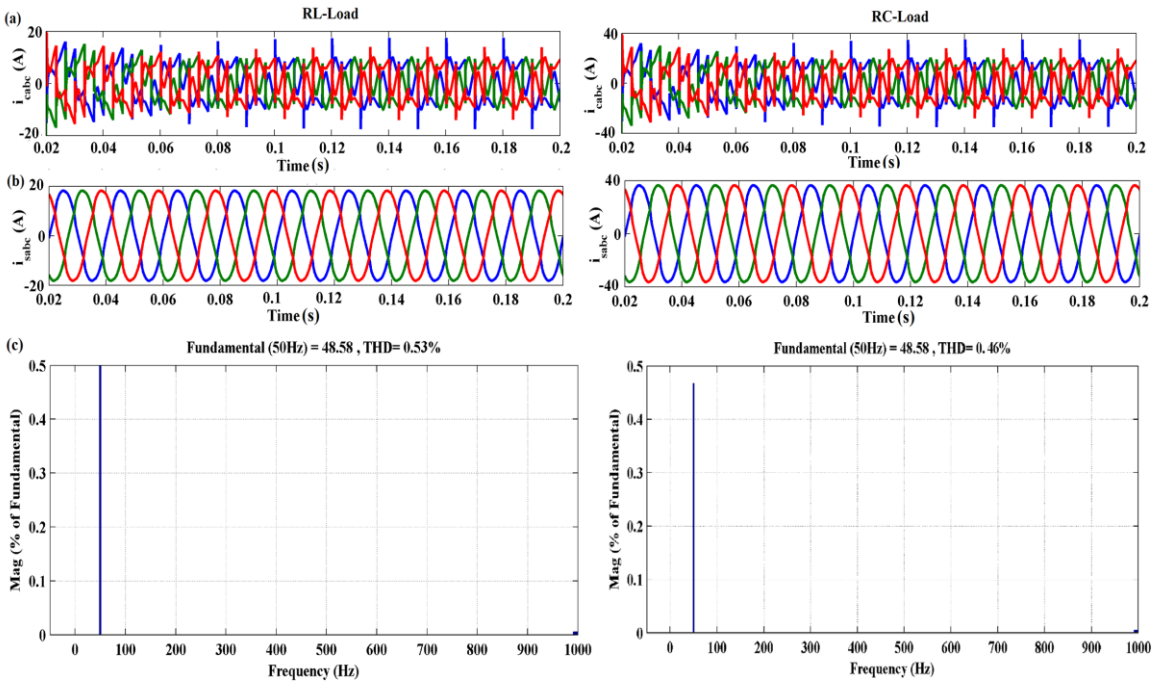

Figure 4.6 Profiles obtained under non-ideal condition under RL- and RC-type nonlinear loads of (a) i_{cabc} generated by SAPF using NFPLL-MSRF-FIED-AFHCC approach, (b) i_{sabc} after compensation, and (c) THD of i_{sabc} after compensation (**Scenario 2**)

Table 4.1: Comparative THD information of i_{sabc}

Studies control schemes	Nonlinear load type	THD of i_{sabc} (in %) under ideal source condition	THD of i_{sabc} (in %) under non-ideal source condition
Without SAPF	RL-Load	26.74	35.51
	RC-Load	20.25	74.29
NFPLL-MSRF-FLC-AFHCC	RL-Load	0.56	0.75
	RC-Load	0.48	0.58
NFPLL-MSRF-FIED-AFHCC	**RL-Load**	**0.32**	**0.53**
	RC-Load	**0.28**	**0.46**

conditions, respectively) using the proposed NFPLL-MSRF-FIED-AFHCC-based combined control scheme is injected at the PCC, due to which the THD of i_{sabc} is reduced to a lower value as shown in Figure 4.5(c) and Figure 4.6(c). The i_{sabc} waveform after reimbursement are addressed in Figure 4.5(b) and Figure 4.6(b) for both ideal and non-ideal source conditions, respectively. It is observed from the Figure 4.5(c) that the lowest THD of 0.32% and 0.28% for nonlinear RL- and RC-loads are obtained under ideal source conditions using the proposed combined NFPLL-MSRF-FIED-AFHCC-based control scheme. Similarly, for the case of non-ideal source condition again, the lowest THD of 0.53% and 0.46% for RL- and RC-loads, respectively, are observed under the proposed combined NFPLL-MSRF-FIED-AFHCC-based control scheme (refer Figure 4.6(c)). Table 4.1 shows the comparative study of THD values of i_{sabc} under different control scheme. A detail on THD information, including individual harmonics order of i_{sabc} (in %) resulting employing different control schemes under ideal and non-ideal source conditions are presented in Table 4.2 and Table 4.3, respectively. From Table 4.2 it is seen that out of the various harmonic components, the 5th harmonic is the predominant one contributing 20.76% and 21.21% to the total harmonic distortion of i_{sabc} for RL- and RC-type nonlinear loads, respectively, under ideal source condition. It contributes 32.57% and 56.69% to the harmonic distortions under non-ideal source conditions for RL- and RC-loads, respectively. Apart from the above, 7th, 11th, 13th and 17th harmonics also appeared in the source current with magnitudes of 12.66%, 6.86%, 4.09% and 1.97%, respectively, in the case of RL-load; and 17.23%, 8.64%, 5.11%, and 2.91% for RC-load, respectively, under ideal source condition. Likewise, 7th, 11th, 13th and 17th harmonics with a respective magnitude of 16.41%, 11.92%, 8.83% and 3.05% for RL-load and 28.54%, 12.89%, 4.20%, and 2.93% for RC-load are perceived under non-ideal source condition. It is observed from Tables 4.2 and 4.3 that the minimum THD of 0.32% (for RL-load) and 0.28% (for RC-load), and 0.53% (for RL-load) and 0.46% (for RC-load) are obtained under ideal and non-ideal source conditions, respectively, employing the proposed controller-based designed SAPF. Again, referring to the presence of individual THD components, the contribution of 5th, 7th, 11th, 13th and

17th harmonics is nearly reduced to zero for both cases. It is observed from the analysis presented above that the proposed NFPLL-MSRF has further enhanced the performance of the SAPF. To further establish the superiority of the proposed NFPLL-MSRF, considering the scenario of only ideal source and nonlinear load conditions, its performance with the other combination of controllers (as given in Table 4.2 (for ideal source condition) is compared with the results obtained with the traditional MSRF-based approaches (for ideal source condition) presented in Chapter 3 and is represented in Table 4.3. It is observed from Table 4.3 that replacing traditional MSRF by the proposed NFPLL-MSRF in the MSRF-FLC-AHCC topology studied in Chapter 3, a good reduction in THD is observed (i.e., it reduces to 1.35 and 1.28 for RL- and RC-type loads, respectively, in comparison to respective THD of 2.22 and 2.15 obtained under MSRF-FLC-AHCC approach). Table 4.3 shows that the MSRF-FIED-AHCC combination gives a better THD profile than the MSRF-FLC-AHCC (i.e., 2.05 and 2.03 for RL-and RC-loads, respectively). However, the NFPLL-MSRF technique, even with FLC (less superior than FIED) and AHCC controller, offers further improved THD profiles. The proposed topology of Chapter 3 (i.e., MSRF-FIED-AFHCC) gives better performance than the MSRF-FIED-AHCC technique, offering the lowest THD values of 1.05 and 1.01,

Table 4.2: Comparative THD information of i_{sabc} under ideal source condition

Studied control schemes		Nonlinear load type	THD of i_{sabc} (in %)	Individual harmonics order of i_{sabc} (in %)				
				5th	7th	11th	13th	17th
	Without SAPF	RL-Load	26.74	20.76	12.66	6.86	4.09	1.97
		RC-Load	20.25	15.85	10.56	4.08	2.15	1.36
SAPF with control scheme	NFPLL-MSRF-PI-AHCC	RL-Load	2.25	1.28	1.34	0.87	0.68	0.47
		RC-Load	2.15	0.50	1.23	0.22	0.32	0.67
	NFPLL-MSRF-PI-AFHCC	RL-Load	1.85	0.64	0.58	0.25	0.17	0.43
		RC-Load	1.62	0.56	0.45	0.25	0.18	0.42
	NFPLL-MSRF-FLC-AHCC	RL-Load	1.35	0.48	0.33	0.27	0.19	0.37
		RC-Load	1.28	0.51	0.46	0.26	0.18	0.36
	NFPLL-MSRF-FLC-AFHCC	RL-Load	0.56	0.2	0.25	0.15	0.18	0.13
		RC-Load	0.48	0.25	0.10	0.20	0.15	0.17
	NFPLL-MSRF-FIED-AHCC	RL-Load	0.55	0.21	0.23	0.13	0.17	0.12
		RC-Load	0.42	0.23	0.14	0.21	0.14	0.16
	NFPLL-MSRF-FIED-AFHCC	**RL-Load**	**0.32**	**0.18**	**0.21**	**0.11**	**0.15**	**0.90**
		RC-Load	**0.28**	**0.15**	**0.12**	**0.13**	**0.11**	**0.80**

respectively, for RL- and RC-loads (refer Table 4.4) due to that fact that AFHCC method for PWM is superior to AHCC. However, the proposed NFPLL-MSRF in combination with FIED and AHCC (less superior than the AFHCC) only (i.e. , NFPLL-MSRF-FIED-AHCC topology) presents an even lower THD value than the MSRF-FIED-AFHCC (the best approach of Chapter 3), which offers a THD values of 0.55 and 0.42 for RL and RC-load, respectively. Thus, the above discussion infers that adding the proposed NFPLL-MSRF offers superior performance. The superiority of the proposed NFPLL-MSRF is also found true when similar comparisons of the results presented in Chapter 3 and Chapter 4 are made for non-ideal source conditions.

4.3.3 Performance Analysis Pertaining to Scenario 3

In this scenario, two different case studies have been carried out highlighting the performance of the proposed NFPLL-MSRF-FIED-AFHCC-based combined strategy considering (i) asymmetrical loading conditions and (ii) change in load parameters.

(a) Case study 1: System performance under asymmetrical loading

(b) Case study 2: System performance under a change in nonlinear load parameters

Table 4.3: Comparative THD information of i_{sabc} under non-ideal source condition

Studied control schemes		Nonlinear load type	THD of i_{sabc} (in %)	Individual harmonics order of i_{sabc} in (%)				
				5th	7th	11th	13th	17th
Without SAPF		RL-Load	35.51	32.57	16.41	11.92	8.83	3.05
		RC-Load	74.29	56.69	28.54	12.89	4.20	2.93
SAPF with control scheme	NFPLL-MSRF-PI-AHCC	RL-Load	2.82	1.32	0.87	0.56	0.63	0.47
		RC-Load	2.45	1.25	0.54	0.32	0.45	0.53
	NFPLL-MSRF-PI-AFHCC	RL-Load	1.98	0.54	0.83	0.31	0.21	0.54
		RC-Load	1.65	0.64	0.52	0.25	0.18	0.43
	NFPLL-MSRF-FLC-AHCC	RL-Load	1.43	0.43	0.32	0.27	0.19	0.35
		RC-Load	1.32	0.52	0.46	0.28	0.18	0.32
	NFPLL-MSRF-FLC-AFHCC	RL-Load	0.75	0.2	0.3	0.1	0.2	0.2
		RC-Load	0.58	0.3	0.1	0.2	0.15	0.25
	NFPLL-MSRF-FIED-AHCC	RL-Load	0.75	0.21	0.23	0.13	0.17	0.12
		RC-Load	0.58	0.23	0.14	0.21	0.14	0.16
	NFPLL-MSRF-FIED-AFHCC	**RL-Load**	**0.53**	**0.21**	**0.26**	**0.18**	**0.15**	**0.13**
		RC-Load	**0.46**	**0.13**	**0.11**	**0.17**	**0.14**	**0.11**

(a) Case study 1

In order to operate the system in asymmetrical loading conditions, different nonlinear loads are connected in each of the three phases through three circuit breakers (CB1, CB2, and CB3) (refer Figure 4.7). CB1 and CB3 will be in close condition for asymmetrical nonlinear inductive loading, while CB2 and CB3 will be in close condition for asymmetrical nonlinear capacitive loading. To understand the effectiveness of the proposed controller under asymmetrical loadings, the profile of different waveforms is presented in Figures 4.8(a)-(d). It is observed from Figure 4.8(a) that the load current profile (i_{labc}) shown up to t = 0.2s pertains to RL-type asymmetrical load. At t = 0.2s,

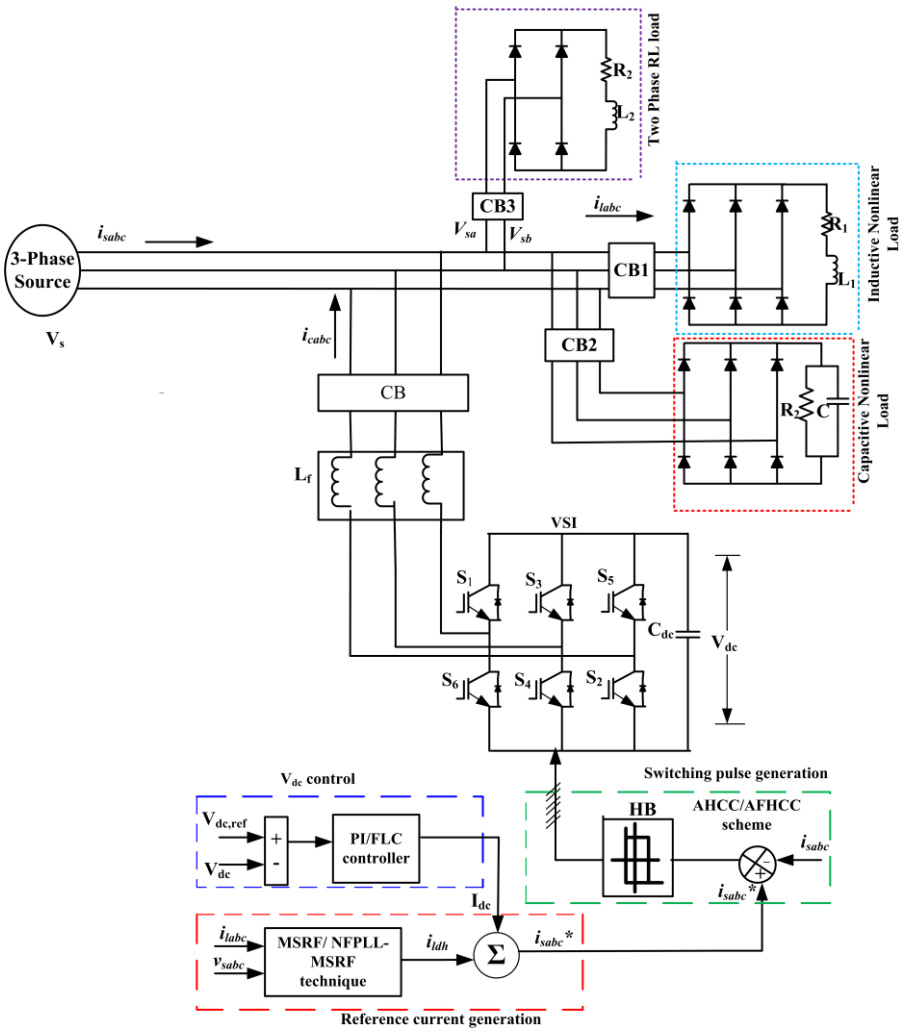

Figure 4.7 SAPF with asymmetrical loading arrangement

the load is changed to asymmetrical RC-load, and accordingly, the changed profile in load

current is depicted from t = 0.2s onwards. Similarly, in Figure 4.8(b), the complete i_{sabc} waveform, before compensation, is presented under the changing asymmetrical nonlinear load-type. When the SAPF using the proposed NFPLL-MSRF-FIED-AFHCC-based combined control approach is turned on from t = 0.1s to 0.4s, the generated i_{cabc} waveform (refer Figure 4.8(c)) from t = 0.1s onwards is able to mitigate the harmonics and, thus, make the distorted i_{sabc} waveform pure sinusoidal under changing load-type dynamics. The i_{sabc} waveform after compensation is presented in Figure 4.8(d). The above results conclude that the proposed controller-based SAPF performs well even under changing asymmetrical load dynamics.

(b) Case study 2

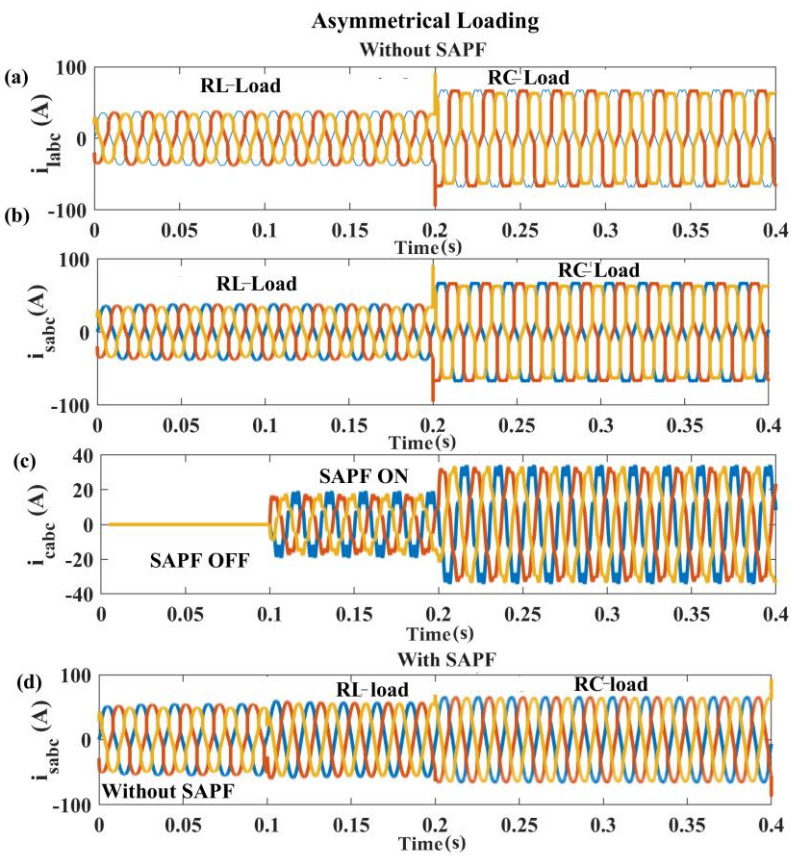

Figure 4.8 Profiles obtained under asymmetrical loading conditions (a) i_{labc} considering RL- and RC-load, (b) i_{sabc} before compensation (c) i_{cabc} considering with and without SAPF, and (d) i_{sabc} considering with and without SAPF (**Case study 1**)

In this case study, the proposed controller's effectiveness is further measured by changing the load parameters; however, the time of switching of RL-load to RC-load is considered same as that of previous case study i.e., at t=0.2s. The profiles of load current, source current before compensation, compensating current, and the compensated source current obtained for unchanged RL- and RC-load parameters and changed resistive component only in the considered loads (i.e., R_1 of RL-load is altered from 45 Ω to 90 Ω and R_2 of RC-load is changed from 18 Ω to 36 Ω) are displayed in Figures 4.9(a)-(d) and Figures 4.10(a)-(d), respectively. Figures 4.9(a) and 4.10(a) show the profile of i_{labc} for RL- and RC-type nonlinear loads. Similarly, in Figures 4.9(b) and 4.10(b), the complete i_{sabc} waveform, before compensation is presented. When SAPF is turned on at t = 0.1s, the

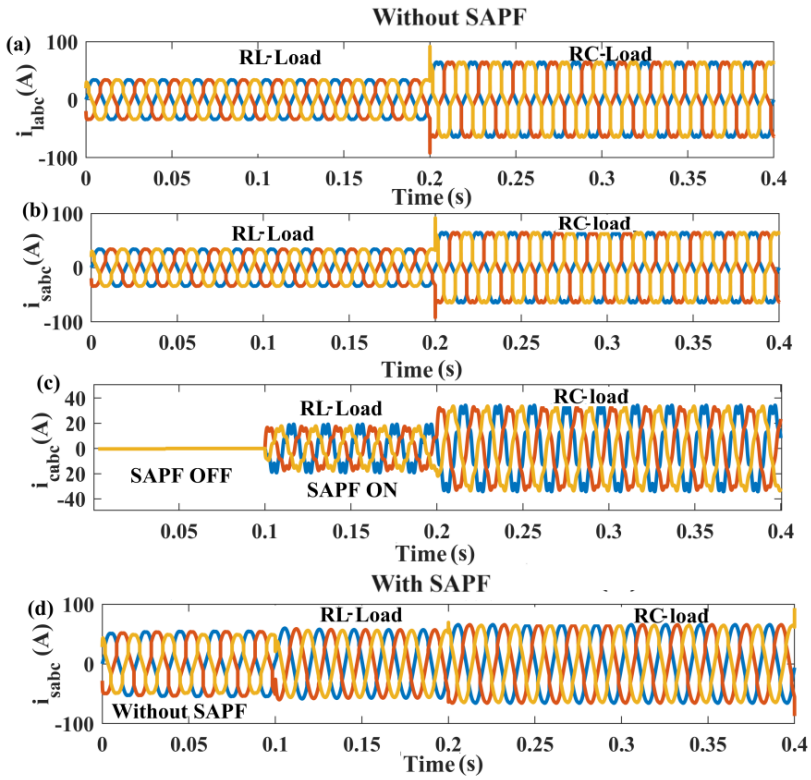

Figure 4.9 Profiles obtained under different loading conditions (considering R_1 =45 Ω , L_1 = 5 mH , R_2=18 Ω , and C=1μF) (a) i_{labc} under RL- and RC-load, (b) i_{sabc} before compensation (c) i_{cabc} considering with and without SAPF, and (d) i_{sabc} considering with and without SAPF (**Case study 2**)

desired amount of i_{cabc} (see Figure 4.9(c) and Figure 4.10(c)) is injected into the system

to maintain the source current sinusoidal as shown in Figures 4.9(d) and 4.10(d). It is concluded from the above-deduced results that the performance of the proposed controller-based SAPF is immune to the changes in load parameters.

4.3.4 Performance Analysis Pertaining to Scenario 4

It is observed from the results obtained from the series of simulations that the combination of the NFPLL-MSRF-FIED-AFHCC technique gives the best result for harmonics reduction in comparison to other control approaches. As reviewed from the literature, the V_{dc} regulation is very significant during SAPF operation, as it may cause overshoot and undershoot in the V_{dc} waveform. Due to this, harmonics in i_{sabc} profile will increase. As presented in Chapter 3, the proposed FIED control technique regulates the I_{dc} in such a

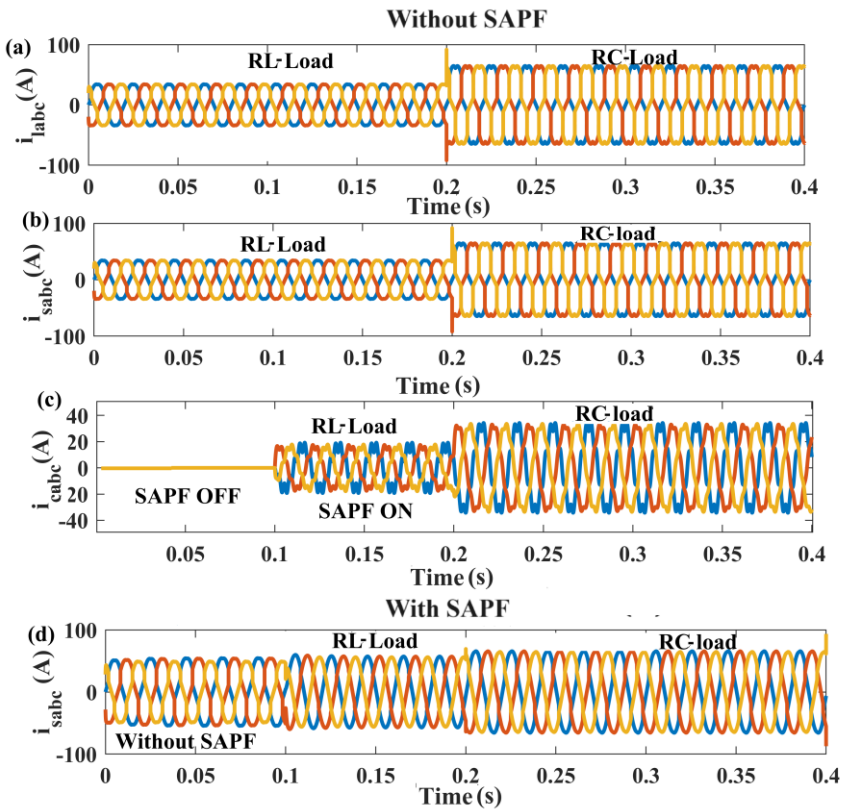

Figure 4.10 Profiles obtained under different loading conditions (considering R_1=90 Ω, L_1=5 mH , R_2= 36 Ω, and C=1μF) (a) i_{labc} considering RL and RC load, (b) i_{sabc} before compensation (c) i_{cabc} considering with and without SAPF, and (d) i_{sabc} considering with and without SAPF (**Case study 2**)

way that V_{dc} deviation is less than that of conventional controllers. Moreover, it diminishes the ripple in the V_{dc} to an acceptable level, which reduces the harmonics present in the i_{sabc}. However, to verify the superiority of the projected approach under the steady-state and load-changing conditions, a comparative performance analysis with that of other studied controllers is presented in this scenario.

(a) V_{dc} *profile under steady-state conditions*

Figures 4.11(a)-(c) show the ripple in V_{dc} waveforms obtained considering different controller-based SAPFs. To analyse the accuracy under steady-state condition, a performance indicator called as percentage of accuracy (% ACC) is used as presented in equation (2.42) of Section 2.54 of Chapter 2. It is evident from Figures 4.11(a)-(c) and from Table 4.4 that the maximum deviations of 11V and 10V in V_{dc} waveform are

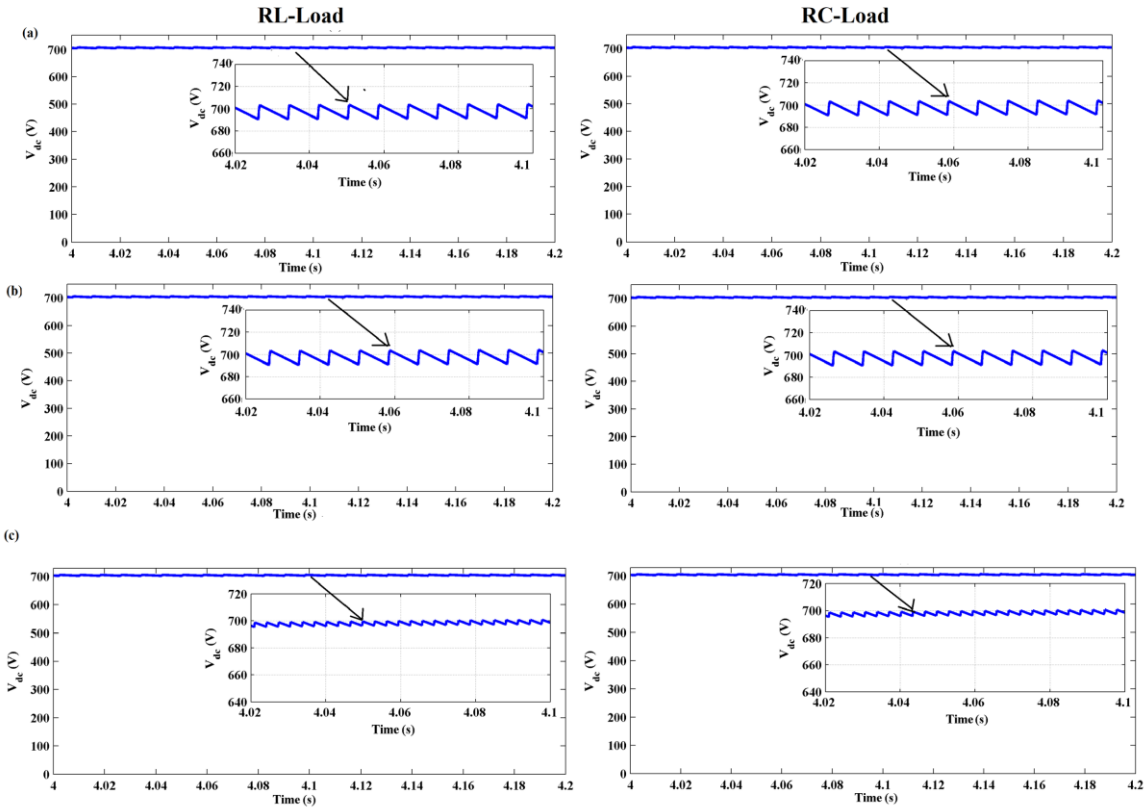

Figure 4.11 V_{dc} profiles obtained considering RL-and RC-type nonlinear loads under different controller-based SAPF (a) NFPLL-MSRF-PI-AFHCC scheme, (b) NFPLL-MSRF-FLC-AFHCC scheme, and (c) NFPLL-MSRF-FIED-AFHCC (**Scenario 4**)

observed under the studied NFPLL-MSRF-PI-AFHCC technique for RL- and RC-load type nonlinear loads, respectively. Also, the %ACC of 98.51% and 98.58% are found for RL- and RC-load types, respectively. While the same is further reduced to 6V and 5V for RL- and RC-load types, respectively, employing the NFPLL-MSRF-FLC-AFHCC approach and the %ACC improved to 99.14% and 99.28% for RL- and RC-load types, respectively. However, under steady-state condition, the maximum deviation from the nominal value in the V_{dc} waveform is further reduced to 4V and 3V for RL- and RC-type nonlinear loads, respectively, using the proposed NFPLL-MSRF-FIED-AFHCC approach and with further improvement observed in %ACC as 99.42% and 99.57 % for RL- and RC-type nonlinear loads, respectively.

(b) V_{dc} *profile under load-changing conditions*

In this case, the performance of the proposed NFPLL-MSRF-FIED-AFHCC-based combined strategy is compared with that of studied traditional methods in regulating V_{dc} profile and reducing its settling time (t_s) during load-changing conditions. Under load-changing conditions, the performance of the studied controller is evaluated in terms of the overshoot (O_s), undershoot (U_s), and settling time (t_s). Two dynamic load situations are considered in this study (i) switching the nonlinear load from RC- to RL-type and (ii) from RL- type to RC-type. Figures 4.12(a)-(b) show the effect of each of the control schemes in regulating V_{dc} under the considered load scenarios, i.e., switching of RC-load to RL-load and vice-versa. Firstly, the simulation model is run with a RC-load and the steady-state condition is obtained. It is revealed from Figure 4.12(a) that the V_{dc} waveform remains steady up to $t = 0.2$ s. At $t = 0.2$ s, when the load is switched from RC- to RL-type, V_{dc} deviates from its reference value (i.e., 700 V). It is also observed from the Figure 4.12(a) that the NFPLL-MSRF-PI-AFHCC control technique do not offer better performance and results in O_s of 14 V (i.e., 2% deviation from the reference value) with t_s of 0.1 s.

In case of NFPLL-MSRF-FLC-AHCC technique, the V_{dc} deviation still exists but O_s decreases to 12V (i.e., deviates 1.71 % from the reference value) and t_s reduces to 0.07 s. In the NFPLL-MSRF-FLC-AFHCC technique, the O_s further reduces to 6V (i.e., 0.85 % deviation from the reference value) with a reduced t_s of 0.05s. However, among all the studied schemes, the proposed NFPLL-MSRF-FIED-AFHCC topology performs exceptionally well offering the minimum V_{dc} deviation of 3V (i.e., a deviation of 0.42 %)

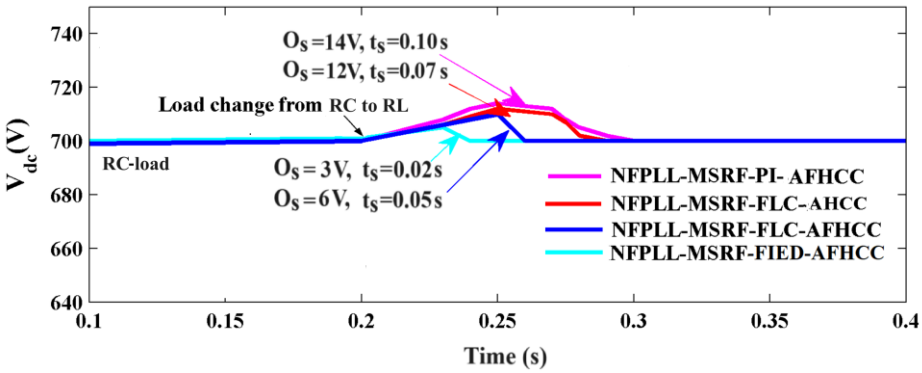

(a)

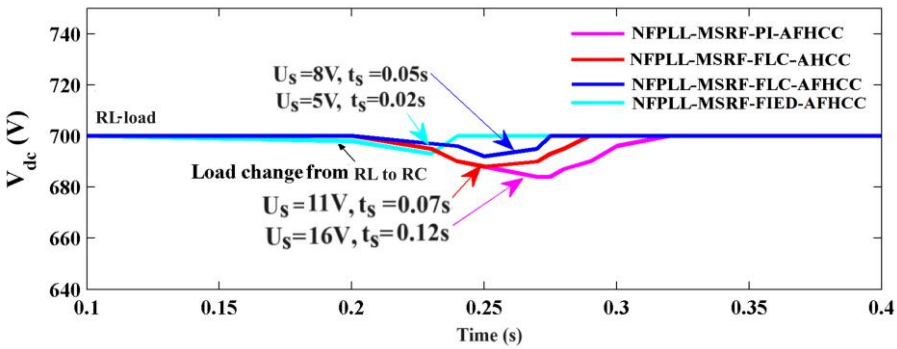

(b)

Figure 4.12 Comparative profiles of V_{dc} obtained using NFPLL-MSRF-PI-AHCC, NFPLL-MSRF-FLC-AHCC, NFPLL-MSRF-FLC-AFHCC and NFPLL-MSRF-FIED-AFHCC methods under load-changing conditions (a) from RC-to RL-type and (b) from RL- to RC-type (**Scenario 4**)

Table 4.4: Comparison of V_{dc} deviation under steady-state condition

Studied Control approach	Voltage deviation (in V)		(% ACC)	
	RL-Load	RC-Load	RL-Load	RC-Load
NFPLL-MSRF-PI-AFHCC	11	10	98.51%	98.58%
NFPLL-MSRF-FLC-AFHCC	6	5	99.14%	99.28%
NFPLL-MSRF-FIED-AFHCC	**4**	**3**	**99.42%**	**99.57%**

and the quickest t_s of 0.02 s. When the load is changed from RL- to RC-type, as revealed in Figure 4.12(b), the V_{dc} again deviates from its reference value (i.e., 700 V). It is observed from Figure 4.12(b) that the projected technique again offers the best outcome with the minimum undershoot U_s of 4V (i.e., a deviation of 0.57 %) and the fastest t_s of 0.02 s. In contrast to this, the NFPLL-MSRF-PI-AHCC controller offers an U_s of 16V (i.e., 2.21 % deviation from the reference value) and t_s of 0.12 s. The NEPLL-MSRF-FLC-AHCC, even though it is better than the PI controller, but has still an U_s of 11 V (i.e., 1.57 % deviation from the reference value) and t_s of 0.07 s. The NFPLL-MSRF-FLC-AFHCC technique has an U_s of 8V (i.e., deviation of 1.11 % from the reference value) and t_s of 0.05s with respect to the proposed one. Table 4.5 shows the detailed comparison of the performance of the proposed and the other studied controllers in terms of regulating V_{dc} and its t_s.

Table 4.5: V_{dc} deviation and t_s comparison under load-changing conditions

Studied control approach	Load change from			
	RC- to RL-type		RL- to RC-type	
	O_s (V)	t_s (s)	U_s (V)	t_s (s)
NFPLL-MSRF-PI-AFHCC	14 (2.00%)	0.10	16 (2.21%)	0.12
NFPLL-MSRF-FLC-AHCC	12 (2.71%)	0.07	11 (1.57%)	0.07
NFPLL-MSRF-FLC-AFHCC	6 (0.85%)	0.05	8 (1.11%)	0.05
NFPLL-MSRF-FIED-AFHCC	**3 (0.42%)**	**0.02**	**4 (0.57%)**	**0.02**

Further, performance of the proposed control strategy (i.e., NEPLL-MSRF-FLC-AHCC) in terms of specific parameters and operating conditions considered are compared with that of other reported works [153,166, 167, 192] and is presented in comparative format in Table 4.6. The table reveals that the proposed NEPLL-MSRF-FIED-AHCC approach is found better in terms of THD and mitigation of deviation in V_{dc} profile in comparison to the proposed MSRF-FIED-AFHCC strategy studied in Chapter 3 and other control combinations mentioned in literature [166, 167, 192].

Table 4.6 Comparative illustration of the proposed control topology-based SAPF with that of other reported works

Description	Control strategy					
	NFPLL-MSRF-FIED-AFHCC [Proposed]	**MSRF-FIED-AFHCC [Proposed]**	**DPC-PI-AHCC [167]**	**MSRF-FLC-AFHCC [192]**	**IPLL-FLC-HCC [166]**	**PQ-PI-HCC [153]**
Core Technique	NEPLL-MSRF with FIED and AFHCC	MSRF with FIED and AFHCC	Deadbeat-based direct power control and PI controller with anti-windup compensator	Advanced PLL with FLC and AFHCC	Improved PLL with FLC and HCC technique	Hardware-in-the-Loop Implementation with P-Q, PI and HCC technique
Performance Metrics	(i) THD-0.53% (RL-load) and 0.46% (RC-load) (ii) V_{dc} deviation – 0.42% undershoot and 0.57% overshoot under load changing condition	(i) THD-1.08% (RL-load) and 1.05% (RC-load) (ii) V_{dc} deviation – 0.71% undershoot and 0.85% overshoot under load changing condition	(i) THD- 1.68% (ii) V_{dc} deviation – 3% undershoot and 5% overshoot under load changing condition	(i) THD- 1.27% (ii) V_{dc} deviation – NA	(i) THD 2.46% (ii) V_{dc} deviation– NA	(i) THD- 2.01% (ii) V_{dc} deviation -4.5% undershoot
Operating scenario	Ideal and non-ideal source conditions with load changing conditions considering RL- and RC-type non-linear loads.	Ideal and non-ideal source conditions with load changing conditions considering RL- and RC-type non-linear loads.	Ideal and non-ideal source conditions with load changing conditions considering RL- and RC-type non-linear loads..	Ideal source condition with RL-type non-linear loads.	Ideal source condition with RL-type nonlinear load under balanced and un-balanced conditions.	Ideal source condition with balanced RL-type nonlinear load.
Key Advantages	High adaptive performance both under steady-state and dynamic conditions.	Better performance and robust against disturbances.	Simplified control with good stability.	Good performance with adaptive capabilities.	Improved harmonic compensation with additional features.	Simplified control with good stability
Novelty Aspect	Introduces a new PLL approach with negative feedback concept –based RCG for enhanced performance of SAPF.	Introduces a new dc-link voltage control concept – based SAPF for minimizing V_{dc} deviation.	Direct Power Controller (DPC)-based RCG with other traditional approaches for dc-link voltage control and PWM signal generation.	Improved approach for PWM signal generation with traditional fuzzy logic.	Improved PLL-based RCG and other standard approach with traditional fuzzy logic.	Conventional approach with PI control

4.4 SUMMARY

The harmonic mitigation in a standalone MG system is studied in this chapter under the action of the proposed NFPLL-MSRF-based realized SAPF. Apart from this, the best combination among the techniques used for RCG, V_{dc} regulation, and generation of switching pulses for VSI has been found and compared. It is observed from the results obtained from the series of simulation-based experiments that the proposed NEPLL-MSRF-FIED-AFHCC control technique performs exceptionally well in mitigating the harmonics and curbing the deviation and settling time in V_{dc} profile in comparison to other counterparts under load-changing conditions. The comparative numerical results infer that the proposed technique reduces the source current harmonics to a level of 0.32% and 0.28% under RL- and RC-type nonlinear loads, respectively. It is observed that the proposed NEPLL-MSRF-FIED-AFHCC technique has made a further reduction in THD of source current with respect to the studied NFPLL-MSRF-FLC-AFHCC, which is (i) 42.85%, and 41.66%, in case of RL- and RC-type nonlinear loads, respectively, under ideal source condition and (ii) 29.37%, and 20.68%, in case of RL- and RC-type nonlinear loads, respectively, under non-ideal source condition. Thus, the proposed control topology has offered the best results in terms of harmonics mitigation. It is also inferred from the results obtained that the proposed scheme has performed best in curbing the deviation and settling time in V_{dc} profile compared to other counterparts under load-changing conditions. The proposed NFPLL-MSRF-FIED-AFHCC technique has offered the minimum V_{dc} deviation of 4V and the quickest response time of 0.02 s, when switching the load from RC- to RL-type. Likewise, the minimum deviation of 3V and the fastest response time of 0.02 s is obtained during the switching of the load from RL- to RC-type. It is revealed from the above simulation-based tests that the proposed NFPLL-MSRF-FIED-AFHCC control technique performs extraordinarily well under both steady-state and load-changing conditions. Hence, the performance of this control method is tested in OPAL-RT 4510 real-time digital simulator platforms for further validation in the next chapter.

Chapter 5

REAL-TIME IMPLEMENTATION OF THE NOVEL NFPLL-MSRF-FIED-AFHCC-BASED SAPF USING OPAL-RT 4510 DIGITAL SIMULATOR

5.1 INTRODUCTION

In the previous chapter, the performance of the projected NFPLL-MSRF-FIED-AFHCC-based controller is examined in detail through a series of simulation-based experiments. It is concluded from the various results presented in Chapter 4 that the proposed NFPLL-MSRF-FIED-AFHCC-based control strategy is the most suitable compared to other studied controller configurations in mitigating harmonics present in the source current even when the source voltage is distorted. Moreover, the controller also works effectively in different load-changing conditions. Therefore, in this chapter, the performance of the proposed NFPLL-MSRF-FIED-AFHCC-based shunt active power filter (SAPF) is validated using a real-time digital simulator (OPAL-RT 4510).

5.1.1 Motivation of the Present Chapter

The rapid progress of computing technologies has propelled the advancement of simulation tools over the past thirty years. With the decreasing cost and increasing performance of computer technologies, simulation tools have progressively enhanced their ability to solve intricate issues quickly. Furthermore, the price of digital simulators has consistently declined, rendering them accessible to a broader range of users and for a more extensive array of purposes. The real-time digital simulator (RTDS) has the potential to execute complex Simulink® models and simultaneously support any input/output capabilities. The primary distinguishing feature of this system is its capacity to efficiently distribute the workload among several central processing units (CPUs), including multiple simulators connected by real-time communication links. The RTDS is realized using OPAL-RT technology for the purpose of real-time and distributed simulation applications. The platform is fully compatible with fixed-step solvers of SimPowerSystems toolbox in Simulink, allowing real-time operation on a personal computer (PC) Cluster. The MATLAB/Simulink application serves as the front-end platform for modifying and presenting block diagram along visual models. The above functionality of OPAL-RT motivated us to test our simulation results with this real-time simulation platform. A comprehensive simulation with MATLAB has been conducted, and the outcomes yielded confirm the excellent performance of the proposed NFPLL-

MSRF-FIED-AFHCC-based SAPF. The reported results, obtained through the use of a real-time digital simulator, provide precise and up-to-date evidence to validate the practicality of the proposed control techniques and controllers.

5.1.2 Contribution of the Present Chapter

In this chapter, the function and benefits of using simulation real-time, along with its working principles, are presented. A detail on the employed RT-Lab simulator is briefly explained. Also, a comparative study of MATLAB-based simulation and real-time simulator-based results of the proposed model is carried out.

The following are the main findings of the current work.

a) The performance of the proposed NFPLL-MSRF-FIED-AFHCC controller-based SAPF has been deeply analyzed under different source and load-changing conditions using MATLAB simulation.
b) To prove the effectiveness of the proposed approach, a comparative performance analysis is carried out between the MATLAB simulation and real-time model employing the OPAL-RT 4510 digital simulator under both steady-state and loading-changing conditions.

5.1.3 Chapter Orientation

The rest of this chapter is structured as follows. Section 5.2 presents RT-LAB, its working principles, and the configuration details of OPAL-RT 4510. Section 5.3 presents the simulation results of NFPLL-MSRF-FIED-AFHCC-based SAPF and their corresponding real-time results as different studied scenarios. Finally, the research findings of the present chapter are summarized in Section 5.4.

5.2 ARCHITETURE OF RT-LAB SIMULATOR

The potential of computing technology has significantly improved in recent years, and its use has expanded along with continuous price reductions. Researchers and engineers can now utilize the low-cost and efficient simulation technologies that used to be exclusively

available to large manufacturers and organizations in the past [194]. Given the above, the RT-Lab simulator is one of the presently available low-cost and efficient solutions. It has been designed to address the constraints of conventional real-time simulators and fulfill the transient modeling requirements of electromechanical drives and electric systems [195]. In real-time simulation, the model is solved at regular intervals using fixed-step solvers from the start of the simulation until its end. The interval's size is referred to as the step size. The time step in a real-time system is defined as a preset duration of time (for example, step size = 10 s, or 5 ms). The CPU must read input signals from sensors, do all necessary computations, and write all the required outputs, including control actuators, in the given time interval [196].

5.2.1 Graphical Interface and Block Diagram

In order to execute Simulink in real-time on a PC cluster with efficient fixed-step solvers, the present real-time electric simulator is tuned for the RT-LAB networked real-time simulation platform. It uses the standard MATLAB/Simulink front-end to edit and display visual models using block diagrams [197]. The block diagram model is the source from which code may be automatically generated, altered, and sent to target processors for real-time or distributed simulation.

5.2.2 Inputs and Outputs (I/O)

Interfacing with real-world hardware components, such as controllers or physical plants, is a need for real-time applications. Inputs and outputs (I/O) interfaces are organized using convention blocks that are provided as a Simulink toolbox in the RT-LAB real-time simulator. To avoid low-level driver programming, the engineer only has to link the I/O to the blocks by dragging and dropping them into the visual model. I/O drivers and model code are automatically developed by RT-LAB and directed to drive the model's data flow onto the actual I/O card [198].

5.2.3 Simulator Configuration

Figure 5.1 shows the OPAL-RT 4510 system-based complete setup. It consists of digital simulator (OPAL-RT 4510), master PC, host PC, digital storage oscilloscope (DSO), and a connector. The master PC controls communication between all target PCs as well as between hosts and targets. One host is in complete control of the simulator, whereas the rest are only able to receive and show signals from the real-time simulator in read-only mode. This simulator consists of different types of I/O devices such as timers, encoders, analog and digital in and out, etc [199].

5.2.4 Working of RT-LAB

With RT-LAB's real-time workshop, Simulink models can be seamlessly transformed into real-time applications that can be run in real time on several target computers equipped with multi-core PC processors. The Simulink models are made on a host PC and deployed using the OPAL-RT program [200, 201]. The studied SAPF model with the proposed control strategy (i.e., NFPLL-MSRF-FIED-AFHCC) is first developed on a MATLAB/Simulink (2018b) platform directly via RT-LAB already integrated with MATLAB.

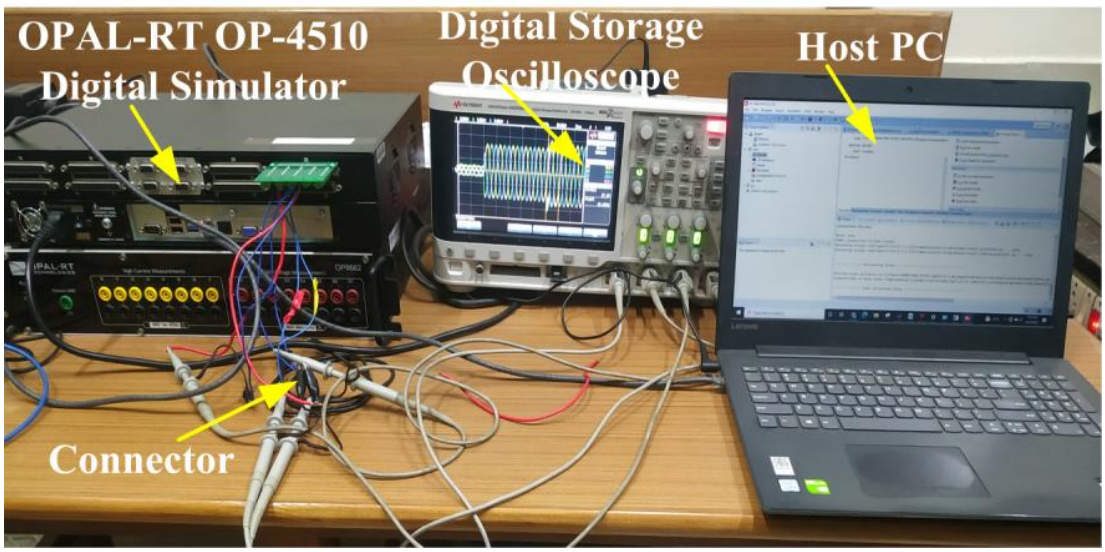

Figure 5.1 RT-LAB simulator model

5.3 RESULTS AND DISCUSSIONS

It is revealed from Chapter 4 that the proposed NFPLL-MSRF-FIED-AFHCC control technique performs extraordinarily under both steady-state and load-changing conditions in comparison to other studied controllers. Therefore, in this chapter, the above-mentioned proposed control approach is finally adopted for real-time validation. This chapter investigates the performance of NFPLL-MSRF-FIED-AFHCC-based realized SAPF both in MATLAB/simulation and OPAL-RT 4510 digital simulator platforms. Firstly, a simulation-based experiment is performed without considering SAPF in the adopted MG structure and, thereafter, with SAPF employing the proposed NFPLL-MSRF-FIED-AFHCC control technique in the presence of different sources (both ideal and non-ideal types) and nonlinear load-changing conditions. Correspondingly, the real-time experiment is also performed employing OPAL-RT 4510 digital simulator for the validation of the simulation-based results obtained considering the same operating scenario. In this study, the nonlinear loads (i.e., RL- and RC-type) used are the same as those of Chapter 4. The model of nonlinear loads used is illustrated in Figure 4.1 of Chapter 4, and its various parameters are tabulated in Table 2.6 of Chapter 2. Firstly, the MG model is simulated considering both MATLAB simulation and OPAL-RT 4510 real-time digital simulator platforms in the presence of the nonlinear RL- and RC-loads without connecting the SAPF. Thereafter, its performance is evaluated with SAPF using the proposed control technique under different source conditions referred to as different scenarios.

(a) Scenario 1: Performance analysis under ideal source condition.
(b) Scenario 2: Performance analysis under non-ideal source condition
(c) Scenario 3: Dc-link voltage regulation under ideal and non-ideal source conditions.

5.3.1 Performance Analysis Pertaining to Scenario 1

In this scenario, the performance SAPF is examined employing the proposed NFPLL-MSRF-FIED-AFHCC control approach under ideal source condition. Firstly, a simulation-based experiment is performed without considering SAPF. Thereafter, to mitigate the THD of the source current SAPF with the proposed control technique, a

suitable amount of compensating current (i_{cabc}) is injected at the PCC. Figure 5.2(a)-(d) shows the profiles of different waveforms (i.e., of source current before and after compensation (i_{sabc}), source voltages (V_{sabc}) and the compensating current) obtained considering the ideal source condition using MATLAB simulation platform. Figure 5.2(a) shows the 3-phase source voltage profile (V_{sabc}) before compensation under RL-type nonlinear load, which is maintained till t = 0.2s. From t = 0.2s to 0.4s, the RL-load is changed to nonlinear RC-load. Similarly, Figure 5.2(b) shows the profile of i_{sabc} waveform before compensation (t = 0 s to 0.2 s in the presence of RL-load and from t =

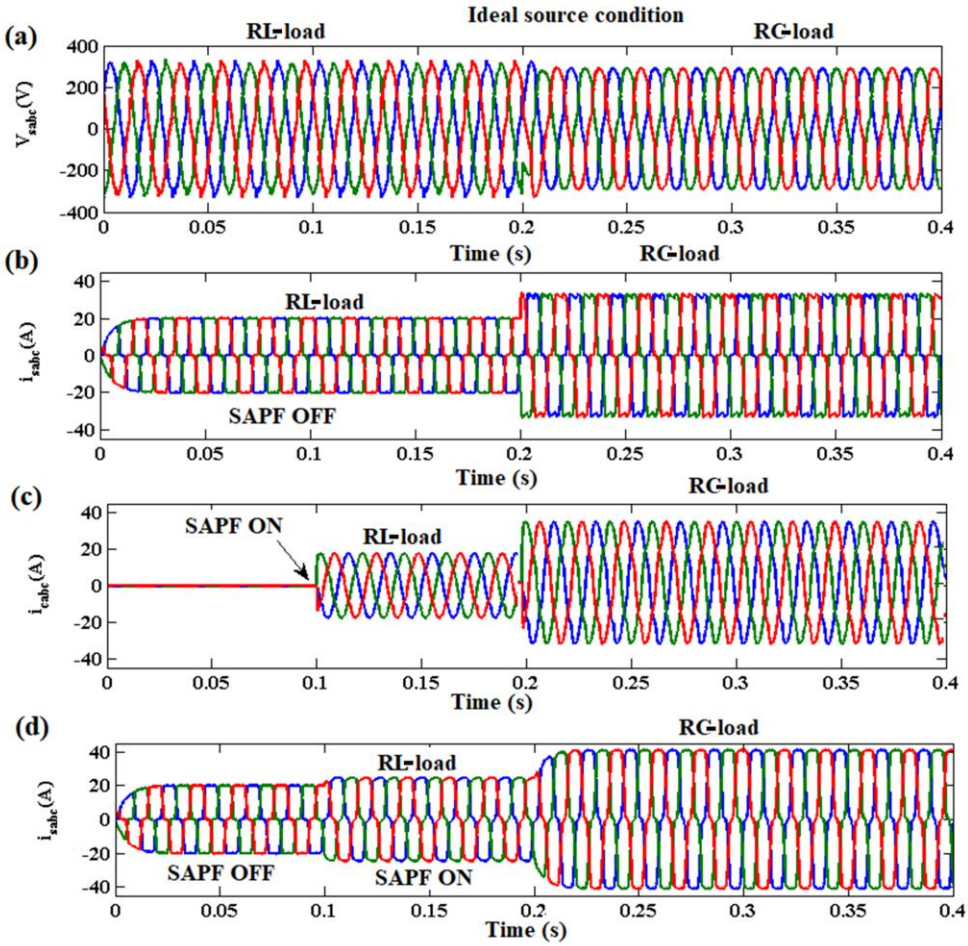

Figure 5.2 Profiles obtained under load-changing (i.e., RL- to RC-type) and ideal source conditions (a) V_{sabc} before compensation, (b) i_{sabc} before compensation, (c) i_{cabc} generated using the proposed NFPLL-MSRF-FIED-AFHCC-based SAPF, and (d) i_{sabc} after compensation (**Scenario 1**)

0.2s to 0.4s for RC-load). It is revealed from Figure 5.2(b) that i_{sabc} is highly distorted due to the presence of nonlinear load. However, when the SAPF using the proposed NEPLL-MSRF-FIED-AFHCC-based control approach is turned on for t =0.1s to 0.4s (as shown in Figure 5.2(c)), the i_{cabc} waveforms generated under both the load types (considering one at a time) is able to mitigate the harmonics from the i_{sabc} profile. The i_{sabc} waveform after compensation is presented in Figure 5.2(d). It is viewed from Figure 5.2(d) that the i_{sabc} waveform seems to be pure sinusoidal during t =0.1s to 0.4s, whereas it appears distorted during t = 0s to 0.1s as the SAPF was in turn-off condition till t =0.1s. In the similar manner, the SAPF performance is tested using the OPAL-RT 4510 digital simulator. Since, it can perform parallel computation in real-time, the outcomes obtained are analogous to those of hardware. Figure. 5.1 shows the OPAL-RT 4510 system-based

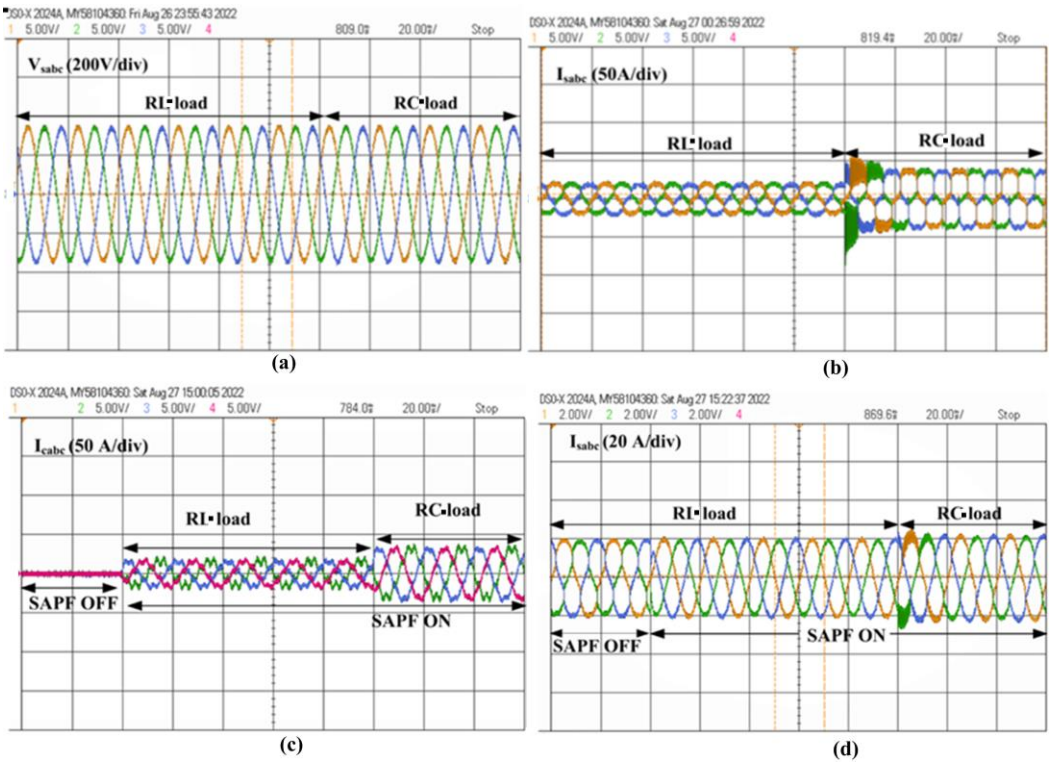

Figure 5.3 Various profiles obtained using OPAL-RT 4510 under load-changing (i.e., RL- to RC-type) and ideal source conditions (a) V_{sabc} before compensation, (b) i_{sabc} before compensation, (c) i_{cabc} using the proposed NFPLL-MSRF-FIED-AFHCC-based SAPF, and (d) i_{sabc} after compensation (**Scenario 1**)

complete experimental setup. Figures 5.3(a)-(d) show the profiles of different waveforms obtained considering the ideal source using OPAL-RT 4510-based digital simulator technique. Figure 5.3(a) showcase the waveform of V_{sabc} before compensation. Similarly, in Figure 5.3(b), the i_{sabc} waveform before compensation are displayed. However, when the SAPF using the proposed NFPLL-MSRF-FIED-AFHCC-based approach is turned-on (refer Figure 5.3(c)), the generated profiles of i_{cabc} are able to mitigate the harmonics and make the i_{sabc} waveforms (obtained under both the load types) pure sinusoidal. The i_{sabc} waveform after compensation is presented in Figure 5.3(d). It is viewed from Figure

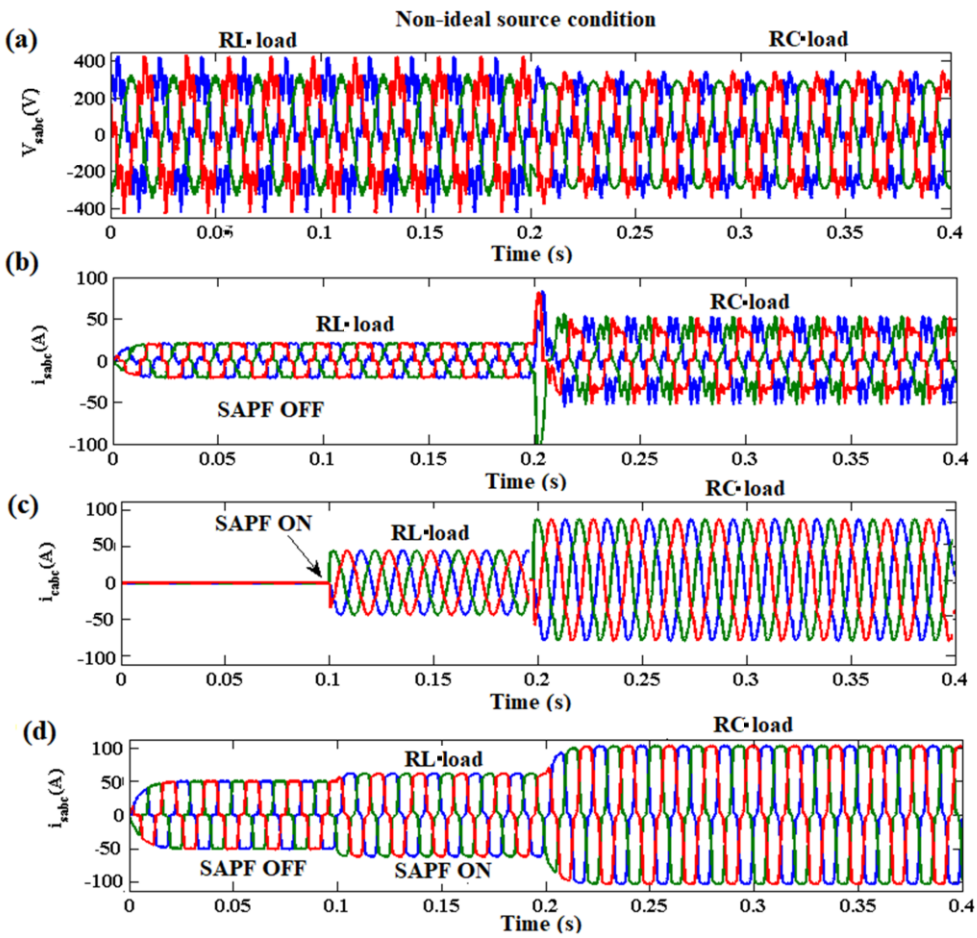

Figure 5.4 Various profiles obtained under load-changing (i.e., RL to RC) and non-ideal source conditions (a) V_{sabc} before compensation, (b) i_{sabc} before compensation, (c) i_{cabc} generated using the proposed NFPLL-MSRF-FIED-AFHCC-based SAPF, and (d) i_{sabc} after compensation (**Scenario 2**)

5.3(d) that the when the SAPF is off during t = 0s to 0.1s, the i_{sabc} waveform is highly distorted, whereas, it is purely sinusoidal during t =0.1s to 0.2s (with RL-load) and t = 0.2s to 0.4s (with RC-load) due to the injection of suitable amount of i_{cabc} by the SAPF in turned-on state.

5.3.2 Performance Analysis Pertaining to Scenario 2

In this scenario, the performance of SAPF is examined by employing the proposed NFPLL-MSRF-FIED-AFHCC control approach under non-ideal source conditions. Figures 5.4(a)-(d) display the profiles of different waveforms obtained considering the non-ideal source using MATLAB-based simulation. Figure 5.4(a) shows the V_{sabc} profile

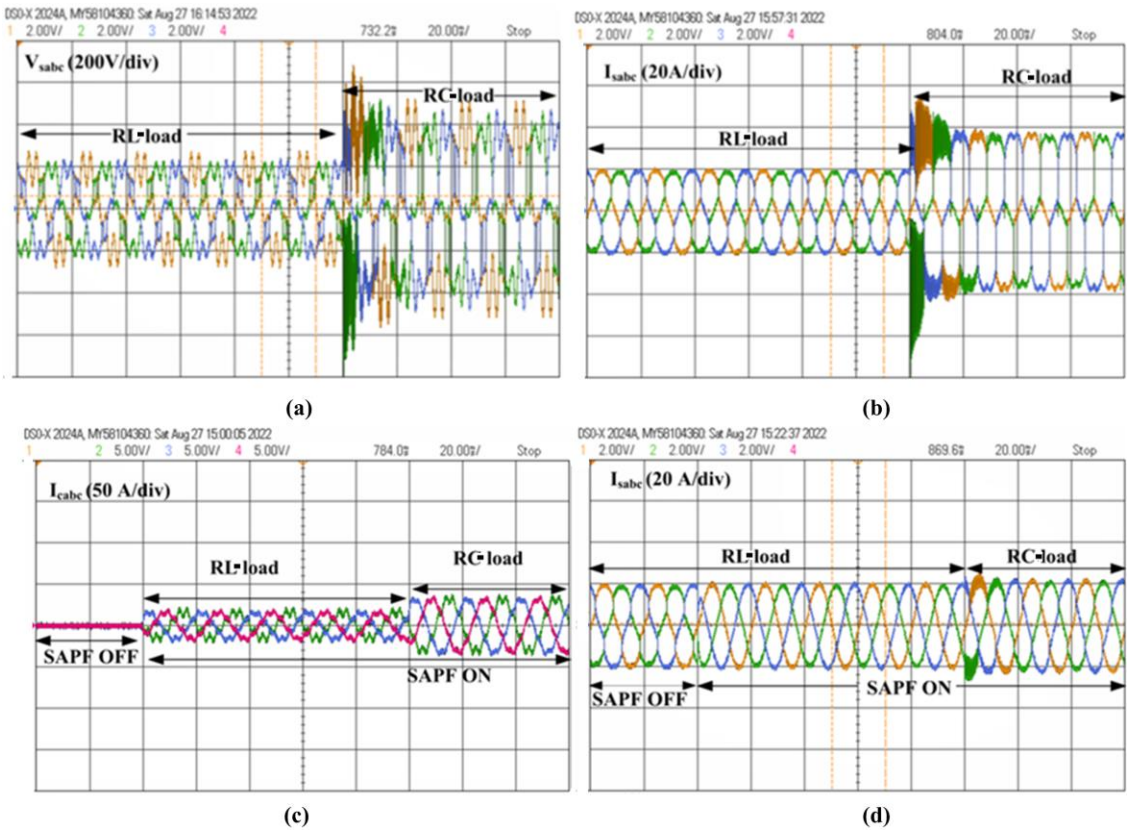

Figure 5.5 Profiles obtained using OPAL-RT 4510 under load-changing (i.e., RL to RC) and non-ideal source conditions (a) V_{sabc} before compensation, (b) i_{sabc} before compensation, (c) i_{cabc} generated using proposed NFPLL-MSRF-FIED-AFHCC-based SAPF, and (d) i_{sabc} after compensation (**Scenario 2**)

before compensation having RL type nonlinear load maintained till t = 0.2s, which is changed to RC type from t = 0.2s onwards up till t = 0.4s. Similarly, Figure 5.4(b) showcases the before compensation profile of the i_{sabc} waveform during t = 0s to 0.2s with RL-load on and during t = 0.2s to 0.4s with RC-load on. It is revealed from Figure 5.4(b) that i_{sabc} is highly distorted due to nonlinear load in the absence of SAPF. However, when the SAPF employing the proposed NEPLL-MSRF-FIED-AFHCC-based control approach is turned on from t = 0.1s to 0.4s (as shown in Figure 5.4(c), the i_{cabc} waveform for both the load types is able to mitigate the harmonics and make the i_{sabc} waveform pure sinusoidal. The i_{sabc} waveform post-compensation is presented in Figure

5.4(d). It is viewed from Figure 5.2(d) that the i_{sabc} waveform is distorted during time interval t =0s to 0.1s due to SAPF being in off-state. It appears to be pure sinusoidal from t =0.1s to 0.4s, when the SAPF is turn on at t = 0.1s. In a similar manner, the SAPF's performance is tested using the OPAL-RT 4510 real-time digital simulator under a non-ideal source case. Figures 5.5(a)-(d) demonstrate the profiles of different waveforms obtained using the OPAL-RT 4510-based digital simulator. Figure 5.5(a) shows the V_{sabc} waveform before compensation. Similarly, in Figure 5.5(b) showcases the i_{sabc} waveform before compensation. However, when the SAPF using the proposed NFPLL-MSRF-

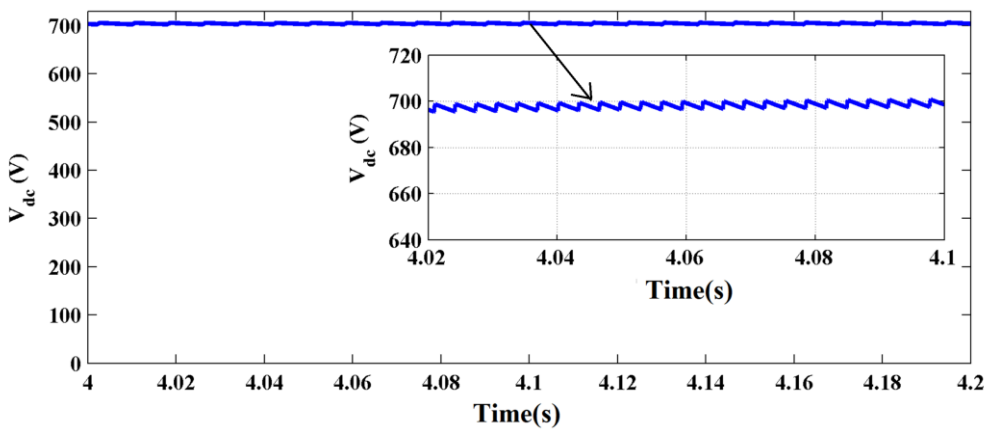

(a)

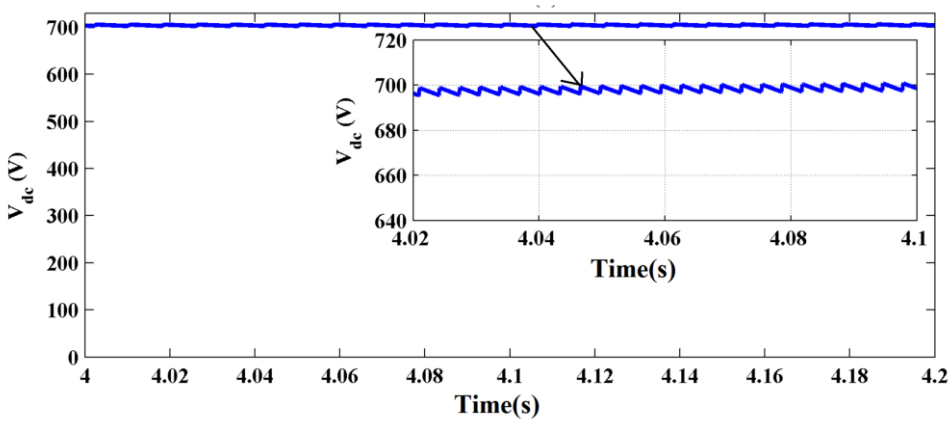

(b)

Figure 5.6 MATLAB simulation-based V_{dc} profiles obtained under ideal source condition employing proposed controller-based SAPF for (a) RL-load (b) RC-load (**Scenario 3**)

FIED-AFHCC-based approach is turned on (refer Figure 5.5(c)), the generated profiles of i_{cabc} are able to mitigate the harmonics present in the i_{sabc} waveform. The i_{sabc} waveform after compensation is presented in Figure 5.5(d). It is viewed from Figure 5.5(d) that when SAPF is in off state during t =0s to 0.1s, the waveform of i_{sabc} is highly distorted, whereas, it is observed to be purely sinusoidal during t =0.1s to 0.2s (with RL-load) and t =0.2s to 0.4s (with RC-load) due to the injection of suitable amount of i_{cabc} by the SAPF in a turned-on state.

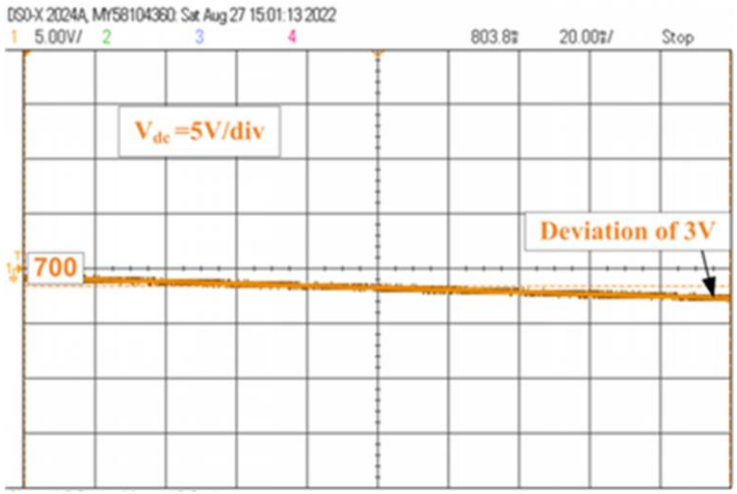

(a)

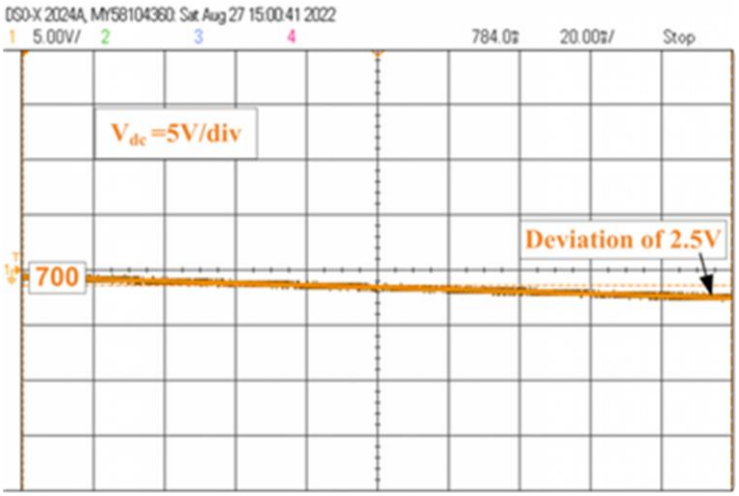

(b)

Figure 5.7 OPAL-RT simulator-based V_{dc} profiles obtained under ideal source condition employing the proposed NFPLL-MSRF-FIED-AFHCC-based SAPF for (a) RL-load (b) RC-load (**Scenario 3**)

5.3.3 Performance Analysis Pertaining to Scenario 3

The findings obtained through the series of simulations indicate that the suggested NFPLL-MSRF-FIED-AFHCC approach gives the best result in mitigating harmonics caused by ideal and non-ideal source conditions and nonlinear loads. However, to verify

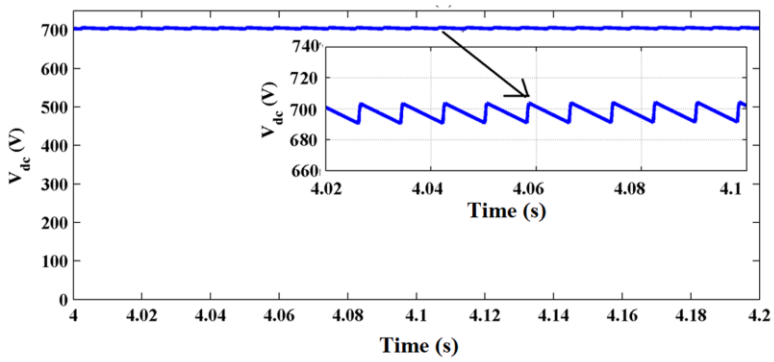

(a)

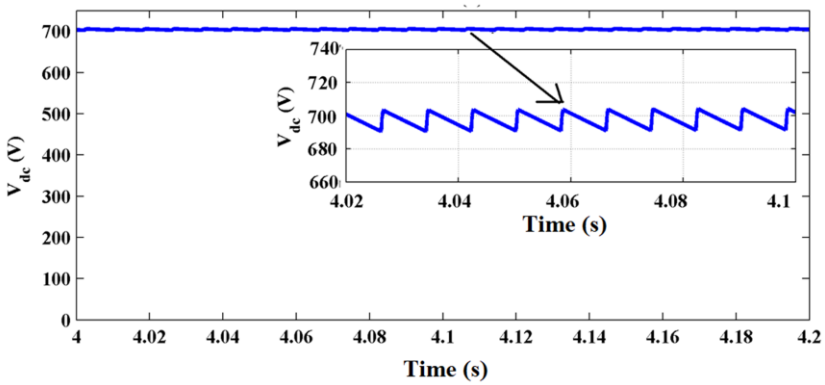

(b)

Figure 5.8 MATLAB simulation-based V_{dc} profiles obtained under non-ideal source condition employing the proposed NFPLL-MSRF-FIED-AFHCC-based SAPF for (a) RL-load (b) RC-load (**Scenario 3**)

the superiority of the projected approach in regulating V_{dc} profile under both ideal and non-ideal source conditions employing a real-time simulation environment, a comparative performance analysis of its results with that of MATLAB simulation-based obtained results is also presented in this scenario.

(a) V_{dc} *regulation during ideal source condition*

Figures 5.6(a) and (b) show the ripple in V_{dc} waveforms obtained from MATLAB-based simulations of the proposed controller-based SAPF in the presence of RL- and RC-type nonlinear loads, respectively. It is evident from the figures that in the presence of the proposed NFPLL-MSRF-FIED-AFHCC approach, the deviations from the nominal value in the V_{dc} waveform are found as 3V for RL-load and 2.5V for RC-load under steady-state conditions. In the case of real-time OPAL-RT simulator-based obtained results

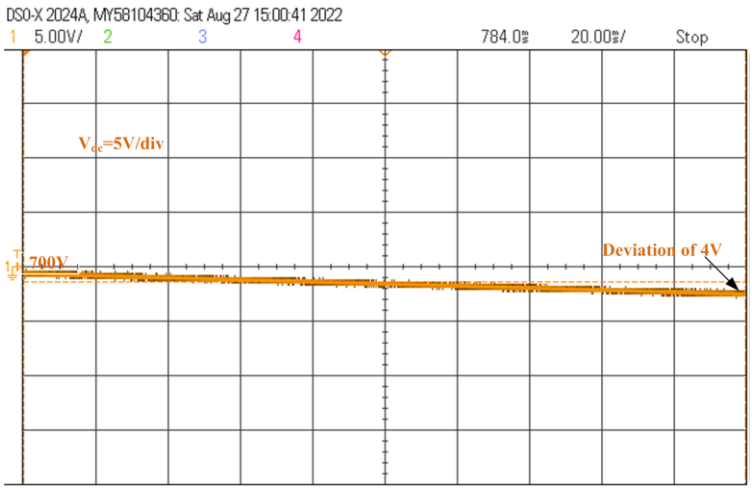

(a)

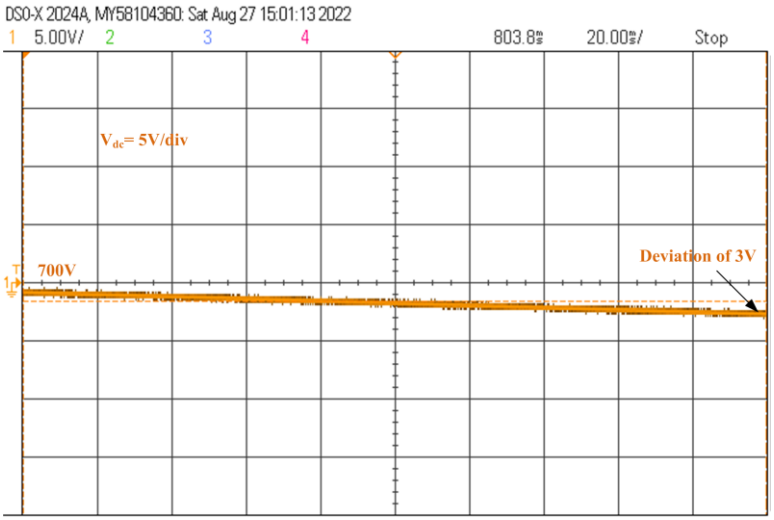

(b)

Figure 5.9 OPAL-RT simulator-based V_{dc} profiles obtained under non-ideal source condition employing the proposed NFPLL-MSRF-FIED-AFHCC-based SAPF for (a) RL-load (b) RC-load (**Scenario 3**)

(shown in Figures 5.7 (a) and (b)), the V_{dc} deviation is also found to be nearly similar to

that of simulation-based outcomes, i.e., 3V and 2.5V for RL- and RC-type nonlinear loads, respectively.

(b) V_{dc} *regulation during non-ideal source*

In this case, the performance of the proposed NFPLL-MSRF-FIED-AFHCC-based SAPF is tested under non-ideal source conditions. Figures 5.8(a) and (b) show the ripple in V_{dc} waveforms obtained using MATLAB-based simulation in the presence of RL- and RC-type nonlinear loads, respectively. It is observed from the figures that the deviations in the V_{dc} waveform from the nominal value appeared to be 4V for RL-load and 3V for RC-type nonlinear load under steady-state conditions. In the case of real-time OPAL-RT digital simulator-based obtained results (shown in Figures 5.9 (a) and (b)), the V_{dc} deviation is also observed to be the same as that of MATLAB-based results, i.e., 4V and 3V for RL- and RC-type nonlinear loads, respectively. Thus, real-time simulator validates the results of the simulation model.

5.4 SUMMARY

In this chapter, the simulation-based performance of the proposed NFPLL-MSRF-FIED-AFHCC-based SAPF is validated using OPAL-RT 4510 digital simulator platform considering both ideal and non-ideal source and nonlinear load-changing conditions. In the proposed control approach, the NFPLL-MSRF method, FIED scheme, and the AFHCC technique are utilized for the reference current generation, dc-link voltage regulation, and switching pulses generation for the voltage source inverter, respectively. The analysis carried out reveals that using the proposed NFPLL-MSRF-FIED-AFHCC-based SAPF, the simulation-based results, in terms of mitigation of harmonics and V_{dc} regulations, are successfully validated using the OPAL-RT 4510 digital simulator.

Chapter 6

CONCLUSION AND FUTURE WORK

6.1 CONCLUSION

This dissertation provides a thorough analysis of the use of a shunt active power filter (SAPF) to improve power quality (PQ) in a standalone microgrid (MG) system. The study was conducted utilizing a variety of previously investigated and proposed controllers. The studied MG system comprises of solar photovoltaic (SPV), wind energy system (WES), and fuel cell (FC)-based distributed generators. The sources for PQ distortions in the distribution system have been identified from the different literature, and their effects on the system's performance have been successfully analyzed. PQ improvement in a MG system connected with nonlinear load is a challenging issue nowadays. Among the various PQ issues, harmonics compensation and regulation of dc-link voltage (V_{dc}) are considered the foremost objective of this thesis. It has been discussed in great detail that most literature advocates the wide use of SAPF to mitigate harmonics present in the system. The SAPF primarily works under the harmonious action of the three different control loops used for reference current generation (RCG), V_{dc} control, and the generation of switching pulses for the associated voltage source inverter. An exhaustive literature survey has been carried out highlighting various propositions made by researchers worldwide regarding these control loops. The reported methods have their own advantages and limitations. However, there is still a huge opportunity left to either come up with an improved version of the existing methods or propose a new approach. Therefore, the main objective of the present dissertation is to explore strategies to improve the performance of the main control loops to enhance the performance of the SAPF in mitigating harmonics and reducing the deviation in V_{dc} profile.

The major outcomes of the thesis are summarized below in chapter wise:

Chapter 2 of this dissertation presents the design of the studied standalone MG system, which consists of SPV, WES, and FC-based generating units and is implemented in MATLAB/Simulink software. Further, modeling of the SAPF based on conventional synchronous reference frame (SRF) and modified synchronous reference frame (MSRF) techniques for the RCG, proportional-integral (PI) controller, and fuzzy logic controller (FLC) (considering one at a time) for V_{dc} regulation and hysteresis current controller

(HCC) method for switching pulse generation is carried out to study its performance in mitigating harmonics in the studied MG system. The simulation results illustrate the effectiveness of the studied MSRF-FLC-HCC control algorithm over the other adopted control schemes in mitigating the harmonics present in the source current and for regulation of V_{dc} waveform. The result demonstrates that the 3-phase source current (i_{sabc}) is almost sinusoidal, with a very low total harmonic distortion (THD) content of 3.22% and 3.12% observed in the presence of RL- and RC-type nonlinear loads, respectively.

In Chapter 3, a novel fuzzy inverted error deviation (FIED) method is proposed for the V_{dc} control loop to improve the performance of the SAPF. Thereafter, a comparative study of different control techniques i.e., MSRF for RCG, FLC and the proposed FIED control for V_{dc} (considering one at a time), and the adaptive HCC (AHCC) and adaptive fuzzy HCC (AFHCC) for switching pulse generation (considering one at a time) are demonstrated. Further, mainly THD (as the PQ issue) in the i_{sabc} waveform is analyzed under ideal and non-ideal source conditions in the presence of nonlinear load models adopted in Chapter 2. Moreover, the efficacy of the proposed controller is also verified in regulating V_{dc} profile and reduction of its settling time under load-changing conditions. Apart from this, the best combination among the methods used for the RCG, regulation of V_{dc}, and generation of switching pulse for the inverter is evaluated and compared. According to the findings of a number of simulation-based experiments, the suggested MSRF-FIED-AFHCC scheme performs exceptionally well in curbing the deviation and settling time in V_{dc} profile compared to other counterparts under load-changing conditions. It is viewed from the profile of i_{sabc} that the waveform is nearly sinusoidal, offering very low THD values of 1.08% (for RL-load) and 1.05% (for RC-load) obtained under the combined action of the proposed MSRF-FIED-AFHCC technique. The result reveals that the proposed MSRF-FIED-AFHCC technique performs exceptionally well under load-changing conditions (i.e., changing the load from RC- to RL-type). The proposed methods result in a minimum V_{dc} deviation of 5V and the quickest response time

of 0.02 s. Likewise, in case of a change of nonlinear load from RL- to RC-type, the proposed approach has again offered the best outcome with a minimum undershoot of 6V and the fastest response time of 0.03 s. Hence, it is concluded that the proposed MSRF-FIED-AFHCC combination provides improved harmonic mitigation performance with minimum THD under all operating scenarios lying within the limit as prescribed by the IEEE-519 standard.

Related to the RCG signal of SAPF, a novel negative feedback phase-locked loop-based MSRF (NFPLL-MSRF) technique has been proposed in Chapter 4 to overcome the drawbacks of the existing MSRF approach. Besides, the FLC and FIED (considering one at a time) approaches are adopted to regulate the V_{dc} profile and the AFHCC is used for switching pulse generation. Different combinations of controllers thus formed like NFPLL-MSRF-FLC-AFHCC and NFPLL-MSRF-FIED-AFHCC are proposed. Both combinations effectively reduce THD in the source current to make the SAPF adaptable to all diverse conditions. However, the comparative numerical results infer that amongst the two and other studied topologies of Chapter 3, the proposed NEPLL-MSRF-FIED-AFHCC scheme offers the best performance in reducing the source current harmonics, which is reduced to 0.32% and 0.28% under RL- and RC-type nonlinear loads considering ideal source condition, respectively. During non-ideal source conditions, it is reduced to 0.75% and 0.58% for RL- and RC-type loads, respectively. It is also observed that employing the proposed approach, the deviation in V_{dc} profile is found to be the minimum under steady-state conditions, which is 4V for RL-load and 3V for RL-type nonlinear loads. Similarly, the proposed NFPLL-MSRF-FIED-AFHCC topology performs exceptionally well under load-changing conditions (from RC- to RL-type) by offering the minimum V_{dc} deviation of 3V and the quickest response time of 0.02 s. Likewise, in the case of changing the load type from RL- to RC- type, the proposed technique again presents the best outcome with minimum undershoot of 4V and the fastest response time of 0.02 s. It is revealed from the above-mentioned simulation-based results that the proposed NFPLL-MSRF-FIED-AFHCC control technique outperforms over other counterparts under source and load-changing conditions. Further, in Chapter 5, the proposed NFPLL-MSRF-FIED-AFHCC control technique has been adopted to

validate its performance using a real-time digital simulator (OPAL-RT 4510). In this chapter, the simulation-based performance of the proposed NFPLL-MSRF-FIED-AFHCC-based SAPF is validated using the OPAL-RT 4510 real-time digital simulator platform considering both ideal and non-ideal source and nonlinear load-changing conditions. The OPAL-RT 4510 simulator successfully validates the simulated performance of the proposed NFPLL-MSRF-FIED-AFHCC-based realized SAPF in mitigating the source current harmonics and regulating the V_{dc} profile.

6.2 FUTURE WORK

This dissertation presents an attempt to examine and enhance the PQ level of a SAPF-assisted studied standalone MG system based on several studied and the proposed controllers. The main objective is to reduce the harmonics in the source current and keep the dc-link voltage constant. The research outcomes of this work resulted in some promising concepts and viable remedies; however, further scope of investigation may be carried. The various paths in which the presented work can be extended are listed below:

- The objective of this research is to raise the PQ level by lowering source current harmonics and maintaining a constant dc-link voltage. Many applications need managing voltage and current-related problems at the same time (since they are related). Thus, in addition to suppressing harmonics and controlling the dc-link voltage, it may also be explored to combine the effects of series and shunt active filters to handle other PQ concerns, such as voltage swell/sag, reactive power compensation, etc.
- The current study has focused on the utilization of the proposed NEPLL-MSRF-based synchronization method for the generation of reference currents. The use of other advanced PLL-based synchronization approach may be explored to further enhance the PQ level.
- In order to keep the dc-link voltage constant, a detailed performance analysis based on a PI controller, FLC technique, and the proposed FIED approach has been carried out. Further, an advanced controller based on the Neuro-Fuzzy approach may be tested to enhance the PQ level.

REFERENCES

[1] Mahmoud, M. S., Saif Ur Rahman, M., and AL-Sunni, F. M. Review of microgrid architectures-a system of systems perspective. *IET Renewable Power Generation*, *9*(8), pp.1064-1078, 2015.

[2] Khalid, M. Smart grids and renewable energy systems: Perspectives and grid integration challenges. *Energy Strategy Reviews*, *51*, pp. 101299, 2024.

[3] Panwar, N.L., Kaushik, S.C. and Kothari, S. Role of renewable energy sources in environmental protection: A review. *Renewable and sustainable energy reviews*, *15*(3), pp.1513-1524, 2011.

[4] Unamuno, E. and Barrena, J.A., Hybrid ac/dc microgrids-Part II: Review and classification of control strategies. *Renewable and Sustainable Energy Reviews*, *52*, pp.1123-1134, 2015.

[5] Basu, A.K., Chowdhury, S.P., Chowdhury, S. and Paul, S. Microgrids: Energy management by strategic deployment of DERs-A comprehensive survey. *Renewable and Sustainable Energy Reviews*, *15*(9), pp.4348-4356, 2011.

[6] Fazal, S., Haque, M.E., Arif, M.T., Gargoom, A. and Oo, A.M.T. Grid integration impacts and control strategies for renewable based microgrid. *Sustainable Energy Technologies and Assessments*, *56*, pp.103069, 2023.

[7] Shyni, R. and Kowsalya, M. HESS-based microgrid control techniques empowered by artificial intelligence: A systematic review of grid-connected and standalone systems. *Journal of Energy Storage*, *84*, pp.111012, 2024.

[8] Li, D., Wang, T., Pan, W., Ding, X. and Gong, J. A comprehensive review of improving power quality using active power filters. *Electric Power Systems Research*, *199*, pp.107389, 2021.

[9] Khetarpal, P. and Tripathi, M.M. A critical and comprehensive review on power quality disturbance detection and classification. *Sustainable Computing: Informatics and Systems*, *28*, pp.100417, 2020.

[10] Sahoo, B., Alhaider, M.M. and Rout, P.K. Power quality and stability improvement of microgrid through shunt active filter control application: An overview. *Renewable Energy Focus*, *44*, pp.139-173, 2023.

[11] Tronchin, L., Manfren, M. and Nastasi, B. Energy efficiency, demand side management and energy storage technologies-A critical analysis of possible paths of integration in the built environment. *Renewable and Sustainable Energy Reviews*, *95*, pp.341-353, 2018.

[12] Dixit, S., Singh, P., Ogale, J., Bansal, P. and Sawle, Y. Energy Management in Microgrids with Renewable Energy Sources and Demand Response. *Computers and Electrical Engineering*, *110*, pp.108848, 2023.

[13] Kumaravel, S. and Ashok, S. Optimal power management controller for a stand-alone solar PV/wind/battery hybrid energy system. *Energy Sources, Part A: Recovery, Utilization, and Environmental Effects*, *37*(4), pp.407-415, 2015.

[14] Bruni, G., Cordiner, S., Mulone, V., Sinisi, V. and Spagnolo, F. Energy management in a domestic microgrid by means of model predictive controllers. *Energy*, *108*, pp.119-131, 2016.

[15] Roslan, M.F., Hannan, M.A., Ker, P.J. and Uddin, M.N. Microgrid control methods toward achieving sustainable energy management. *Applied Energy*, *240*, pp.583-607, 2019.

[16] Basnet, S., Deschinkel, K., Le Moyne, L. and Péra, M.C. A review on recent standalone and grid integrated hybrid renewable energy systems: System optimization and energy management strategies. *Renewable Energy Focus*, *46*, pp.103-125, 2023.

[17] Dixit, S., Singh, P., Ogale, J., Bansal, P. and Sawle, Y. Energy Management in Microgrids with Renewable Energy Sources and Demand Response. *Computers and Electrical Engineering*, *110*, pp.108848, 2023.

[18] Vakili-Nezhaad, G., Mishra, S.B., Mousa, H. and Ziaiefar, H. Simulation and optimization of hybrid green energy systems for desalination purposes. *Environmental Progress & Sustainable Energy*, *40*(2), pp. e13515, 2021.

[19] Mirzaeva, G. and Miller, D., DC and AC microgrids for standalone applications. *IEEE Transactions on Industry Applications, 59*(6), pp.7908 - 7918, 2023.

[20] Subramanian, V., Vairavasundaram, I. and Aljafari, B. Analysis of optimal load management using a stand-alone hybrid AC/DC microgrid system. *International Transactions on Electrical Energy Systems*. *2023*(1), pp.7519436, 2023.

[21] Khan, F.A., Pal, N. and Saeed, S.H. Review of solar photovoltaic and wind hybrid energy systems for sizing strategies optimization techniques and cost analysis methodologies. *Renewable and Sustainable Energy Reviews*, *92*, pp.937-947, 2018.

[22] Kiehbadroudinezhad, M., Rajabipour, A., Cada, M. and Khanali, M. Modeling, design, and optimization of a cost-effective and reliable hybrid renewable energy system integrated with desalination using the division algorithm. *International Journal of Energy Research*, *45*(1), pp.429-452, 2021.

[23] Olatomiwa, L., Mekhilef, S., Ismail, M.S. and Moghavvemi, M. Energy management strategies in hybrid renewable energy systems: A review. *Renewable and Sustainable Energy Reviews*, *62*, pp.821-835, 2016.

[24] Ansari, M.S., Jalil, M.F. and Bansal, R.C. A review of optimization techniques for hybrid renewable energy systems. *International Journal of Modelling and Simulation*, *43*(5), pp.722-735, 2023.

[25] Karimi, H. and Jadid, S. A strategy-based coalition formation model for hybrid wind/PV/FC/MT/DG/battery multi-microgrid systems considering demand response programs. *International Journal of Electrical Power & Energy Systems*, *136*, pp.107642, 2022.

[26] Sedighizadeh, M., Esmaili, M., Jamshidi, A. and Ghaderi, M.H. Stochastic multi-objective economic-environmental energy and reserve scheduling of microgrids considering battery energy storage system. *International Journal of Electrical Power & Energy Systems*, *106*, pp.1-16, 2019.

[27] Fakhar, A., Haidar, A.M., Abdullah, M.O. and Das, N. Smart grid mechanism for green energy management: a comprehensive review. *International Journal of Green Energy*, *20*(3), pp.284-308, 2023.

[28] Zhang, Y., Sun, Q., Zhou, J., Li, L., Wang, P. and Guerrero, J.M. Coordinated control of networked AC/DC microgrids with adaptive virtual inertia and governor-gain for stability enhancement. *IEEE Transactions on Energy Conversion*, *36*(1), pp.95-110, 2020.

[29] Wang, Y., Rousis, A.O. and Strbac, G. On microgrids and resilience: A comprehensive review on modeling and operational strategies. *Renewable and Sustainable Energy Reviews*, *134*, pp.110313, 2020.

[30] Meera, P.S. and Hemamalini, S. Reliability assessment and enhancement of distribution networks integrated with renewable distributed generators: A review. *Sustainable Energy Technologies and Assessments*, *54*, pp.102812, 2022.

[31] D'silva, S., Shadmand, M., Bayhan, S. and Abu-Rub, H. Towards grid of microgrids: Seamless transition between grid-connected and islanded modes of operation. *IEEE Open Journal of the Industrial Electronics Society*, *1*, pp.66-81, 2020.

[32] Pfeifer, A., Dobravec, V., Pavlinek, L., Krajačić, G. and Duić, N. Integration of renewable energy and demand response technologies in interconnected energy systems. *Energy*, *161*, pp.447-455, 2018.

[33] Tavakoli, A., Saha, S., Arif, M.T., Haque, M.E., Mendis, N. and Oo, A.M. Impacts of grid integration of solar PV and electric vehicle on grid stability, power quality and energy economics: A review. *IET Energy Systems Integration*, *2*(3), pp.243-260, 2020.

[34] Singh, S., Verma, R.K., Shakya, A.K. and Pratap Singh, S. Frequency regulation of micro-grid connected hybrid power system with SMES. *Technology and Economics of Smart Grids and Sustainable Energy*, *2*, pp.1-13, 2017.

[35] Boscaino, V., Ditta, V., Marsala, G., Panzavecchia, N., Tine, G., Cosentino, V., Cataliotti, A. and Di Cara, D. Grid-connected photovoltaic inverters: Grid codes, topologies and control techniques. *Renewable and Sustainable Energy Reviews*, *189*, pp.113903, 2024.

[36] Chandak, S. and Rout, P.K. Seamless transition of microgrid between islanded and grid-connected mode of operation. *IET Energy Systems Integration*, *3*(1), pp.60-72, 2021

[37] Al-Shetwi, A.Q., Hannan, M.A., Jern, K.P., Mansur, M. and Mahlia, T.M.I. Grid-connected renewable energy sources: Review of the recent integration requirements and control methods. *Journal of Cleaner Production*, *253*, pp.119831, 2020.

[38] Zhang, H., Xiang, W., Lin, W. and Wen, J. Grid forming converters in renewable energy sources dominated power grid: Control strategy, stability, application, and challenges. *Journal of Modern Power Systems and Clean Energy*, *9*(6), pp.1239-1256, 2021.

[39] Kondaiah, V.Y., Saravanan, B., Sanjeevikumar, P. and Khan, B. A review on short-term load forecasting models for micro-grid application. *The Journal of Engineering*, *2022*(7), pp.665-689, 2022.

[40] Nawaz, A., Zhou, M., Wu, J. and Long, C. A. comprehensive review on energy management, demand response, and coordination schemes utilization in multi-microgrids network. *Applied Energy*, *323*, pp.119596, 2022.

[41] Choudhury, S. Review of energy storage system technologies integration to microgrid: Types, control strategies, issues, and future prospects. *Journal of Energy Storage*, *48*, p.103966, 2022.

[42] Zidar, M., Georgilakis, P.S., Hatziargyriou, N.D., Capuder, T. and Škrlec, D. Review of energy storage allocation in power distribution networks: applications, methods and future research. *IET Generation, Transmission & Distribution*, *10*(3), pp.645-652, 2016.

[43] Götz-Köhler, M., Banik, U., Meddeb, H., Neugebohrn, N., Berends, D., Gehrke, K., Vehse, M. and Agert, C. Switchable photovoltaic window for on-demand shading and electricity generation. *Solar Energy*, *232*, pp.433-443, 2022.

[44] Sampaio, P.G.V. and González, M.O.A. Photovoltaic solar energy: Conceptual framework. *Renewable and Sustainable Energy Reviews*, *74*, pp.590-601, 2017.

[45] Ding, K., Bian, X., Liu, H. and Peng, T. A MATLAB-Simulink-based PV module model and its application under conditions of nonuniform irradiance. *IEEE Transactions on Energy Conversion*, *27*(4), pp.864-872, 2012.

[46] Koondhar, M.A., Laghari, I.A., Asfaw, B.M., Kumar, R.R. and Lenin, A.H. Experimental and simulation-based comparative analysis of different parameters of PV module. *Scientific African*, *16*, pp.01197, 2022.

[47] Baba, A.O., Liu, G. and Chen, X., Classification and evaluation review of maximum power point tracking methods. *Sustainable Futures*, *2*, pp.100020, 2020.

[48] Senapati, M.K., Pradhan, C. and Calay, R.K. A computational intelligence based maximum power point tracking for photovoltaic power generation system with small-signal analysis. *Optimal Control Applications and Methods*, *44*(2), pp.617-636, 2023.

[49] Femia, N., Petrone, G., Spagnuolo, G. and Vitelli, M. Optimization of perturb and observe maximum power point tracking method. *IEEE Transactions on Power Electronics*, *20*(4), pp.963-973, 2005.

[50] Yang, Y. and Wen, H. Adaptive perturb and observe maximum power point tracking with current predictive and decoupled power control for grid-connected photovoltaic inverters. *Journal of Modern Power Systems and Clean Energy*, *7*(2), pp.422-432, 2019.

[51] Balachandran, K. and Ramasamy, K. Maximum power point tracking based on self-adaptive neural network combined with incremental conductance. *Energy Sources, Part A: Recovery, Utilization, and Environmental Effects*, *44*(3), pp.7895-7913, 2022.

[52] Bakar Siddique, M.A., Asad, A., Asif, R.M., Rehman, A.U., Sadiq, M.T. and Ullah, I. Implementation of incremental conductance MPPT algorithm with integral regulator by using boost converter in grid-connected PV array. *IETE Journal of Research*, *69*(6), pp.3822-3835. 2023.

[53] Zhang, F., Maddy, J., Premier, G. and Guwy, A. Novel current sensing photovoltaic maximum power point tracking based on sliding mode control strategy. *Solar Energy*, *118*, pp.80-86, 2015.

[54] Bakhshi, R. and Sadeh, J. Voltage positive feedback based active method for islanding detection of photovoltaic system with string inverter using sliding mode controller. *Solar Energy*, *137*, pp.564-577, 2016.

[55] Ullah, K., Ishaq, M., Tchier, F., Ahmad, H. and Ahmad, Z. Fuzzy-based maximum power point tracking (MPPT) control system for photovoltaic power generation system. *Results in Engineering*, *20*, p.101466, 2023.

[56] Kaur, S., Kaur, T. and Khanna, R. Adaptive neuro-fuzzy inference system-based output power controller in grid-connected photovoltaic systems. *Energy Sources, Part A: Recovery, Utilization, and Environmental Effects*, pp.1-24, 2021.

[57] Kanagaraj, N., An enhanced maximum power point tracking method for thermoelectric generator using adaptive neuro-fuzzy inference system. *Journal of Electrical Engineering & Technology*, *16*(3), pp.1207-1218, 2021.

[58] Mohamed, S.A. and Abd El Sattar, M. A comparative study of P&O and INC maximum power point tracking techniques for grid-connected PV systems. *SN Applied Sciences*, *1*(2), pp.174, 2019.

[59] Raj, A. and Praveen, R.P. Highly efficient DC-DC boost converter implemented with improved MPPT algorithm for utility level photovoltaic applications. *Ain Shams Engineering Journal*, *13*(3), pp.101617, 2022.

[60] Jalilyan, S., Abbasi, V., Ahmadian, S., Varmenjeh, A.R. and Moghadam, F.Y. High Step-Up Three-Port DC–DC Converter with Few Limitations in Performance Suitable for Stand-Alone Renewable Energy Applications. *IEEE Transactions on Industrial Electronics*, *71*(10), pp. 12389 – 12401, 2024.

[61] Padmanaban, M., Chinnathambi, S., Parthasarathy, P. and Pachaivannan, N. An improved BAS MPPT algorithm in DC–DC converter for grid connected SPVS with PQ enhancement. *Sādhanā*, *48*(3), pp.126, 2023.

[62] Li, J., Wang, G., Li, Z., Yang, S., Chong, W.T. and Xiang, X. A review on development of offshore wind energy conversion system. *International Journal of Energy Research*, *44*(12), pp.9283-9297, 2020.

[63] Ackermann, T.; Söder, L. Wind energy technology and current status: a review. *Renewable and Sustainable Energy Reviews*, 4 (4), pp.315-374, 2000.

[64] Rajamohan, S., Vinod, A., Aditya, M.P.V.S., Vadivudaiyanayaki, H.G., Arıcı, M., Nižetić, S., Le, T.T., Hidayat, R. and Nguyen, D.T. Approaches in performance and structural analysis of wind turbines-A review. *Sustainable Energy Technologies and Assessments*, *53*, pp.102570, 2022.

[65] Tasneem, Z., Al Noman, A., Das, S.K., Saha, D.K., Islam, M.R., Ali, M.F., Badal, M.F.R., Ahamed, M.H., Moyeen, S.I. and Alam, F. An analytical review on the evaluation of wind resource and wind turbine for urban application: Prospect and challenges. *Developments in the Built Environment*, *4*, pp.100033, 2020.

[66] Xie, S., Archer, C.L., Ghaisas, N. and Meneveau, C. Benefits of collocating vertical-axis and horizontal-axis wind turbines in large wind farms. *Wind Energy*, *20*(1), pp.45-62, 2017.

[67] Hossain, M.M. and Ali, M.H. Future research directions for the wind turbine generator system. *Renewable and Sustainable energy reviews*, *49*, pp.481-489, 2015.

[68] Karthikeyan, N., Murugavel, K.K., Kumar, S.A. and Rajakumar, S. Review of aerodynamic developments on small horizontal axis wind turbine blade. *Renewable and Sustainable Energy Reviews*, *42*, pp.801-822, 2015.

[69] Kumar, R., Raahemifar, K. and Fung, A.S. A critical review of vertical axis wind turbines for urban applications. *Renewable and Sustainable Energy Reviews*, *89*, pp.281-291, 2018.

[70] Möllerström, E., Gipe, P., Beurskens, J. and Ottermo, F. A historical review of vertical axis wind turbines rated 100 kW and above. *Renewable and Sustainable Energy Reviews*, *105*, pp.1-13, 2019.

[71] Hansen, J.T., Mahak, M. and Tzanakis, I. Numerical modelling and optimization of vertical axis wind turbine pairs: A scale up approach. *Renewable Energy*, *171*, pp.1371-1381, 2021.

[72] Paraschivoiu, I., Ammar, S. and Saeed, F. VAWT versus HAWT: a comparative performance study of 2–6 MW rated capacity turbines. *Transactions of the Canadian Society for Mechanical Engineering*, *42*(4), pp.393-403, 2018.

[73] Parker, M.A., Soraghan, C. and Giles, A. Comparison of power electronics lifetime between vertical-and horizontal-axis wind turbines. *IET Renewable Power Generation*, *10*(5), pp.679-686, 2016.

[74] Krishnan, A., Al-Obaidi, A.S.M. and Hao, L.C. A comprehensive review of innovative wind turbine airfoil and blade designs: Toward enhanced efficiency and sustainability. *Sustainable Energy Technologies and Assessments*, *60*, pp.103511, 2023.

[75] Liu, J., Lin, H. and Zhang, J. Review on the technical perspectives and commercial viability of vertical axis wind turbines. *Ocean Engineering*, *182*, pp.608-626, 2019.

[76] Ghorani, M.M., Karimi, B., Mirghavami, S.M. and Saboohi, Z. A numerical study on the feasibility of electricity production using an optimized wind delivery system (Invelox) integrated with a Horizontal axis wind turbine (HAWT). *Energy*, *268*, p.126643, 2023.

[77] Abdelateef Mostafa, M., El-Hay, E.A. and ELkholy, M.M. Recent trends in wind energy conversion system with grid integration based on soft computing methods: comprehensive review, comparisons and insights. *Archives of Computational Methods in Engineering*, *30*(3), pp.1439-1478, 2023.

[78] Quinonez-Varela, G. and Cruden, A, Modelling and validation of a squirrel cage induction generator wind turbine during connection to the local grid. *IET generation, transmission & distribution*, *2*(2), pp.301-309, 2008.

[79] Jain, A., Shankar, S. and Vanitha, V.J.J.O.G.E., 2017. Power generation using permanent magnet synchronous generator (PMSG) based variable speed wind energy conversion system (WECS): An overview. *Journal of Green Engineering*, *7*(4), pp.477-504.

[80] Yaramasu, V., Dekka, A., Durán, M.J., Kouro, S. and Wu, B. PMSG-based wind energy conversion systems: survey on power converters and controls. *IET Electric Power Applications*, *11*(6), pp.956-968, 2017.

[81] Khodabakhsh, J., Mohammadi, E. and Moschopoulos, G. PMSG-based wind energy conversion systems integration into DC microgrids with a novel compact converter. *IEEE Access*, *8*, pp.83583-83595, 2020.

[82] Cheng, M. and Zhu, Y. The state of the art of wind energy conversion systems and technologies: A review. *Energy conversion and management*, *88*, pp.332-347, 2014.

[83] Kumar, D. and Chatterjee, K. A review of conventional and advanced MPPT algorithms for wind energy systems. *Renewable and sustainable energy reviews*, *55*, pp.957-970, 2016.

[84] Kumar, D. and Chatterjee, K. A review of conventional and advanced MPPT algorithms for wind energy systems. *Renewable and sustainable energy reviews*, *55*, pp.957-970, 2016.

[85] Abdullah, M.A., Yatim, A.H.M., Tan, C.W. and Saidur, R. A review of maximum power point tracking algorithms for wind energy systems. *Renewable and sustainable energy reviews*, *16*(5), pp.3220-3227, 2012.

[86] Youssef, A.R., Mousa, H.H. and Mohamed, E.E. Development of self-adaptive P&O MPPT algorithm for wind generation systems with concentrated search area. *Renewable Energy*, *154*, pp.875-893, 2020.

[87] Rezaei, M.M. A nonlinear maximum power point tracking technique for DFIG-based wind energy conversion systems. *Engineering Science and Technology, an International Journal*, *21*(5), pp.901-908, 2018.

[88] Mousa, H.H., Youssef, A.R. and Mohamed, E.E. Variable step size P&O MPPT algorithm for optimal power extraction of multi-phase PMSG based wind generation system. *International Journal of Electrical Power & Energy Systems*, *108*, pp.218-231, 2019.

[89] Meghni, B., Saadoun, A., Dib, D. and Amirat, Y. Effective MPPT technique and robust power control of the PMSG wind turbine. *IEEJ Transactions on Electrical and Electronic Engineering*, *10*(6), pp.619-627, 2015.

[90] Kirubakaran, A., Jain, S. and Nema, R.K. A review on fuel cell technologies and power electronic interface. *Renewable and Sustainable Energy Reviews*, *13*(9), pp.2430-2440, 2009.

[91] Tariq, A.H., Kazmi, S.A.A., Hassan, M., Ali, S.M. and Anwar, M. Analysis of fuel cell integration with hybrid microgrid systems for clean energy: A comparative review. *International Journal of Hydrogen Energy*, *52*, pp.1005-1034, 2024.

[92] Nascimento, A.L., Yahyaoui, I., Fardin, J.F., Encarnação, L.F. and Tadeo, F. Modeling and experimental validation of a PEM fuel cell in steady and transient regimes using PSCAD/EMTDC software. *International Journal of Hydrogen Energy*, *45*(55), pp.30870-30881, 2020.

[93] Daud, W.R.W., Rosli, R.E., Majlan, E.H., Hamid, S.A.A., Mohamed, R. and Husaini, T. PEM fuel cell system control: A review. *Renewable Energy*, *113*, pp.620-638, 2017.

[94] Yang, B., Wang, J., Zhang, M., Shu, H., Yu, T., Zhang, X., Yao, W. and Sun, L. A state-of-the-art survey of solid oxide fuel cell parameter identification: Modelling, methodology, and perspectives. *Energy Conversion and Management*, *213*, pp.112856, 2020.

[95] Singh, M., Zappa, D. and Comini, E. Solid oxide fuel cell: Decade of progress, future perspectives and challenges. *International Journal of Hydrogen Energy*, *46*(54), pp.27643-27674, 2021.

[96] Shu, Q.Z., Xia, Z.X., Wei, W., Xu, X.L., Wang, S.L., Zhao, H. and Sun, G.Q. A novel gas diffusion layer and its application to direct methanol fuel cells. *New Carbon Materials*, *36*(2), pp.409-419, 2021.

[97] Paronen, M., Abdelhamid, M.E. and Johansson, P. The Role of Solvated Electrons in Direct Methanol Fuel Cells. *ChemElectroChem*, *10*(22), pp. e202300357, 2023.

[98] Ferriday, T.B. and Middleton, P.H. Alkaline fuel cell technology-A review. *International Journal of Hydrogen Energy*, *46*(35), pp.18489-18510, 2021.

[99] Cui, C., Li, S., Gong, J., Wei, K., Hou, X., Jiang, C., Yao, Y. and Ma, J. Review of molten carbonate-based direct carbon fuel cells. *Materials for Renewable and Sustainable Energy*, *10*, pp.1-24, 2021.

[100] Orfanidi, A., Daletou, M.K., Sygellou, L. and Neophytides, S.G. The role of phosphoric acid in the anodic electrocatalytic layer in high temperature PEM fuel cells. *Journal of Applied Electrochemistry*, *43*(11), pp.1101-1116, 2013.

[101] Samosir, A.S. and Yatim, A.H.M. Implementation of dynamic evolution control of bidirectional DC-DC converter for interfacing ultracapacitor energy storage to fuel-cell system. *IEEE Transactions on Industrial Electronics*, *57*(10), pp.3468-3473, 2010.

[102] Mungporn, P., Thounthong, P., Yodwong, B., Ekkaravarodome, C., Bilsalam, A., Pierfederici, S., Guilbert, D., Nahid-Mobarakeh, B., Bizon, N., Shah, Z. and Khomfoi, S. Modeling and control of multiphase interleaved fuel-cell boost converter based on Hamiltonian control theory for transportation applications. *IEEE Transactions on Transportation Electrification*, *6*(2), pp.519-529, 2020.

[103] Singh, B., Al-Haddad, K. and Chandra, A. A review of active filters for power quality improvement. *IEEE Transactions on Industrial Electronics*, *46*(5), pp.960-97, 1999.

[104] Bajaj, M. and Singh, A.K., Grid integrated renewable DG systems: A review of power quality challenges and state-of-the-art mitigation techniques. *International Journal of Energy Research*, *44*(1), pp.26-69, 2020.

[105] Key, T. S.; Flory, J. E.; Smith, W. M.; Statford, R. P.; Smith, J. C.; Clemmensen, J. M.; Singletary, B. The electric utility-industrial user partnership in solving power quality problems. *IEEE Transactions on Power Systems*, 5 (3), 878-886, 1990.

[106] Subjak, J.S. and Mcquilkin, J.S. Harmonics-causes, effects, measurements, and analysis: an update. *IEEE Transactions on Industry Applications*, *26*(6), pp.1034-1042, 1990.

[107] Akagi, H. New trends in active filters for power conditioning. *IEEE Transactions on Industry Applications*, *32*(6), pp.1312-1322, 1996.

[108] Ray, P. K.; Mohanty, S. R.; Kishor, N. Classification of power quality disturbances due to environmental characteristics in distributed generation system. *IEEE Transactions on Sustainable Energy*, 4(2), pp.302-313, 2013.

[109] Baier, C. R.; Espinoza, J. R.; Rivera, M.; Muñoz, J. A.; Wu, B.; Melín, P. E.; Yaramasu, V. Improving power quality in cascade multilevel converters based on single-phase non-regenerative power cells. *IEEE Transactions on Industrial Electronics*, 61(9), pp. 4498-4509, 2014.

[110] Naderi, Y., Hosseini, S.H., Zadeh, S.G., Mohammadi-Ivatloo, B., Vasquez, J.C. and Guerrero, J.M. An overview of power quality enhancement techniques applied to distributed generation in electrical distribution networks. *Renewable and Sustainable Energy Reviews*, *93*, pp.201-214, 2018.

[111] Li, D., Wang, T., Pan, W., Ding, X. and Gong, J. A comprehensive review of improving power quality using active power filters. *Electric Power Systems Research*, *199*, pp.107389, 2021.

[112] Zhou, Y., Wu, J., Li, H. and Li, Y. Analysis of nonlinear characteristics for forced oscillation affected by quadratic nonlinearity. *IEEE Transactions on Power Systems*, *37*(1), pp.804-807, 2021.

[113] Sharma, A., Rajpurohit, B.S. and Singh, S.N. A review on economics of power quality: Impact, assessment and mitigation. *Renewable and sustainable energy reviews*, *88*, pp.363-372, 2018.

[114] Poisson, O., Rioual, P. and Meunier, M. Detection and measurement of power quality disturbances using wavelet transform. *IEEE Transactions on Power Delivery*, *15*(3), pp.1039-1044, 2000.

[115] Li, D., Wang, T., Pan, W., Ding, X. and Gong, J. A comprehensive review of improving power quality using active power filters. *Electric Power Systems Research*, *199*, pp.107389, 2021.

[116] Chavez, J.J., Popov, M., López, D., Azizi, S. and Terzija, V. S-Transform based fault detection algorithm for enhancing distance protection performance. *International Journal of Electrical Power & Energy Systems*, *130*, pp.106966, 2021.

[117] Nagata, E.A., Ferreira, D.D., Bollen, M.H., Barbosa, B.H., Ribeiro, E.G., Duque, C.A. and Ribeiro, P.F. Real-time voltage sag detection and classification for power quality diagnostics. *Measurement*, *164*, pp.108097, 2020.

[118] Zhan, L. and Bollen, M.H. Characteristic of voltage dips (sags) in power systems. *IEEE Transactions on Power Delivery*, *15*(2), pp.827-832, 2000

[119] Naidoo, R. and Pillay, P. A new method of voltage sag and swell detection. *IEEE Transactions on Power Delivery*, *22*(2), pp.1056-1063, 2007.

[120] Lam, C.S., Wong, M.C. and Han, Y.D. Voltage swells and overvoltage compensation with unidirectional power flow controlled dynamic voltage restorer. *IEEE Transactions on Power Delivery*, *23*(4), pp.2513-2521, 2008.

[121] Choi, S.S., Li, J.D. and Vilathgamuwa, D.M. A generalized voltage compensation strategy for mitigating the impacts of voltage sags/swells. *IEEE Transactions on Power Delivery*, *20*(3), pp.2289-2297, 2005.

[122] Alkandari, A.M. and Soliman, S.A. Measurement of a power system nominal voltage, frequency and voltage flicker parameters. *International Journal of Electrical Power & Energy Systems*, *31*(7-8), pp.295-301, 2009

[123] Zheng, T. and Makram, E.B. Wavelet representation of voltage flicker. *Electric Power Systems Research*, *48*(2), pp.133-140, 1998.

[124] Alhasheem, M., Mattavelli, P. and Davari, P. Harmonics mitigation and non-ideal voltage compensation utilising active power filter based on predictive current control. *IET Power Electronics*, *13*(13), pp.2782-2793, 2020.

[125] Rustemli, S., Satici, M.A., Şahin, G. and van Sark, W. Investigation of harmonics analysis power system due to non-linear loads on the electrical energy quality results. *Energy Reports*, *10*, pp.4704-4732, 2023.

[126] Hu, Z., Han, Y., Zalhaf, A.S., Zhou, S., Zhao, E. and Yang, P. Harmonic sources modeling and characterization in modern power systems: A comprehensive overview. *Electric Power Systems Research*, *218*, pp.109234, 2023.

[127] Kalair, A., Abas, N., Kalair, A.R., Saleem, Z. and Khan, N. Review of harmonic analysis, modeling and mitigation techniques. *Renewable and Sustainable Energy Reviews*, *78*, pp.1152-1187, 2017.

[128] Sinvula, R., Abo-Al-Ez, K.M. and Kahn, M.T. Harmonic source detection methods: A systematic literature review. *IEEE Access*, *7*, pp.74283-74299, 2019.

[129] Subjak, J.S. and Mcquilkin, J.S. Harmonics-causes, effects, measurements, and analysis: an update. *IEEE Transactions on Industry Applications*, *26*(6), pp.1034-1042, 1990.

[130] Eroğlu, H., Cuce, E., Cuce, P.M., Gul, F. and Iskenderoğlu, A. Harmonic problems in renewable and sustainable energy systems: A comprehensive review. *Sustainable Energy Technologies and Assessments*, *48*, pp.101566, 2021.

[131] Hu, Z., Han, Y., Zalhaf, A.S., Zhou, S., Zhao, E. and Yang, P. Harmonic sources modeling and characterization in modern power systems: A comprehensive overview. *Electric Power Systems Research*, *218*, pp.109234, 2023.

[132] de Souza, L.L., Rocha, N., Fernandes, D.A., De Sousa, R.P. and Jacobina, C.B. Grid harmonic current correction based on parallel three-phase shunt active power filter. *IEEE Transactions on Power Electronics*, *37*(2), pp.1422-1434, 2021.

[133] Akagi, H. New trends in active filters for power conditioning. *IEEE Transactions on Industry Applications*, *32*(6), pp.1312-1322. 1996.

[134] Mishra, M. Power quality disturbance detection and classification using signal processing and soft computing techniques: A comprehensive review. *International Transactions on Electrical Energy Systems*, *29*(8), pp.e12008. 2019.

[135] Beres, R.N., Wang, X., Liserre, M., Blaabjerg, F. and Bak, C.L. A review of passive power filters for three-phase grid-connected voltage-source converters. *IEEE Journal of Eemerging and Selected Topics in Power Electronics*, *4*(1), pp.54-69, 2015.

[136] Melo, I.D., Pereira, J.L., Variz, A.M. and Ribeiro, P.F. Allocation and sizing of single tuned passive filters in three-phase distribution systems for power quality improvement. *Electric Power Systems Research*, *180*, pp.106128, 2020.

[137] Brand, J.R. and Schaumann, R. Active power filters: review of theory and practice. *IEE Journal on Electronic Circuits and Systems*, *2*(4), pp.89-101, 1978.

[138] Hossain, E., Tür, M.R., Padmanaban, S., Ay, S. and Khan, I. Analysis and mitigation of power quality issues in distributed generation systems using custom power devices. *IEEE Access*, *6*, pp.16816-16833, 2018.

[139] Kumar, R. and Bansal, H.O. Shunt active power filter: Current status of control techniques and its integration to renewable energy sources. *Sustainable Cities and Society*, *42*, pp.574-592, 2018.

[140] Asiminoaei, L., Blaabjerg, F., Hansen, S. and Thoegersen, P. Adaptive compensation of reactive power with shunt active power filters. *IEEE Transactions on Industry Applications*, *44*(3), pp.867-877, 2008.

[141] Umadevi, A., Lakshminarasimman, L. and Sakthivel, A. Optimal design of shunt active power filter for mitigation of inter-harmonics in grid tied photovoltaic system. *Electric Power Systems Research*, *220*, pp.109232, 2023.

[142] El Ghaly, A., Tarnini, M., Al Barakeh, Z. and Chahine, K. Compensating voltage waveform distortions using a practical topology of series active power filters. *Results in Engineering*, *22*, pp.102032, 2024.

[143] Swain, S.D., Ray, P.K. and Mohanty, K.B. Improvement of power quality using a robust hybrid series active power filter. *IEEE Transactions on Power Electronics*, *32*(5), pp.3490-3498, 2016.

[144] Srimatha, S., Mallala, B. and Upendar, J. A novel ANFIS-controlled customized UPQC device for power quality enhancement. *Journal of Electrical Systems and Information Technology*, *10*(1), pp.55, 2023.

[145] Heenkenda, A., Elsanabary, A., Seyedmahmoudian, M., Mekhilef, S., Stojcevski, A. and Ab Aziz, N.F. Unified power quality conditioners based different structural arrangements: A comprehensive review. *IEEE Access*, *11*, pp.43435-43457 2023.

[146] Swain, S.D., Ray, P.K. and Mohanty, K.B.Improvement of power quality using a robust hybrid series active power filter. *IEEE Transactions on Power Electronics*, *32*(5), pp.3490-3498, 2016.

[147] Corasaniti, V.F., Barbieri, M.B., Arnera, P.L. and Valla, M.I. Hybrid power filter to enhance power quality in a medium-voltage distribution network. *IEEE Transactions on Industrial Electronics*, *56*(8), pp.2885-2893, 2009.

[148] Melo, I.D., Pereira, J.L., Variz, A.M. and Ribeiro, P.F. Allocation and sizing of single tuned passive filters in three-phase distribution systems for power quality improvement. *Electric Power Systems Research*, *180*, pp.106128, 2020.

[149] Das, J.C. Passive filters-potentialities and limitations. *IEEE Transactions on Industry Applications*, *40*(1), pp.232-241, 2004.

[150] Nassif, A.B., Xu, W. and Freitas, W. An investigation on the selection of filter topologies for passive filter applications. *IEEE Transactions on Power Delivery*, *24*(3), pp.1710-1718, 2009.

[151] Sahoo, B., Alhaider, M.M. and Rout, P.K. Power quality and stability improvement of microgrid through shunt active filter control application: An overview. *Renewable Energy Focus*, *44*, pp.139-173, 2023.

[152] Chauhan, S.K., Shah, M.C., Tiwari, R.R. and Tekwani, P.N. Analysis, design and digital implementation of a shunt active power filter with different schemes of reference current generation. *IET Power Electronics*, *7*(3), pp.627-639, 2014.

[153] Khan, A., Jaffery, M.H., Javed, Y., Arshad, J., Rehman, A.U., Khan, R., Bajaj, M. and Kaabar, M.K. Hardware-in-the-Loop Implementation and Performance Evaluation of Three-Phase Hybrid Shunt Active Power Filter for Power Quality Improvement. *Mathematical Problems in Engineering*, *2021*(1), p.8032793, 2021.

[154] Sundaram, E. and Venugopal, M. On design and implementation of three phase three level shunt active power filter for harmonic reduction using synchronous reference frame theory. *International Journal of Electrical Power & Energy Systems*, *81*, pp.40-47, 2016.

[155] Czarnecki, L. Comparison of instantaneous reactive power p–q theory with theory of the current's physical components. *Electrical Engineering*, *85*, pp.21-28, 2003.

[156] Pouresmaeil, E., Montesinos-Miracle, D., Gomis-Bellmunt, O. and Sudrià-Andreu, A. Instantaneous active and reactive current control technique of shunt active power filter based on the three-level NPC inverter. *European Transactions on Electrical Power*, *21*(7), pp.2007-2022, 2011.

[157] Golestan, S., Monfared, M. and Freijedo, F.D. Design-oriented study of advanced synchronous reference frame phase-locked loops. *IEEE Transactions on Power Electronics*, *28*(2), pp.765-778, 2012.

[158] Shakerighadi, B., Ebrahimzadeh, E., Taul, M.G., Blaabjerg, F. and Bak, C.L. Modeling and adaptive design of the SRF-PLL: Nonlinear time-varying framework. *IEEE Access*, *8*, pp.28635-28645, 2020.

[159] Abdusalam, M., Poure, P., Karimi, S. and Saadate, S. New digital reference current generation for shunt active power filter under distorted voltage conditions. *Electric Power Systems Research*, *79*(5), pp.759-765, 2009.

[160] Patnaik, S.S. and Panda, A.K. Power quality enhancement using a novel SAPF control scheme employing high selectivity filter. *International Journal of Emerging Electric Power Systems*, *25*(3), pp.367-381, 2024.

[161] Barik, P.K., Shankar, G. and Sahoo, P.K., Power quality assessment of microgrid using fuzzy controller aided modified SRF based designed SAPF. *International Transactions on Electrical Energy Systems*, *30*(4), pp.12289, 2020.

[162] Golestan, S., Monfared, M. and Freijedo, F.D. Design-oriented study of advanced synchronous reference frame phase-locked loops. *IEEE Transactions on Power Electronics*, *28*(2), pp.765-778, 2012.

[163] Al-Ammar, E.A., Ul-Haq, A., Iqbal, A., Jalal, M. and Anjum, A. SRF based versatile control technique for DVR to mitigate voltage sag problem in distribution system. *Ain Shams Engineering Journal*, *11*(1), pp.99-108, 2020.

[164] Gautam, S., Xiao, W., Ahmed, H. and Lu, D.D.C. Enhanced single-phase phase locked loop based on complex-coefficient filter. *IEEE Transactions on Instrumentation and Measurement*, *71*, pp.1-8, 2022.

[165] Monfared, M., Golestan, S. and Guerrero, J.M. Analysis, design, and experimental verification of a synchronous reference frame voltage control for single-phase inverters. *IEEE Transactions on Industrial Electronics*, *61*(1), pp.258-269, 2013..

[166] Pal, K., Kumar, S., Singh, B. and Kandpal, T.C. Improved phase-locked loop-based control for grid-integrated PV system. *IET Renewable Power Generation*, *14*(5), pp.705-712, 2020.

[167] Pichan, M., Seyyedhosseini, M. and Hafezi, H. A new DeadBeat-based direct power control of shunt active power filter with digital implementation delay compensation. *IEEE Access*, *10*, pp.72866-72878, 2022.

[168] Mohammed, N., Zhou, W. and Bahrani, B. Double-synchronous-reference-frame-based power-synchronized PLL-less grid-following inverters for unbalanced grid faults. *IEEE Open Journal of Power Electronics*, *4*, pp.474-486, 2023.

[169] Xiao, P., Corzine, K.A. and Venayagamoorthy, G.K. Multiple reference frame-based control of three-phase PWM boost rectifiers under unbalanced and distorted input conditions. *IEEE Transactions on Power Electronics*, *23*(4), pp.2006-2017, 2008.

[170] Al-Ammar, E.A., Ul Haq, A., Iqbal, A., Ko, W., Jalal, M., Anjum, M.A., Choi, H.J. and Kang, H.K. Synchronous reference frame theory based intelligent controller for current THD reduction. *Journal of Electrical Engineering & Technology*, *16*, pp.2917-2936, 2021.

[171] Escobar, G., Ibarra, L., Valdez-Resendiz, J.E., Mayo-Maldonado, J.C. and Guillen, D. Nonlinear stability analysis of the conventional SRF-PLL and enhanced SRF-EPLL. *IEEE Access*, *9*, pp.59446-59455, 2021.

[172] Barik, P.K., Shankar, G., Sahoo, P.K., Elavarasan, R.M., Kumar, S., Ibanez, F.M., Abou Houran, M., Srivastava, A.K. and Terzija, V. A novel negative feedback phase locked loop-based reference current generation technique for shunt active power filter. *International Journal of Electrical Power & Energy Systems*, *153*, pp.109389, 2023.

[173] Dubey, A.K., Mishra, J.P. and Kumar, A. Modified CCF based shunt active power filter operation with dead-band elimination for effective harmonic and unbalance compensation in 3-phase 3-wire system. *IEEE Transactions on Power Delivery*, *37*(3), pp.2131-2142, 2021

[174] Zainuri, M.A.A.M., Radzi, M.A.M., Soh, A.C., Mariun, N. and Rahim, N.A. DC-link capacitor voltage control for single-phase shunt active power filter with step size error cancellation in self-charging algorithm. *IET Power Electronics*, *9*(2), pp.323-335, 2016.

[175] de Araujo Ribeiro, R.L., Rocha, T.D.O.A., de Sousa, R.M., dos Santos, E.C. and Lima, A.M.N. A robust DC-link voltage control strategy to enhance the performance of shunt active power filters without harmonic detection schemes. *IEEE Transactions on Industrial Electronics*, *62*(2), pp.803-813, 2014.

[176] Zhou, J., Yuan, Y. and Dong, H. Adaptive DC-link voltage control for shunt active power filters based on model predictive control. *IEEE Access*, *8*, pp.208348-208357, 2020.

[177] Chaoui, A., Gaubert, J.P., Krim, F. and Champenois, G. PI controlled three-phase shunt active power filter for power quality improvement. *Electric Power Components and Systems*, *35*(12), pp.1331-1344, 2007

[178] Patel, R. and Panda, A.K. Real time implementation of PI and fuzzy logic controller based 3-phase 4-wire interleaved buck active power filter for mitigation of harmonics with id–iq control strategy. *International Journal of Electrical Power & Energy Systems*, *59*, pp.66-78, 2014.

[179] Karuppanan, P. and Mahapatra, K.K. PI and fuzzy logic controllers for shunt active power filter-A report. *ISA Transactions*, *51*(1), pp.163-169, 2012.

[180] Mishra, A.K., Ray, P.K., Mallick, R.K., Mohanty, A. and Das, S.R. Adaptive fuzzy controlled hybrid shunt active power filter for power quality enhancement. *Neural Computing and Applications*, *33*, pp.1435-1452, 2021.

[181] Panda, A.K. and Mikkili, S. FLC based shunt active filter (p–q and Id–Iq) control strategies for mitigation of harmonics with different fuzzy MFs using MATLAB and real-time digital simulator. *International Journal of Electrical Power & Energy Systems*, *47*, pp.313-336, 2013.

[182] Saad, S. and Zellouma, L. Fuzzy logic controller for three-level shunt active filter compensating harmonics and reactive power. *Electric Power Systems Research*, *79*(10), pp.1337-1341, 2009.

[183] Nabae, A., Ogasawara, S., and Akagi, H. A novel control scheme for current-controlled PWM inverters. *IEEE Transactions on Industry Applications*, (4), 697-701, 1986.

[184] Mao, H., Yang, X., Chen, Z., and Wang, Z. A hysteresis current controller for single-phase three-level voltage source inverters. *IEEE Transactions on Power Electronics*, *27*(7), pp.3330-3339, 2012

[185] Holmes, D.G., Davoodnezhad, R. and McGrath, B.P. An improved three-phase variable-band hysteresis current regulator. *IEEE Transactions on power electronics*, *28*(1), pp.441-450, 2012.

[186] Mohanty, A., Ray, P.K., Das, S.R., Soudagar, M.E.M., Ramesh, S., Khan, T.Y., Almakayeel, N., Ali, M.M. and Bashir, M.N., Enhancing power quality in contemporary utility systems: A comprehensive analysis of active power filters and control strategies. *Energy Reports*, *11*, pp.5575-5592, 2024.

[187] Suresh, Y., Panda, A.K. and Suresh, M. Real-time implementation of adaptive fuzzy hysteresis-band current control technique for shunt active power filter. *IET Power Electronics*, *5*(7), pp.1188-1195, 2012.

[188] Barik, P.K., Samal, S., Gupta, D.K., Appasani, B., Jha, A.V., Islam, M.M. and Ustun, T.S., Split-source inverter with adaptive control scheme-based shunt active power filter for power quality improvement. *IET Power Electronics*, 2024.

[189] Kwon, B.H., Kim, T.W. and Youm, J.H. A novel SVM-based hysteresis current controller. *IEEE Transactions on Power Electronics*, *13*(2), pp.297-307, 1998.

[190] Bose, B.K. An adaptive hysteresis-band current control technique of a voltage-fed PWM inverter for machine drive system. *IEEE Transactions on Industrial Electronics*, *37*(5), pp.402-408, 1990.

[191] Radmanesh, H. and Gharehpetian, G.B., Harmonic distortion reduction of commercial airplane electrical power system using fuzzy logic based current control of active power filter. *International Transactions on Electrical Energy Systems*, *31*(4), pp.e12811, 2021.

[192] Durna, E. Adaptive fuzzy hysteresis band current control for reducing switching losses of hybrid active power filter. *IET Power Electronics*, *11*(5), pp.937-944, 2018.

[193] Karuppanan, P., Active power filter using a novel adaptive fuzzy hysteresis current controller. *International Journal of Power Electronics*, *10*(4), pp.315-332, 2019.

[194] Pazhanimuthu, C. and Ramesh, S. Grid integration of renewable energy sources (RES) for power quality improvement using adaptive fuzzy logic controller-based series hybrid active power filter (SHAPF). *Journal of Intelligent & Fuzzy Systems*, *35*(1), pp.749-766, 2018

[195] Mikkili, S. and Panda, A.K. Review of RT-LAB and steps involved for implementation of a simulink model from MATLAB to REAL-TIME. *International Journal of Emerging Electric Power Systems*, *14*(6), pp.641-658, 2013.

[196] Ravinder, K. and Bansal, H.O. Investigations on shunt active power filter in a PV-wind-FC based hybrid renewable energy system to improve power quality using hardware-in-the-loop testing platform. *Electric Power Systems Research*, *177*, pp.105957, 2019.

[197] Acharya, D.P., Hannon, N., Choudhury, S., Nayak, N. and Satpathy, A. Design and hardware in loop testing of an intelligent controller for power quality improvement in a complex micro grid. *Energy Reports*, *9*, pp.4135-4156, 2023.

[198] Kumar, R. and Bansal, H.O. Hardware in the loop implementation of wavelet-based strategy in shunt active power filter to mitigate power quality issues. *Electric Power Systems Research*, *169*, pp.92-104, 2019.

[199] Govind, A., Jayaswal, K., Tayal, V.K. and Kumar, P. Simulation and real time implementation of shunt active power filter for power quality enhancement using adaptive neural network topology. *Electric Power Systems Research*, *228*, pp.110042, 2024.

[200] Kumar, R. Fuzzy particle swarm optimization control algorithm implementation in photovoltaic integrated shunt active power filter for power quality improvement using hardware-in-the-loop. *Sustainable Energy Technologies and Assessments*, *50*, pp.101820, 2022.

[201] Bey, H., Krim, F. and Gherouat, O. FPGA-Based Hardware in the Loop of Optimized Synergetic Controller for Active Power Filter. *International Transactions on Electrical Energy Systems*, *2023*(1), pp.5810353, 2023.

List of Publications

International Journals

Published

1. **Barik PK**, Shankar G, and Sahoo PK. Power quality assessment of microgrid using fuzzy controller aided modified SRF based designed SAPF. *International Transactions on Electrical Energy Systems. 2020, 30(4), pp. e12289*. SCI, (IF:2.860), (Q2)

2. **Barik PK**, Shankar G, Sahoo PK, Elavarasan RM, Kumar S, Ibanez FM, Abou Houran M, Srivastava AK. and Terzija V. A novel negative feedback phase locked loop-based reference current generation technique for shunt active power filter. *International Journal of Electrical Power & Energy Systems, 2023, 153, pp.109389*. SCI, (IF:5.2), (Q1)

Communicated

Barik PK, Shankar G, Sahoo PK. Power quality enhancement using a novel fuzzy-inverted error deviation controller-based shunt active power filter. (Heliyon**,** Elsevier**)**

International Conferences/Book Chapters

Published

1. **Barik PK**, Shankar G, Sahoo PK. Dc-link capacitor voltage stabilization of a shunt active power filter using fuzzy logic controller under dynamic loading condition. InProceedings of Symposium on Power Electronic and Renewable Energy Systems Control: In Proceedings of Symposium on Power Electronic and Renewable Energy Systems Control*: PERESC 2020*, pp. 403-414. Singapore: Springer Singapore, 2021.

2. **Barik PK**, Shankar G, Sahoo PK. Performance assessment of MSRF-FLC-AFHCC control strategy for shunt active power filters to mitigate power quality issues. In *AIP Conference Proceedings*, 2022, Vol. 2681, no. 1. AIP Publishing.

CURRICULUM VITA

Prasanta Kumar Barik was born on 1983 at Jatni, Bhubaneswar, Odisha, India. He received his B.Tech. degree in Electrical Engineering from Utkal University in the year 2005, India, and M.Tech. degree in Power Electronics and Drives from Kalinga Institute of Industrial Technology, India in the year 2009. He is pursuing his Ph.D. degree at Indian Institute of Technology (Indian School of Mines) Dhanbad, India from 2017. His current research interests include power quality improvement and application of power electronics with non-conventional energy sources. Currently, he is working in the capacity of Assistant Professor in the Department of Mechanical and Electrical Engineering, CAET, OUAT, Bhubaneswar, Odisha, India.

He will be available at *prasantbarik05@gmail.com*